AVERTISSEMENT

Ce document est le fruit d'un long travail approuvé par le jury de soutenance et mis à disposition de l'ensemble de la communauté universitaire élargie.

Il est soumis à la propriété intellectuelle de l'auteur. Ceci implique une obligation de citation et de référencement lors de l'utilisation de ce document.

D'autre part, toute contrefaçon, plagiat, reproduction illicite encourt une poursuite pénale.

Contact : ddoc-theses-contact@univ-lorraine.fr

LIENS

Code de la Propriété Intellectuelle. articles L 122. 4
Code de la Propriété Intellectuelle. articles L 335.2- L 335.10
http://www.cfcopies.com/V2/leg/leg_droi.php
http://www.culture.gouv.fr/culture/infos-pratiques/droits/protection.htm

UNIVERSITÉ DE LORRAINE

École Doctorale "Informatique Automatique Électronique-Électrotechnique Mathématiques"
Département de Formation Doctorale "Électronique-Électrotechnique"

THÈSE

Présentée à

L'UNIVERSITÉ DE LORRAINE

En vue de l'obtention du

DOCTORAT DE L'UNIVERSITÉ DE LORRAINE
Spécialité: Génie Électrique

Soutenue par

Songklod SRIPRANG

Master en Génie Electrique de
Rajamangala University of Technology Thanyaburi (RMUTT) – Thaïlande

---

High-Performance Nonlinear Control for Permanent Magnet Assisted Synchronous Reluctance Motor

---

Soutenue publiquement le 14 Décembre 2021 devant le jury :

Président	Prof. Manuela SECHILARIU	Univ. de Technologie de Compiègne
Rapporteurs	Prof. Fei GAO	Univ. de Technologie de Belfort Montbéliard
	Prof. Surin KHOMFOI	King Mongkut's Institute of Technology Ladkrabang, Thaïlande
Examinateurs	Prof. Babak NAHID-MOBARAKEH	Univ. de Lorraine, GREEN (Directeur de thèse)
	Prof. Phatiphat THOUNTHONG	King Mongkut's University of Technology North Bangkok, Thaïlande
	Prof. Noureddine TAKORABET	Univ. de Lorraine, GREEN (Co-directeur de thèse)
Invités	Ass. Prof. Panarit SETHAKUL	King Mongkut's University of Technology North Bangkok, Thaïlande

---

Thèse préparée au Groupe de Recherche en Énergie et Électrique de Nancy-UR4366

DEDICATION

This work is wholeheartedly dedicated to my beloved parents, who have been my source of inspiration and gave me strength. When I thought of giving up, who continually provides moral, spiritual, emotional, and financial support, my love for you can never be quantified. Much appreciated; thank you.

ACKNOWLEDGMENTS

I would like to first express my deepest gratitude to the lord of Buddha Siddhartha Gotama Buddha, who is exemplary of endeavor. I have always been meditating according to his sutras and suggestions, which had led to deep concentration. Following this cultivation, I had accomplished my thesis work. Second, express my deepest gratitude to my family. I could not have accomplished my work without their support.

I would like to express my heartfelt appreciation to my advisors, Prof. Phatiphat THOUNTHONG, Prof. Noureddine TAKORABET, and Prof. Babak NAHID-MOBARAKEH's support continuous help. Their knowledge, invaluable guidance, understanding, and patience inspired the completion of this thesis. I am very grateful to work with such as insightful and caring professor.

I express my gratitude to Prof. Farid MEIBODY-TABAR, Prof. Serge PIERFEDERICI, and Dr. Jean Philippe MARTIN to supervise the committee thesis. Furthermore, I would like to express my gratitude to Associate Prof. Damien Guilbert to give helping me. Their comments and the fruitful discussions that we had helped me increase the quality of my work. I would also like to thank Prof. Noureddine TAKORABET, director of the GREEN laboratory, for his help and support. He made many efforts to make this project available to us. I would also like to thank all my colleagues in the laboratory of GREEN for their help and support. Dr. Adrien Corne, Dr. Davide Dell'isola, Dr. Shengzhao Pang, Dr. Hamidreza Zandi, Dr. Thibaud Plazenet, Dr. Milad Bahrami, Peyman Haghgooei, Abderrahmane Djaouti, Maxime Lapique and Nesser Taghavi thank you all for helping me. I can remember my first days in this laboratory when Mme. Sylvie Colinet and Latifa Zoua were helping me to advance my administrative staff. Thanks, Sylvie and Latifa, for helping me with administrative issues while always smiling.

Finally, I also owe gratitude to all my Thai friends who always supported me in Nancy, France. Paisak POOLPHAKA, Benjamas POOLPHAKA, and Apinya SIANGSANOH. Thank you for being my friend. Thank you for being my friend.

ABSTRACT

The electrification of transportation is a relevant solution to reducing greenhouse gas emissions. Indeed, new European standards impose increasingly restrictive limits on CO2 emissions per km. This context is an essential industrial issue for automobile manufacturers. Therefore, the industries are moving towards electric vehicles (EVs) in which an electric powertrain unit is present. This unit consists of an electrical machine powered by a static power electronic converter connected to an electrical energy source and storage. Different topologies have been studied for more than two decades for electric traction, and several solutions have been marketed. As a result, these products are increasingly light, reliable, and efficient while respecting the constraints of the automobile manufacturers on the costs.

Recently, permanent magnet assisted (PMa)-synchronous reluctance motors (SynRM) have been considered a rare-earth-free machine possible alternative motor drive for high-performance applications suitable for EV powertrain units. However, in order to have an efficient motor drive, performing three steps in the design of the overall drive is not inevitable. These steps are design optimization of the motor, identifying the motor parameter, and implementing an advanced control system to ensure optimum operation. Therefore, this dissertation deal with high-performance nonlinear control of PMa-SynRM to find out the limitation of exiting nonlinear control system.

The differential flatness-based control is first developed for the PMa-SynRM drive system. As it is a model-based control, the system performance relies on system model parameters, i.e., resistance, inertia, and external torque disturbance. Next step, model-free control is presented to be used in the control of both the SPMSM and PMa-SynRM. Finally, this thesis has achieved the main objective of finding out the high-performance nonlinear control of PMa-SynRM. Using a prototype PMa-SynRM drive as a test bench provided by GREEN Lab. at Université de Loraine, this paper gives an exhaustive description of an MFC's design procedure applied to the combined control of the motor speed and current. After a brief introduction of the MPC fundamentals, the design is illustrated in detail, giving a step-by-step discussion of the main critical points and the hints for their successful handling. Suggestions for extending the design to different drive controllers are also included. Simulations and numerous experimental results highlight MFC's promising features and characteristics applied to PMSM drives. As the last contribution, the MFC potentials pointed out in this dissertation should stimulate further exploration and study on this type of controller to achieve the familiarity required to transfer the results to practical applications.

Keyword: Permanent Magnet Assisted Synchronous Reluctance Motor, PMa-SynRM, Differential flatness-based control, Model-free control, Electric vehicle.

RÉSUMÉ

Modélisation, conception et commande de machines synchro-réluctantes assistées par des aimants permanents

L'électrification des transports est l'une des solutions pertinentes pour réduire les émissions de gaz à effet de serre. En effet, les nouvelles normes européennes imposent des limites de plus en plus restrictives sur les émissions de CO2 par km. Ce contexte constitue un enjeu industriel essentiel pour les constructeurs automobiles. Ainsi, les industriels s'orientent vers des véhicules électriques (VE) dans lesquels un groupe motopropulseur électrique est présent. Cette unité est constituée d'une machine électrique alimentée par un convertisseur électronique de puissance statique connecté à une source d'énergie électrique et à un stockage. Différentes topologies ont été étudiées depuis plus de deux décennies pour la traction électrique, et plusieurs solutions ont été commercialisées. En conséquence, ces produits sont de plus en plus légers, fiables et performants tout en respectant les contraintes des constructeurs automobiles sur les coûts.

Récemment, les moteurs à réluctance synchrone (SynRM) assistés par aimant permanent (PMa) ont été considérés comme une machine sans terre rare possible pour des applications de haute performance adaptées aux groupes motopropulseurs des VE. Cependant, pour obtenir un moteur d'entraînement efficace, trois étapes de la conception de l'entraînement global ne sont pas inévitables. Ces étapes sont l'optimisation de la conception du moteur, l'identification des paramètres du moteur et la mise en œuvre d'un système de commande avancé pour assurer un fonctionnement optimal.

Par conséquent, cette thèse traite de la commande non linéaire haute performance du PMa-SynRM afin de découvrir les limites des systèmes de commande non linéaires existants.

La commande différentielle basée sur la planéité est d'abord développée pour le système d'entraînement PMa-SynRM. Comme il s'agit d'une commande basée sur un modèle, les performances du système dépendent des paramètres du modèle du système, c'est-à-dire la résistance, l'inertie et la perturbation du couple externe. Ensuite, une commande sans modèle est présentée pour être utilisée dans la commande du SPMSM et du PMa-SynRM. Enfin, cette thèse a atteint l'objectif principal de découvrir la commande non linéaire haute performance du PMa-SynRM. En utilisant un prototype de PMa-SynRM comme banc d'essai fourni par le GREEN Lab. de l'Université de Loraine, cet article donne une description exhaustive de la procédure de conception d'un MPC appliqué à la commande

combinée de la vitesse et du courant du moteur. Après une brève introduction des principes fondamentaux du MPC, la conception est illustrée en détail, avec une discussion étape par étape des principaux points critiques et des conseils pour les traiter avec succès. Des suggestions pour étendre la conception à différentes commandes d'entraînement sont également incluses. Des simulations et de nombreux résultats expérimentaux mettent en évidence les caractéristiques prometteuses du MFC appliqué aux variateurs PMSM. En guise de dernière contribution, les potentiels du MFC soulignés dans cette thèse devraient stimuler une exploration et une étude plus poussées de ce type de commande afin d'atteindre la familiarité requise pour transférer les résultats vers des applications pratiques.

TABLE OF CONTENTS

DEDICATION			I
ACKNOWLEDGMENTS			II
ABSTRACT			III
RÉSUMÉ			IV
CONTENTS			VI
LIST OF FIGURES			IX
LIST OF TABLES			XIII
1.		**INTRODUCTION**	**1**
1.1.		Background of the study	2
1.2.		The objective of this work	5
1.3.		Contributions	6
1.4.		State-of-the-art powertrain inverter for automotive applications	8
1.5.		Literature review of high-performance nonlinear control	10
2.		**MODELING, OPERATION, AND CONTROL OF PERMANENT MAGNET SYNCHRONOUS MACHINES**	**14**
Introduction			15
2.1.		The Concordia/Clack and Park transformations	15
	2.1.1.	Park transformation preserving amplitude	17
	2.1.2.	The Clarke transformation	18
	2.1.3.	The Park transformation preserving power	19
	2.1.4.	The Concordia transformation	20
	2.1.5.	Transformation matrices	20
2.2.		Permanent Magnet Synchronous Motor	21
	2.2.1.	Description	21
	2.2.2.	Classification of Permanent Magnet Synchronous Motors (PMSMs)	22
2.3.		Permanent Magnet Assisted Synchronous Reluctance Motor (PMa-SynRM)	23
2.4.		Mathematical model of PM synchronous motor	27
	2.4.1.	Model of SPMSM in the rotating reference frame	27
	2.4.2.	Model of IPMSM in the rotating reference frame	28
	2.4.3.	Model of the PMa-SynRM in the rotating reference frame	29
	2.4.4.	Motor torque	29
	2.4.5.	Mechanical motion equation	30
	2.4.6.	Nonlinear model in state-space representation	32
2.5.		Dynamic simulation of the IPMSM and SPMSM	35
2.6.		Dynamic simulation of the PMa-SynRM	36
2.7.		Model of pulse width modulated frequency inverter for PMSM supply	38
2.8.		Simulation of the sinusoidal PWM for supply PMSM	40
2.9.		Current and speed control of PMSM	42
	2.9.1.	Simulation and experimental validation of FOC for controlling PMSM	43
	2.9.2.	Simulation and experimental validation of FOC for controlling PMa-SynRM	51
2.10.		Conclusion	

3.	**DIFFERENTIAL FLATNESS-BASED CONTROL AND ONLINE STATE OBSERVER PARAMETER ESTIMATION**	**58**
Introduction		60
3.1.	A shot briefly differential flatness-based control and control law	60
3.1.1.	Differential flatness briefly:	60
3.1.2.	Control Law	61
3.2.	Applying the differential flatness-based control to SPMSM drive	62
3.2.1.	Design of a differential flatness-based control for SPMSM	63
3.2.2.	Trajectory planning	65
3.3.	Simulation and experimental validation of differential flatness-based controller for SPMSM	66
3.3.1.	Experimental setup	66
3.3.2.	Performance comparison of FOC with traditional PI controller and differential flatness-based control	68
3.4.	Application of the differential flatness-based control to PMa-SynRM	70
3.4.1.	Design of a differential flatness-based control for PMa-SynRM	71
3.4.2.	Differential flatness-based control for outer speed control loop	73
3.5.	Simulation and experimental validation of differential flatness-based controller PMa-SynRM	75
3.6.	State observer parameter estimation	86
3.6.1.	Luenberger observer	87
3.6.2.	Improve performance of differential flatness-based control for SPMSM by the Luenberger state observer	88
3.6.3.	Simulation results of the Luenberger state observer applied to parameter estimation for the SPMSM	90
3.6.4.	Enhance the performance of the differential flatness-based control based on the Luenberger state observer applied for the PMa-SynRM drive	94
3.6.5.	Experimental validation of the differential flatness-based control based on the Luenberger state observer	97
3.6.5.1.	Performance of parameter estimation with Luenberger Observer	97
3.6.5.2.	Performance of Disturbance Rejection	100
3.6.6.	Nonlinear Online Parameter Estimation	100
3.6.6.1.	Lyapunov-based design of the state observer	100
3.6.6.2.	Exponential stability of the proposed observer	101
3.6.7.	Validation of the proposed observer for SPMSM	103
3.6.7.1.	Observer design for SPMSM	103
3.6.7.2.	Simulation and experimental results	104
3.6.7.3.	Variable loss estimation	106
3.6.8.	Validation of the proposed observer for PMa-SynRM	108
3.6.8.1.	Observer design for PMa-SynRM	108
3.6.8.2.	Simulation of the proposed observer applied to PMa-SynRM	109
3.6.8.3.	Experimental validation of the proposed observer applied to the PMa-SynRM	112
3.7.	Conclusion	115
4.	**MODEL-FREE CONTROL**	**116**
Introduction		117
4.1.	A shot briefly model-free control and control law	119
4.1.1.	Model-free control briefly:	119

4.1.2. Control law and intelligent PI controller 120
4.1.3. Controller design 121
4.2. Applying model-free control to SPMSM drive 122
4.2.1. Model-free control of SPMSM: development 123
4.2.2. Trajectory planning 126
4.3. Simulation and experimental validation of model-free control applied to SPMSM 126
4.3.1. Test bench setup 126
4.3.2. Simulation 128
4.3.3. Experimental validation of SPMSM drive based on the model-free control 134
4.4. Applying model-free control to PMa-SynRM drive 139
4.4.1. Model-free control of PMa-SynRM driving development 139
4.4.2. Trajectory planning 143
4.5. Simulation and experimental validation of the model-free control applied to PMa-SynRM 143
4.5.1. Test Bench Setup 143
4.5.2. Simulation 145
4.5.3. Experimental validation of PMa-SynRM drive based on the model-free control 148
4.6. Conclusion 153
CONCLUSION **154**
FUTURE WORK **158**
PUBLICATIONS **159**
APPENDIX: FRENCH VERSION OF THE INTRODUCTION **161**
REFERENCES **179**

LIST OF FIGURES

Figure 1.1	Traction motor of Tesla Model S based on AC induction motor [photo courtesy of CHARGED Electric Vehicles Magazine].	2
Figure 1.2	Classification of synchronous machines by torque generation mechanism.	3
Figure 1.3	Tesla Model 3 drive unit [photo courtesy of CHARGED Electric Vehicles Magazine https://insideevs.com].	4
Figure 1.4	Tesla Model 3 powertrain unit.	4
Figure 1.5	Stator and rotor part of Tesla Model 3 traction motor [photo courtesy of CHARGED Electric Vehicles Magazine Bloomberg].	5
Figure 1.6	Battery Electric Vehicles Inverter [photo courtesy of chargedevs.com].	8
Figure 1.7	Tesla's SiC MOSFET inverter sourced from ST Microelectronics.	9
Figure 1.8	Stator current control based on hysteresis comparators directly generates gate signals to the three-phase inverter.	11
Figure 1.9	Sliding mode control definition.	11
Figure 2.1	Definition of *abc* to *dq* transformation.	16
Figure 2.2	The Clarke /Concordia-Park transformation.	17
Figure 2.3	PMSM Rotor permanent magnet layout: (a) surface mounted permanent magnet, (b) inset permanent magnet, (c) interior permanent magnets, (d) flux concentrating.	22
Figure 2.4	PMa-SynRM rotor structure.	24
Figure 2.5	Single saliency RM rotor structure.	25
Figure 2.6	Flux barrier type rotor of the reluctance motor.	25
Figure 2.7	Four-pole transversally-laminated PM assisted rotor design.	26
Figure 2.8	Block scheme of the SPMSM and IPMSM in rotating *d*, *q* frame.	32
Figure 2.9	Block scheme of the PMa-SynRM in rotating *d*, *q* frame.	32
Figure 2.10	Diagram representation of the simulation model for the PMSM.	34
Figure 2.11	Simulink model expressing the current calculation block of the SPMSM and IPMSM.	35
Figure 2.12	Simulink model expressing the flux calculation block of the SPMSM and IPMSM.	36
Figure 2.13	Simulink model expressing the calculation of the shaft speed for SPMSM and IPMSM.	36
Figure 2.14	Simulink model expressing the current calculation block of the PMa-SynRM.	37
Figure 2.15	Simulink model expressing the flux calculation block of the PMa-SynRM.	37
Figure 2.16	Simulink model expressing the calculation of the shaft speed for PMa-SynRM.	38
Figure 2.17	VSD inverter system powered PMSM block diagram.	38
Figure 2.18	The ideal inverter is implemented in the Simulink environment.	39
Figure 2.19	A produced voltage of six positions switching.	39
Figure 2.20	Simulation model of voltage source inverter circuit supplied to SPMSM.	40
Figure 2.21	Simulation results of VSD inverter supplied to the PMSM in which v_{AN}, v_{BN}, and v_{CN} are phase voltages, i_A, i_B, and i_C are phase currents.	42
Figure 2.22	Classification of PMSM control approaches.	43
Figure 2.23	Block diagram of the VSD powered SPMSM.	44
Figure 2.24	Block diagram of the FOC with PI controller for controlling SPMSM.	44
Figure 2.25	The setting of the controllers by choosing the crossover frequency in the frequency space.	46
Figure 2.26	Simulation results of the FOC with the PI controller applied to SPMSM.	47
Figure 2.27	Experimental results of the FOC with the PI controller controlling SPMSM.	48
Figure 2.28	Simulation results: The external torque disturbance of FOC with PI controller controlling the SPMSM.	49

Figure 2.29 Experimental results of the external torque disturbance rejection of the FOC with PI control applied to SPMSM. 50
Figure 2.30 Block diagram of the FOC with MTPA control for the PMa-SynRM. 51
Figure 2.31 MTPA curve of the studied PMa-SynRM. 53
Figure 2.32 Simulation of the copper losses minimization by the MPTA. 53
Figure 2.33 MPTA control of PMa-SynRM. 54
Figure 2.34 Experimental results: dynamic performance of speed reversal under constant torque operation. 55
Figure 2.35 Experimental results: dynamic performance of the disturbance rejection, (a) load torque turned on, (b) load torque turned off. 56
Figure 3.1 Differential flatness-based Control law's block diagram. 61
Figure 3.2 Control system of SPMSM based on differential flatness-based control diagram. 63
Figure 3.3 The natural frequency setting of the proposed controller. 66
Figure 3.4 Test Bench Setup. 67
Figure 3.5 Simulation Results: (a) FOC with the traditional PI controller. (b) Different flatness-based controller. 69
Figure 3.6 Simulation Results: The external disturbance rejection ability, (a) PI controller. (b) Differential flatness-based controller. 70
Figure 3.7 Different flatness-based control systems applied to PMa-SynRM. 72
Figure 3.8 Ψ_d, Ψ_q in the function of i_d and i_q of the prototype PMa-SynRM. 74
Figure 3.9 Simulation results: Inner current control loop response of the differential flatness-based control. 75
Figure 3.10 Simulation results: Disturbance rejection of the differential flatness-based control. 76
Figure 3.11 Simulation results: Inner current control loop response (a) *d*-axis current (b) *q*-axis current. 78
Figure 3.12 Simulation results: Inner current control loop response of the FOC with the PI controller. 79
Figure 3.13 Laboratory test bench setup of PMa-SynRM drive at UL. 80
Figure 3.14 Simulation results: dynamic performance of speed reversal. 81
Figure 3.15 Experimental results: dynamic performance of speed reversal. 81
Figure 3.16 Experimental results: Dynamic performance of different control approaches (a) FOC base PI controller. (b) Differential flatness-based control. 82
Figure 3.17 Experimental results: dynamic performance of speed reversal (a) FOC based PI controller (b) Differential flatness-based control. 83
Figure 3.18 Experimental results: Disturbance rejection (a) FOC based PI controller (b) Differential flatness-based control. 84
Figure 3.19 Equivalent circuit of PMSM drive. 86
Figure 3.20 Differential flatness-based control with state observer based on Luenberger Observer (LOB). 90
Figure 3.21 Simulation results: Comparison between the flatness-based control with and without the Luenberger observer. 91
Figure 3.22 Simulation results: Dynamic performance of the proposed control scheme (a) *d*-axis and *q*-axis currents (b) T_L and estimated v_{tq} (c) the current of phase A and C. 92
Figure 3.23 Simulation results: (a) Dynamic performance of the proposed control without an observer (b) The proposed control based on the Luenberger state observer. 93
Figure 3.24 Differential flatness-based control based on the reduced-order Luenberger state observer block diagram applied to PMa-SynRM. 95

Figure 3.25 Simulation results: Dynamic performance of the proposed control based on the reduced-order Luenberger state observer applied to PMa-SynRM. 96
Figure 3.26 Experimental results: Simulation and experimental results of T_L estimation based on the Luenberger state observer (a) Simulation. (b) Experimental. 98
Figure 3.27 Experimental results: Simulation and experimental results of v_{tq} estimation based on the Luenberger state observer. (a) Simulation. (b) Experimental. 98
Figure 3.28 Experimental results: Disturbance rejection of the differential flatness-based control based on the Luenberger state observer. 99
Figure 3.29 Simulation (left) and experimental (right) results: Comparison between the different state observers. 105
Figure 3.30 Experimental results: Dynamic performance of the external disturbance rejection. 107
Figure 3.31 Simulation results: Dynamic performance of the external disturbance rejection. 110
Figure 3.32 Simulation results: Dynamic performance of parameter variation. 111
Figure 3.33 Experimental results: Dynamic performance of the external disturbance rejection during suddenly adding load torque. 113
Figure 3.34 Experimental results: Dynamic performance of the external disturbance rejection during suddenly removing load torque. 114
Figure 4.1 Architecture of MBC and Model-Free Control (MFC) block diagram. 117
Figure 4.2 Categorization of the modern control system into MBC and MFC. 118
Figure 4.3 Control law of MFC. 120
Figure 4.4 The natural frequency setting of the proposed MFC. 122
Figure 4.5 SPMSM drive system based on model-free control diagram. 122
Figure 4.6 Control system of SPMSM based on model-free control diagram. 123
Figure 4.7 Test bench provided at KMUTNB, Bangkok. 127
Figure 4.8 Simulation results: Dynamic response of d-axis currents with the controller based on the model-free control. 128
Figure 4.9 Simulation results: Dynamic response of q-axis currents with the controller based on the model-free control. 129
Figure 4.10 Simulation results: Speed acceleration and deceleration. 130
Figure 4.11 Simulation results: R_s variation. 131
Figure 4.12 Simulation results: Disturbance rejection. 132
Figure 4.13 Simulation results: Speed reversal. 133
Figure 4.14 Test beach setup for SPMSM drive based on MFC. 134
Figure 4.15 Simulation results: d-axis current response by FOC based on the traditional PI controller. 135
Figure 4.16 Simulation results: d-axis current response based on MFC. 135
Figure 4.17 Experimental results: d-axis current response based on MFC. 136
Figure 4.18 Simulation and Experimental results of MFC applied to SPMSM drive (a) Simulation (b) Experimental. 137
Figure 4.19 Experimental results: Disturbance rejection of MFC applied to SPMSM drive. 138
Figure 4.20 VSD inverter system powered PMSM block diagram. 140
Figure 4.21 Control system of PMa-SynRM based on model-free control diagram. 140
Figure 4.22 Laboratory test bench setup of PMa-SynRM drive at UL. 145
Figure 4.23 Simulation results: Dynamic response of d-axis currents with the controller based on the model-free control. 146
Figure 4.24 Simulation results: Dynamic response of q-axis currents with the controller based on the model-free control applied to PMa-SynRM drive. 146

Figure 4.25 Simulation results: Simulated drive response to a 0–1000 rpm reference speed pulse. From top to bottom: speed reference and response, d- and q-currents, d- and q-voltages, and active region number of the MFC controller. 147
Figure 4.26 Simulation results: Disturbance rejection of MFC applied to PMa-SynRM drive. 148
Figure 4.27 Experimental result: d-axis response curve based on MFC. 149
Figure 4.28 Experimental result: q-axis response curve based on MFC. 150
Figure 4.29 Experimental result: speed acceleration curve based on MFC. 151
Figure 4.30 Experimental result: disturbance rejection based on MFC. 152

LIST OF TABLES

TABLE 2.1	Studied SPMSM Parameters	41
TABLE 2.2	Studied PMa-SynRM Parameters (linear case)	41
TABLE 2.3	Speed and current regulation parameters for PMa-SynRM	54
TABLE 3.1	Studied SPMSM Parameters for the differential flatness-based control development	67
TABLE 3.2	Speed/Current controller parameters	68
TABLE 3.3	PMa-SynRM Parameters for the differential flatness-based control development	74
TABLE 3.4	Speed/Current regulation parameters of the differential flatness-based control	74
TABLE 3.5	SPMSM parameters for the Luenberger development	90
TABLE 3.6	PMa-SynRM parameters for the Luenberger development	95
TABLE 4.1	Speed and Current regulation parameters of SPMSM drive based on model-free control	127
TABLE 4.2	SPMSM Parameters for the Model-Free Control development	134
TABLE 4.3	PMa-SynRM parameters (linear case) for the Model-Free Control development	144
TABLE 4.4	Speed and Current regulation parameters of PMa-SynRM drive based on Model-free Control	144

Chapter-1 INTRODUCTION

Contents

1.1. Background of the study
1.2. The objective of this work
1.3. Contributions
1.4. State-of-the-art powertrain inverter for automotive applications
1.5. Literature review of the high-performance nonlinear control of PMa-SynRM

1.1. Background of study

With the emergence of field-orientated control (FOC), which K. Hasse proposed at the end of the 1960s systems of AC induction motors and the development of semiconductor power devices, it was pointed out that, in theory, the induction motor can be controlled in the same way as the DC motor. Moreover, semiconductor power devices and microcomputers developed, and digital signal processing made it possible to build frequency converters for AC motors, allowing a sinusoidal three-phase current supply with continuous frequency control. Thus, in the 1980s, frequency converter fed AC drives using FOC were ready to challenge DC drives commercially. At present, the frequency converter fed induction machines is the most common choice in the industry when adjustable speed operation is required in the power range from a few hundred Watt to a few Mwatt. Moreover, recently, AC induction motors have been used in electric vehicles (EVs); for instance, as shown in Figure 1.1, the electric motor sits between the rear wheels of the Tesla Model S, contributing significantly to the 47/53-percent front/rear weight distribution. The motor is an AC-induction type, the basic principles of which were demonstrated in the 1880s by Nikola Tesla himself, and it does not need expensive rare earth metals [1] [2] [3]. The state-of-the-art Model S' motor achieves a high power-to-weight ratio. It generates 362 horsepower (according to the official specs) and only weighs 70 pounds with the coaxial rotor cooling. However, induction motors are characterized by relatively low efficiencies and power factors compared to permanent magnet motors. It is possible to improve the efficiency of high or medium power induction motors with an acceptable extra cost. Still, for low-power machines, the mechanical dimensions of the gaps remain a significant obstacle to obtaining high performance.

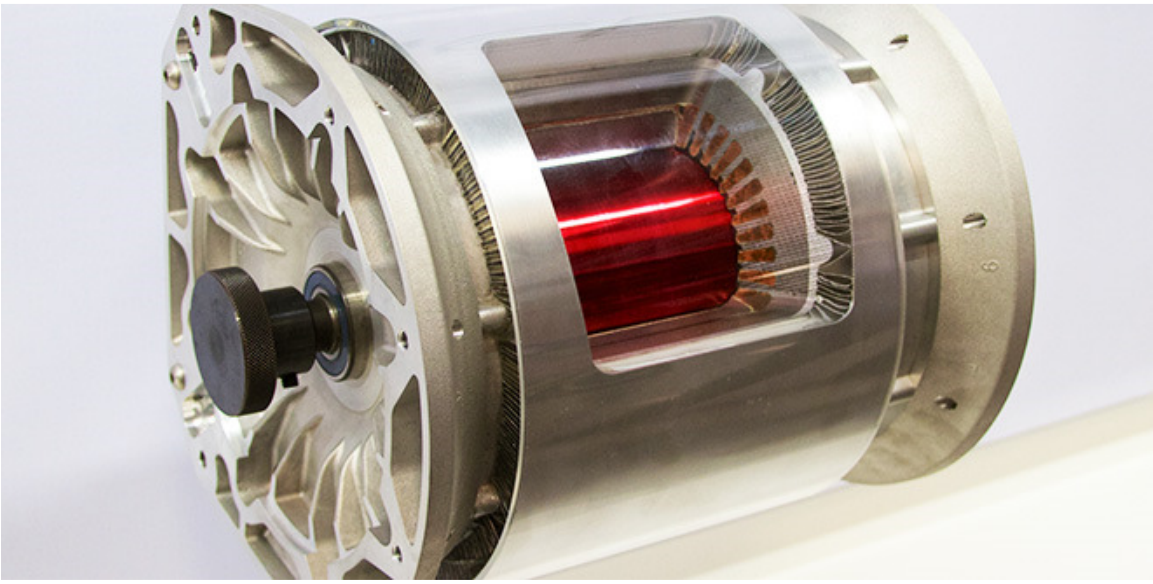

Figure 1.1 Traction motor of Tesla Model S based on AC induction motor [photo courtesy of CHARGED Electric Vehicles Magazine] [4].

Permanent magnet synchronous machines (PMSMs) have higher output torque and density than induction machines, but because there are so many permanent magnets, it has

become a problem to produce cheap electric motors with acceptable efficiency, and we want to avoid the use of rare earth permanent magnets. Alternatively, at least PMSM, minimize this number of permanent magnets in the design as much as possible, showing higher output torque and density than inductors, but the number of permanent magnets used in the design is essential. Furthermore, some disadvantages such as a sizeable *d*-axis current at high speed and the uncontrolled generator mode following unexpected inverter shutdowns restrict this motor's high-speed electric vehicle applications. The interior permanent magnet synchronous motor (IPMSM) has a high output factor and torque density, but the torque generated by this machine is mainly magnet torque, low reluctance torque, and saliency ratio (L_d/ L_q) to operate at a wide speed range operation. Moreover, it can offer a constant-power operation by a flux-weakening technique. Therefore, the state-of-the-art modern motor is revolutionized by the following illustration.

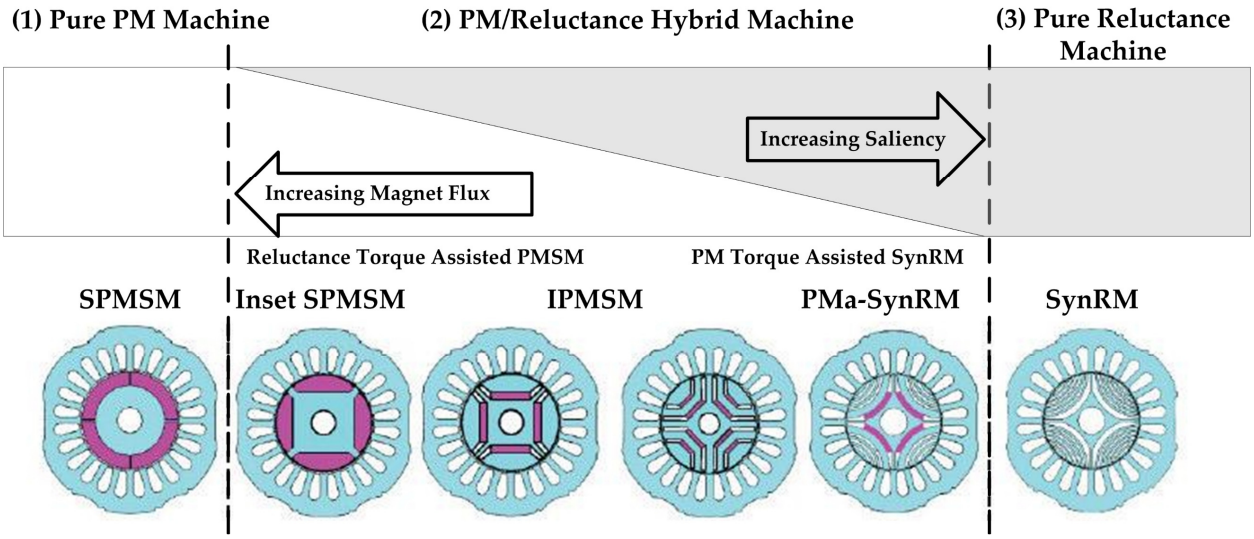

Figure 1.2 Classification of synchronous machines by torque generation mechanism.

The subsequent investigation can overcome the disadvantages mentioned above:

- Efforts to improve manufacturing technology ferromagnets by lowering product costs and looking for new alloys towards improving the quality of permanent magnets.
- Research to find appropriate solutions for the machine structure so that the magnetic optimization system will use inexpensive but high-performance magnetic magnets.
- Thanks to modern power semiconductors (i.e., SiC MOSET, GaN FET, and Wide bandgap semiconductors) usage and real-time digital signal processing, optimizing the frequency converter design and stabilizing the output is a possible machine.
- Research to achieve high-performance control for the state-of-the-art permanent magnet synchronous motor

According to the list described above, in Model 3, the Tesla company used an IPM-SynRM motor (Internal Permanent Magnet - Synchronous Reluctance Motor) [5] [6], also known as PMa-SynRM Permanent Magnet Assisted Synchronous Reluctance Motor [7].

In general, it is a type that combines Internal Permanent Magnet motor type with the Synchronous Reluctance Motor rotor type to achieve a more desired characteristic in EV application - high efficiency at low and high speeds [8]. Tesla is not the first to use this type of motor, but its version is considered one of the best (simply because of the high efficiency and range of Tesla cars).

Figure 1.3 shows Tesla Model 3 drive unit utilized Permanent Magnet Switched Reluctance Motor, and Figure 1.4 shows Tesla Model 3 powertrain unit. The stator and rotor instruction of the Tesla Model 3 traction motor is shown in Figure 1.5.



Figure 1.3 Tesla Model 3 drive unit [photo courtesy of CHARGED Electric Vehicles Magazine https://insideevs.com] [5] [6].

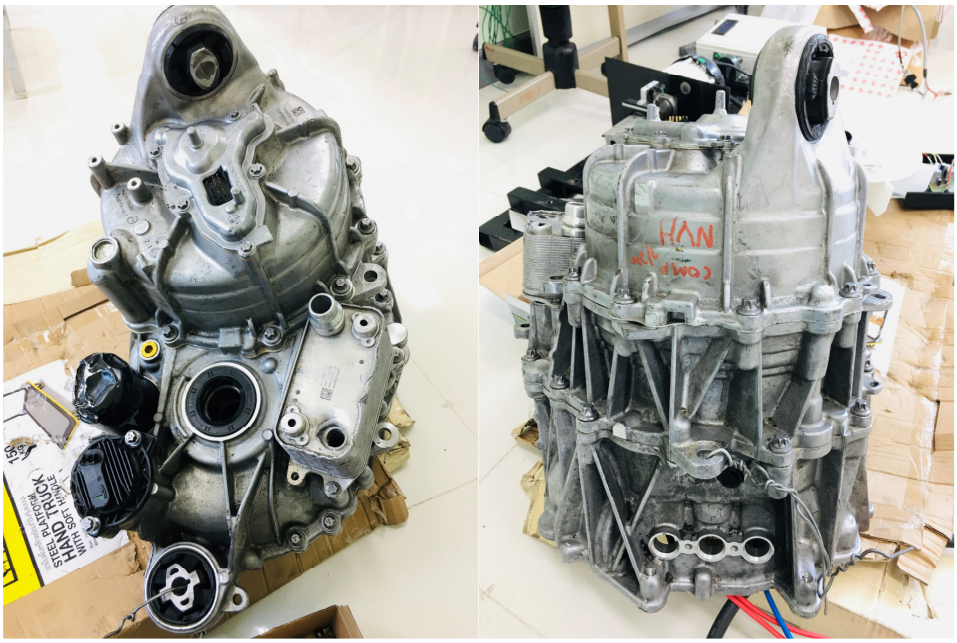

Figure 1.4 Tesla Model 3 powertrain unit.

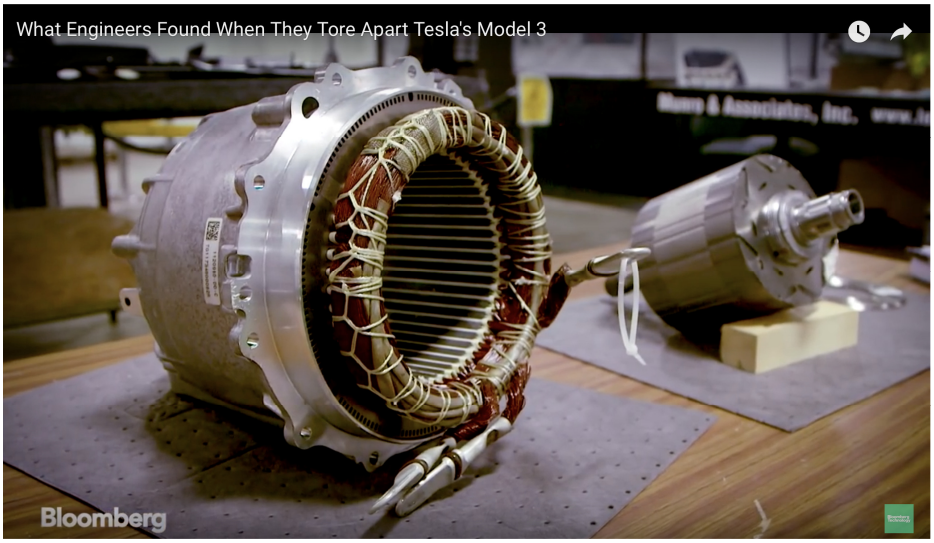

Figure 1.5 Stator and rotor part of Tesla Model 3 traction motor [photo courtesy of CHARGED Electric Vehicles Magazine Bloomberg] [9].

As it can observe, the state-of-the-art traction motor of the EV powertrain unit is interested in reducing the use of permanent magnets in order to increase much more wide speed operation.

Furthermore, More Electric Aircraft (MEA) [10] [11] has become the consensus in both industry and academia as next-generation aviation technology since this concept first arose in the 1990s. The MEA concept means using electric systems in applications that have traditionally been powered by hydraulic, mechanical, or pneumatic power [11]. Therefore, electric machines will replace these systems (i.e., hydraulically driven actuator, gearbox driven fuel and lubrication

pumps, and pneumatically driven compressor), which the PMSM will be a significant key player in these applications.

As explained above, the modern machine has a much more complicated structure, affecting the control system, and its model has become much more strongly nonlinear. Therefore, traditional control such as FOC based on PI controller does not have enough to provide high-performance for all conditions operating of these modern machines. These problems will be addressed in this thesis.

1.2. The objective of this work

1.2.1. Develop nonlinear control based on the model-based control (MBC) (i.e., differential flatness-based control) for surface-mount permanent magnet synchronous motor (SPMSM) and permanent magnet assisted synchronous reluctance motor (PMa-SynRM) to compare to the FOC based on the traditional PI controller.

1.2.2. Apply state observer based on Luenberger state observer and nonlinear state observer based on asymptotical stability and exponentially stability to enhance differential flatness-based control performance and the performance comparison between the different state observer taken to account for underlining the interest of each state observer approach.

1.2.3. Develop Model-Free Control (MFC) as a novel control approach to SPMSM and PMa-SynRM and demonstrate the performance comparison of MFC to MBC and FOC based on PI controller to underline the interest of the proposed MFC in terms of disturbance and parameter uncertainty rejection.

1.3. Contributions

All the work in this thesis considers the design of a control system in the field-oriented frame for rotating three-phase AC machines, which include surface-mount permanent magnet synchronous motor. It is a widespread drive for highly dynamic servo systems. Besides the permanent magnet assisted synchronous reluctance motor (PMa-SynRM), a rather exotic variant of a synchronous machine that the most promising rare-earth-free machine for the next generations of EVs and HEVs.

Both model-based differential flatness control and MFC schemes are carried out for these drive systems. Specific goals are highly performant control, i.e., a fast and precise reference response, and optimized control, i.e., exploiting the highest possible energy efficiency. Here, however, some limitations apply. A key issue is a sensitivity to uncertainties arising from nonlinearities, disturbances, noise, unmodeled interactions of the variables, or simply from approximate and inaccurate models. In this thesis, efficient solutions to these problems are proposed using state observers, both the linear state observer and nonlinear observer, as a design aid in order to make these techniques suitable for industrial practice.

The mathematical model of both SPMSM and PMa-SynRM is analyzed and validated by simulation based on the MATLAB/SIMULINK software environment in Chapter 2. Chapter 2 also proposed the FOC based on the traditional PI controller applied to SPMSM and PMa-SynRM. Moreover, the maximum torque per ampere (MTPA) is applied to the PMa-SynRM drive to optimize the inner current loop control of both the d-axis and q-axis current. The prototype PMa-SynRM practically carries out all the presented solutions at the Université de Lorraine.

The robustness of differential flatness-based control to both model parameter uncertainties and time-varying disturbances is discussed in Chapter 3. The differential flatness-based control is applied to both the SPMSM and PMa-SynRM drives. Simulation of the proposed control is performed by MATLAB/SIMULINK software, and experimental validation compared to the simulation is demonstrated. by the prototype PMa-SynRM in the laboratory. Moreover, a state observer based on Luenberger state observation compared to a nonlinear state observer based on asymptotical stability and exponentially stability is proposed to enhance the differential flatness-based control performance leading to a tradeoff between both methods. It can improve parametric robustness to a sufficient extent while maintaining good control performance. Furthermore, it robustly decouples the controller from the disturbance estimator, such that the disturbance attenuation mechanism can be tuned extremely fast. Then, time-varying disturbance effects such as those arising from the voltage drop across power electronic devices of the three-phase inverter and motor winding can be attenuated without explicitly identifying them.

The resulting control scheme is very performant; it has a strong tracking capability and, at the same time, provides good disturbance rejection. Furthermore, it is very robust to parametric uncertainties and less sensitive to measurable noise. These advantages are highlighted by comparison to FOC based on a traditional PI controller in Chapter 2 and by the experimental validation on the two named types of PMSM in Chapter 3.

Chapter 4 develops a novel nonlinear control approach based on unmodeled control called Model-Free Control (MFC). The MFC to both model parameter uncertainties and time-varying disturbances is discussed in Chapter 4. After a brief introduction of the MFC fundamentals, the design is illustrated in detail, giving a step-by-step discussion of the main critical points and the hints for their successful handling. Suggestions for extending the design to different drive controllers are also included. The resulting control scheme is very performant; it has a strong tracking capability and, at the same time, provides good disturbance rejection.

Furthermore, it is very robust to parametric uncertainties and less sensitive to measurable noise. These advantages are highlighted by comparing FOC based on a traditional PI controller in Chapter 2 and the differential flatness-based control with nonlinear state observer in Chapter 3 and the experimental validation on both the SPMSM and PMa-SynRM. Significantly, the PMa-SynRM is suitable for electric vehicle traction instead of high-cost permanent machines such as SPMSM and IPMSM. Therefore, this machine has the capability required for the traction systems of EVs and HEVs. In conclusion, by utilizing MFC, the performance of PMa-SynRM has significantly improved not only the inner current control loop but also the outer speed control

loop. Moreover, the controller coefficient of the proposed MFC is not complicated to define and obtain the suitable control system for both the SPMSM and PMa-SynRM drive.

The most important aspects of the work are concluded at the end of this thesis, where an outlook on possible future works is given.

1.4. State-of-the-Art Powertrain Inverter for Automotive applications

Battery Electric Vehicles (BEV) - Inverter

	2018 Tesla Model 3 Inverter	2019 Nissan Leaf Inverter	2019 Jaguar I-Pace Inverter
			
Cost (USD)	$810.54	$468.41	$555.29
Max. Input Voltage (V_{DC})	430	450	500
Dimensions (mm)	370 x 278 x 122	386 x 386 x 223	407 x 272 x 83
Parts / Fasteners	1275 / 44	1287 / 56	2185 / 106
Weight (kg)	4.81	11.15	8.23
Coolant Medium	Water/Glycol	Water/Glycol	Water/Glycol

Cost and weights include: Housing, PCBA, IGBT Module & Cooling Structure, DC-link Capacitor, Motor Phase Lead, Connectors, Self-contained structural and connected components.

Figure 1.6 Battery Electric Vehicles Inverter [photo courtesy of chargedevs.com] [12].

Figure 1.6 compares the powertrain inverter used in commercial traction inverter, including Tesla Model 3, Nissan Leaf, and Jaguar I-Pace. The traction inverter of an EV plays an essential role as its power conversion unit (PCU), which converts the DC battery into a three-phase AC for the smooth operation of the electric traction motor.

Currently, the research and development of new electronic components are constantly evolving, and with it also the achieved results [13] [14] [15]. As a result, companies are continually developing more and more performing devices characterized by higher efficiency and better electrical characteristics. Silicon carbide (SiC) technology [16] [17] offers definite advantages among potential technologies, mainly related to its electrical resistance. Thanks to this technology, it is possible to obtain the same resistance as using silicon-based technology but employing a smaller mass. Smaller and more efficient components can thus be developed. Furthermore, since switching losses are reduced, it is possible to operate at higher frequencies using smaller passive components.

Moreover, silicon carbide devices can operate at higher temperatures and can be designed with a reduced thermal design. They offer, therefore, an ideal solution for the automotive field. Further benefits arising from SiC usage are the following [13]: power losses, up to ten times lower, can be achieved; devices can operate at higher voltages, with an electric breaking field (V/cm) increased tenfold; the cooling coefficient has tripled (thermal conductivity W/cm x °C); a factor of 10 improves frequency response. Those outstanding electrical and physical characteristics are why most companies are using silicon carbide as their primary technology.

Although today, silicon insulated-gate bipolar transistors (Si IGBTs) dominate the medium power range, including electric vehicle inverters, these technologies are now transitioning to a sixth-generation, with wide-bandgap semiconductor materials taking over: silicon carbide for high voltage/power applications and gallium nitride (GaN) for lower voltage and power. This shift allows smaller and higher-density power modules to operate at higher temperatures and creates new materials opportunities throughout the power module packaging.

As shown in Figure 1.6, Tesla's inverter used SiC MOSFET of the Model 3 in 2018, and Tesla became the first company to add SiC MOSFETs, sourced from ST Microelectronics in an in-house inverter design. The overall design has several innovations beyond using SiC packages, but this is the main one. It has led to the overall weight of the inverter (4.8kg) to be under half that of the 2019 Nissan Leaf (11.15kg) and over a third less than that of the Jaguar I-PACE (8.23kg), which use Si IGBT inverters and off-the-shelf parts.

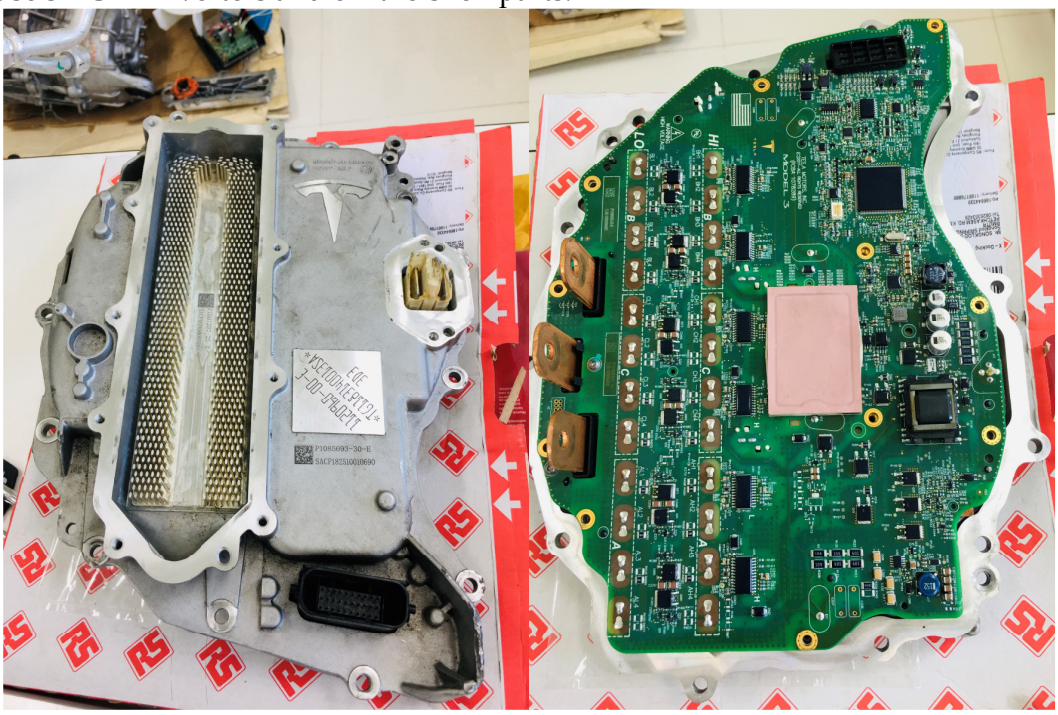

Figure 1.7 Tesla's SiC MOSFET inverter sourced from ST Microelectronics.

The use of SiC MOSFETs further creates new materials opportunities as the limits of traditional materials are stretched. However, as with any emerging technology, the cost has been the main barrier for uptake of SiC MOSFETs and other enabling materials in the power module

packages. Nevertheless, Tesla seems to have solved this too: its inverter has undergone a remarkable cost decline in only three years. Tesla's SiC inverter already looks to be on par with Si IGBT modules used in the 2019 versions of the Nissan Leaf and the Jaguar I-PACE, as shown in Figure 1.7. The result is that Tesla's overall inverter and PMa-SynRM combination is one of the best on the market, achieving a 97% efficiency, yielding more range without increasing expensive battery capacity. All at a similar cost to the older technologies being displaced [18] [19] [20].

So far, besides the better design of the powertrain motor and SiC MOSFET inverter combination, the enhancement of the overall drive could be possible by using more advanced control algorithms. With the advent of high-speed microprocessors, the implementation of advanced control procedures has been possible.

1.5. Literature Review of the High-Performance Nonlinear Control of PMa-SynRM

Over the last few years, frequency converter and the FOC have significantly contributed to the revival of interest in the PMa-SynRM. With the development of new technology, especially in digital electronics (i.e., Microcontroller, Real-time rapid digital signal processing) and power semiconductor devices, as mentioned earlier in the previous section, synchronous drives' performance has improved. Enhancement of drive performance and stable synchronous operation down to very low speeds, including standstill, has been possible using the FOC or vector control based on PI controller. However, achieving this operation was complicated by using conventional V/f control. Significantly, the PMa-SynRM has a much more complicated structure, affecting the control system, and its model has become much more strongly nonlinear. Therefore, traditional control such as FOC based on PI controller does not have enough to provide high-performance for all conditions operating. Accordingly, several nonlinear control methods have been proposed over the last few years to deal with this problem.

The main limitation of most of the work on the optimal control of PMa-SynRM is using an ideal model to perform theoretical analysis and practical implementation. Most modern control algorithms are model-based control (MBC) and are parameter dependent. However, in a real machine, the effects of saturation and iron losses result in a deviation of the current angle from the optimal operating point. Furthermore, PMa-SynRM parameter variations due to temperature and airgap flux have been reported in the literature and discussed in this dissertation. Therefore, knowledge of the motor perimeters and a more realistic model is crucial for optimal control.

In the current control of a PMSM drive system, the crucial objective is to guarantee that the stator currents track their reference values with minimum errors in both transient and steady-state conditions. A couple of current control approaches have been applied for better current tracking performance as proposed in the following pieces of literature.

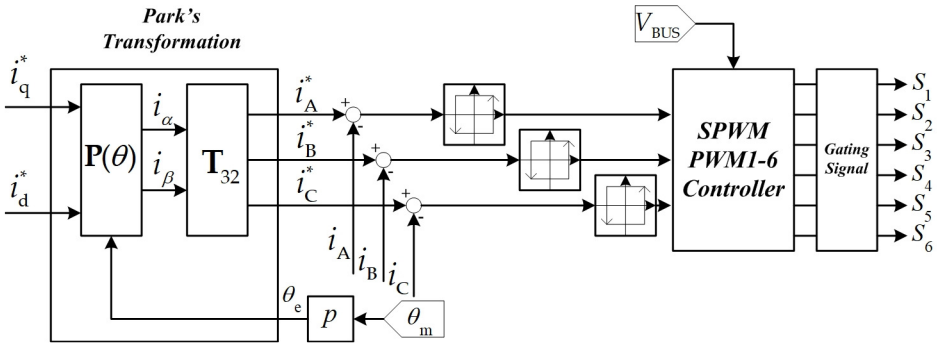

Figure 1.8 Stator current control based on hysteresis comparators directly generates gate signals to the three-phase inverter.

As illustrated in Figure 1.8 [21], Hysteresis-based control schemes have been known for a long time as a simple and effective way of achieving fast dynamic responses. However, the most straightforward implementations of hysteresis current control (HCC) are characterized by variable switching frequency, load-dependent variations in the average switching frequency, and possibilities for limit cycle operation with high frequency switching as well-known disadvantages.

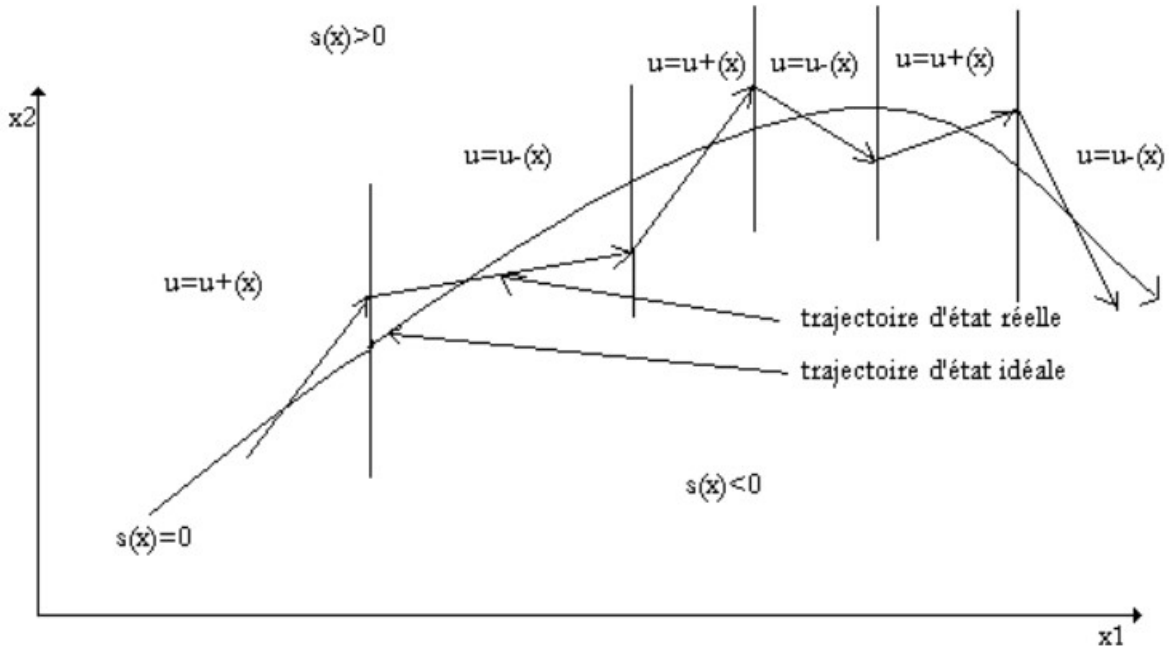

Figure 1.9 Sliding mode control definition.

The sliding-mode control (SMC) [22] [23] has attractive advantages of robustness to disturbances and low sensitivity to the system parameter variations. As a definition in Figure 1.9. the SMC control offers a fast dynamic response. However, the chattering phenomenon exists in the conventional sliding-mode control [24] [25].

P. Thounthong has proposed differential flatness-based control speed/torque control with state-observers of SPMSM drives. It is classified as a model-based control offered for a nonlinear system, especially a strongly nonlinear system. The differential flatness-based control and state observer combination make enhancing the overall SPMSM drive possible. Furthermore, the differential flatness-based control has attractive robustness to disturbance and low sensitivity to the system parameter variations compared to the FOC based on the traditional PI controller.
So far, in order to design a robust controller with acceptable tracking performance, all the mentioned model-based control methods require good knowledge about the dynamics and the model of the studied system. Since the unexpected dynamic variation of system and parametric errors are prevalent in industrial applications, the MBC performance can be effected under such conditions. However, in industrial applications and especially in complex nonlinear systems, it is quite tricky and time-consuming to find a correct dynamic model of the studied system. In addition, since the MBC methods require an accurate model of the controlled system to design the controller, these methods may not be applicable for the systems whose model is not available. So, to overcome the limitation of MBC, the industry demands controllers with less dependence on the model of the system.

Thus, the model predictive control (MPC) technique has been proposed as an appropriate current control scheme for electric machines. MPC has advantages such as high dynamic response, a fast dynamic, straightforward concept, and simple structure, and therefore it has garnered favorable attention in the PMSM drive system. Some of the commonly used predictive control methods include deadbeat predictive control (DPC), continuous control set model predictive control (CCS-MPC), and finite control set model predictive control (FCS-MPC) [27]. DPC is simple to implement. However, it is highly reactive to uncertainties and disturbances [28]. The complex computational process of CCS-MPC is an obstacle to the applications with the digital processor. FCS-MPC predicts the future states of the controlled system based on the finite voltage vector set and the mathematical model, and the optimal voltage vector is chosen according to the cost function. It utilizes the discrete nature of the inverter and designs real-time implementation of nonlinear multi-constrained control [29]-[30] [31]. This method's principle is based on predicting controlled variables in the subsequent calculation step using the measured variables and a mathematical model of the controlled system. Then, analyzing the predicted results using a cost function related to the difference between the system's desired trajectories and actual outputs. Compared to the previously mentioned control techniques, safety and fast dynamics are two remarkable features of the MPC method.

Despite these advantages, since the MPC uses a mathematical model in the prediction section, its performance depends on the model's correctness [31]. In addition, using the prediction at each sampling time of the MPC algorithms, import some additional mathematical calculations into the control algorithm.

In order to solve the problems mentioned earlier, facing those limitations of MPC and MBC clarifies the crucial role of developing model-free control, which is presented in this thesis. This concept will apply to both SPMSM and PMa-SynRM drives. Furthermore, a comparison

between the proposed MFC and the FOC based on PI controller and differential flatness-based control is also discussed in terms of dynamic response and performance of the different control methods.

For the PMa-SynRM drive system, many papers have been proposed in the following literature reviews. Peyman Niazi [32] first proposed online parameter estimation of PMa-SynRM with FOC based on PI controller in 2007. The proposed solution based on MBC is introduced in this work. A different procedure in [33] was introduced to robust sensorless control for PMa-SynRM. The other, a new maximum torque per ampere (MTPA) based direct torque control (DTC) method, is proposed in [34]. As mentioned above, MBC has a disadvantage with an exact model requirement of the controlled system to design the controller. In addition, the d- and q-axis flux linkages are significantly dependent on both d- and q-axis currents variation. Therefore, inductances must be considered by the ratio between the flux linkage variations and the slight increase of the current [35]. Therefore, inductances must be considered by the ratio between the flux linkage variations and the slight increase of the current. This phenomenon is presented in this thesis in order to achieve high-performance nonlinear control of PMa-SynRM.

Chapter-2 MODELING, OPERATION, AND CONTROL OF PERMANENT MAGNET SYNCHRONOUS MACHINES

Contents

Introduction …… --
2.1 Concordia/Clarke and Park transformations
2.1.1. Park Transformation preserving amplitude
2.1.2. Clarke transformation
2.1.3. The Park transformation preserving power
2.1.4. The Concordia transformation
2.2. Permanent Magnet Synchronous Motor
2.2.1. Description
2.2.2. Classification of Permanent Magnet Synchronous Motors (PMSMs)
2.3. Permanent Magnet Assisted Synchronous Reluctance Motor (PMa-SynRM)
2.4. Mathematical model of PM synchronous motor
2.4.1. Model of SPMSM in the rotating reference frame
2.4.2. Model of IPMSM in the rotating reference frame
2.4.3. Model of the PMa-SynRM in the rotating reference frame
2.4.4. Motor torque
2.4.5. Mechanical motion equation
2.4.6. Nonlinear model in state-space representation
2.5. Dynamic simulation of the IPMSM and SPMSM
2.6. Dynamic simulation of the PMa-SynRM
2.7. Model of Pulse width modulated frequency inverter for PMSM supply
2.8. Simulation of the sinusoidal PWM for supply PMSM
2.9. Current and speed control of PMSM
2.9.1 Simulation and experimental validation of FOC for controlling SPMSM
2.9.2. Simulation and experimental validation of FOC for controlling PMa-SynRM
2.10. Conclusion

Introduction

This chapter begins with a classification of the Permanent Magnet machines. Then the main characteristics of the Permanent Assisted Synchronous Reluctance Motor (PMa-SynRM) are presented, together with the electrical parameters of the PMa-SynRM used in this dissertation. Next, the mathematical models of the three wide types of permanent-magnet synchronous machines, namely surface mounted permanent magnet synchronous motor (SPMSM), interior permanent magnet synchronous motor (IPMSM), and permanent magnet assisted synchronous reluctance motor (PMa-SynRM), are presented. And then, based on the given electrical and mechanical model of the machines, dynamic simulation models of the different types of machines are made using MATLAB/Simulink. Finally, vector control or field-oriented control (FOC) using the traditional PI controller is presented to drive the PM machines.

Additionally, with the advantages of PMa-SynRM requiring a small amount of magnetic flux compared to IPMSM, the constant power region, which operates above the base speed thanks to flux-weakening control techniques, can be extended. This will be presented in this chapter. Finally, at the end of the chapter, the optimal control of a PMa-SynRM with copper loss minimization using MTPA is presented.

2.1. Concordia/Clarke and Park transformations

This section determines the mathematical model of AC machines that describes the electromechanical operation. A mathematical model of a PMSM is developed. The classical model using the Concordia/Clarke and Park transformations derives from identifying the equivalent two-phase model of AC machines. Thanks to these transformations, many concepts, interpretations, and simplified models can be obtained to analyze the behavior of AC machines. Indeed, an approach to study AC machines is to transform the variables (voltages, currents, and flux linkages) stated in a fixed reference frame to a rotating frame defined by the Concordia/Clarke and Park transformations. These transformations are used in the analysis of AC machines to reduce the complexity of the differential equation describing the behavior of the AC machines by eliminating time-varying terms in the inductances.

The transformation from three-phase (stationary frame (a, b, c)) to two-phase (orthogonal rotation (d,q) frame) is called Park transformation. However, this transformation can be decomposed into two transformations—a first transformation from a fixed three-phase system to a fixed two-phase system (Clarke or Concordia transformations). Next, a fixed two-phase frame transformation to a rotating two-phase frame is associated with a rotating variable (mechanical position and flux, for instance).

Before applying these transformations to PM machines, some assumptions are introduced:

- Uniform gap thickness and no notch effect;
- Sinusoidal distribution of the induction in the air gap;
- Linear magnetic characteristic (no saturation);

- Temperature effect, skin effect, hysteresis phenomenon, and Foucault's currents are neglected.

Using the Park transformation, the dynamic equations of a three-phase machine (stationary (a, b, c) frame) are transformed into the two-phase model (rotatory (d, q, 0) frame). The (d, q, 0) transformation can reduce three AC variables (voltages, currents, ...) to two DC variables. General representation of the Park transformation is given as

$$\begin{bmatrix} x_{\mathrm{d}}(t) \\ x_{\mathrm{q}}(t) \\ 0 \end{bmatrix} = \mathbf{P}(\theta) \begin{bmatrix} x_{\mathrm{a}}(t) \\ x_{\mathrm{b}}(t) \\ x_{\mathrm{c}}(t) \end{bmatrix} \tag{2.1}$$

where

$$\mathbf{P}(\theta) = K \begin{bmatrix} \cos(\theta) & \cos(\theta - \frac{2\pi}{3}) & \cos(\theta + \frac{2\pi}{3}) \\ -\sin(\theta) & -\sin(\theta - \frac{2\pi}{3}) & -\sin(\theta + \frac{2\pi}{3}) \\ \sigma & \sigma & \sigma \end{bmatrix} \tag{2.2}$$

with θ as the angle between the a-axis of the stationary reference frame and the real d-axis of the rotating reference frame, and with K as the ratio between the amplitude of the three-phase system variables x_{a}, x_{b}, x_{c} (voltages, currents, and flux) concerning the amplitude of the corresponding two-phase $dq0$ system variables x_{d}, x_{q}, x_0 and σ being a constant.
Then, two different Park transformations can be defined:
(1) Park transformation preserving amplitude and
(2) Park transformation preserving power.

It is worth noting that 0 component is often neglected in isolated neutral point machines as it does not contribute to the electrotechnical power conversion since the zero-sequence current is equal to 0 in this case.

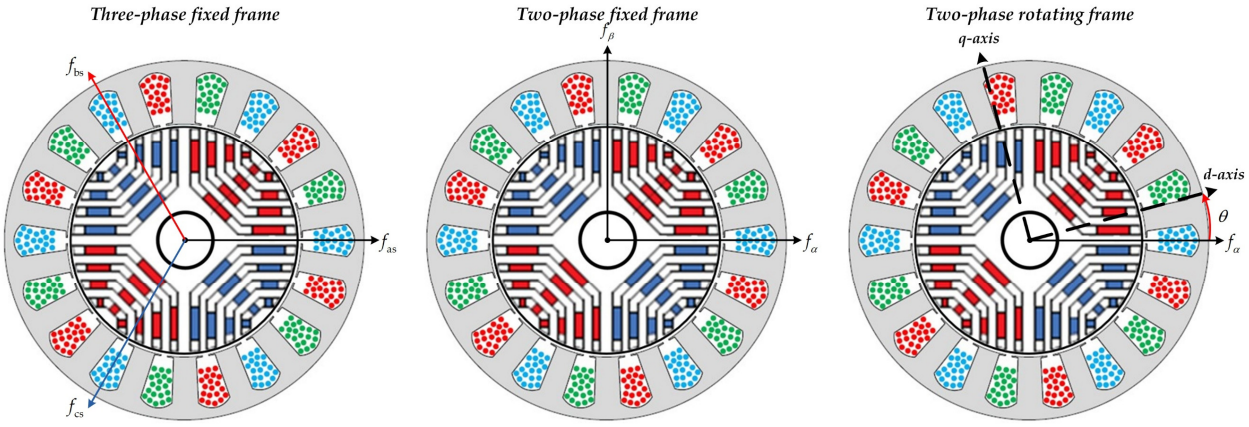

Figure 2.1 Definition of *abc* to *dq* transformation.

2.1.1. Park Transformation preserving amplitude

The P(θ) transformation preserving amplitude transforms a three-phase system stated in a stationary (a, b, c) frame into a rotatory (d, q, 0) frame by choosing

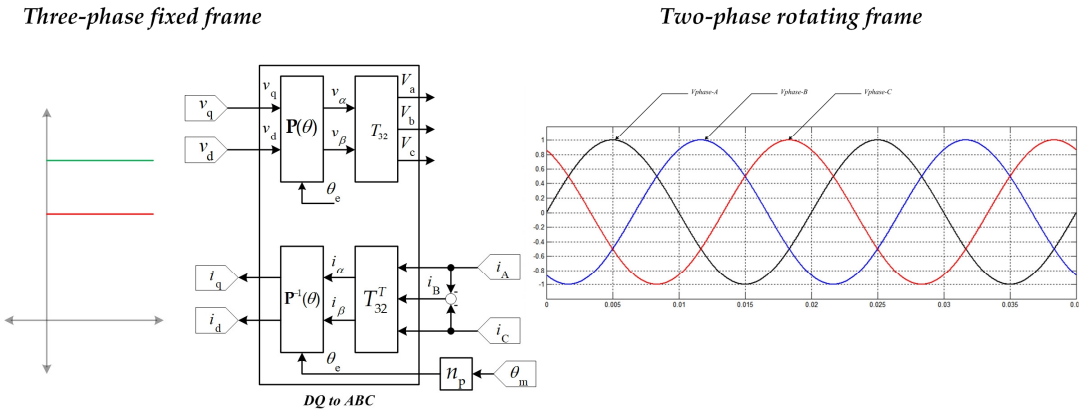

Figure 2.2 The Clarke /Concordia-Park transformation.

$$K = \frac{2}{3}, \sigma = \frac{1}{2} \tag{2.3}$$

It yields

$$\mathbf{P}(\theta) = \frac{2}{3}\begin{bmatrix} \cos(\theta) & \cos(\theta - \frac{2\pi}{3}) & \cos(\theta + \frac{2\pi}{3}) \\ -\sin(\theta) & -\sin(\theta - \frac{2\pi}{3}) & -\sin(\theta + \frac{2\pi}{3}) \\ \frac{1}{2} & \frac{1}{2} & \frac{1}{2} \end{bmatrix} \tag{2.4}$$

The inverse transformation of (2.4) is given by

$$\mathbf{P}^{-1}(\theta) = \begin{bmatrix} \cos(\theta) & -\sin(\theta) & 1 \\ \cos(\theta - \frac{2\pi}{3}) & -\sin(\theta - \frac{2\pi}{3}) & 1 \\ \cos(\theta + \frac{2\pi}{3}) & -\sin(\theta + \frac{2\pi}{3}) & 1 \end{bmatrix} \tag{2.5}$$

2.1.2. Clarke transformation

By choosing $\theta = 0$, in the Park transformation (2.4), the resulting matrix $\mathbf{T}_{32} = \mathbf{P}(0)$ is given as

$$\mathbf{P}(\theta) = \frac{2}{3}\begin{bmatrix} 1 & -\frac{1}{2} & -\frac{1}{2} \\ 0 & \frac{\sqrt{3}}{2} & -\frac{\sqrt{3}}{2} \\ \frac{1}{2} & \frac{1}{2} & \frac{1}{2} \end{bmatrix}, \text{ and } \mathbf{P}^{-1}(\theta) = \begin{bmatrix} 1 & 0 & 1 \\ -\frac{1}{2} & \frac{\sqrt{3}}{2} & 1 \\ -\frac{1}{2} & -\frac{\sqrt{3}}{2} & 1 \end{bmatrix} \tag{2.6}$$

Matrix $\mathbf{T}_{32}$ is known as the Clarke transformation. The Clarke transformation converts the balanced three-phase quantities into balanced two-phase orthogonal quantities by keeping the amplitude of the variables. For an electric system, for example, this implies that power is not kept. Furthermore, the Park transformation (2.4 can be expressed in terms of Clarke transformation $\mathbf{T}_{32}$ and a Rotation matrix $\mathbf{P}(\theta)$, as

$$\mathbf{R}(\theta) = \begin{bmatrix} \cos(\theta) & -\sin(\theta) & 0 \\ \sin(\theta) & \cos(\theta) & 0 \\ 0 & 0 & 1 \end{bmatrix} \tag{2.7}$$

As follows

$$\mathbf{P}(\theta) = \mathbf{R}(\theta)T_{32} \tag{2.8}$$

For symmetrical three-phase machines in a stationary (a, b, c) frame, the three-phase variables can be represented in a two-phase stationary reference (α, β) frame.

They define the plane (α, β) with direct and quadrature axes, as shown in Figure 2.1. If the neutral point is isolated, the currents satisfy $\sum i = 0$. That is

$$i_0 = \frac{1}{\sqrt{3}}\left(i_a, i_b, i_c\right) \tag{2.9}$$

From now on, the 0-axis is not considered. Then, the three-phase to two-phase transformation ($abc \rightarrow \alpha\beta$) is now given by

$$\begin{bmatrix} x_\alpha \\ x_\beta \end{bmatrix} = \mathbf{T}_{32}^T \begin{bmatrix} x_a \\ x_b \\ x_c \end{bmatrix} \tag{2.10}$$

where

$$\mathbf{T}_{32}^{T}=\frac{2}{3}\begin{bmatrix}1 & -\frac{1}{2} & -\frac{1}{2}\\ 0 & \frac{\sqrt{3}}{2} & -\frac{\sqrt{3}}{2}\end{bmatrix} \tag{2.11}$$

Notice that the inverse transformation is given as

$$\begin{bmatrix}x_{\mathrm{a}}\\ x_{\mathrm{b}}\\ x_{\mathrm{c}}\end{bmatrix}=\mathbf{T}_{32}\begin{bmatrix}x_{\alpha}\\ x_{\beta}\end{bmatrix} \tag{2.12}$$

where

$$\mathbf{T}_{32}=\begin{bmatrix}1 & 0\\ -\frac{1}{2} & \frac{\sqrt{3}}{2}\\ -\frac{1}{2} & -\frac{\sqrt{3}}{2}\end{bmatrix} \tag{2.13}$$

2.1.3. The Park Transformation Preserving Power

To pass from the three-phase system (*a*, *b*, *c* frame) to the two-phase system (*dq* frame) preserving the instantaneous power, the following condition must hold:

$$\left[V_{\mathrm{dq}}\right]^{T}\left[I_{\mathrm{dq}}\right]=\left[V_{\mathrm{abc}}\right]^{T}\left[I_{\mathrm{abc}}\right] \tag{2.14}$$

or

$$v_{\mathrm{d}}i_{\mathrm{d}}+v_{\mathrm{q}}i_{\mathrm{q}}=v_{\mathrm{a}}i_{\mathrm{a}}+v_{\mathrm{b}}i_{\mathrm{b}}+v_{\mathrm{c}}i_{\mathrm{c}} \tag{2.15}$$

Then, the modified Park transformation preserving power of the system is obtained by choosing

$$K=\sqrt{\frac{2}{3}},\sigma=\frac{1}{\sqrt{2}} \tag{2.16}$$

This leads to

$$\mathbf{P}(\theta)=\sqrt{\frac{2}{3}}\begin{bmatrix}\cos(\theta) & \cos(\theta-\frac{2\pi}{3}) & \cos(\theta+\frac{2\pi}{3})\\ -\sin(\theta) & -\sin(\theta-\frac{2\pi}{3}) & -\sin(\theta+\frac{2\pi}{3})\\ \frac{1}{\sqrt{2}} & \frac{1}{\sqrt{2}} & \frac{1}{\sqrt{2}}\end{bmatrix} \tag{2.17}$$

And its inverse is given as

$$\mathbf{P}^{-1}(\theta)=\sqrt{\frac{2}{3}}\begin{bmatrix}\cos(\theta) & -\sin(\theta) & 1\\ \cos(\theta-\frac{2\pi}{3}) & -\sin(\theta-\frac{2\pi}{3}) & 1\\ \cos(\theta+\frac{2\pi}{3}) & -\sin(\theta+\frac{2\pi}{3}) & 1\end{bmatrix} \tag{2.18}$$

2.1.4. The Concordia Transformation

Choosing the angle $\theta = 0$ in (2.17), the resulting Park transformation matrix preserving power (2.17) is of the form

$$\mathbf{C}o=\sqrt{\frac{2}{3}}\begin{bmatrix}1 & -\frac{1}{2} & -\frac{1}{2}\\ 0 & \frac{\sqrt{3}}{2} & -\frac{\sqrt{3}}{2}\\ \frac{1}{2} & \frac{1}{2} & \frac{1}{2}\end{bmatrix},(\mathbf{C}o)^{-1}=\sqrt{\frac{2}{3}}\begin{bmatrix}1 & 0 & \frac{1}{\sqrt{2}}\\ -\frac{1}{2} & \frac{\sqrt{3}}{2} & \frac{1}{\sqrt{2}}\\ -\frac{1}{2} & -\frac{\sqrt{3}}{2} & \frac{1}{\sqrt{2}}\end{bmatrix} \tag{2.19}$$

The matrix $\mathbf{C}_o$ is known as Concordia transformation matrix.

Furthermore, Park transformation matrix can be expressed in terms of Concordia transformation **C**o and a Rotation matrix P(θ) as

$$\mathbf{R}(\theta)=\begin{bmatrix}\cos(\theta) & -\sin(\theta) & 0\\ \sin(\theta) & \cos(\theta) & 0\\ 0 & 0 & 1\end{bmatrix} \tag{2.20}$$

as follows

$$\mathbf{P}(\theta)=\mathbf{R}(\theta)\cdot\mathbf{C}o \tag{2.21}$$

2.1.5. Transformation Matrices

The following transformation transforms variables from the stationary reference ($\alpha\beta$) frame into the rotating reference (dq) frame ($\alpha\beta \Rightarrow dq$)

$$\begin{bmatrix}x_{\mathrm{d}}\\ x_{\mathrm{q}}\end{bmatrix}=\mathbf{P}_{\alpha\beta\to dq(\theta)}\begin{bmatrix}x_{\alpha}\\ x_{\beta}\end{bmatrix} \tag{2.22}$$

where

$$\mathbf{P}_{\alpha\beta\to dq(\theta)} = \begin{bmatrix} \cos\theta & \sin\theta \\ -\sin\theta & \cos\theta \end{bmatrix} \tag{2.23}$$

with $\mathbf{P}_{\alpha\beta\Rightarrow dq(\theta)}$ is Park transformation.

where θ is the rotor angle such that $\theta = 0$ refers to a position where the rotor flux vector is aligned with the stator *a*-axis.

The inverse transformation can be easily expressed as

$$x_{\alpha\beta} = \mathbf{P}^{-1}_{\alpha\beta\to \mathrm{dq}(\theta)} \cdot x_{\mathrm{dq}} \tag{2.24}$$

where

$$\mathbf{P}^{-1}_{\alpha\beta\to dq(\theta)} = \begin{bmatrix} \cos\theta & -\sin\theta \\ \sin\theta & \cos\theta \end{bmatrix} \tag{2.25}$$

2.2. Permanent Magnet Synchronous Motor

2.2.1. Description

The permanent-magnet synchronous motor (PMSM) has been widely used in the industry for variable speed applications due to its high-performance reliability and power density. Because of the progress in permanent magnet materials, power electronics, digital signal processors, and modern control techniques, permanent magnet synchronous machines have become more widespread in industrial applications, such as automobiles, robotics, aeronautics, and aerospace domains.
In summary, the main advantages of PM machines are [35]:

- High air gap density
- High power density (power to weight ratio)
- High torque/inertia ratio
- Small torque ripple
- High-speed smooth rotation
- High torque output (high-speed acceleration/deceleration)
- High efficiency and high cos φ (power supply cost)
- Compact design

In the sequel, we introduce the essential characteristics of the PMSM.

2.2.2. Classification of Permanent Magnet Synchronous Motors (PMSMs)

The physical characteristics of the PMSM are associated with its rotor and stator structures. The stator is composed of a three-phase wound such that the rotation of the rotor field generates the Electromotive Forces (EMF). Furthermore, the EMF phase-shifted, one from the other, by 120 electrical degrees.

The rotor incorporates permanent magnets to produce a magnetic field. The permanent magnets have the advantage of eliminating the brushes, the rotor copper losses, and the need for a controlled DC source to provide the excitation current. However, the amplitude of the rotor flux can be easily controlled. On the other hand, several ways exist to place the magnets in the rotor (see Figure 2.3).

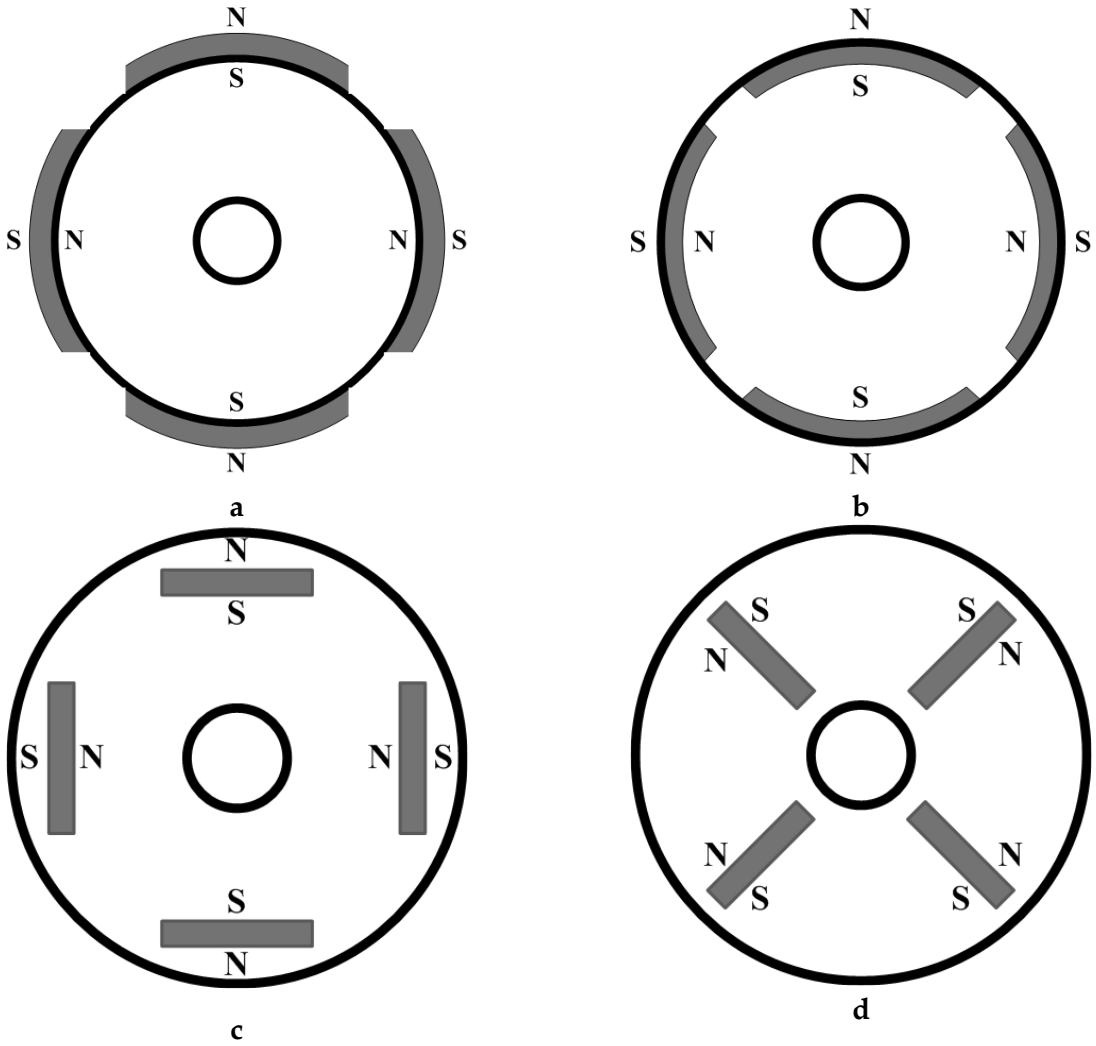

Figure 2.3 PMSM Rotor permanent magnet layout: (a) surface mounted permanent magnet, (b) inset permanent magnet, (c) interior permanent magnets, (d) flux concentrating.

Following the magnet position, the PMSM can be classified into four major types:

- **surface mounted magnets type**

The magnets are placed on the surface of the rotor using high-strength glue. They present a homogeneous gap, and the motor is a non-salient pole. The inductances do not depend on the rotor position (Figure 2.3a). The inductance of the *d*-axis is equal to that of the *q*-axis. On the other hand, the magnets are exposed to a demagnetizing field. Moreover, they are subject to centrifuge forces, which can cause the detachment of the magnets from the rotor, particularly at very high speeds.

- **Inset magnets type**

The inset magnets are placed on the surface of the rotor. However, the space between the magnets is filled with iron (see Figure 2.3b). The alternation between the iron and the magnets causes a salient effect. As a result, the inductance in the *d*-axis is slightly different from the inductance in the *q*-axis.

- **Flux concentrating type**

As shown in Figure 2.3d, the magnets are deeply placed in the rotor's body. The magnets and their axes are redialed. The flux on a polar area of the rotor is a result of two separated magnets. The advance of this configuration is to concentrate the flux generated by the permanent magnet in the rotor and obtain a more robust induction in the gap. This type of machine has a salience effect.

Surface mounted PMSMs, and interior PMSMs are the most used in the industry. Furthermore, the PMSMs can be classified according to the electromotive force profiles:
- Sinusoidal
- Trapezoidal

Trapezoidal PMSMs are more suitable for cheap applications due to their simple structure, reducing their manufacturing and maintenance costs. Their power electronic drive is also simple. However, the power density of the motor drive is less than that of sinusoidal PMSMs. It is why these latter becomes more popular in electrified transportation systems.

2.3. Permanent Magnet Assisted Synchronous Reluctance Motor (PMa-SynRM)

Recently, Permanent Magnet Assisted (PMa)-Synchronous Reluctance Motors (SynRM) have been considered as a possible alternative motor drive for high-performance applications. In particular, electric vehicle traction systems require a wide operating speed range of the electric motor [33] [34]. Interior PMSM (IPMSM) uses magnets and reluctance torque outputs to provide highly efficient drives. In addition, constant power operation or high-speed flux-weakening region is possible with the flux-weakening control technique. However, some drawbacks, such as the relatively sizeable *d*-axis current at high speeds and the uncontrollable generator mode

following unexpected inverter shutdowns, severely limit the application of the motor to high-speed electric vehicles [36] [37]-[38].

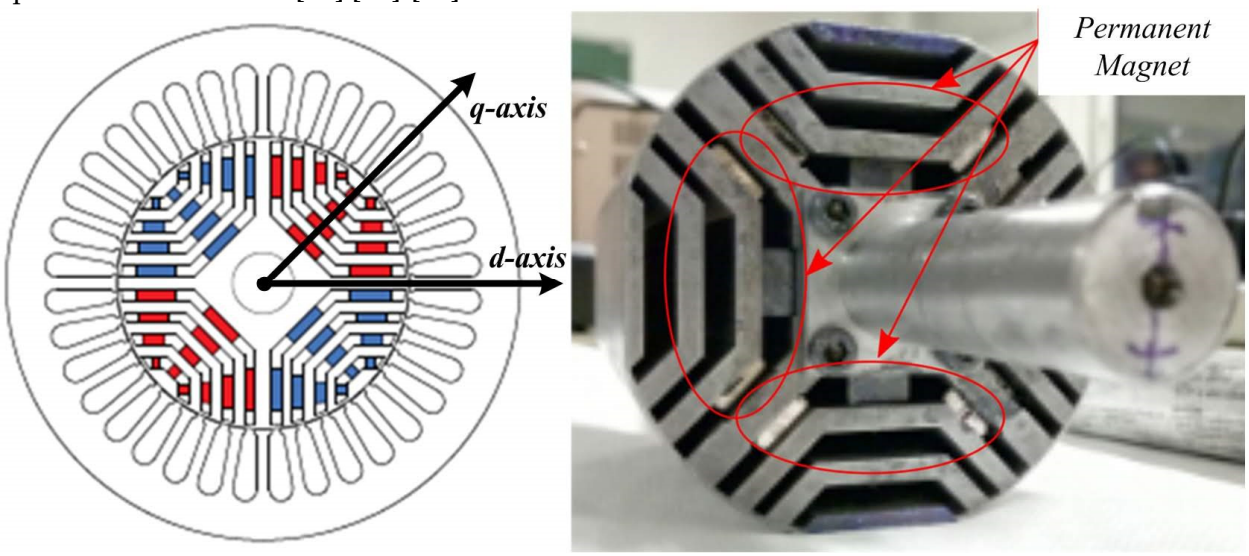

Figure 2.4 PMa-SynRM rotor structure [37].

On the other hand, the PMa-SynRM, similar to IPMSM, shows a promising solution to these problems [38], [39], [41]. In addition, the flux-weakening control technique [42] enables wide constant power operation regions. Figure 2.4 shows the proposed structure for a 4-pole PMa-SynRM with ferrite magnet and reference *dq*-axis. As shown in the figure, one difference between the traditional IPMSM and the PMa-SynRM shown in this figure is that the bar magnets are magnetized along the negative *q*-axis and have a different flux linkage equation, which will discuss in the next section [37].

The PMa-SynRM is mainly a type of synchronous reluctance motor (SynRM), a family member of brushless AC machines consisting of the conventional dc permanent magnet machine, the permanent magnet synchronous machine, and the cage induction machine [38].

The main advantages of the SynRM can be summarized as follows [42]

1. Improved saliency ratio makes the SynRM competitive with an induction machine, particularly in power and inverter kVA requirements.
2. Small to medium-sized high-performance drives may have more straightforward control using the SynRM than the field-oriented controlled induction machine.
3. It can be operated stably down to zero speed at full load, unlike an induction motor which may suffer overheating problems. In addition, SynRM appears to be more efficient at low speed than an induction machine.
4. Adding an appropriate amount of magnet into the rotor core improves efficiency without significant back-EMF and necessary change in the stator design. Because of the existence of flux barriers, demagnetization is hard to occur if solid magnets are used. Demagnetization due to machine overloading and high ambient temperature is a significant problem in IPMs.

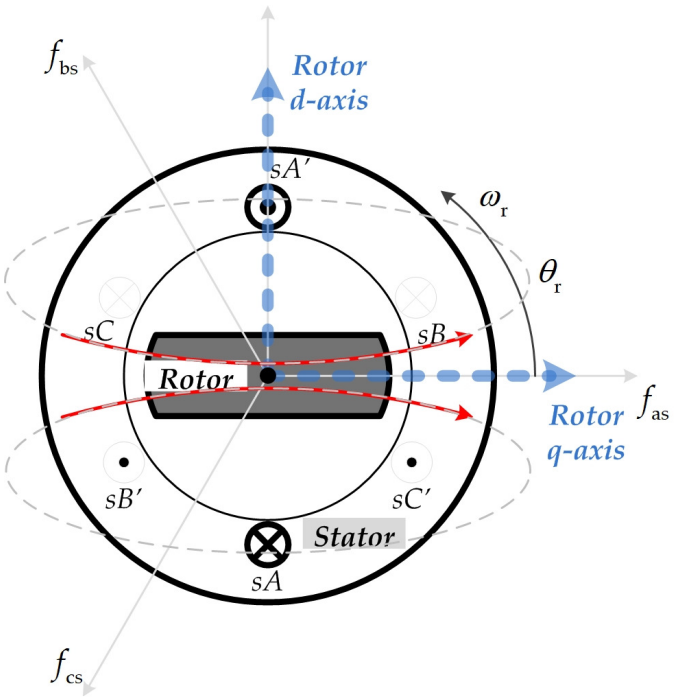

Figure 2.5 Single saliency RM rotor structure [42].

Figure 2.5 shows a cross-sectional view of a single saliency RM consisting of a non-salient stator and a two-pole salient rotor, both made of high-permeability magnetic material. This figure shows a three-phase stator winding, although any number of phases is possible.

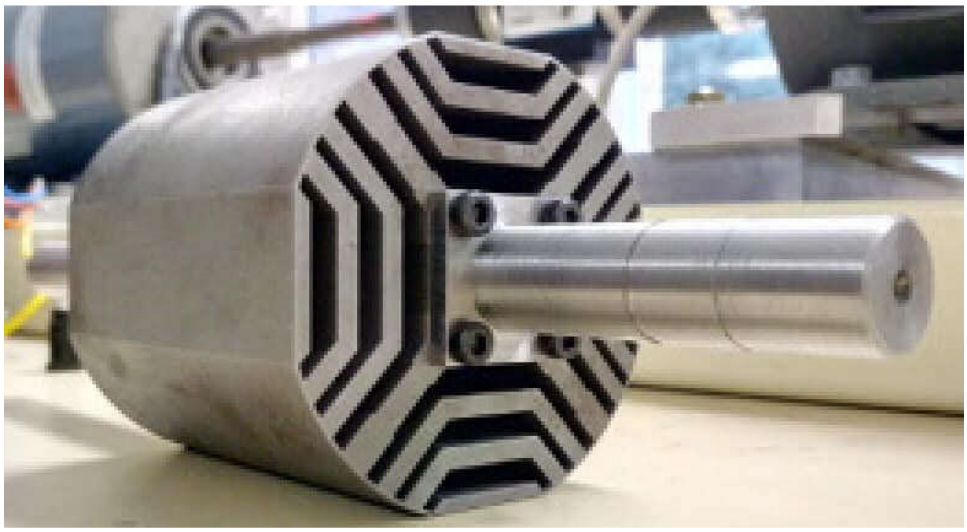

Figure 2.6 Flux barrier type rotor of reluctance motor [37].

In principle, the SynRM is similar to the traditional salient pole synchronous motor, but the rotor has no excitation winding. In this case, only the rotor is constructed with salient poles.

In addition, the internal surface of the stator is cylindrical, which in general eliminates some of the disadvantages of many variable reluctance motors and their advantages.

Figure 2.6 shows a fundamental rotor structure of a typical machine of that era that utilized the flux barriers to form a difference in saliency between the polar axis (d-axis) and interpolar axis (q-axis). The construction of the rotor is a transversally laminated (TLA) rotor. This type of rotor is also called a multiple-flux barrier rotor. Figure 2.6 illustrates a 4-pole transversally laminated rotor with four barriers per pole. The thin ribs are guaranteed mechanical strength, disposed at the air gap, and in the inner rotor laminations for significant speed and/or large rotor diameters. The rotor laminations are made by traditional punching or wire cutting. As a result, construction is easy and cheap. Besides, the TLA rotor has some advantages, including suitability for rotor skewing and ease for mass production. Moreover, the transversally laminated type of rotor can be optimized by proper design in order to minimize the air gap harmonics and their effect on torque ripple. This is obtained by properly shaping the various flux barriers and the proper choice of their access points at the airgap [42].

When permanent magnets are inserted into the rotor flux barrier of a SynRM, it becomes a Permanent Magnet Assisted Synchronous Reluctance Motor (PMa-SynRM), as shown in Figure 2.4. PMs can be mounted in the rotor core of the axially or transversally laminated structure. Figure 2.7 shows a transversally laminated PMa-SynRM.

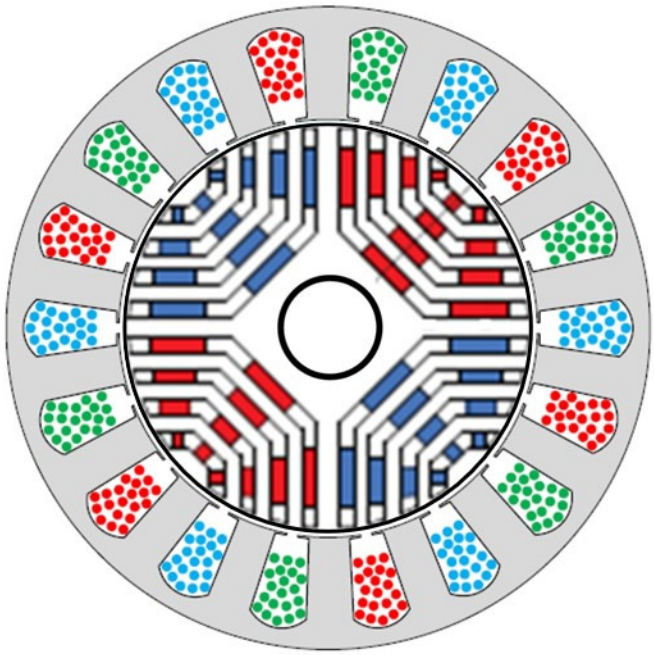

Figure 2.7 Four-pole transversally-laminated PM assisted rotor design.

As explained in [P.Niazi, 2005], the polarity of magnets is chosen such that it counteracts the q-axis flux of the SynRM at rated load. Regardless of the different choice of d, q axes, in principle, the PMa-SynRM seems nothing more than a particular case of IPMSM. However, a substantial difference is the high anisotropy of rotor structure pf PMa-SynRM and the low value of the PM flux. Indeed, the amount of PM flux is relatively lower than the amount of rated flux. In contrast, in the usual IPMSM, the most flux comes from magnets, and the flux produced by

stator currents is not the dominant part of the total flux. This property enables PMa-SynRM to have a large flux-weakening range and, so, more suitable for wide speed range applications.

The actual result of how to mount a rotor magnet is the difference in inductance values between the direct and quadrature axes. The reluctance of the *d*-axis is greater than the reluctance of the q-axis or vice versa, according to the rotor configuration. This is because the effective air gap is different along the *d*-axis and *q*-axis. Consequently, the inductance is higher in the axis with a shorter air gap due to unequal reluctance. As a result, a reluctance torque is produced due to magnet saliency in addition to the interactive torque. This latter is produced due to the interaction of the magnet field and the stator current. If the magnet bars are mounted on the rotor surface, *d*-axis and q-axis reluctances are equal or very close, making the reluctance torque negligible. This is the case with SPMSM. These different properties will be clearly seen in the model of different types of PMSM for control purposes which is the subject of the following sub-chapter.

2.4. Mathematical model of PM synchronous motor

Development of the machine model through the understanding of the physic of the motor is the crucial requirement for any type of electrical motor control. In the following study, the machine has a stator and rotor with symmetric distribution with n_P pairs of poles ($n_P = 2$ in Figure 2.7). The development of those models is under bellow assumptions as [43]-[44] [45] [46] [47]:

The damping effect of the rotor is neglected.
The magnetic circuit of the machine is not saturated.
The distribution of the magnetomotive force (MMF) is sinusoidal.
The coupling capacitors between the winding are neglected.
The hysteresis phenomena and Foucault's currents are neglected.
The gap irregularities owing to the stator slots are neglected.
Only a fundamental harmonic of the magnetomotive force (MMF) is taken into account.

Under these assumptions and using basic concepts, the electrical and mechanical equations describing the dynamical behavior of the SPMSM, IPMSM and PMa-SynRM are obtained in the following paragraphs.

2.4.1. Model of SPMSM in the rotating reference frame

For the SPMSM, the air gap is considered uniform, which makes the effect of saliency negligible. Thus, the *d*-axis magnetizing inductance L_d is equal to the *q*-axis magnetizing inductance L_q, i.e., $L_d = L_q = L_s$ (namely stator magnetizing inductance).

By applying Concordia and Park transformations as described in section 2.1, the two-phase synchronous rotating representation of the PMSM is:

$$\begin{bmatrix} x_{\mathrm{d}} \\ x_{\mathrm{q}} \end{bmatrix} = \mathbf{P}(\theta_{\mathrm{e}})^{T}\,\mathbf{C}o^{T} \begin{bmatrix} x_{\mathrm{a}} \\ x_{\mathrm{b}} \\ x_{\mathrm{c}} \end{bmatrix} \tag{2.26}$$

The resulting voltage equations are given as [44]

$$\begin{aligned} v_{\mathrm{d}} &= R_{\mathrm{s}} i_{\mathrm{d}} + \frac{d\Psi_{\mathrm{d}}}{dt} - \omega_{\mathrm{e}} \Psi_{\mathrm{q}} \\ v_{\mathrm{q}} &= R_{\mathrm{s}} i_{\mathrm{q}} + \frac{d\Psi_{\mathrm{q}}}{dt} + \omega_{\mathrm{e}} \Psi_{\mathrm{d}} \end{aligned} \tag{2.27}$$

The stator and rotor flux linkage in rotor reference frames are defined as

$$\begin{aligned} \Psi_{\mathrm{q}} &= L_{\mathrm{s}} i_{\mathrm{q}} \\ \Psi_{\mathrm{d}} &= L_{\mathrm{s}} i_{\mathrm{d}} + \Psi_{\mathrm{m}} \end{aligned} \tag{2.28}$$

where,
Ψ_{d} and Ψ_{q} are the flux linkage in the *d*-*q* axes,
Ψ_{m} is the rotor magnet flux linkages supposed constant,
$\omega_{\mathrm{e}} = n_{\mathrm{p}}\omega_{\mathrm{m}}$ is the electrical angular speed, and
ω_{m} is the mechanical angular speed.

By substituting (2.28) into (2.27), it yields

$$\begin{aligned} v_{\mathrm{d}} &= R_{\mathrm{s}} i_{\mathrm{d}} + L_{\mathrm{s}} \frac{di_{\mathrm{d}}}{dt} - \omega_{\mathrm{e}} \Psi_{\mathrm{q}} \\ v_{\mathrm{q}} &= R_{\mathrm{s}} i_{\mathrm{q}} + L_{\mathrm{s}} \frac{di_{\mathrm{q}}}{dt} + \omega_{\mathrm{e}} \Psi_{\mathrm{d}} \end{aligned} \tag{2.29}$$

2.4.2. Model of IPMSM in the rotating reference frame

For the IPMSM, the inductance in the *d*-axis is slightly different from the inductance in the *q*-axis. Therefore, the flux linkage equations are defined as

$$\begin{aligned} \Psi_{\mathrm{q}} &= L_{\mathrm{q}} i_{\mathrm{q}} \\ \Psi_{\mathrm{d}} &= L_{\mathrm{d}} i_{\mathrm{d}} + \Psi_{\mathrm{m}} \end{aligned} \tag{2.30}$$

Substituting (2.30) into (2.27), the voltage equations of the IPMSM are obtained as

$$\begin{aligned} v_{\mathrm{d}} &= R_{\mathrm{s}} i_{\mathrm{d}} + L_{\mathrm{d}} \frac{di_{\mathrm{d}}}{dt} - \omega_{\mathrm{e}} \Psi_{\mathrm{q}} \\ v_{\mathrm{q}} &= R_{\mathrm{s}} i_{\mathrm{q}} + L_{\mathrm{q}} \frac{di_{\mathrm{q}}}{dt} + \omega_{\mathrm{e}} \Psi_{\mathrm{d}} \end{aligned} \tag{2.31}$$

2.4.3. Model of the PMa-SynRM in the rotating reference frame

As shown in Figure 2.4, one difference between the traditional IPMSM and PMa-SynRM is that the bar magnets are magnetized along the negative q-axis and have a different flux linkage equation. That is:

$$\begin{aligned} \Psi_{\mathrm{q}} &= L_{\mathrm{q}} i_{\mathrm{q}} - \Psi_{\mathrm{m}} \\ \Psi_{\mathrm{d}} &= L_{\mathrm{d}} i_{\mathrm{d}} \end{aligned} \tag{2.32}$$

Substituting (2.32) into (2.27), the voltage equations of the PMa-SynRM are obtained as:

$$\begin{aligned} v_{\mathrm{d}} &= R_{\mathrm{s}} i_{\mathrm{d}} + L_{\mathrm{d}} \frac{di_{\mathrm{d}}}{dt} - \omega_{\mathrm{e}} \Psi_{\mathrm{q}} \\ v_{\mathrm{q}} &= R_{\mathrm{s}} i_{\mathrm{q}} + L_{\mathrm{q}} \frac{di_{\mathrm{q}}}{dt} + \omega_{\mathrm{e}} \Psi_{\mathrm{d}} \end{aligned} \tag{2.33}$$

2.4.4. Motor torque

The electromagnetic torque T_{e} is generated by the interaction between the rotor magnet poles and the poles induced by the magnetomotive forces in the air gap. Then, the electromagnetic torque T_{e} is given as

$$T_{\mathrm{e}} = n_{\mathrm{p}} \left(\Psi_{\mathrm{d}} i_{\mathrm{q}} - \Psi_{\mathrm{q}} i_{\mathrm{d}} \right) \tag{2.34}$$

For SPMSM and IPMSM, the torque expression yields

$$T_{\mathrm{e}} = n_{\mathrm{p}} \left\{ \Psi_{\mathrm{m}} + \left(L_{\mathrm{d}} - L_{\mathrm{q}} \right) i_{\mathrm{d}} \right\} \cdot i_{\mathrm{q}} \tag{2.35}$$

In the case of PMa-SynRM, the torque equation is

$$T_{\mathrm{e}} = n_{\mathrm{p}} \left\{ \Psi_{\mathrm{m}} + \left(L_{\mathrm{d}} - L_{\mathrm{q}} \right) i_{\mathrm{q}} \right\} \cdot i_{\mathrm{d}} \tag{2.36}$$

It can be seen from (2.35) that the developed torque consists of two parts, one produced by the permanent magnet flux called synchronous torque (T_{es}) and the second called reluctance torque (T_{er}), which is produced by the difference of the inductance in rotor d- and q-axes, i.e., $L_{\mathrm{d}} - L_{\mathrm{q}}$. For SPMSM $L_{\mathrm{d}} \cong L_{\mathrm{q}}$, the reluctance torque is negligible.

2.4.5. Mechanical motion equation

In general, the load torque, friction, and inertia of the PMSM drive can be a function of time, rotor position, and angular speed. The inertia, *J*, and friction coefficients are assumed to be constants during the test sequences. Therefore, the equation of motion can be written as:

$$T_e - T_L = J\frac{d\omega_m}{dt} + B_f\omega_m + \frac{F \cdot sign(\omega_m)}{|\omega_m|} \tag{2.37}$$

In (2.37), T_L is the external torque (namely load torque) on the motor shaft, *J* is the inertia, ω_m is the mechanical angular speed of the rotor, and B_f is the friction constant. *F* denotes the Coulomb friction component. Usually, *F* is ignored at medium, high and very high speeds. The following equation holds between the angular speed and the rotor position:

$$\theta_m = \int \omega_m dt + \theta_0 \Leftrightarrow \omega_m = \frac{d\theta_m}{dt} \tag{2.38}$$

Thus, from (2.38), the acceleration of the angular speed is given as:

$$\frac{d\omega_m}{dt} = \frac{1}{J}(T_e - T_L - B_f\omega_m) \tag{2.39}$$

Finally, the whole mathematical models of the SPMSM, IPMSM, and PMa-SynRM, which are used in simulation studies, are described in *d*, *q* reference frame as:

For SPMSM:

$$\begin{aligned}
v_d &= R_s i_d + L_s\frac{di_d}{dt} - \omega_e\Psi_q \\
v_q &= R_s i_q + L_s\frac{di_q}{dt} + \omega_e\Psi_d \\
\Psi_q &= L_s i_q \\
\Psi_d &= L_s i_d + \Psi_m \\
\frac{d\omega_m}{dt} &= \frac{1}{J}(T_e - T_L - B_f\omega_m) \\
T_e &= n_p\Psi_m i_q
\end{aligned} \tag{2.40}$$

For IPMSM:

$$
\begin{aligned}
v_{\mathrm{d}} &= R_{\mathrm{s}} i_{\mathrm{d}} + L_{\mathrm{d}} \frac{di_{\mathrm{d}}}{dt} - \omega_{\mathrm{e}} \Psi_{\mathrm{q}} \\
v_{\mathrm{q}} &= R_{\mathrm{s}} i_{\mathrm{q}} + L_{\mathrm{q}} \frac{di_{\mathrm{q}}}{dt} + \omega_{\mathrm{e}} \Psi_{\mathrm{d}} \\
\Psi_{\mathrm{q}} &= L_{\mathrm{q}} i_{\mathrm{q}} \\
\Psi_{\mathrm{d}} &= L_{\mathrm{d}} i_{\mathrm{d}} + \Psi_{\mathrm{m}} \\
\frac{d\omega_{\mathrm{m}}}{dt} &= \frac{1}{J}\left[T_{\mathrm{e}} - T_{\mathrm{L}} - B_{\mathrm{f}} \omega_{\mathrm{m}}\right] \\
T_{\mathrm{e}} &= n_{\mathrm{p}} \left\{\Psi_{\mathrm{m}} - (L_{\mathrm{d}} - L_{\mathrm{q}}) i_{\mathrm{d}}\right\} \cdot i_{\mathrm{q}}
\end{aligned}
\tag{2.41}
$$

For PMa-SynRM:

$$
\begin{aligned}
v_{\mathrm{d}} &= R_{\mathrm{s}} i_{\mathrm{d}} + L_{\mathrm{d}} \frac{di_{\mathrm{d}}}{dt} - \omega_{\mathrm{e}} \Psi_{\mathrm{q}} \\
v_{\mathrm{q}} &= R_{\mathrm{s}} i_{\mathrm{q}} + L_{\mathrm{q}} \frac{di_{\mathrm{q}}}{dt} + \omega_{\mathrm{e}} \Psi_{\mathrm{d}} \\
\Psi_{\mathrm{q}} &= L_{\mathrm{q}} i_{\mathrm{q}} - \Psi_{\mathrm{m}} \\
\Psi_{\mathrm{d}} &= L_{\mathrm{d}} i_{\mathrm{d}} \\
\frac{d\omega_{\mathrm{m}}}{dt} &= \frac{1}{J}\left[T_{\mathrm{e}} - T_{\mathrm{L}} - B_{\mathrm{f}} \omega_{\mathrm{m}}\right] \\
T_{\mathrm{e}} &= n_{\mathrm{p}} \left\{\Psi_{\mathrm{m}} - (L_{\mathrm{d}} - L_{\mathrm{q}}) i_{\mathrm{q}}\right\} \cdot i_{\mathrm{d}}
\end{aligned}
\tag{2.42}
$$

Based on the above models, the following figure shows the block diagram of SPMSM/IPMSM and PMa-SynRM in which the inputs are the voltage component in d, q reference frame v_{d}, v_{q}, and the output are the mechanical speed of the rotor ω_{m}. As the external load torque, T_{L} is a disturbance. In this figure, the friction torque is included in the load torque.

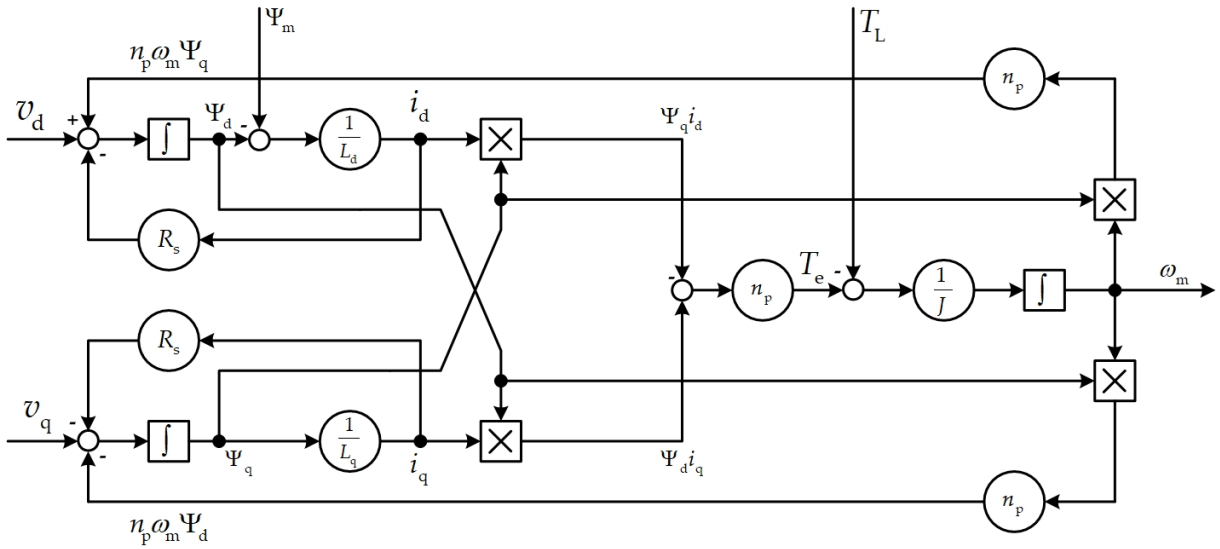

Figure 2.8 Block scheme of the SPMSM and IPMSM in rotating *d*, *q* frame.

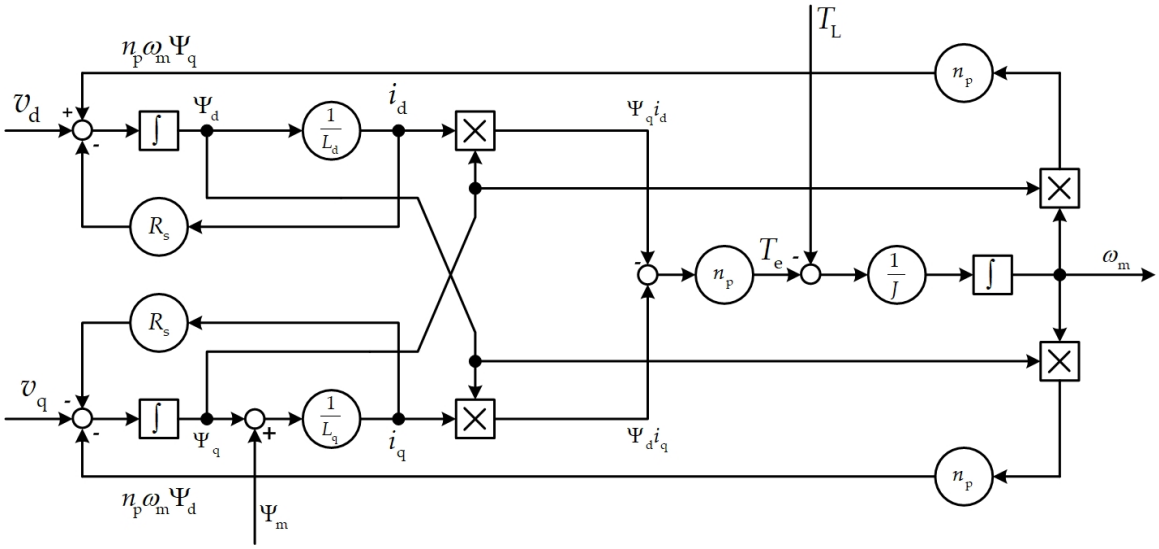

Figure 2.9 Block scheme of the PMa-SynRM in rotating *d*, *q* frame.

2.4.6. Nonlinear model in state-space representation

The state-space model of a dynamic system is represented by the following equations:

$$\sum : \begin{cases} \dot{x}(t) = f\{x(t), u(t)\} \\ y(t) = h\{x(t)\} \end{cases} \tag{2.43}$$

where the first equation is an ordinary differential equation

$$\dot{x}(t) = f\{x(t), u(t)\} \tag{2.44}$$

where f is a smooth vector field, x is the state vector, and u is the input vector. The relation between the state and the output is described through the function h as follows:

$$y(t) = h\{x(t)\} \tag{2.45}$$

However, in most of the systems, the input acts in an affine manner; therefore, the following representation is used:

$$\sum : \begin{cases} \dot{x}(t) = f(x) + g(x)u \\ y(t) = h(x) \end{cases} \tag{2.46}$$

For electric motors, the vector state is composed of stator current and mechanical speed: $[i_d \; i_q \; \omega_m]^T$. The input is composed of stator voltages. An additional input is the load torque, considered as external disturbance, which is not controllable. So, the vector is $[v_d \; v_q \; T_L]^T$.

The outputs are stator currents and mechanical speed. If the only current control is of interest, or in sensorless control, the output vector does not include mechanical speed.

The state-space representation of the SPMSM and IPMSM is respectively given below

$$\underbrace{\begin{bmatrix} \frac{di_d}{dt} \\ \frac{di_q}{dt} \\ \frac{d\omega_m}{dt} \end{bmatrix}}_{\dot{x}} = \underbrace{\begin{bmatrix} \left(-R_s i_d + \omega_e L_s i_q\right)/L_s \\ \left\{-R_s i_q - \omega_e (L_s i_d + \Psi_m)\right\}/L_s \\ \left(n_p \Psi_m i_q - B_f \omega_m\right)/J \end{bmatrix}}_{f(x)} + \underbrace{\begin{bmatrix} \frac{1}{L_s} & 0 & 0 \\ 0 & \frac{1}{L_s} & 0 \\ 0 & 0 & -\frac{1}{J} \end{bmatrix}}_{\mathbf{B}} \underbrace{\begin{bmatrix} v_d \\ v_q \\ T_L \end{bmatrix}}_{u}$$

$$y = \underbrace{\begin{bmatrix} 1 & 0 & 0 \\ 0 & 1 & 0 \end{bmatrix}}_{\mathbf{C}} \begin{bmatrix} i_d \\ i_q \\ \omega_m \end{bmatrix} \tag{2.47}$$

and

$$\underbrace{\begin{bmatrix} \frac{di_{\mathrm{d}}}{dt} \\ \frac{di_{\mathrm{q}}}{dt} \\ \frac{d\omega_{\mathrm{m}}}{dt} \end{bmatrix}}_{\dot{x}} = \underbrace{\begin{bmatrix} \left(-R_{\mathrm{s}} i_{\mathrm{d}} + \omega_{\mathrm{e}} L_{\mathrm{d}} i_{\mathrm{q}}\right) / L_{\mathrm{d}} \\ \left\{-R_{\mathrm{s}} i_{\mathrm{q}} - \omega_{\mathrm{e}} (L_{\mathrm{d}} i_{\mathrm{d}} + \Psi_{\mathrm{m}})\right\} / L_{q} \\ \left[n_{\mathrm{p}} \left\{\Psi_{\mathrm{m}} i_{\mathrm{q}} + (L_{\mathrm{d}} - L_{\mathrm{q}}) i_{\mathrm{d}} i_{\mathrm{q}}\right\} - B_{f} \omega_{m}\right] / J \end{bmatrix}}_{f(x)} + \underbrace{\begin{bmatrix} \frac{1}{L_{\mathrm{d}}} & 0 & 0 \\ 0 & \frac{1}{L_{\mathrm{q}}} & 0 \\ 0 & 0 & -\frac{1}{J} \end{bmatrix}}_{\mathbf{B}} \underbrace{\begin{bmatrix} v_{\mathrm{d}} \\ v_{\mathrm{q}} \\ T_{\mathrm{L}} \end{bmatrix}}_{u}$$

$$y = \underbrace{\begin{bmatrix} 1 & 0 & 0 \\ 0 & 1 & 0 \end{bmatrix}}_{\mathbf{C}} \begin{bmatrix} i_{\mathrm{d}} \\ i_{\mathrm{q}} \\ \omega_{\mathrm{m}} \end{bmatrix} \tag{2.48}$$

The state-space representation of the PMa-SynRM is given by (2.49).

$$\underbrace{\begin{bmatrix} \frac{di_{\mathrm{d}}}{dt} \\ \frac{di_{\mathrm{q}}}{dt} \\ \frac{d\omega_{\mathrm{m}}}{dt} \end{bmatrix}}_{\dot{x}} = \underbrace{\begin{bmatrix} \left\{-R_{\mathrm{s}} i_{\mathrm{d}} + \omega_{\mathrm{e}} (L_{\mathrm{q}} i_{\mathrm{q}} - \Psi_{\mathrm{m}})\right\} / L_{d} \\ \left(-R_{\mathrm{s}} i_{\mathrm{q}} - \omega_{\mathrm{e}} L_{\mathrm{d}} i_{\mathrm{d}}\right) / L_{q} \\ \left[n_{\mathrm{p}} \left\{\Psi_{\mathrm{m}} i_{\mathrm{d}} + (L_{\mathrm{d}} - L_{\mathrm{q}}) i_{\mathrm{q}} i_{\mathrm{d}}\right\} - B_{\mathrm{f}} \omega_{\mathrm{m}}\right] / J \end{bmatrix}}_{f(x)} + \underbrace{\begin{bmatrix} \frac{1}{L_{d}} & 0 & 0 \\ 0 & \frac{1}{L_{q}} & 0 \\ 0 & 0 & -\frac{1}{J} \end{bmatrix}}_{\mathbf{B}} \underbrace{\begin{bmatrix} v_{\mathrm{d}} \\ v_{\mathrm{q}} \\ T_{\mathrm{L}} \end{bmatrix}}_{u}$$

$$y = \underbrace{\begin{bmatrix} 1 & 0 & 0 \\ 0 & 1 & 0 \end{bmatrix}}_{\mathbf{C}} \begin{bmatrix} i_{\mathrm{d}} \\ i_{\mathrm{q}} \\ \omega_{\mathrm{m}} \end{bmatrix} \tag{2.49}$$

The input is [v_{d}, v_{q}, T_{L}], where T_{L} is assumed to be an unknown input. The measured output is the stator currents [i_{d}, i_{q}].

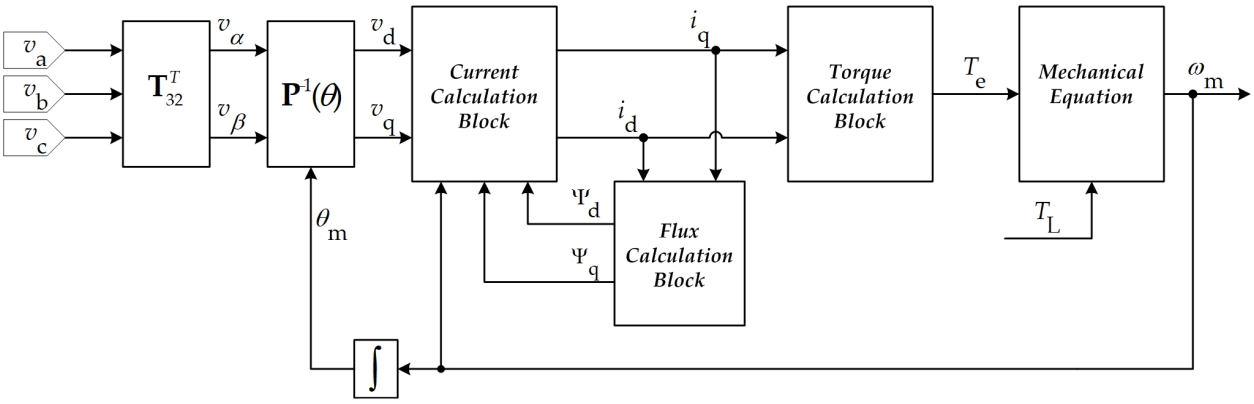

Figure 2.10 Diagram representation of the simulation model for the PMSM.

2.5. Dynamic simulation of the IPMSM and SPMSM

The model of the PMSM is carried on in the Matlab/Simulink to validate the motor's behavior at different speeds and torque levels. In addition, the Simulink model is also used in the overall control model, presented in the next chapter. The structure of the Simulink model is presented in Figure 2.10.

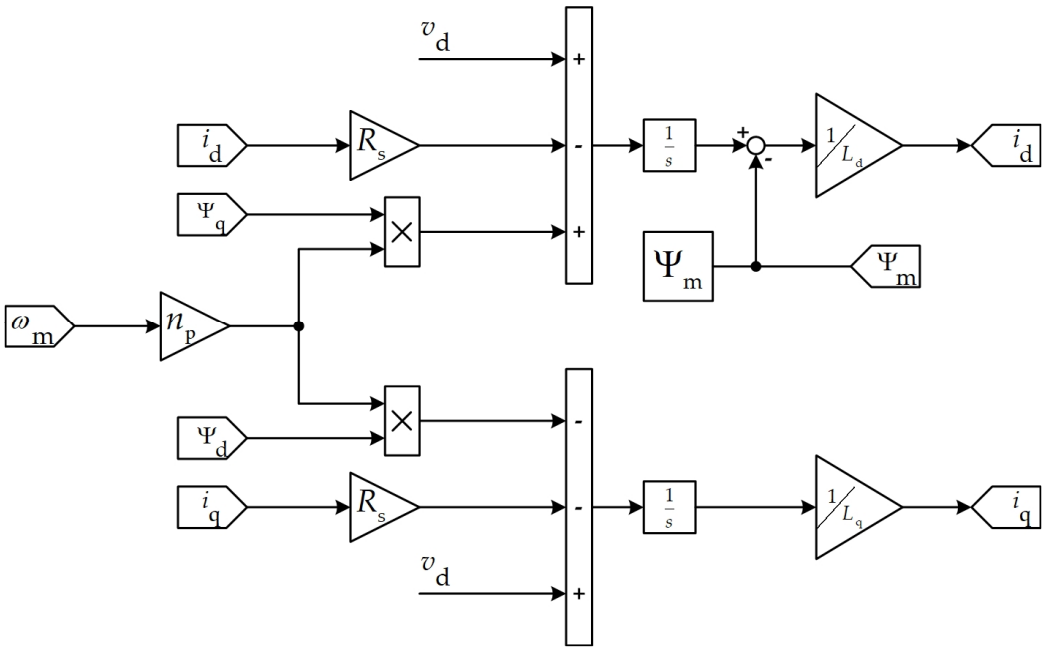

Figure 2.11 Simulink model expressing the current calculation block of the of the SPMSM and IPMSM.

The simulation model inputs are the phase voltages: v_a, v_b, and v_c. The model outputs are the shaft speed, stator currents, i_A, i_B, and i_C. Using the Concordia transformation, the input voltages are transformed into a dq reference frame (2.26). By utilizing the flux equation in (2.30) and also voltage equation from (2.31), the *dq* stator currents can be expressed as:

$$\begin{aligned} i_d &= \frac{1}{L_d}\left\{\int\left(v_d - R_s i_d + \omega_e \Psi_q\right)dt - \Psi_m\right\} \\ i_q &= \frac{1}{L_q}\int\left(v_q - R_s i_q - \omega_e \Psi_d\right)dt \end{aligned} \tag{2.50}$$

The current calculation block is represented in Figure 2.11. The flux linkage calculation block is represented in Figure 2.12.

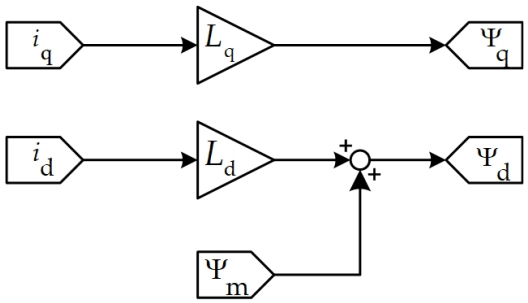

Figure 2.12 Simulink model expressing the flux calculation block of the SPMSM and IPMSM.

The produced torque can be calculated according to (2.35) when the current is known. By considering the mechanical equation presented in (2.39), the shaft speed can be calculated as in the following:

$$\omega_m = \frac{1}{J}\int (T_e - T_L - B_f \omega_m)dt \tag{2.51}$$

The Simulink model calculating the shaft speed and also the angle is presented in Figure 2.13.

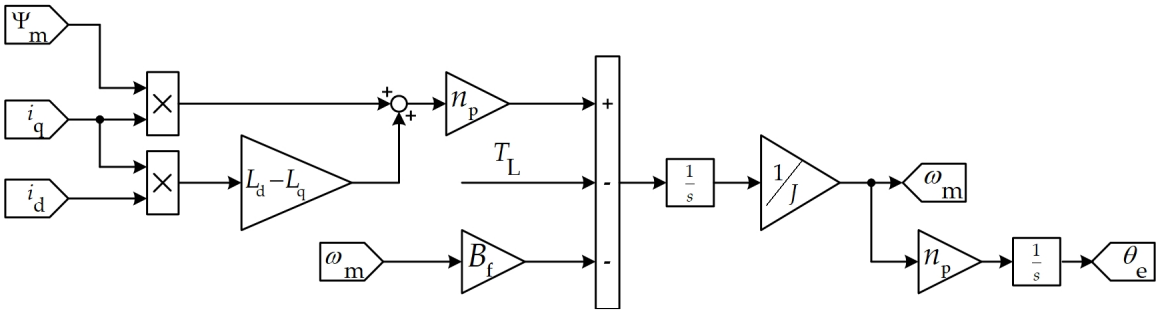

Figure 2.13 Simulink model expressing the calculation of the shaft speed for SPMSM and IPMSM.

2.6. Dynamic simulation of the PMa-SynRM

By using the flux equation in (2.32) and also voltage equations from (2.32), the *dq* stator current is given as:

$$\begin{aligned} i_d &= \frac{1}{L_d}\int \left\{ v_d - R_s i_d + \omega_e \Psi_q \right\} dt \\ i_q &= \frac{1}{L_q}\left\{ \int (v_q - R_s i_q - \omega_e \Psi_d)dt + \Psi_m \right\} \end{aligned} \tag{2.52}$$

$$\begin{aligned} \Psi_q &= L_q i_q - \Psi_m \\ \Psi_d &= L_d i_d \end{aligned} \tag{2.53}$$

$$v_{\mathrm{d}} = R_{\mathrm{s}} i_{\mathrm{d}} + L_{\mathrm{d}} \frac{di_{\mathrm{d}}}{dt} - \omega_{\mathrm{e}} \Psi_{\mathrm{q}}$$
$$v_{\mathrm{q}} = R_{\mathrm{s}} i_{\mathrm{q}} + L_{\mathrm{q}} \frac{di_{\mathrm{q}}}{dt} - \frac{d\Psi_{\mathrm{m}}}{dt} + \omega_{\mathrm{e}} \Psi_{\mathrm{d}} \tag{2.54}$$

The current calculation block is in Figure 2.14.

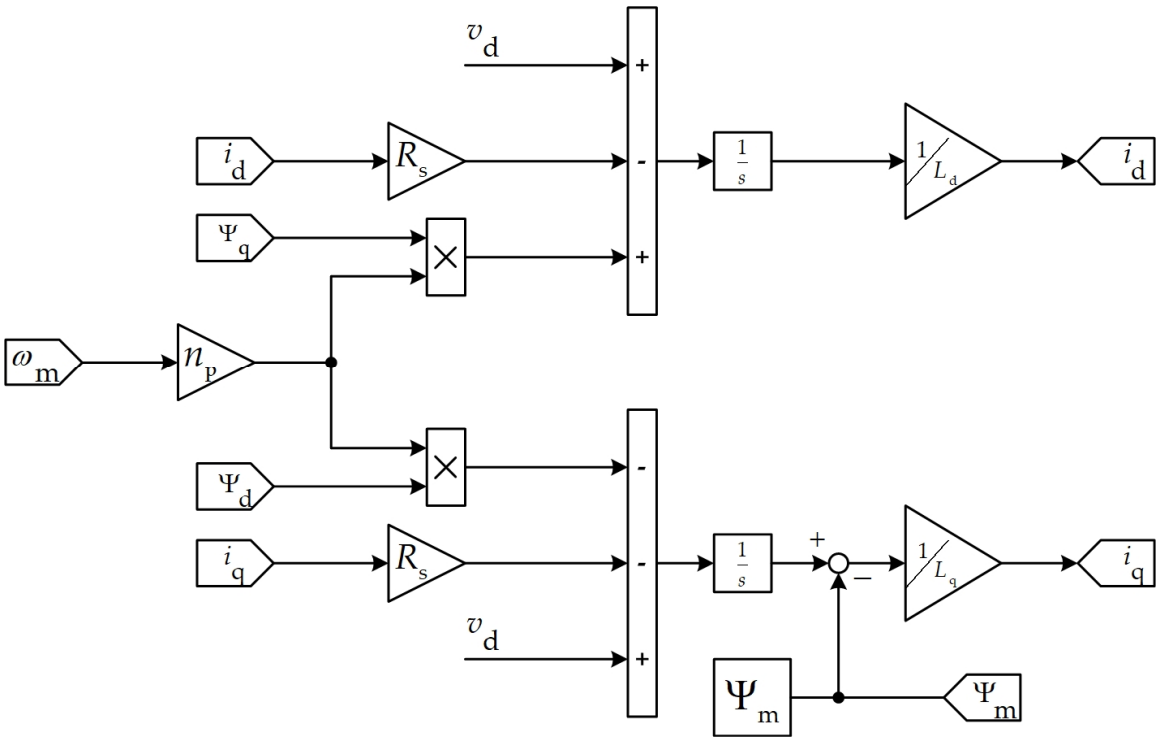

Figure 2.14 Simulink model expressing the current calculation block of the PMa-SynRM.

The flux linkage calculation block is given in Figure 2.15.

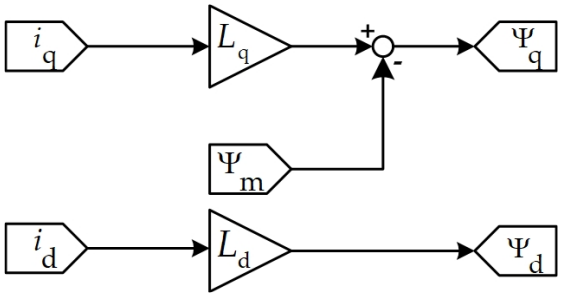

Figure 2.15 Simulink model expressing the flux calculation block of the PMa-SynRM.

The produced torque can be calculated according to (2.36). The Simulink model calculating the shaft speed and the angle is shown in Figure 2.16.

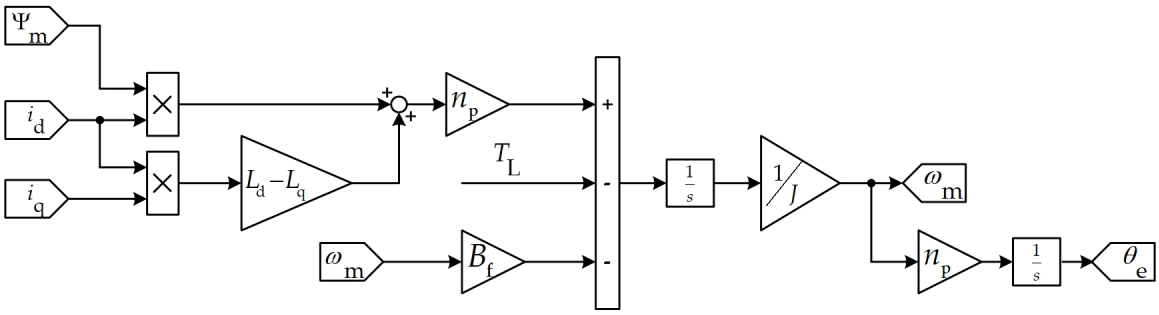

Figure 2.16 Simulink model expressing the calculation of the shaft speed for PMa-SynRM.

2.7. Model of Pulse width modulated frequency inverter for PMSM supply

Figure 2.17 shows a block diagram of a two-level Voltage-Source Inverter (VSI) commonly used in Adjustable Speed Drives (ASDs) that drives PMSMs. The ASD includes a DC-link with a filter capacitor supplied by the grid or battery. The VSI converts direct current into variable AC voltage, a variable frequency for motor speed or control (torque/current). The power switch for the inverter bridge is typically an IGBT or silicon carbide MOSFET, i.e., SiC, MOSFET.

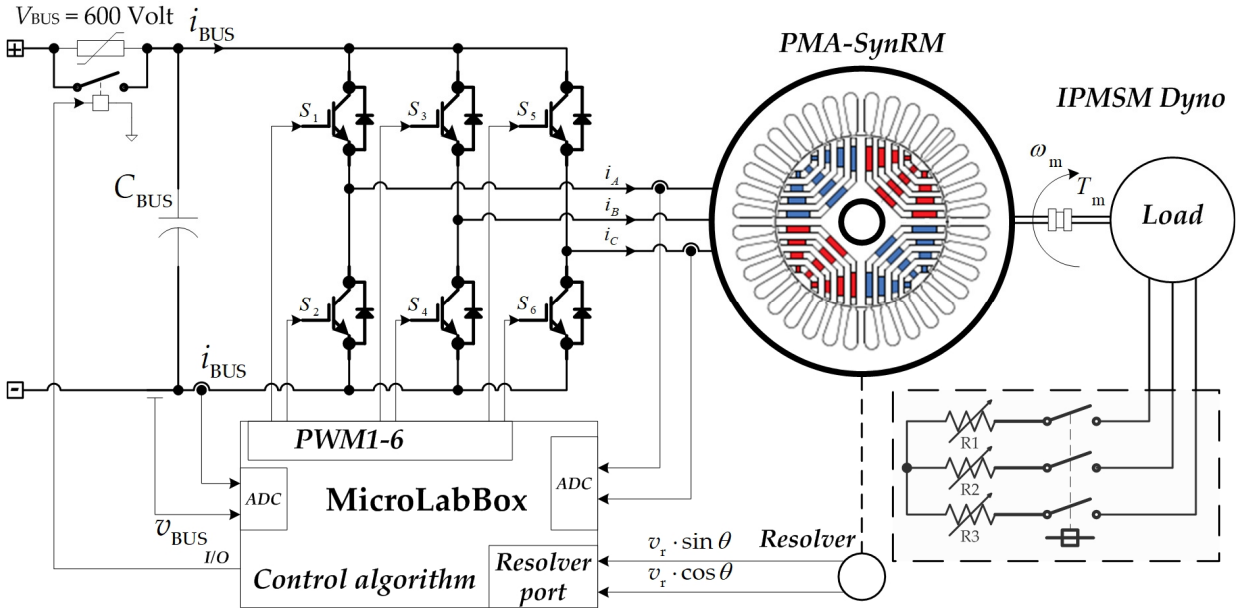

Figure 2.17 VSD inverter system powered PMSM block diagram.

The following figure illustrates the simplified model of an ideal (lossless) VSI for implementation under Simulink.

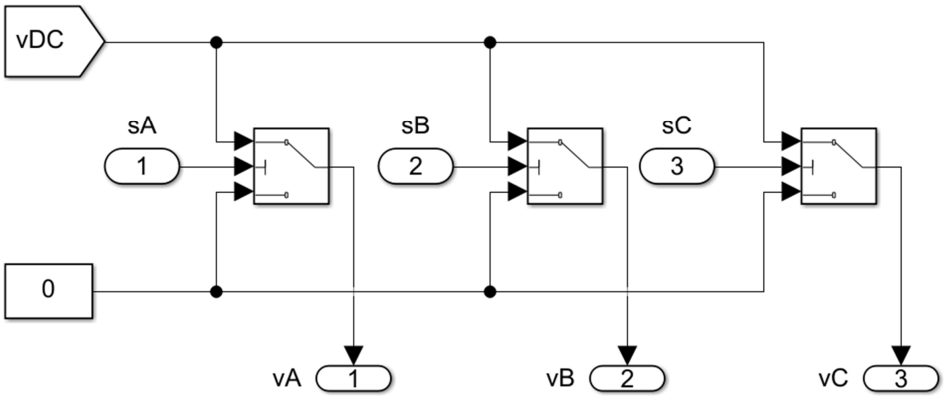

Figure 2.18 The ideal inverter implemented in the Simulink environment.

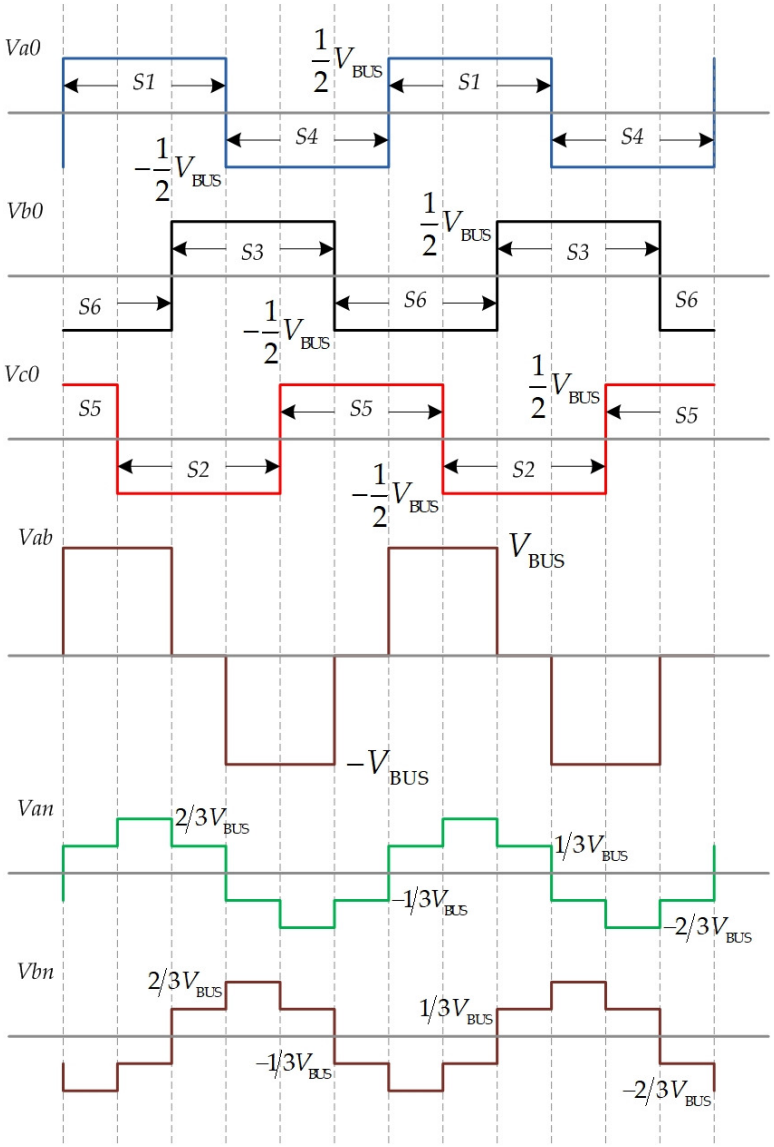

Figure 2.19 Produced voltage of six positions switching.

The six positions of switches (U1-U6) produce an output phase voltage equal to ±1/3 or ±2/3 of the DC voltage (Figure 2.19). The last two (U0, U7) give zero output voltage. Therefore, the output phase voltages and line to line voltages calculated by (2.55) are presented in Figure 2.19.

$$\begin{aligned} V_{AB} &= V_{AN} - V_{BN} \\ V_{BC} &= V_{BN} - V_{CN} \\ V_{CA} &= V_{CN} - V_{AN} \end{aligned} \tag{2.55}$$

The maximum amplitude of fundamental phase voltage for a given DC voltage is obtained by:

$$V_{amp} = \frac{2}{\pi} V_{BUS} \tag{2.56}$$

2.8. Simulation of the sinusoidal PWM for supply PMSM

The simulation block implemented in the MATLAB/SIMULINK software is presented in Figure 2.20. This simulation uses the two types of PMSM, SPMSM and PMa-SynRM. Table 2.1 shows the parameters of SPMSM, and table 2.2 shows the parameters of PMa-SynRM.

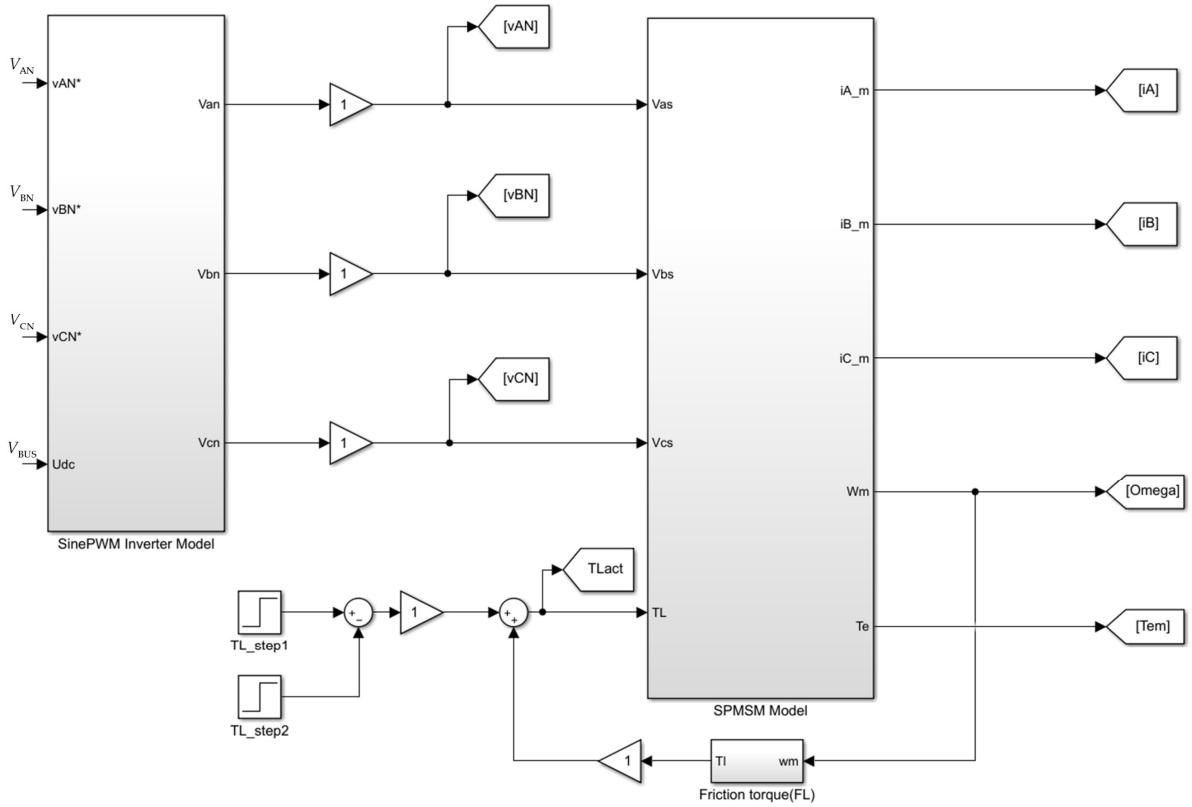

Figure 2.20 Simulation model of voltage source inverter circuit supplied to SPMSM.

TABLE 2.1
Studied SPMSM Parameters

Symbol	Meaning	Value
P_{rated}	Rated Power	1kW
n_{rated}	Rated Speed	3000 rpm
n_p	Number of pole pairs	3
R_s	Resistance (Motor + Inverter)	10 Ohm
$L_s = L_d = L_q$	Stator inductance	35.31 mH
Ψ_m	Permanent-magnet flux	0.2214 [Wb]
J	Equivalent inertia	0.002 kg.m2

TABLE 2.2:
Studied PMa-SynRM Parameters (linear case)

Symbol	Meaning	Value
P_{rated}	Rated Power	1kW
n_{rated}	Rated Speed	1350 rpm
n_p	Number of pole pairs	2
R_s	Resistance (Motor + Inverter)	3.2 Ohm
L_d	Normal *d*-axis inductance	288 mH
L_q	Normal *q*-axis inductance	38 mH
L_{dq}	Mutual inductance	4 mH
Ψ_m	Permanent-magnet flux	0.138 [Wb]
J	Equivalent inertia	0.0017 kg.m^2

The PMa-SynRM parameters are considered in the linear case. Therefore, the *d*- and *q*-axis inductances are assumed to be a constant value.

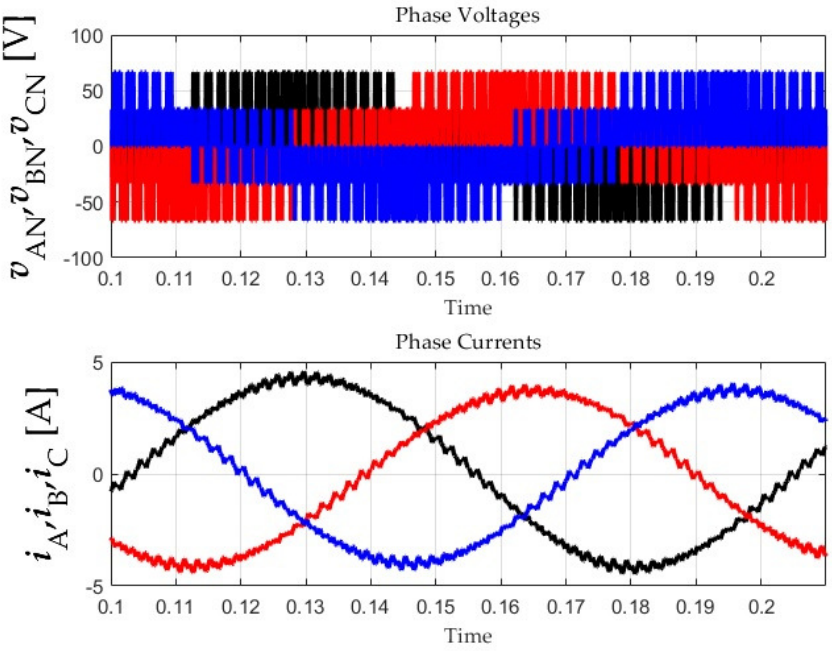

Figure 2.21 Simulation results of VSD inverter supplied to the PMSM in which v_{AN}, v_{BN}, and v_{CN} are phase voltages, i_A, i_B, and i_C are phase currents.

2.9. Current and speed control of PMSM

Regardless of the permanent magnet mounting method, the basic principle of motor control is the same, and the only difference is specific characteristics. In this thesis, we consider PM drives, including a two-level VSI and a PMSM (SPMSM, IPMSM of PMa-SynRM). The main requirements for a high-performance PM drive can be formulated as follows:

- Operating over a wide speed range at minimum losses
- Maximum utilization of DC-link voltage
- Low flux and torque ripples
- Robustness to parameters variation
- Regeneration operation
- Constant (or controlled) switching frequency

Various control methods can be used to meet the above requirements [43] [45] [51] [52]-[53]. Control methods for electric motors can be divided into two main categories depending on what quantities they control. Scalar Control contains only magnitudes, whereas Vector Control controls both magnitude and angle. These two main methods can be further divided into several different forms depending on their functionality; an overview of control methods for PMSMs can be seen in Figure 2.22.

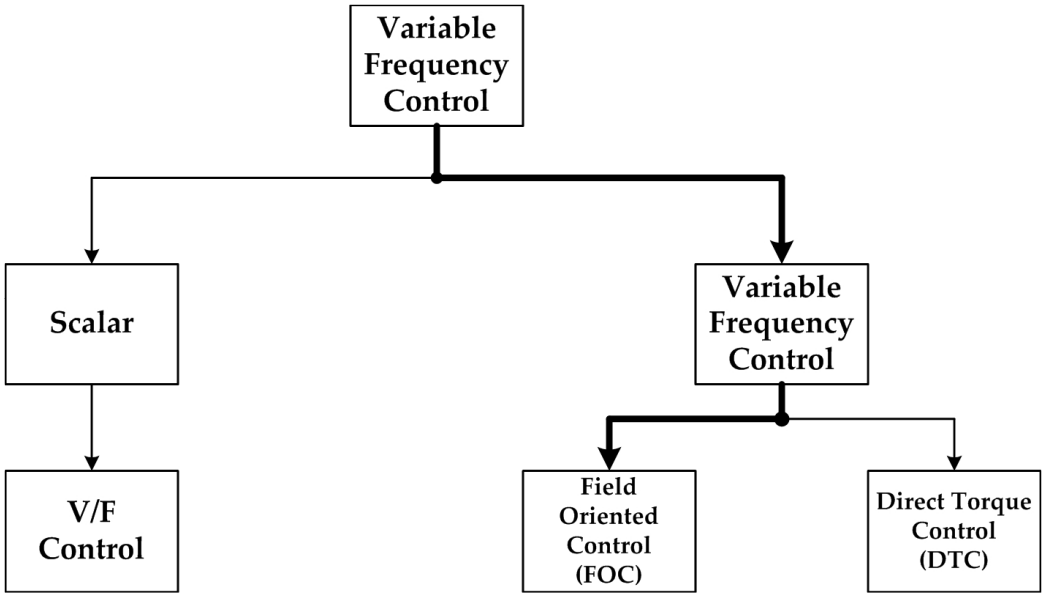

Figure 2.22 Classification of PMSM control approaches.

According to [43], scalar control is based on stability relationships that control only the amplitude and frequency (angular velocity) of the limiting vectors of voltage, current, and spatial flux. Thus, the control system does not affect the position of the space vector in the transient state. Therefore, this control is intended for applications that do not require high dynamics. In contrast, vector control controls both amplitude and instantaneous position of the spatial vectors of voltage, current, and flux, based on relationships for the dynamic model. Therefore, the control system will adjust the position of the space vector to ensure the correct orientation for stable transients. This method often uses the motor equation in the dq reference frame that rotates synchronously with the rotor. The motor control consists of a torque control loop by applying an adequate control voltage vector. In the framework of Field-Oriented Control (FOC), one of the most frequently employed vector control techniques, the torque control implies *dq* current control. Therefore, a current control loop is designed and implemented first to realize the torque control. Then, an external loop may be considered for the speed control if needs be. In the following paragraphs, FOC has been implemented to control SPMSM and PMa-SynRM.

2.9.1. Simulation and experimental validation of FOC for controlling SPMSM

The SPMSM drive is presented in Figure 2.23, and the block diagram of the FOC with PI controller is illustrated in Figure 2.24. According to its rotor geometry, the SPMSM is classified as a non-salient pole machine, as represented in Figure 2.3a. For the non-salient pole machines, the *d*- and *q*-axes inductances are equal. The torque (2.35) can hence be simplified to (2.40).

From (2.40), it can be seen that the only torque producing current is along the *q*-axis. Therefore, reaching the maximum efficiency of the machine is easily achieved by keeping the *d*-

axis current equal to zero. The control system reference currents i_{qREF} and i_{dREF} can easily be calculated as follows:

$$i_{qREF} = \frac{T_{eREF}}{n_p \Psi_m} \tag{2.57}$$

$$i_{dREF} = 0 \tag{2.58}$$

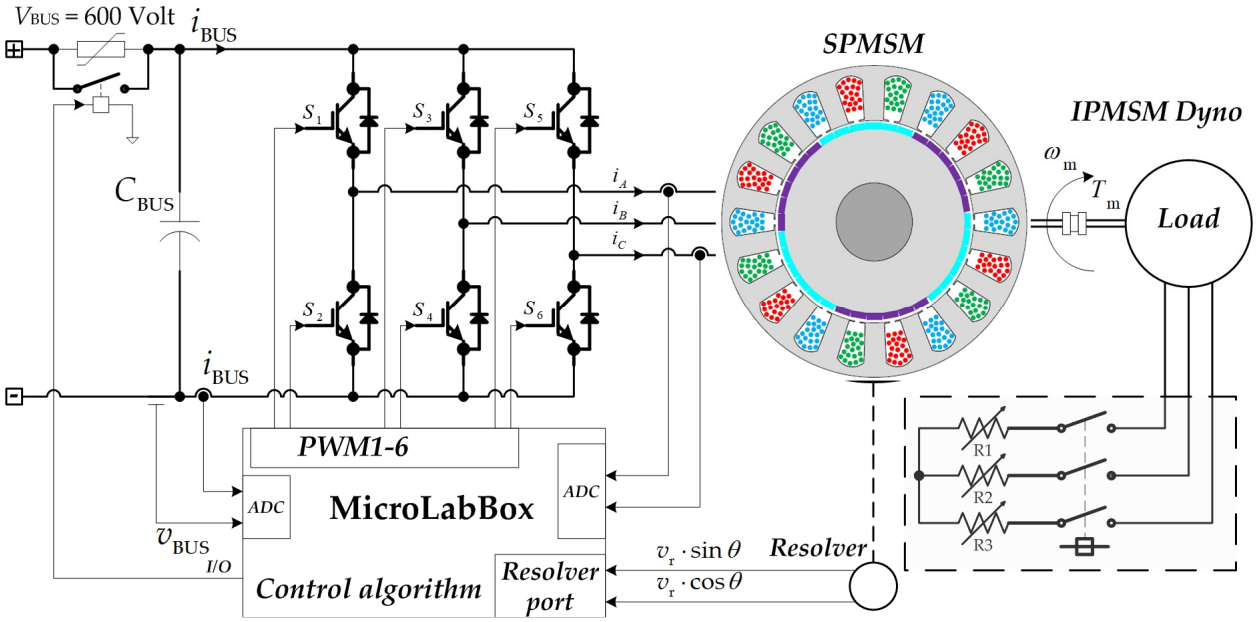

Figure 2.23 Block diagram of the VSD powered SPMSM.

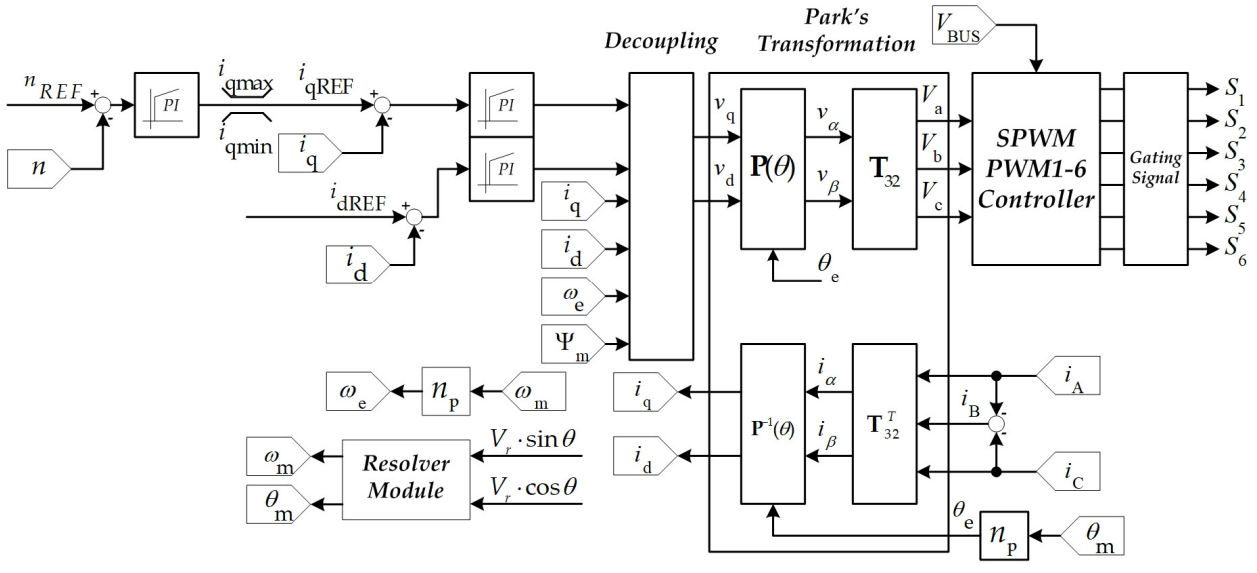

Figure 2.24 Block diagram of the FOC with PI controller for controlling SPMSM.

The two current loops must be much faster than the speed loop. Therefore, the PI current controllers are tuned first. By decoupling crossing terms of the voltage equations (2.40), the two currents i_d and i_q can be controlled independently [44]. The open-loop transfer functions of the i_d and i_q of the current can be expressed as shown in (2.59) and (2.60).

$$G_{old}(s) = K_{pd}\frac{\tau_{id}s+1}{\tau_{id}s}\cdot\frac{1}{R_s\left(\tau_{sd}s+1\right)} \tag{2.59}$$

$$G_{olq}(s) = K_{pq}\frac{\tau_{iq}s+1}{\tau_{iq}s}\cdot\frac{1}{R_s\left(\tau_{sq}s+1\right)} \tag{2.60}$$

where:

$\tau_{sd} = L_d/R_s$ is the electrical time constant of the *d*-axis,
$\tau_{sq} = L_q/R_s$ is the electrical time constant of the *q*-axis,
K_{pd} is the proportional gain of the *d*-axis controller,
K_{pq} is the proportional gain of the *q*-axis controller,
τ_{id} is the time constant of the *d*-axis current loop,
τ_{iq} is the time constant of the *d*-axis current loop,
$G_{old}(s)$ is the open-loop transfer function of the *d*-axis current loop, and
$G_{olq}(s)$ is the open-loop transfer function of the *q*-axis current loop.

By using pole-zero cancellation [58] [59]-[60], that is, $\tau_{sd} = \tau_{id}$ and $\tau_{sq} = \tau_{iq}$, the controller parameters can be obtained:

$$K_{pd} = \omega_{cd}\cdot L_d, K_{id} = \omega_{cd}\cdot R_s \tag{2.61}$$

$$K_{pq} = \omega_{cq}\cdot L_q, K_{iq} = \omega_{cq}\cdot R_s \tag{2.62}$$

where ω_{cd} is the *d*-axis crossover frequency and ω_{cq} is the *q*-axis crossover frequency.

The open-loop transfer function of the speed control is:

$$G_{o\omega}(s) = K_{p\omega}\frac{\tau_{i\omega}\cdot s+1}{\tau_{i\omega}\cdot s}\cdot\frac{1}{\tau_{s\omega}\cdot s+1} \tag{2.63}$$

where $\tau_{s\omega} = J/B_f$ is the electrical time constant of the speed loop, J is the inertia, B_f is the viscous friction, $K_{p\omega}$ is the proportional gain of the speed controller, and $\tau_{i\omega}$ is the time constant speed loop.

By using pole-zero cancellation, that is, $\tau_{s\omega} = \tau_{i\omega}$, the speed controller parameters can be obtained:

$$K_{p\omega} = 3 \cdot J / \left(\tau_{r\omega} / 3\right), K_{i\omega} = K_{p\omega} / \tau_{s\omega} \tag{2.64}$$

The $\tau_{r\omega}$ is the closed-loop response time considered from the crossover frequency $\omega_{c\omega}$.

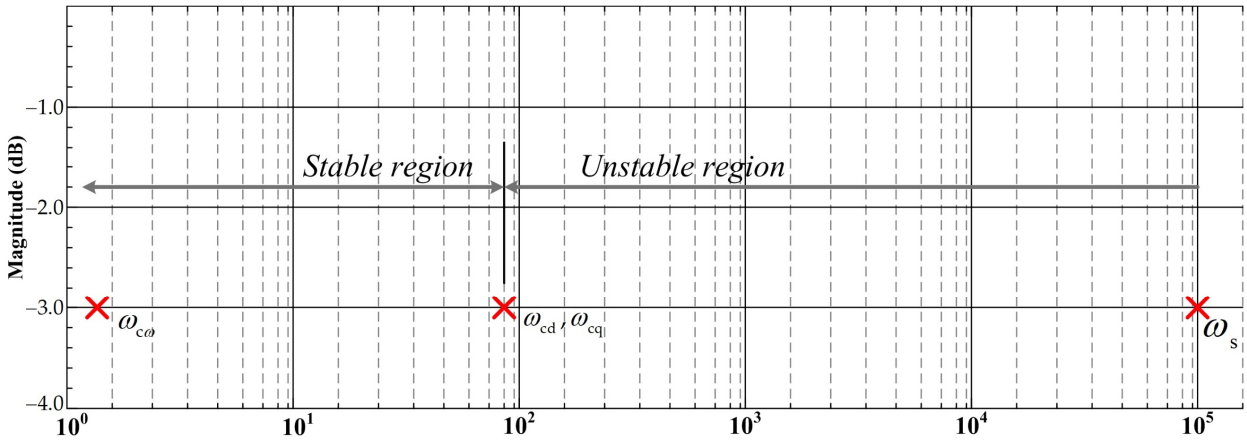

Figure 2.25 The setting of the controllers by choosing the crossover frequency in the frequency space.

Note that the stability and response of the FOC with PI controller are set by defining and selecting the dominant damping and natural frequency, as shown in Figure 2.25. Thus, the controller parameters of current and speed loop control can calculate by (2.61), (2.62), and (2.64), respectively.

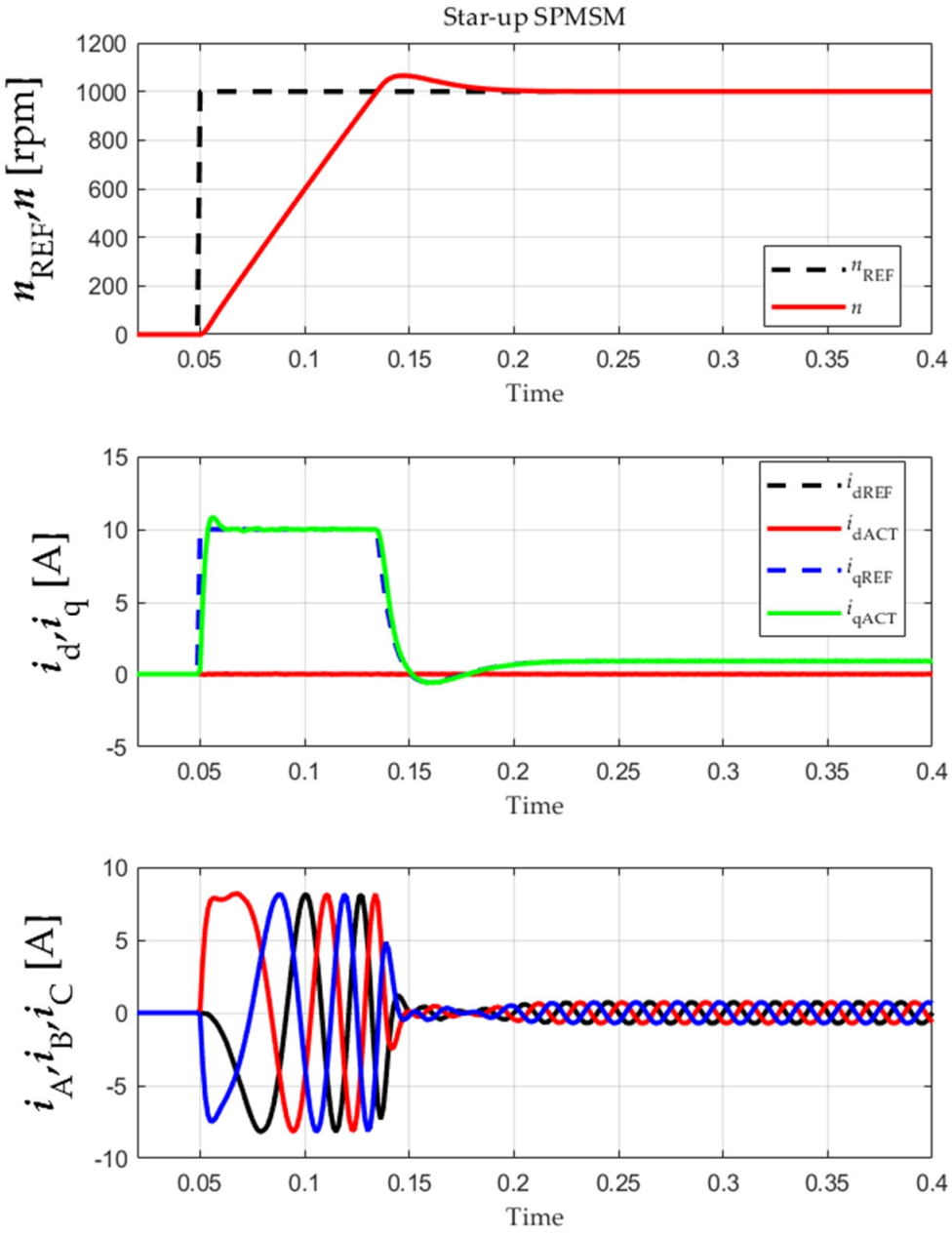

Figure 2.26 Simulation results of the FOC with the PI controller applied to SPMSM.

The following figure shows simulation results. First, the system performance when FOC with the traditional PI controller controls the SPMSM is presented. In Figure 2.26, in which the speed reference n_{REF}, measured speed n, the q-axis current reference i_{qREF}, the measured q-axis current i_q, the d-axis current reference ($i_{dREF} = 0$), the measured d-axis current i_d, and phase currents (i_A, i_B, and i_C) are shown. These results are used for comparison and benchmarking purposes.

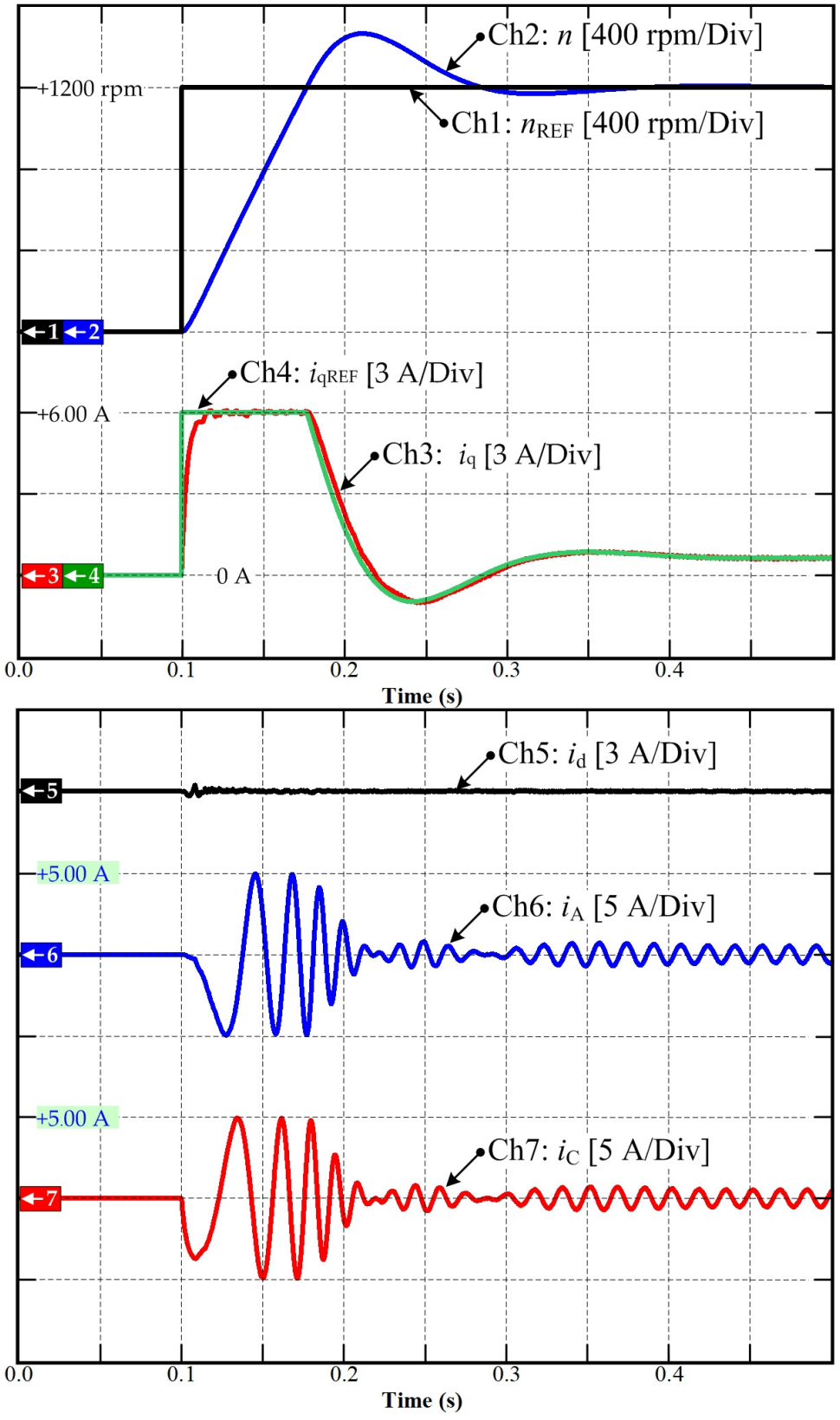

Figure 2.27 Experimental results of the FOC with the PI controller controlling SPMSM.

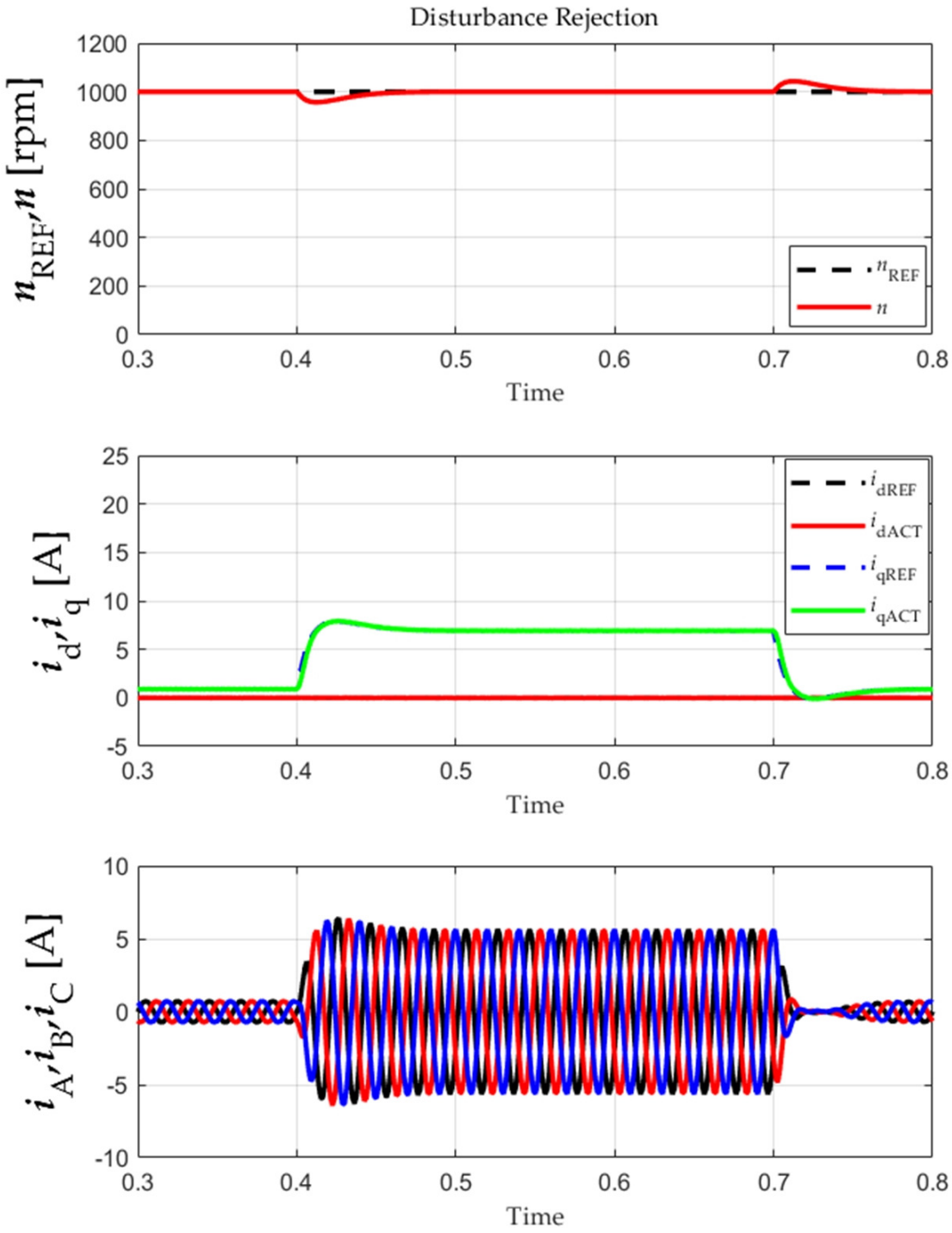

Figure 2.28 Simulation results: The external torque disturbance of FOC with PI controller controlling the SPMSM.

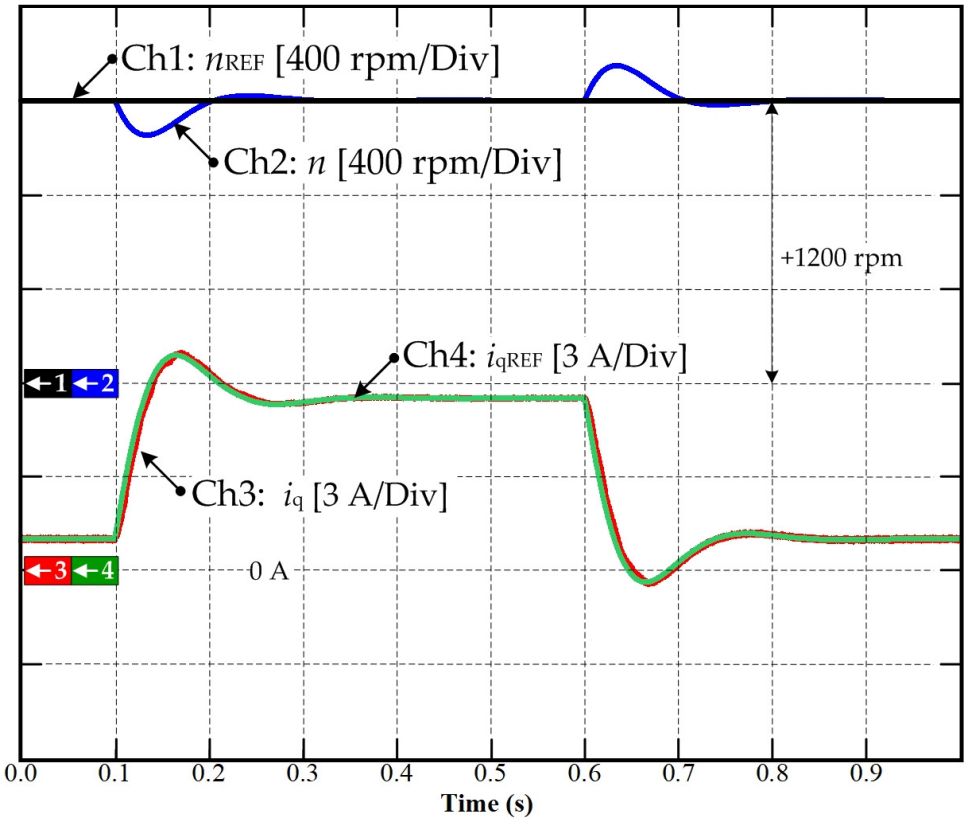

Figure 2.29 Experimental results of the external torque disturbance rejection the FOC with PI control applied to SPMSM.

Figure 2.27 shows the experimental validation of the FOC with the PI controller controlling the SPMSM. In Figure 2.27, Ch1 is the speed reference n_{REF}, Ch2 is the measured speed n, Ch3 is the measured q-axis current i_q, Ch4 is the q-axis current reference i_{qREF}, Ch5 is the measured d-axis current i_d, and Ch6, Ch7 are the measured phase currents (i_A, and i_C). The results reflect that when the controllers represented in (2.61), (2.62), and (2.64) are appropriately tuned, all behave, giving the desired d- and q-axis currents control loop performance. K_{pd}, K_{id}, K_{pq}, K_{iq}, $K_{p\omega}$, and $K_{i\omega}$ are proportional and integral coefficients, respectively, and correspond to simulation and experimental setup with $K_{pd} = K_{pq} = 35.31$, $K_{id} = K_{iq} = 10000$, $K_{p\omega} = 0.9$, $K_{i\omega} = 48$. In a transient process, the measured q-axis current i_q (Ch3) can be retrained to its limit (+6 Ampere), and i_d (Ch5) is controlled to be zero (0) at all times. However, in a transient process, the response of iq shows a slight oscillate. This demonstrates that the FOC with PI controller is not able to give high-performance control for SPMSM.

Then, the disturbance rejection ability of the FOC with PI controller applied to SPMSM is validated by adding an external disturbance torque T_L. Figure 2.28 shows the simulation validation results, in which the speed reference n_{REF}, measured speed n, q-axis current reference i_{qREF}, measured q-axis current i_q, d-axis current reference i_{dREF}, measured d-axis current i_d, and measured phase currents (i_A, i_B, and i_C) are shown. Finally, the experimental validation is implemented to show the external torque disturbance ability of the FOC with the PI controller

controlling SPMSM. Figure 2.29 illustrates the results, in which Ch1 is the speed reference n_{REF}, Ch2 is the measured speed n, Ch3 is the measured q-axis current i_q, Ch4 is the q-axis current reference i_{qREF}. As shown in Figures (2.28) and (2.29), the FOC with PI controller offers the external torque disturbance rejection ability when the external load torque is suddenly added and removed respectively at times 0.1 s and 0.6 s (in Figure 2.29), the measured speed n deviates from its reference by 200 rpm. The disturbance effect can be reduced by increasing the speed controller gains, but the system will be more sensitive to measurement noise.

2.9.2. Simulation and experimental validation of FOC for controlling PMa-SynRM

The PMa-SynRM drive is shown in Figure 2.17, and the block diagram of the FOC with the PI controller is shown in Figure 2.30. The controller parameters for PI control are designed as described in 2.9.1. According to the rotor geometries of the PMa-SynRM discussed in 2.3, the current control strategies differ. The rotor geometries of PMa-SynRM are the salient pole where $L_d > L_q$. The torque equation is given by (2.36). In this case, the optimal value of dq currents must be calculated to take advantage of the reluctance torque produced by the high saliency ratio. This strategy is called Maximum Torque Per Ampere (MTPA). The main idea of this strategy is to produce the requested torque using the minimum value of the stator current magnitude. Based on the torque equation Eq. (2.41), the torque of the PMa-SynRM can be divided into two the interaction torque and the reluctance torque (due to the difference in the inductances of the d and q axes). Therefore, to minimize the copper losses and increase the motor's efficiency, the MTPA will be applied to define optimal dq currents.

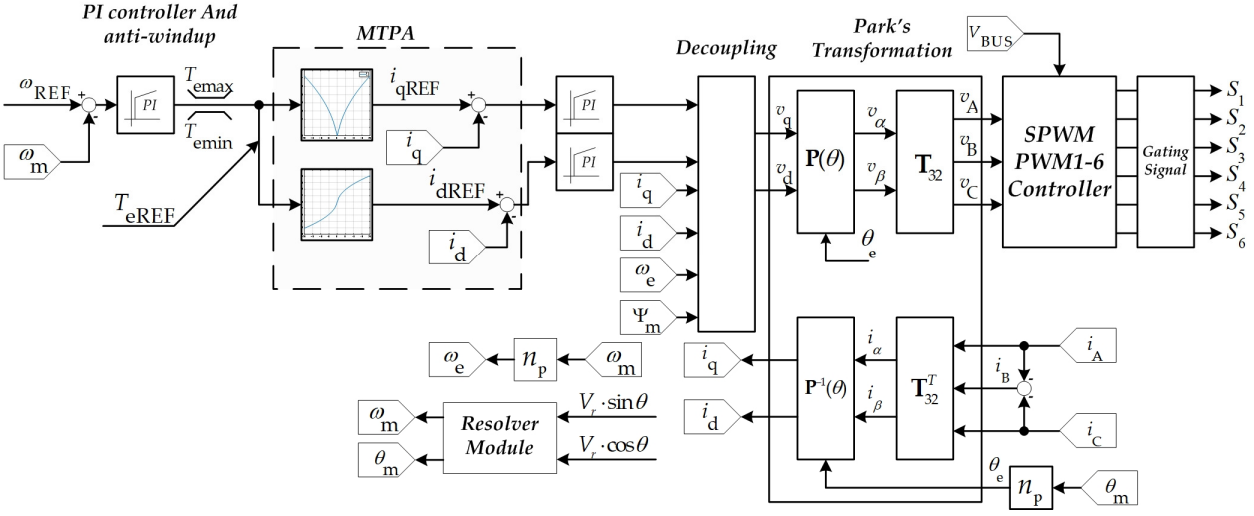

Figure 2.30 Block diagram of the FOC with MTPA control for the PMa-SynRM.

The copper loss equation is as follows:

$$P_{Copper} = R_s \cdot \left(i_d^2 + i_q^2 \right) \tag{2.65}$$

As shown in Figure 2.30, the torque equation of PMa-SynRM is given by:

$$T_{\text{ref}} = n_{\text{p}} \cdot \left(\Delta L \cdot i_{\text{q}} + \Psi_{\text{m}} \right) \cdot i_{\text{d}} \tag{2.66}$$

where ΔL is the difference in the inductances $\Delta L = (L_{\text{d}} - L_{\text{q}})$.

Based on this equation, there is no produced torque if the direct current is set to zero ($i_{\text{d}} = 0$). In contrast, the reference torque is equal to the interaction torque if the quadrature current is zero ($i_{\text{q}} = 0$). Therefore, to assure that the torque reference is achieved with minimum copper losses, the current iq and the current id must be minimized using the MTPA concept.

As shown in Figure 2.30, the minimum current vectors are stored in lookup tables for the iq and id references. However, to obtain the MTPA curve for the PMa-SynRM, the current vectors are the solution of the following optimization problem:

$$\begin{aligned} &Max: T_{\text{ref}} = n_{\text{p}} \cdot \left[\Delta L \cdot i_{\text{q}} \cdot i_{\text{d}} + \Psi_{\text{m}} \cdot i_{\text{d}} \right] \\ &Min: P_{\text{Copper}} = R_{\text{s}} \cdot \left(i_{\text{d}}^2 + i_{\text{q}}^2 \right) \end{aligned} \tag{2.67}$$

The quadrature current i_{d} can be obtained by using (2.68):

$$i_{\text{d}} = \frac{T_{\text{ref}}}{n_{\text{p}} \cdot \left(\Delta L \cdot i_{\text{q}} + \Psi_{\text{m}} \right)} \tag{2.68}$$

By substituting (2.68) into (2.65), the copper loss equation can be obtained:

$$P_{\text{Copper}} = R_{\text{s}} \cdot \left[\left(\frac{T_{\text{ref}}}{n_{\text{p}} \cdot \left(\Delta L \cdot i_{\text{q}} + \Psi_{\text{m}} \right)} \right)^2 + i_{\text{q}}^2 \right] = P_{\text{Copper}} \left(i_{\text{q}} \right) \tag{2.69}$$

To obtain the MTPA curve of i_{q}, the derivative of the copper loss equation (2.69) concerning i_{q} can be expressed by using (2.70) and assuming ΔL to be a constant parameter.

$$\left. \frac{dP_{\text{copper}}}{diq} \right|_{i_{\text{qopt}}} = 0 = 2 \cdot i_{\text{q}}^2 + \frac{T_{\text{ref}}^2}{n_{\text{p}}^2} \left(\frac{-2 \cdot \Delta L}{\left(\Psi_{\text{m}} + \Delta L \cdot i_{\text{q}} \right)^3} \right) \Bigg|_{i_{\text{qopt}}} = 0 \tag{2.70}$$

where i_{qopt} is the optimum quadrature current.

Using the numerical Newton–Raphson method, the MTPA curve can be obtained *dq* axis current references. As shown in Figure 2.31, optimal *dq* currents are plotted when T_{eREF} sweeps from -20 Nm to +20 Nm.

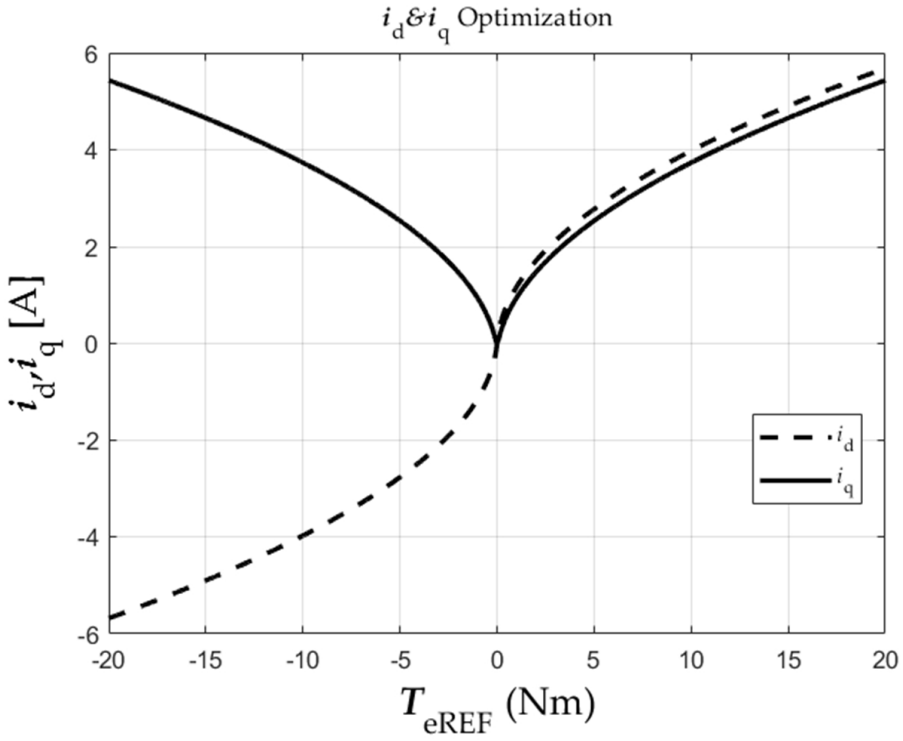

Figure 2.31 MTPA curve of the studied PMa-SynRM.

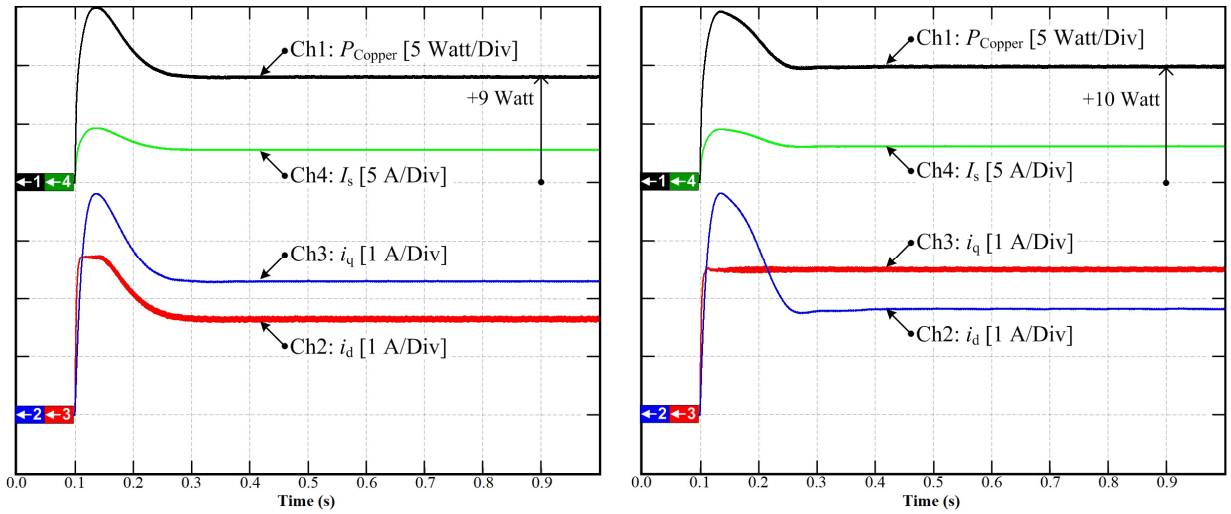

a b

Figure 2.32 Simulation of the copper losses minimization by the MTPA.

For clarity, Figure 2.32a depicts the simulation results of the PMa-SynRM control with the MTPA algorithm, and Figure 2.32b shows the simulation without the MTPA algorithm. In Figure 2.32, Ch1 is the total Copper losses power P_{copper}, Ch2 is the d-axis current i_d, Ch3 is the q-axis current, and Ch4 is the magnitude of the current vector defined by $I_s = \sqrt{i_d^2 + i_q^2}$. Based on the copper loss equation (2.65), the signal is illustrated as Ch1 in both Figures. In the case of the FOC with PI controller without MTPA, the q-axis current reference i_{qREF} is set to 2.5 Ampere. The results show that the total copper losses of the control system with the MTPA algorithm are less than those of the control system without MTPA. A reduction of almost 10% can be noticed. Therefore, the MTPA is necessary for the high-performance control of the PMa-SynRM.

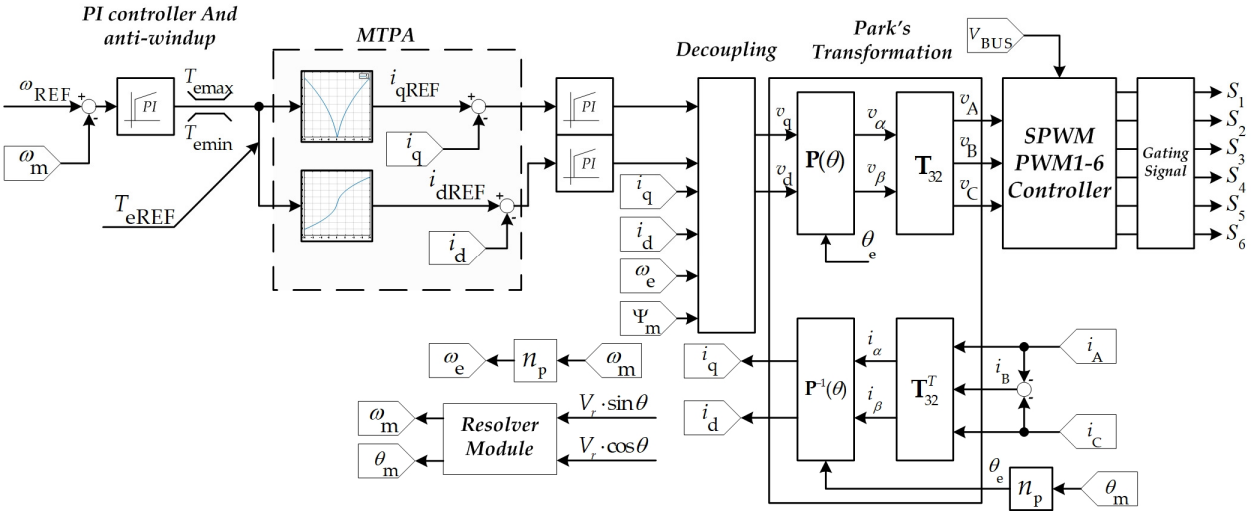

Figure 2.33 MTPA control of PMa-SynRM.

TABLE 2.3
Speed and current regulation parameters for PMa-SynRM

Symbol	Meaning	Value
K_{pq}	q-axis proportional gain	19.2
K_{iq}	q-axis integral gain	1.5015×10^3
K_{pd}	d-axis proportional gain	19.2
K_{id}	d-axis integral gain	1.2243×10^3
K_{pw}	Speed proportional gain	0.2
K_{iw}	Speed integral gain	2
K_{pfw}	Field-weakening proportional gain	0.2
K_{ifw}	Field-weakening integral gain	2
I_{smax}	Maximum quadrature current	+6 A
I_{smin}	Minimum quadrature current	-6 A
Vdc	DC bus voltage	400 V
f_s	Switching frequency	16 KHZ

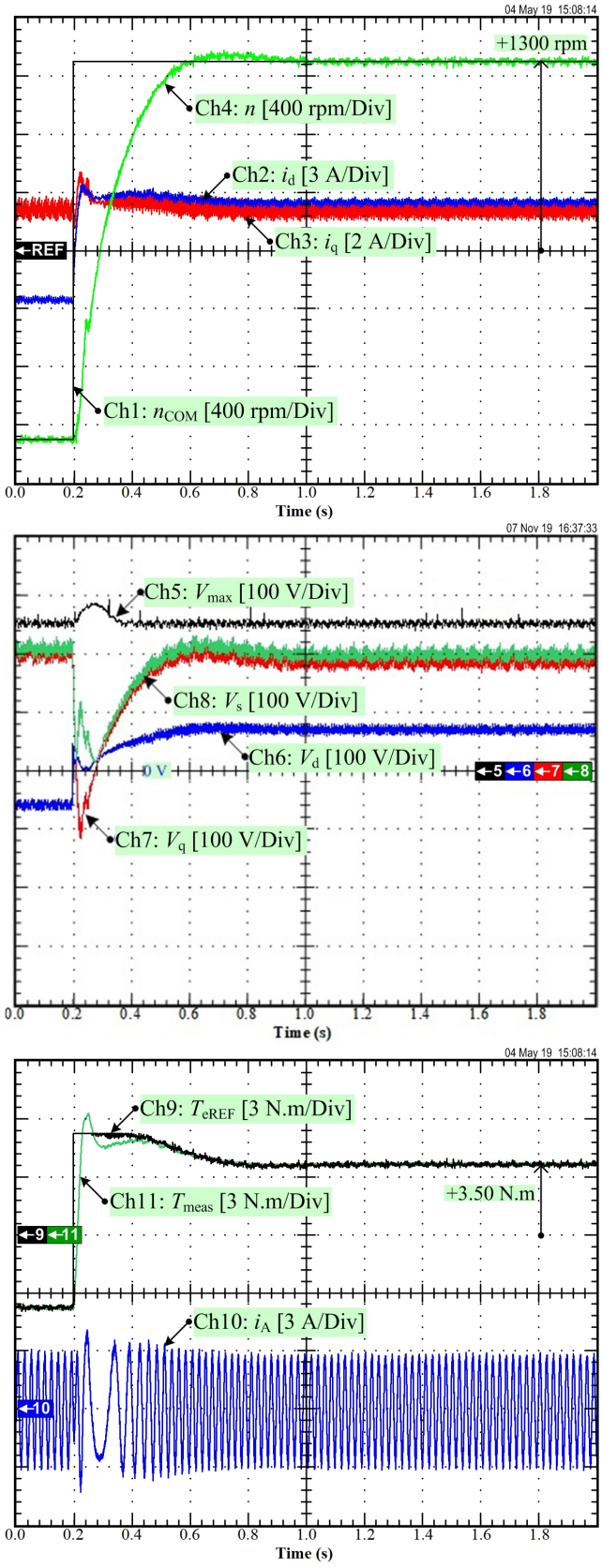

Figure 2.34 Experimental results: dynamic performance of speed reversal under torque constant operation.

The block diagram of the MTPA control of PMa-SynRM is shown in Figure 2.33, and the controller parameters are given in Table 2.3. Figure 2.34 illustrates the dynamic performance test under-speed reversal operation of the PMa-SynRM. Ch1 is the speed reference n_{REF}, Ch2 is the measured d-axis current, Ch3 is the measured q-axis current, and Ch4 is the measured speed n. Ch5 is the maximum allowed voltage for linear PWM (V_{max}) which is proportional to V_{dc}, Ch6 is the d-axis voltage, Ch7 is the q-axis voltage, and Ch8 is the stator voltage vector magnitude V_{s}. Ch9 is the torque reference T_{eREF}, Ch10 is the phase current i_{A}, and Ch11 is the measured load torque T_{L}. The speed reference changes from -1300 rpm to +1300 rpm.

As can be seen, the measured speed tracks very well its reference. The d- and q-axis current references are optimized based on the MTPA curve (see Figure 2.31), and the actual currents track them. The motor works well in two quadrants with satisfactory dynamic performance.

The load torque disturbance rejection is tested with the MTPA control of PMa-SynRM. Figure 2.35 illustrates experimental measurements. Ch2 is the measured d-axis current, Ch3 is the measured q -axis current and Ch4 is the measured speed n when the load is added (Figure (a)) and removed (Figure (b)) suddenly. It is obvious that the speed controller effectively rejects the load torque variations by producing adequate compensating motor torque. This latter torque is realized thanks to optimal dq currents according to the MTPA curve shown in Figure 2.31.

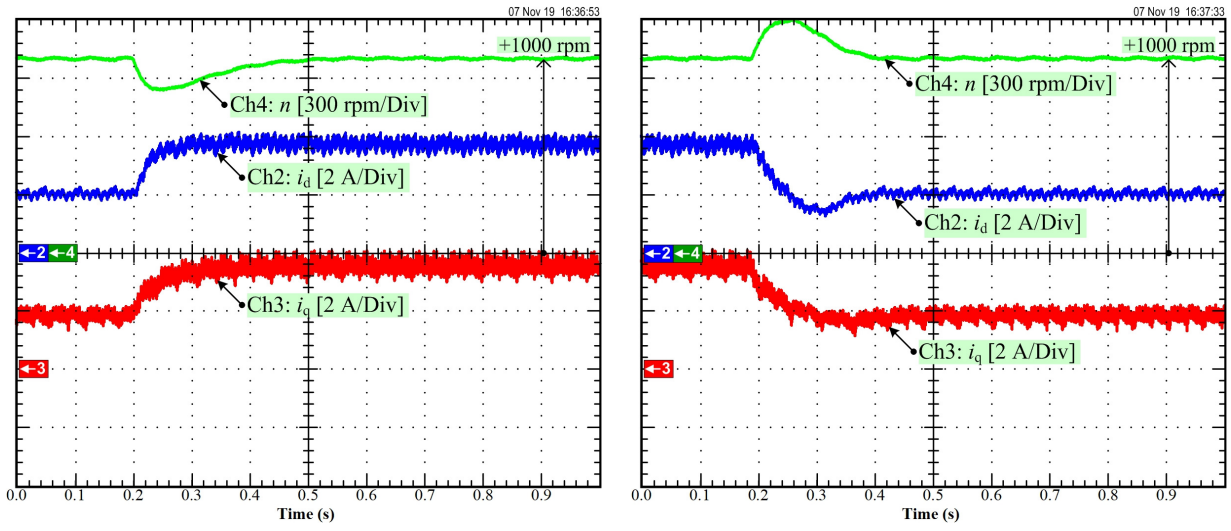

Figure 2.35 Experimental results: dynamic performance of the disturbance rejection, (a) load torque turned on, (b) load torque turned off.

2.10. Conclusion

In this chapter, mathematical models of permanent magnet synchronous machines are presented in the rotating reference frame for surface mounted and interior PM motors as well as PMa-SynRM. These models are used to design current and speed controllers under Field-Oriented Control (FOC) framework. Only PI controllers are considered in this chapter. The simulation and experimental validation are implemented to show the closed-loop PM drive behavior. These results will be used as a benchmark for comparison purposed with more advanced controllers developed in the following chapters.

Furthermore, an MTPA strategy is developed to minimize copper losses in the PMa-SynRM. The outcome of this strategy is optimal dq currents for a given torque. A lookup table is generated to provide optimal currents as functions of the requested torque. The simulation results show a 10% reduction in copper losses with the MTPA strategy compared to the control strategy without MTPA. Several experimental tests show the effectiveness of the FOC of the PMa-SynRM and its good dynamic performance.

To improve the closed-loop performance of the above motor drives, we will design new controllers in the following chapters. Two objectives will be considered: improve set-point tracking and disturbance rejection performances of the controllers using a model-based control technique; or make the controlled system more robust by applying a model-free control approach. For the first objective, we will take advantage of experts' knowledge on the motor drive to address the performance improvement requirement in high power applications. The aim of the second objective is to develop an almost universal controller with acceptable performances which does not require deep knowledge of the motor drive for cost-effective applications.

Chapter-3 DIFFERENTIAL FLATNESS-BASED CONTROL AND ONLINE STATE OBSERVER PARAMETER ESTIMATION

Contents

Introduction ..... --

3.1. A shot briefly Differential Flatness-Based Control and Control Law

3.1.1. Differential Flatness Briefly:

3.1.2. Control Law

3.2. Application of the differential flatness-based control to SPMSM drive

3.2.1. Design of a differential flatness-based control for SPMSM

3.2.2. Trajectory planning

3.3. Simulation and experimental validation of differential flatness-based controller for SPMSM

3.3.1. Experimental setup

3.3.2. Performance comparison of FOC with traditional PI controller and differential flatness-based control

3.4. Application of the differential flatness-based control to PMa-SynRM

3.4.1. Design of a differential flatness-based control for PMa-SynRM

3.4.2. Differential flatness-based control for outer speed control loop

3.5. Simulation and experimental validation of differential flatness-based controller PMa-SynRM

3.6. State Observer Parameter Estimation

3.6.1. Luenberger Observer

3.6.2. Improve performance of differential flatness-based control for SPMSM by the Luenberger state observer

3.6.3. Simulation results of the Luenberger state observer applied to parameter estimation for the SPMSM

3.6.4. Enhance the performance of the differential flatness-based control based on the Luenberger state observer applied for the PMa-SynRM drive

3.6.5. Experimental validation of the differential flatness-based control based on the Luenberger state observer

3.6.5.1. Performance of parameter estimation with Luenberger Observer

3.6.5.2. Performance of Disturbance Rejection

3.6.6. Nonlinear Online Parameter Estimation

3.6.6.1. Lyapunov-based design of the state observer

3.6.6.2. Exponential stability of the proposed observer

3.6.6.3. Stability of the proposed nonlinear state observers

3.6.7. Validation of the proposed observer for SPMSM

3.6.7.1. Observer design for SPMSM

3.6.7.2. Simulation and experimental results

3.6.7.3. Variable loss estimation

3.6.8. Validation of the proposed observer for PMa-SynRM

3.6.8.1. Observer design for PMa-SynRM

3.6.8.2. Simulation of the proposed observer applied to PMa-SynRM

3.6.8.3. Experimental validation of the proposed observer applied to the PMa-SynRM

3.7. Conclusion

Introduction

The application of flatness theory to engineering problems of interest has grown steadily in recent years. But, first, it is essential to note that many system classes commonly used in nonlinear control theory are flat. For example, coordinates, static feedback transforms (nonlinear input and coordinate changes), or dynamic feedback transforms are flat. Thus, many of the procedures available for solid-state nonlinear control techniques are, in fact, flat systems and raise the question of how flat structure plays a role in controlling such systems [61] [62] [63].

This chapter presents the differential flatness-based control applied to control the PMSM, including SPMSM and PMa-SynRM. In addition, the comparison between the differential flatness-based control and FOC with PI controller, proposed in the previous chapter, is presented to show the benefit of the proposed control. Furthermore, an online state observer parameter estimation is also present in this chapter to improve the performance of the differential flatness-based control. Finally, the proposed control and the online observer parameter estimation are tested on an experimental setup with SPMSM and PMa-SynRM.

3.1. A shot briefly differential flatness-based control and control law

3.1.1. Differential flatness briefly:

A Flat system is a generalization of a linear system. This section focuses on a particular type of system known as differentially flat systems. This system can thoroughly characterize the trajectories structure of the nonlinear dynamics. However, the techniques used to control flat systems are pretty different from many existing linear system methods. One is based on the fundamental solution of using flatness structures to solve more common control problems.

Flatness was first determined by Fliess et al. [64] [65]-[66] by using the differential algebra form. In differential algebra, think of the system as a differential field created by a set of variables (states and inputs). If a set of variables is found, the system is flat and is called flat output. This system is a non-differential algebra on the differential field produced by all flat outputs. The system is essentially flat if it can find a set of flat outputs (a number equal to the number of inputs) so that the set of outputs can determine outputs without integrating all the states and inputs. The differential flatness is an essential structure of many control systems [67] [68]-[72]. A brief theory of differentially flatness control is proved as follows. Discuss a nonlinear system given by a state-variable expression [73] [74]:

$$\dot{x} = f(x,u) \tag{3.1}$$

More precisely, if the system has the states $x \in \mathbb{R}^n$ and the input is $u \in \mathbb{R}^m$, then the system is flat if it can find an output $y \in \mathbb{R}^m$ such that the system (3.1) is said to be differentially flat if there exists an output variable (denoted by the flat output y) of the form as:

$$y = h(x,u,\dot{u},...,u^{(p)}) \tag{3.2}$$

where x and u can be written as a function of this flat output and its successive derivatives (order β for expression of x and (β+1) for the expression of u)

$$\begin{aligned} x &= \phi(y, \dot{y}, ..., y^{(\beta)}) \\ u &= \psi(y, \dot{y}, ..., y^{(\beta+1)}) \end{aligned} \tag{3.3}$$

where: β is the finite number of derivatives.

Functions $h \in \mathbb{R}^n \times (\mathbb{R}^m)^{p+1} \to \mathbb{R}^m$, $\phi : (\mathbb{R}^m)^{\beta+1} \to \mathbb{R}^n$, and $\psi : (\mathbb{R}^m)^{\beta+2} \to \mathbb{R}^m$ are regular functions [72].

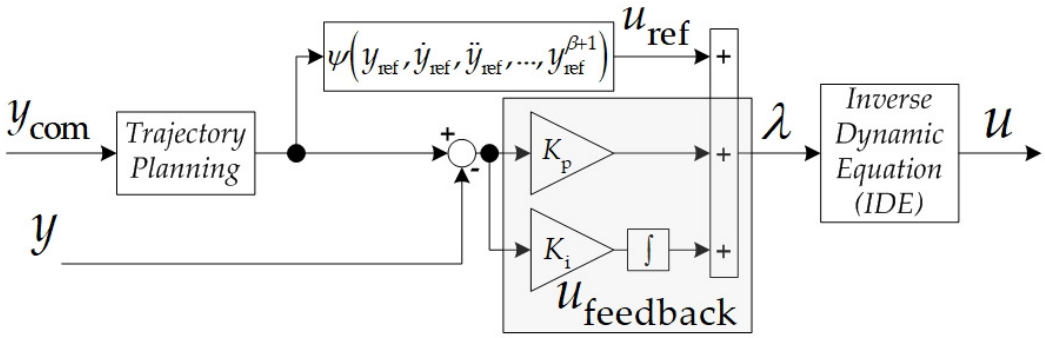

Figure 3.1 Differential flatness-based Control law's block diagram.

3.1.2. Control law

A control law is applied to deal with some inevitable modeling errors and uncertainties. As shown in Figure 3.1, a controller output, λ can be defined as follows:

$$\lambda = u_{ref} + u_{feedback}(\varepsilon) \tag{3.4}$$

with

$$u_{ref} = \psi\left(y_{ref}, \dot{y}_{ref}, \ddot{y}_{ref}, ..., y_{ref}^{(\beta+1)}\right) \tag{3.5}$$

and the error of the desired value and the measured value is

$$\varepsilon = y_{ref} - y \tag{3.6}$$

As will be seen later, thank to "Inverse Dynamic Equation" (IDE), we will obtain

$$\dot{y} = \lambda \tag{3.7}$$

According to the control law's block diagram, combining (3.4), (3.5), and (3.6) yields

$$\dot{y} = \dot{y}_{ref} + K_p \cdot \varepsilon + \int \left(K_i \cdot \varepsilon\right) dt \tag{3.8}$$

Bringing $\dot{y}$ to the right-hand side, it yields

$$\ddot{\varepsilon}+K_p\cdot\dot{\varepsilon}+K_i\cdot\varepsilon=0 \tag{3.9}$$

By comparing to the standard second-order equation, parameters K_P and K_i can be defined as follow:

$$\ddot{q}(s)+2\zeta\omega_n\cdot\dot{q}(s)+\omega_n^2\cdot q(s)=0 \tag{3.10}$$

$$\begin{aligned} K_\mathrm{p}&=2\zeta\omega_\mathrm{n}\\ K_\mathrm{i}&=\omega_\mathrm{n}^2 \end{aligned} \tag{3.11}$$

3.2. Application of the differential flatness-based control to SPMSM drive

The SPMSM drive system is presented in Figure 2.23, and its state-space representation model is represented in Eq. (2.47) as in Eq. (3.12). The control system of the differential flatness-based control for the SPSM is illustrated in Figure 3.2.

$$\underbrace{\begin{bmatrix} \frac{di_\mathrm{d}}{dt}\\ \frac{di_\mathrm{q}}{dt}\\ \frac{d\omega_\mathrm{m}}{dt}\end{bmatrix}}_{\dot{x}}=\underbrace{\begin{bmatrix} \left(-R_\mathrm{s}i_\mathrm{d}+\omega_\mathrm{e}L_\mathrm{s}i_\mathrm{q}\right)/L_\mathrm{s}\\ \left\{-R_\mathrm{s}i_\mathrm{q}-\omega_\mathrm{e}(L_\mathrm{s}i_\mathrm{d}+\Psi_\mathrm{m})\right\}/L_\mathrm{s}\\ \left(n_\mathrm{p}\Psi_\mathrm{m}i_\mathrm{q}-B_f\omega_m\right)/J\end{bmatrix}}_{f(x)}+\underbrace{\begin{bmatrix} \frac{1}{L_\mathrm{s}} & 0 & 0\\ 0 & \frac{1}{L_\mathrm{s}} & 0\\ 0 & 0 & -\frac{1}{J}\end{bmatrix}}_{\mathbf{B}}\underbrace{\begin{bmatrix} v_\mathrm{d}\\ v_\mathrm{q}\\ T_\mathrm{L}\end{bmatrix}}_{u}$$

$$y=\underbrace{\begin{bmatrix} 1 & 0 & 0\\ 0 & 1 & 0\end{bmatrix}}_{\mathbf{C}}\begin{bmatrix} i_\mathrm{d}\\ i_\mathrm{q}\\ \omega_\mathrm{m}\end{bmatrix} \tag{3.12}$$

3.2.1. Design of a differential flatness-based control for SPMSM

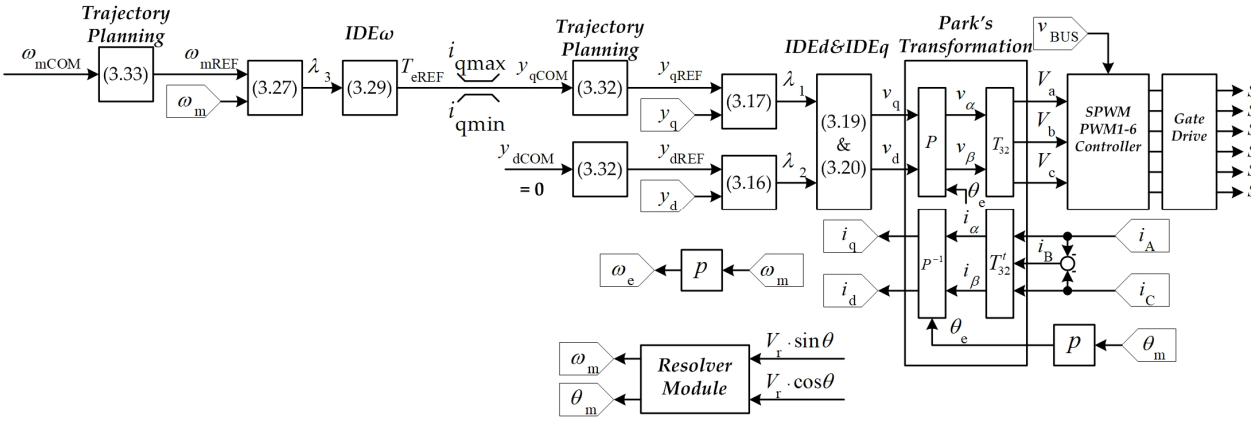

Figure 3.2 Control system of SPMSM based on differential flatness-based control diagram.

As mentioned in Section 2.9.1, SPMSM is a non-salient poles machine such that the torque producing is along the q-axis proportional to i_q and keeps the d-axis current to zero in order to reach maximum efficiency. Besides the $L_s = L_d = L_q$ is defined as in Section 2.4.1. The system from (3.12) is flat if it is possible to express all state variables (i.e., ω_m, i_d, and i_q) and input variables (i.e., u_d and u_q) as a function of candidate flat outputs and their successive derivatives.

As shown in Figure 3.2, the control system has a cascade construction consisting of two loops (i.e., inner current control loop and outer speed control loop). The inner current loop is much faster than the outer speed control loop such that the differential flatness-based control for the current control is developed first.

For the current control loop, the chosen flat output candidates are dq-currents, and the control variables are dq-voltages. The state variables are dq-currents, too. That is:

$$y=\begin{bmatrix} i_d \\ i_q \end{bmatrix}, u=\begin{bmatrix} v_d \\ v_q \end{bmatrix}, x=\begin{bmatrix} i_d \\ i_q \end{bmatrix} \tag{3.13}$$

The state variable can be written as:

$$x=\begin{bmatrix} \phi(y_1) \\ \phi(y_2) \end{bmatrix} \tag{3.14}$$

From (3.12), the control variable can be calculated from the chosen flat output y and, its successive derivatives as follows:

$$\begin{aligned} u_1 &= L_s\frac{di_d}{dt}+R_s i_d-\omega_e L_s i_q=\psi(\dot{y}_1,y_1,y_2)=v_{dREF} \\ u_2 &= L_s\frac{di_q}{dt}+R_s i_q+\omega_e(L_s i_d+\Psi_m)=\psi(\dot{y}_2,y_2,y_1)=v_{qREF} \end{aligned} \tag{3.15}$$

This property allows all the state and input variables to be directly expressed without integrating any differential equation.

Note that this formalism might work in open-loop control without feedback state if all parameters were well known. However, in practice, regulators based on feedback linearization are set, as subsequently shown, to ensure both a zero static error and rejection of the parameters' uncertainties. Therefore, according to (3.7) and (3.8), the control law of each inner current control is given as

$$\dot{y}_1 = \dot{y}_{dREF} + K_{pd} \cdot \varepsilon_d + K_{id} \cdot \int \varepsilon_d dt \tag{3.16}$$

$$\dot{y}_2 = \dot{y}_{qREF} + K_{pq} \cdot \varepsilon_q + K_{iq} \cdot \int \varepsilon_q dt \tag{3.17}$$

where the input references y_{REF} of each module are represented by

$$y_{REF} = \begin{bmatrix} y_{dREF} = i_{dREF} \\ y_{qREF} = i_{qREF} \end{bmatrix} \tag{3.18}$$

Consequently, from (3.15) the output control variables can be rewritten as:

$$u_1 = v_d = L_s \cdot \dot{y}_1 + IDE_d \tag{3.19}$$

$$u_2 = v_q = L_s \cdot \dot{y}_2 + IDE_q \tag{3.20}$$

where IDE is the inverse dynamic equation of each module defined as:

$$IDE_d = R_s i_d - \omega_e L_s i_q \tag{3.21}$$

$$IDE_q = R_s i_q + \omega_e (L_s i_q + \Psi_m) \tag{3.22}$$

The regulators parameters K_{pd}, K_{id}, K_{pq}, and K_{iq}, are the proportional and integral coefficients, respectively, and they can be defined according to (3.11) as follows:

$$K_{pd} = K_{pq} = 2 \cdot \zeta_1 \cdot \omega_{n1} \tag{3.23}$$

and

$$K_{id} = K_{iq} = \omega_{n1}^2 \tag{3.24}$$

where ζ_1 and ω_{n1} are the desired dominant damping ratio and natural frequency, respectively.

The second differential flatness-based control of the outer speed control loop is developed. The output of the speed control loop provides the reference of the q-axis current i_q according to the mechanical equation in (2.39). Therefore, the i_q is chosen as a control variable u_3. The relation between torque, q-axis current, and the mechanical equation of the SPMSM provided by (2.40) is given as:

$$u_3 = i_q = \frac{J\frac{d\omega_m}{dt} + B_f\omega_m + T_L}{n_p\Psi_m} \tag{3.25}$$

The candidate flat output is $y_3 = \omega_m$, and the state variable is $x_3 = \omega m$. From (3.25), the control variable can be written as a function of the flat output and its successive derivatives; that is:

$$u_3 = i_q = \frac{J\cdot\dot{y}_3 + B_f\omega_m + T_L}{n_p\Psi_m} = \psi(y_3, \dot{y}_3) \tag{3.26}$$

According to the control law' block diagram (Figure. 3.1) and equation (3.8), the control law of the outer speed control loop is

$$\dot{y}_3 = \dot{y}_{3REF} + K_{p\omega}\varepsilon_\omega + K_{i\omega}\int\varepsilon_\omega dt \tag{3.27}$$

with $y_{3REF} = \omega_{REF}$.

From (3.25), the control variable can be rewritten as

$$u_3 = \left(\frac{J}{n_p\Psi_m}\right)\cdot\dot{y}_3 + IDE_\omega \tag{3.28}$$

where IDE is the inverse dynamic equation of each module defined as:

$$IDE_\omega = \frac{1}{n_p\Psi_m}\left(B_f\omega_m + T_L\right) \tag{3.29}$$

The coefficients $K_{p\omega}$ and $K_{i\omega}$ are the proportional and integral gains of the outer speed control loop, respectively, and they can be determined according to (3.11) as follows:

$$K_{p\omega} = 2\cdot\zeta_2\cdot\omega_{n2} \tag{3.30}$$

and

$$K_{i\omega} = \omega_{n2}^2 \tag{3.31}$$

where ζ_2 and ω_{n2} are the desired dominant damping factor and natural frequency of the outer speed control loop, respectively.

3.2.2. Trajectory planning

As shown in Figure 3.1, trajectory planning is a crucial part of differential flatness-based control and makes the input reference y_{REF} derivable. A second-order low-pass filter is often

utilized to plan the desired trajectory for the output component. It allows limiting the derivative terms. The proposed trajectory planning for the two inner current control loops is:

$$\frac{y_{1REF}}{y_{1COM}} = \frac{y_{2REF}}{y_{2COM}} = 1 \Big/ \left\{ \left(\frac{s}{\omega_{n3}} \right)^2 + \frac{2\zeta_3}{\omega_{m3}} s + 1 \right\} \tag{3.32}$$

where ζ_3 and ω_{n3} are the desired dominant damping ratio and natural frequency.

The trajectory planning for the outer speed loop is

$$\frac{y_{3REF}}{y_{3COM}} = 1 \Big/ \left\{ \left(\frac{s}{\omega_{n4}} \right)^2 + \frac{2\zeta_4}{\omega_{m4}} s + 1 \right\} \tag{3.33}$$

where ζ_4 and ω_{n4} are the desired dominant damping ratio and natural frequency of the speed loop trajectory planning.

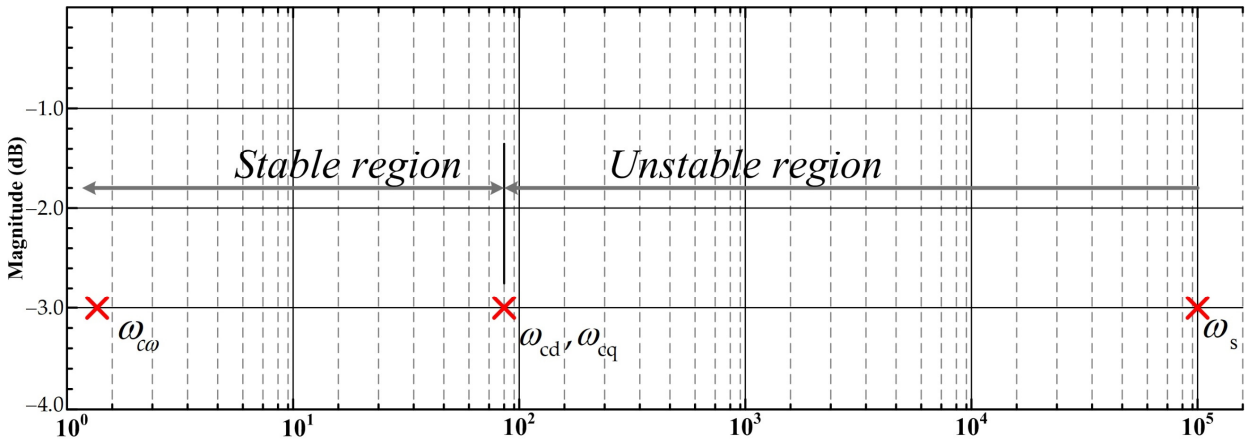

Figure 3.3 The natural frequency setting of the proposed controller.

Note that the stability and response of the differential flatness-based control are easy to set compared to the traditional PI controller. For example, defining and selecting the dominant damping and natural frequency is shown in Figure 3.3. Moreover, the controller parameters of current and speed loop control can calculate by Eqs (3.23), (3.24), (3.30), and (3.31), respectively.

3.3. Simulation and experimental validation of differential flatness-based controller for SPMSM

3.3.1. Experimental setup

The main PMSM parameters are presented in Table 3.1, and the flatness-based controller parameters are defined in Table 3.2. The laboratory setup is shown in Figure 3.4, composed of a 6-pole, 1kW PMSM coupled with a DC machine dyno which supplies a resistive load. The stator windings of the PMSM were fed by a 3-kW, 3Φ dc-ac voltage-source inverter (VSI) that was

operated at a switching frequency of 10 kHz. The input voltage is obtained through a diode rectifier or DC sources, as shown in Figure 2.23. The drive system was also equipped with an incremental encoder mounted on the rotor shaft and 4096 lines/revolution resolution.

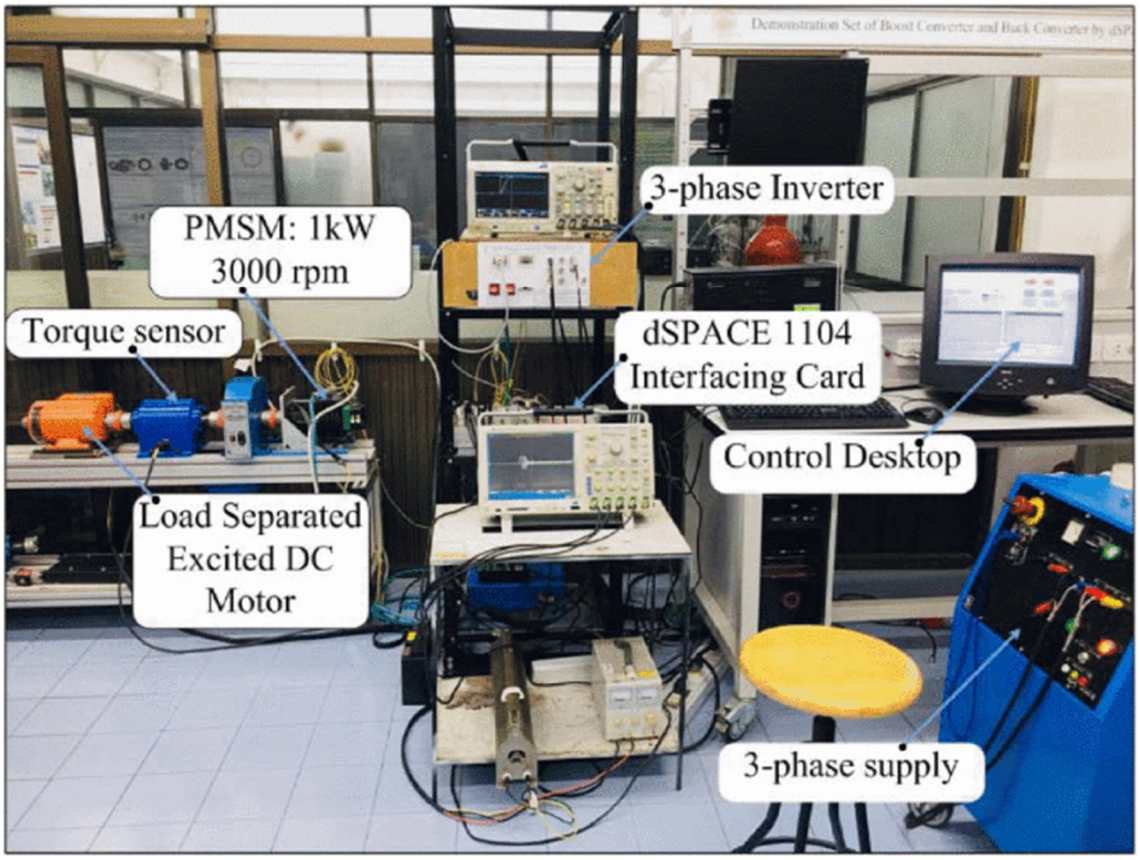

Figure 3.4 Test Bench Setup.

The measurement of the electromagnetic torque was realized by a torque transducer mounted on the rotor shaft. The proposed controller was implemented on a dSPACE DS1104 board, with a time step of T_s = 1e−4 s.

TABLE 3.1
Studied SPMSM Parameters for the differential flatness-based control development

Symbol	Meaning	Value
P_{rated}	Rated Power	1kW
n_{rated}	Rated Speed	3000 rpm
n_p	Number of pole pairs	3
R_s	Resistance (Motor + Inverter)	10 Ohm
$L_s = L_d = L_q$	Stator inductance	35.31 mH
Ψ_m	Permanent-magnet flux	0.2214 [Wb]
J	Equivalent inertia	0.002 kg.m2

TABLE 3.2
Speed/Current controller parameters

Symbol	Meaning	Value
ζ_1	Damping ratio 1	0.7
ω_{n1}	Natural frequency 1	30,000 rad.s^{-1}
ζ_2	Damping ratio 2	0.7
ω_{n2}	Natural frequency 2	300 rad.s^{-1}
ζ_3	Damping ratio 3	1
ω_{n3}	Natural frequency 3	3000 rad.s^{-1}
ζ_4	Damping ratio 4	1
ω_{n4}	Natural frequency 4	300 rad.s^{-1}
I_{dmax}	Maximum *d*-axis current	+6 A
I_{dmin}	Minimum *d*-axis current	-6 A
Vdc	DC bus voltage	600 V
f_s	Switching frequency	16 kHz

3.3.2. Performance comparison of FOC with traditional PI controller and differential flatness-based control

Figure. 3.5 shows the comparison of the inner current loop control, in which the FOC with traditional PI controller (Figure 3.5(a)) and the differential flatness-based control are implemented. According to Section 2.9.1, the coefficients for traditional PI regulators in this simulation are given as:

$$K_{pid} = \frac{3L_s}{t_{rd}}, \qquad K_{iid} = \frac{K_{pd}}{\tau_{sd}} \tag{3.34}$$

and

$$K_{piq} = \frac{3L_s}{t_{rq}}, \qquad K_{iiq} = \frac{K_{pq}}{\tau_{sq}} \tag{3.35}$$

t_{rd} is the desired closed-loop response time of the *d*-axis current control loop, and t_{rq} is the closed-loop response time of the *q*-axis current control loop, which is considered by the crossover frequency (Figure.3.30).

By choosing $t_{rd} = t_{rq} = 0.5$ ms, the coefficients are obtained as:

$$K_{pid} = K_{piq} = 70.62, \text{ and } K_{iid} = K_{iiq} = 20{,}000$$

The coefficients of the differential flatness-based controller are given in Table 3.2, and using (3.23) and (3.24), the K_{pd}, K_{id}, K_{pq}, and K_{iq} are obtained.

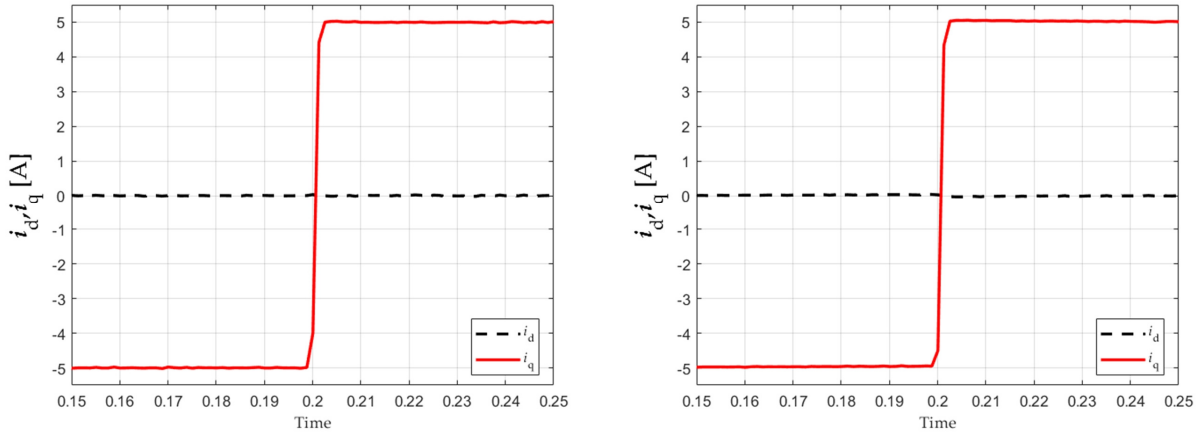

Figure 3.5 Simulation Results: (a) FOC with traditional PI controller. (b) Different flatness-based controller.

As shown in Figueres 3.5(a) and 3.5(b), the responses of both approaches are satisfactory. There are no significant differences between both methods. The response requirement can be changed by changing the desired closed-loop response time for the PI control to the crossover frequency for the differential flatness-based control.

Figure 3.6 shows the simulation results of the FOC with the traditional PI controller (Figure 3.6(a)) and the differential flatness-based control (Figure 3.6(b)), in which the external disturbance rejection ability of both approaches is illustrated. The outer speed control loop of the PI control is presented in equation (2.64). More precisely, by choosing the desired closed-loop response time $\tau_{r\omega} = 10$ ms, the $K_{pp\omega}$, $K_{ip\omega}$ are obtained as $K_{pp\omega} = 4.5481$ and $K_{ii\omega} = 240.6423$. As shown in Figure 3.6(a) (see n_{REF} and the measured speed n), the recovery time of the measured speed is approximately ≈ 0.03 s to reach the reference speed. In comparison, the recovery time of the measured speed, which is compensated by the differential flatness-based control, is better, which the time is lower than 0.02 s. So, the differential flatness-based control performance is slightly better than the traditional PI control for the external disturbance rejection.

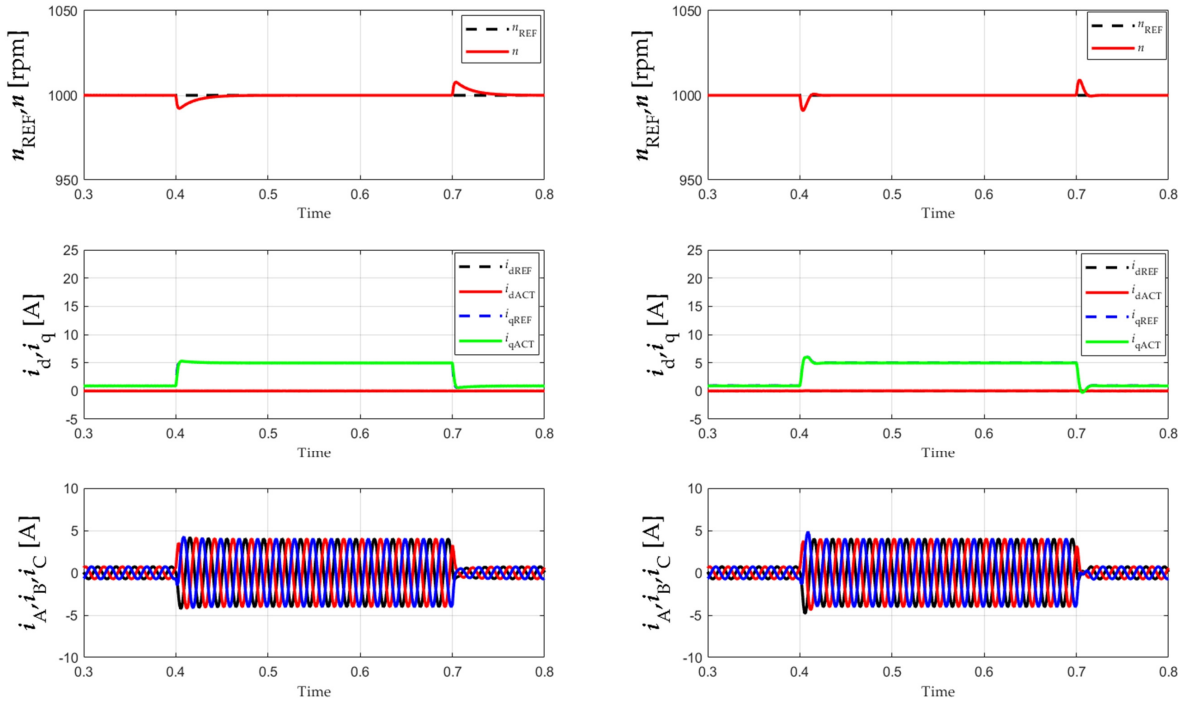

Figure 3.6 Simulation Results: The external disturbance rejection ability, (a) PI controller. (b) Differential flatness-based controller.

3.4. Application of the differential flatness-based control to PMa-SynRM

This section presents the differential flatness control to control permanent magnet assisted synchronous reluctance motor. Initially, the mathematical models of PMa-SynRM are proved to show the differential flat property. And then, the intelligent proportional-integral (*i*PI) [66] [67] controller is discussed as a control law to compensate torque and speed of the motor. Next, a nonlinear estimator is introduced to estimate external torque disturbance. Finally, the comparison between differential flatness and conventional PI control is discussed to demonstrate the benefits of the proposed control algorithm. A small-scale 1kW prototype PMa-SynRM with a ferrite magnet was manufactured to examine the proposed control scheme in the laboratory [75].

The inverter shown in Figure 2.17 provides a symmetric sinusoidal three-phase AC voltage source for supplying to PMa-SynRM. The nonlinear case discusses in Section 2.4.6, The electrical modeling equations of PMa-SynRM. For example, the flux linkage of direct and quadrature axes can be defined as a function of *d*- and *q*-axes current i_d and i_q. as in the following equations.

$$\begin{aligned} \Psi_d &= \Psi_d(i_d, i_q) \\ \Psi_q &= \Psi_q(i_d, i_q) \end{aligned} \tag{3.36}$$

From the above equations, the inductances of the PMa-SynRM can be computed by the following expression.

$$L_{\mathrm{d}}=\frac{\partial\Psi_{\mathrm{d}}(i_{\mathrm{d}},i_{\mathrm{q}})}{\partial i_{\mathrm{d}}}=\frac{\Delta\Psi_{\mathrm{d}}(i_{\mathrm{d}},i_{\mathrm{q}})}{i_{\mathrm{d}}}\bigg|_{i_{\mathrm{q}}=\text{constant}} \tag{3.37}$$

$$L_{\mathrm{q}}=\frac{\partial\Psi_{\mathrm{q}}(i_{\mathrm{d}},i_{\mathrm{q}})}{\partial i_{\mathrm{q}}}=\frac{\Delta\Psi_{\mathrm{q}}(i_{\mathrm{d}},i_{\mathrm{q}})}{i_{\mathrm{q}}}\bigg|_{i_{\mathrm{d}}=\text{constant}} \tag{3.38}$$

Taking into account (3.36) and substituting to (2.29), the voltage equation in the rotating reference frame of the PMa-SynRM is given as:

$$v_{\mathrm{d}}=R_{\mathrm{s}}\cdot i_{\mathrm{d}}+\frac{d\Psi_{\mathrm{d}}(i_{\mathrm{d}},i_{\mathrm{q}})}{dt}-\omega_{\mathrm{e}}\cdot\Psi_{\mathrm{q}}(i_{\mathrm{d}},i_{\mathrm{q}}) \tag{3.39}$$

$$v_{\mathrm{q}}=R_{\mathrm{s}}\cdot i_{\mathrm{q}}+\frac{d\Psi_{\mathrm{q}}(i_{\mathrm{d}},i_{\mathrm{q}})}{dt}+\omega_{\mathrm{e}}\cdot\Psi_{\mathrm{d}}(i_{\mathrm{d}},i_{\mathrm{q}}) \tag{3.40}$$

3.4.1. Design of a differential flatness-based control for PMa-SynRM

From (3.36), the Ψ_{d} and Ψ_{q} are determined as the state variables (x). The voltages v_{d} and v_{q} are control variables (u). The flat output (y) candidates are the measured currents, i_{d} and i_{q}. That is:

$$y=\begin{bmatrix}y_1=i_{\mathrm{d}}\\ y_2=i_{\mathrm{q}}\end{bmatrix},u=\begin{bmatrix}u_1=v_{\mathrm{d}}\\ u_2=v_{\mathrm{q}}\end{bmatrix} \tag{3.41}$$

By considering (3.39) and (3.40), the *dq*-inductances are given by the function of *dq*-flux linkages with respect to *dq*-currents. So, the state variables of state-space PMa-SynRM model representation are considered by choosing *dq*-currents. That is:

$$x=\begin{bmatrix}x_1=i_{\mathrm{d}}\\ x_2=i_{\mathrm{q}}\end{bmatrix} \tag{3.42}$$

The system is said to be differentially flat if the control output variable must be written as the function of the flat output, which are

$$v_{\mathrm{d}}=u_1=R_{\mathrm{s}}y_1-\omega_{\mathrm{e}}\Psi_{\mathrm{q}}\left(y_1,y_2\right)+\frac{\partial\Psi_{\mathrm{d}}\left(y_1,y_2\right)}{\partial y_1}\cdot\dot{y}_1+\frac{\partial\Psi_{\mathrm{d}}\left(y_1,y_2\right)}{\partial y_2}\cdot\dot{y}_2=\psi_1\left(y_1,y_2,\dot{y}_1,\dot{y}_2\right) \tag{3.43}$$

$$v_q = u_2 = R_s y_2 + \omega_e \Psi_d(y_1, y_2) + \frac{\partial \Psi_q(y_1, y_2)}{\partial y_1} \cdot \dot{y}_1 + \frac{\partial \Psi_q(y_1, y_2)}{\partial y_2} \cdot \dot{y}_2 = \psi_2(y_1, y_2, \dot{y}_1, \dot{y}_2) \tag{3.44}$$

The control law of the inner current control loop is given as:

$$\dot{y}_1 = \dot{\Psi}_{dref}(y_{1ref}, y_{2ref}) + K_{pd}\varepsilon_d + K_{id}\int \varepsilon_d dt \tag{3.45}$$

$$\dot{y}_2 = \dot{\Psi}_{qref}(y_{1ref}, y_{2ref}) + K_{pq}\varepsilon_q + K_{iq}\int \varepsilon_q dt \tag{3.46}$$

where K_{pd}, K_{id}, K_{pq}, and K_{iq} are the proportional and integral coefficients, which define as

$$\begin{aligned} K_{pd} &= K_{pq} = 2\zeta_1 \omega_{n1}, \\ K_{id} &= K_{iq} = \omega_{n1}^2 \end{aligned} \tag{3.47}$$

where the ζ_1 and ω_{n1} are the desired dominant damping ratio and natural frequency, respectively.

From the equations (3.37), (3.38), (3.43) and (3.44), the control variables can be rewritten to separate inverse dynamic equations as follows:

$$u_1 = v_d = \frac{\partial \Psi_d(y_1, y_2)}{\partial y_1} \cdot \dot{y}_1 + \frac{\partial \Psi_d(y_1, y_2)}{\partial y_2} \cdot \dot{y}_2 + IDE_d \tag{3.48}$$

$$u_2 = v_q = \frac{\partial \Psi_q(y_1, y_2)}{\partial y_1} \cdot \dot{y}_1 + \frac{\partial \Psi_q(y_1, y_2)}{\partial y_2} \cdot \dot{y}_2 + IDE_q \tag{3.49}$$

where the inverse dynamic equations of the inner current control loop are

$$IDE_d = -R_s i_d + \omega_e \Psi_q(i_d, i_q) \tag{3.50}$$

$$IDE_q = -R_s i_q - \omega_e \Psi_d(i_d, i_q) \tag{3.51}$$

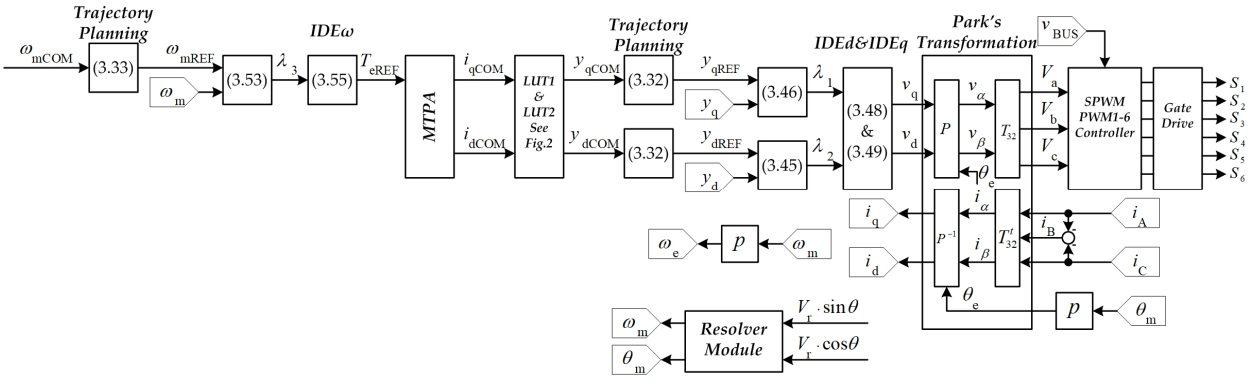

Figure 3.7 Different flatness-based control system applied to PMa-SynRM.

3.4.2. Differential flatness-based control for outer speed control loop

Figure 3.7 shows the proposed control diagram. The outer speed loop provides the torque reference value of the maximum torque per ampere (MTPA), which generates the current commands for the inner current loop.

The MTPA algorithm was proposed in Section 2.9.2. So, the T_e is defined as the control variable u_3, and the flat output y_3 is ω_m (measured angular speed). The system is flat if the control variable is a function of the flat output that is

$$u_3 = T_e = J \cdot \dot{y}_3 + B_f y_3 + T_L = \psi_3\left(y_3, \dot{y}_3\right) \tag{3.52}$$

The control law of the outer speed control is

$$\dot{y}_3 = \dot{\omega}_{ref} + K_{p\omega}\varepsilon_\omega + K_{i\omega}\int \varepsilon_\omega dt \tag{3.53}$$

where $K_{p\omega}$ and $K_{i\omega}$ are defined as follows:

$$\begin{aligned} K_{p\omega} &= 2\zeta_2\omega_{n2} \\ K_{i\omega} &= \omega_{n2}^2 \end{aligned} \tag{3.54}$$

where: ζ_2 and ω_{h2} are the desired dominant damping ratio and the natural frequency of the speed control loop.

Note that the stability and response of the differential flatness-based control are easy to set by defining and selecting the dominant damping and natural frequency, as shown in the figure. Moreover, the current and speed loop control controller parameters can be calculated using (3.47) and (3.53), respectively. Finally, the trajectory planning (in Section 3.2.2) is also implemented to define trajectory reference for the inner current and outer speed loops.

Rearrange (3.52) to show the inverse dynamic equation is obtained as:

$$u_3 = J \cdot \dot{y}_3 + J \cdot IDE_\omega \tag{3.55}$$

where the inverse dynamic equation of the differential flatness-based for outer speed control loop is

$$IDE_\omega = \frac{1}{J}\left(B_f \cdot y_3 + T_L\right) \tag{3.56}$$

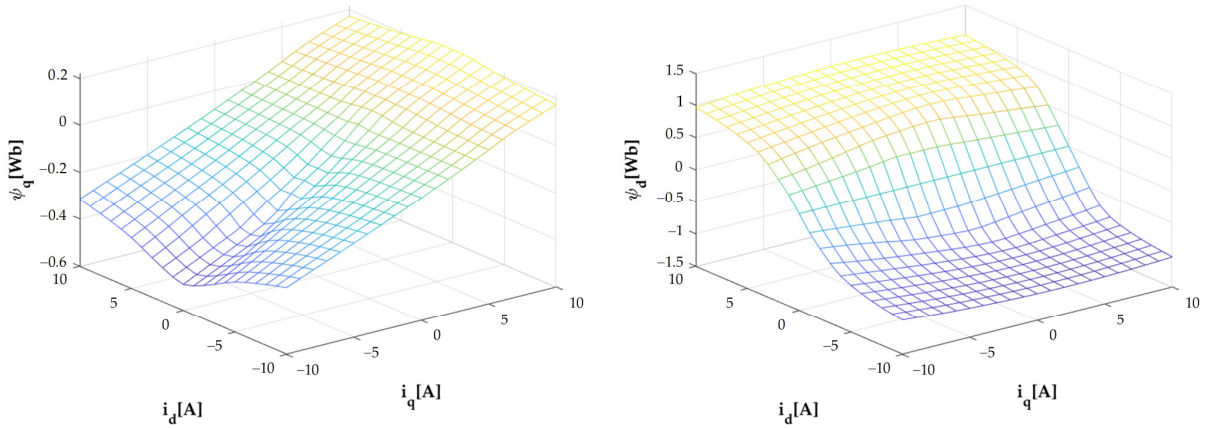

Figure 3.8 Ψ_d, Ψ_q in function of i_d and i_q of the prototype PMa-SynRM.

TABLE 3.3
PMa-SynRM Parameters for the differential flatness-based control development

Symbol	Meaning	Value
P_{rated}	Rated Power	1kW
n_{rated}	Rated Speed	1350 rpm
n_p	Number of pole pairs	2
R_s	Resistance (Motor + Inverter)	3.2 Ohm
Ψ_m	Permanent-magnet flux	0.138 [Wb]
J	Equivalent inertia	0.0017 kg.m²

TABLE 3.4
Speed/current regulation parameters of the differential flatness-based control

Symbol	Meaning	Value
ζ_1	Damping ratio 1	0.7 pu.
ω_{n1}	Natural frequency 1	9,600 rad.s^{-1}
ζ_2	Damping ratio 2	0.7
ω_{n2}	Natural frequency 2	96 rad.s^{-1}
ζ_3	Damping ratio 3	1
ω_{n3}	Natural frequency 3	960 rad.s^{-1}
ζ_4	Damping ratio 4	1
ω_{n4}	Natural frequency 4	96 rad.s^{-1}
I_{dmax}	Maximum *d*-axis current	+10 A
I_{dmin}	Minimum *d*-axis current	-10 A
Vdc	DC bus voltage	400 V
f_s	Switching frequency	16 kHz

The drive system with the proposed differential flatness-based control has been simulated extensively before the laboratory experimentation. Matlab/Simulink has been used to model the PMa-SynRM, the differential flatness-based control, and the sine PWM. The main parameters of prototype PMa-SynRM are in Table 3.3 except the *d-q* inductances. As in Figure 3.8, it can be seen saturation effect has been considered in the simulation study. However, cross saturation has been ignored in the simulation due to the complex model of the cross-saturation effect.

Figure 3.9 shows the behavior of the proposed control. As can be seen, both the measured *dq* axis currents track their reference very well. The T_{eREF} is a reference of the MTPA lookup table as represented in Figure 2.31.

3.5. Simulation and experimental validation of differential flatness-based controller PMa-SynRM

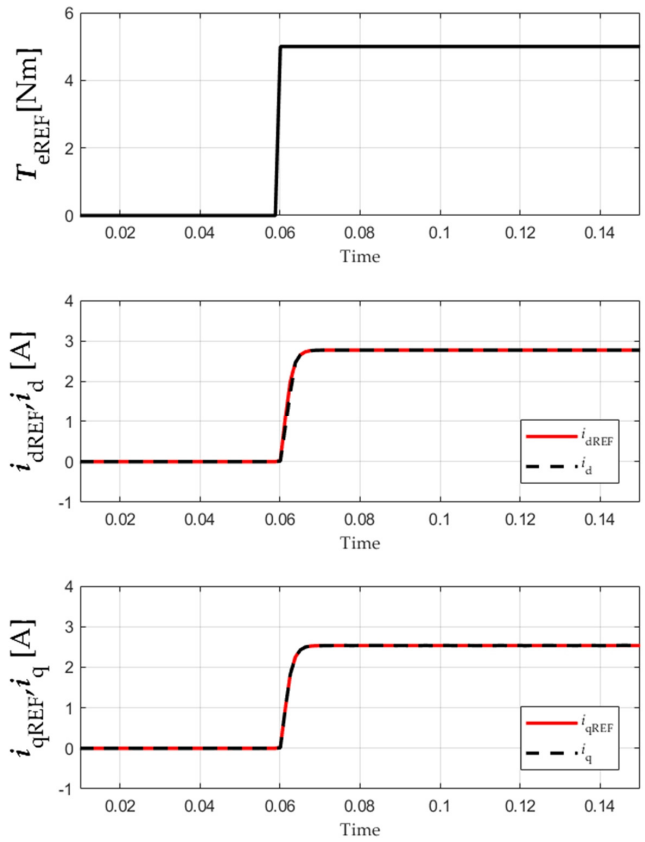

Figure 3.9 Simulation results: Inner current control loop response of the differential flatness-based control.

The simulation results of the external torque disturbance rejection are illustrated in the following. The differential flatness-based control has a good disturbance rejection that the measured speed n drop is approximately 40 rpm. Figure 3.10 shows the simulation response of the disturbance rejection when suddenly adding or removing load torque.

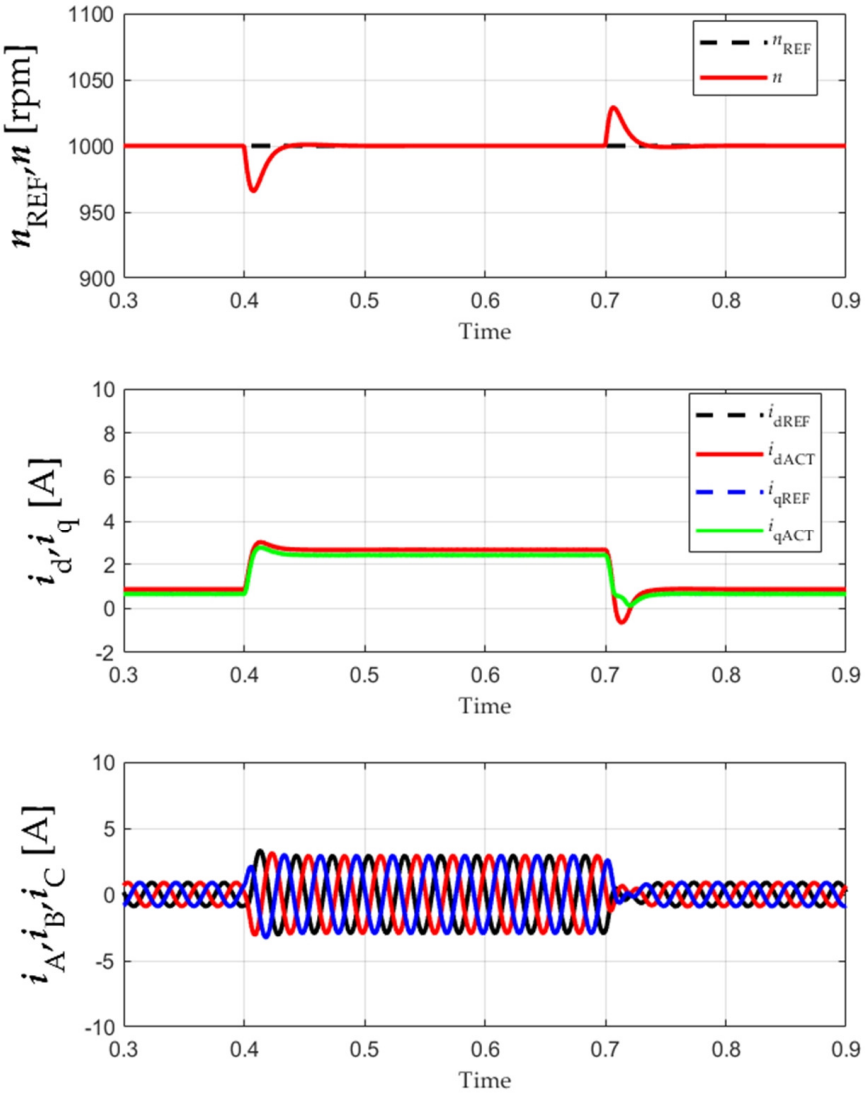

Figure 3.10 Simulation results: Disturbance rejection of the differential flatness-based control.

As can be seen, the PMa-SynRM model is a nonlinear system compared to the SPMSM (see Section 2.4). The traditional PI regulator with a conventional Field-Oriented Control (FOC) is designed around an operating point, and its performance is not optimal under all conditions. However, the differential flatness-based can address this problem. More clearly, although the FOC with traditional PI regulators was performed in Section 2.9.2, it will be discussed in this section to show that the PI controller design for controlling PMa-SynRM is very complex in order to achieve high performance. First, let us get started with the inner current loop control development. By referring to Eq. (2.33), the two voltages equations of PMa-SynRM are coupled by the back-emf term. By subtracting this term in the two current loops, the dq-axis currents can be controlled independently. This also simplifies the transfer function of the PMa-SynRM in the two current loops. The voltage equations, which are expressed in the s-plane, are in the following equation with defining the back-emf term by u_d and u_q, which are the d- and q-axis current controller outputs:

$$
\begin{aligned}
L_{\mathrm{d}}\frac{di_{\mathrm{d}}}{dt} &= -R_{\mathrm{s}}i_{\mathrm{d}}\overbrace{+\omega_{\mathrm{e}}(L_{\mathrm{q}}i_{\mathrm{q}}-\Psi_{\mathrm{m}})+v_{\mathrm{d}}}^{u_{\mathrm{d}}} \\
L_{\mathrm{q}}\frac{di_{\mathrm{q}}}{dt} &= -R_{\mathrm{s}}i_{\mathrm{q}}\overbrace{-\omega_{\mathrm{e}}L_{\mathrm{d}}i_{\mathrm{d}}+v_{\mathrm{q}}}^{u_{\mathrm{q}}}
\end{aligned}
\tag{3.57}
$$

$$
\begin{aligned}
U_{\mathrm{d}}(s) &= sL_{\mathrm{d}}+R_{\mathrm{s}}I_{\mathrm{d}}(s) \\
U_{\mathrm{q}}(s) &= sL_{\mathrm{q}}+R_{\mathrm{s}}I_{\mathrm{q}}(s)
\end{aligned}
\tag{3.58}
$$

$$
\begin{aligned}
G_{oid}(s) &= \frac{I_{\mathrm{d}}(s)}{U_{\mathrm{d}}(s)} = \frac{1}{sL_{\mathrm{d}}+R_{\mathrm{s}}} \\
G_{oiq}(s) &= \frac{I_{\mathrm{q}}(s)}{U_{\mathrm{q}}(s)} = \frac{1}{sL_{\mathrm{q}}+R_{\mathrm{s}}}
\end{aligned}
\tag{3.59}
$$

where $G_{oid}(s)$ and $G_{oiq}(s)$ are the open-loop transfer function of the PMa-SynRM for the *d* and *q* current loop.

From the open-loop transfer functions of *dq*-current (3.58) and (3.59), they can be expressed by (3.60) combined with PI controllers as in the following:

$$
\begin{aligned}
G_{\mathrm{oid}}(s) &= \left(\frac{sK_{\mathrm{pid}}+K_{\mathrm{iid}}}{s}\right)\cdot\frac{1/R_{\mathrm{s}}}{\tau_{\mathrm{d}}s+1} \\
G_{\mathrm{oiq}}(s) &= \left(\frac{sK_{\mathrm{piq}}+K_{\mathrm{iiq}}}{s}\right)\cdot\frac{1/R_{\mathrm{s}}}{\tau_{\mathrm{q}}s+R_{\mathrm{s}}}
\end{aligned}
\tag{3.60}
$$

Rewriting and rearranging (3.60) to obtain the closed-loop transfer function of *dq* current control, it yields

$$
\begin{aligned}
G_{\mathrm{cid}} &= \frac{G_{\mathrm{oid}}(s)}{1+G_{\mathrm{oid}}(s)} = \frac{\dfrac{sK_{\mathrm{pid}}+K_{\mathrm{iid}}}{R_{\mathrm{s}}\tau_{\mathrm{d}}}}{s^2+\left(\dfrac{R_{\mathrm{s}}+K_{\mathrm{pid}}}{R_{\mathrm{s}}\tau_{\mathrm{d}}}\right)s+\dfrac{K_{\mathrm{iid}}}{R_{\mathrm{s}}\tau_{\mathrm{d}}}} \\
G_{\mathrm{ciq}} &= \frac{G_{\mathrm{oiq}}(s)}{1+G_{\mathrm{oiq}}(s)} = \frac{\dfrac{sK_{\mathrm{pid}}+K_{\mathrm{iid}}}{R_{\mathrm{s}}\tau_{\mathrm{q}}}}{s^2+\left(\dfrac{R_{\mathrm{s}}+K_{\mathrm{piq}}}{R_{\mathrm{s}}\tau_{\mathrm{q}}}\right)s+\dfrac{K_{\mathrm{iiq}}}{R_{\mathrm{s}}\tau_{\mathrm{q}}}}
\end{aligned}
\tag{3.61}
$$

By comparing (3.61) to the standard second-order equation as in (3.10), controller parameters K_{pid}, K_{iid}, K_{piq}, and K_{iiq} can be defined as follow:

$$\frac{R_s + K_{pid}}{R_s \tau_d} = 2 \cdot \zeta_{id} \cdot \omega_{nid}$$
$$\frac{K_{iid}}{R_s \tau_d} = \omega_{nid}^2 \tag{3.62}$$

$$\frac{R_s + K_{piq}}{R_s \tau_q} = 2 \cdot \zeta_{iq} \cdot \omega_{nid}$$
$$\frac{K_{iiq}}{R_s \tau_q} = \omega_{niq}^2 \tag{3.63}$$

By determining ζ_{id}, ζ_{iq} and $\omega_{nid}, \omega_{niq}$ using the parameters in Table 2.2, the controller coefficients Kpid, Kiid, Kpiq, and Kiiq can be achieved by (3.64) and (3.65).

$$K_{pid} = \left(2 \cdot \zeta_{id} \cdot \omega_{nid} \cdot R_s \cdot \tau_d\right) - R_s$$
$$K_{iid} = \omega_{nid}^2 \cdot R_s \cdot \tau_d \tag{3.64}$$

$$K_{piq} = \left(2 \cdot \zeta_{iq} \cdot \omega_{niq} \cdot R_s \cdot \tau_q\right) - R_s$$
$$K_{iiq} = \omega_{niq}^2 \cdot R_s \cdot \tau_q \tag{3.65}$$

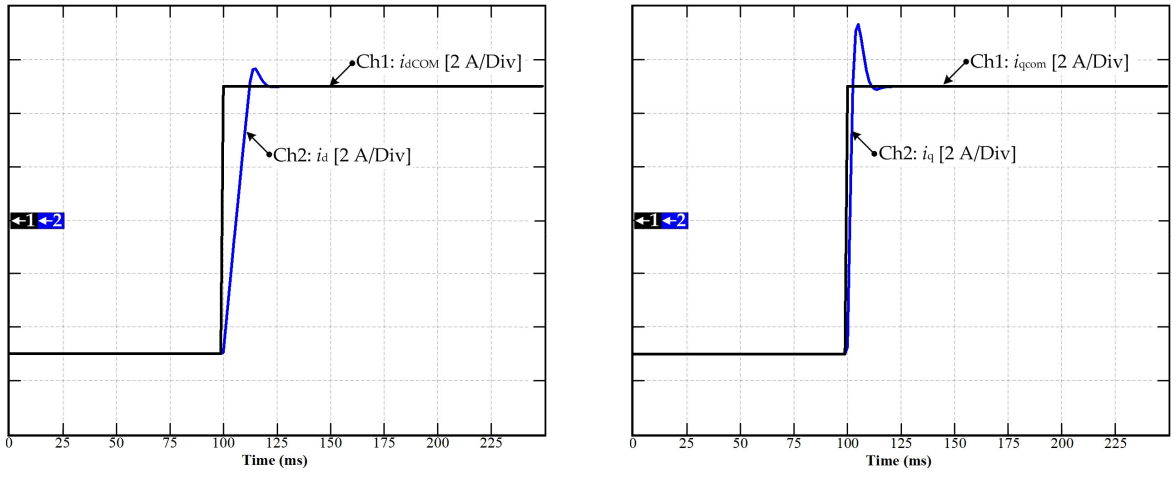

a b

Figure 3.11 Simulation results: Inner current control loop response (a) *d*-axis current (b) *q*-axis current.

Therefore, the closed-loop transfer function of the two current loops can be defined by combining the controller transfer function as represented in (2.59) and (2.60), and the controller coefficients are determined by (2.61) and (2.62) or used Equations (3.64), (3.65). By choosing t_{rd} = 0.1 ms, the coefficients K_{pid} = 363.85, K_{iid} = 3200, and t_{rq} = 0.5 ms, the given q-axis controller gains K_{piq} = 134.72, K_{iiq} = 6400. However, tuning the controller coefficients will achieve the fast response of the inner current control loops. In order to verify the designed control system, a simulation of the PMa-SynRM for the inner current control loop is performed in Figure 3.11. Figure 3.11(a) shows the response of the q-axis current, and Figure 3.11(b) shows the response of the d-axis current. As can be seen, the response behavior is faster than the d-axis response due to the time constant τ_{sd} of the d-axis being greater than that of the q-axis.

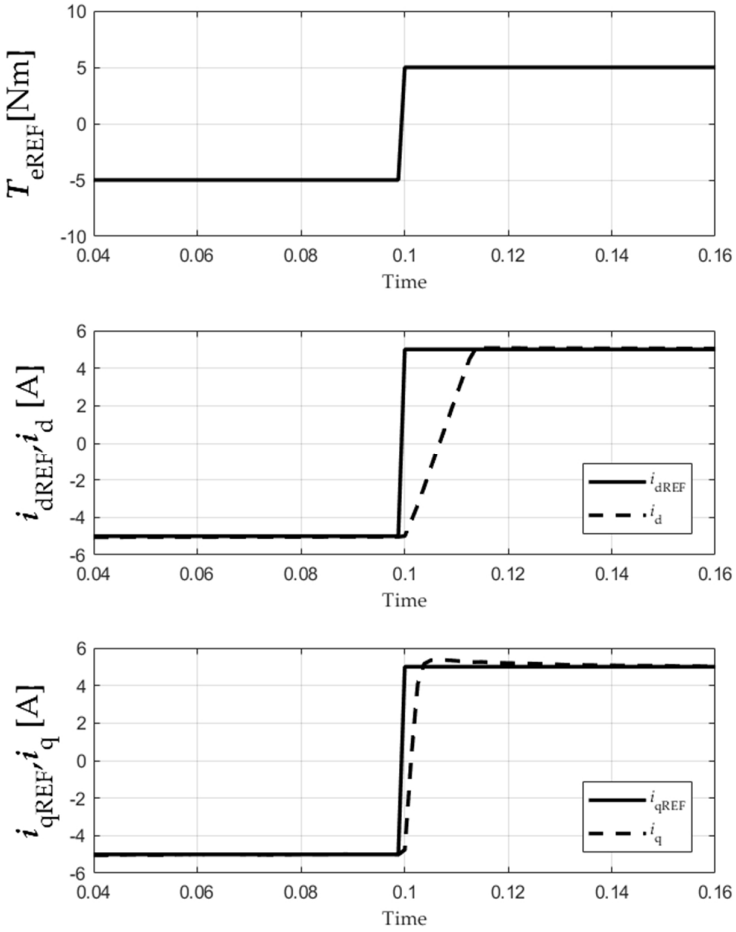

Figure 3.12 Simulation results: Inner current control loop response of the FOC with the PI controller.

Figure 3.12 shows the simulation result of the two inner current control loop responses when the T_{eREF} is the reference input of the MTPA lookup table (see Section 2.9.2 of Chapter 2). If it compares to Figure 3.9, it can be seen that the differential flatness-based control provides the highest performance. So, if the inner current control loop cannot offer high performance and rapid response for the system, it could not provide a good enough ability to reject external disturbance as good as the requirement. This results in the weak reaction of the outer speed control loop, as shown in the experimental result of dynamic performance rejection (see Figure

2.35 in chapter 2). Therefore, it is evident that the FOC with a traditional PI controller is not the best choice for the PMa-SynRM control system.

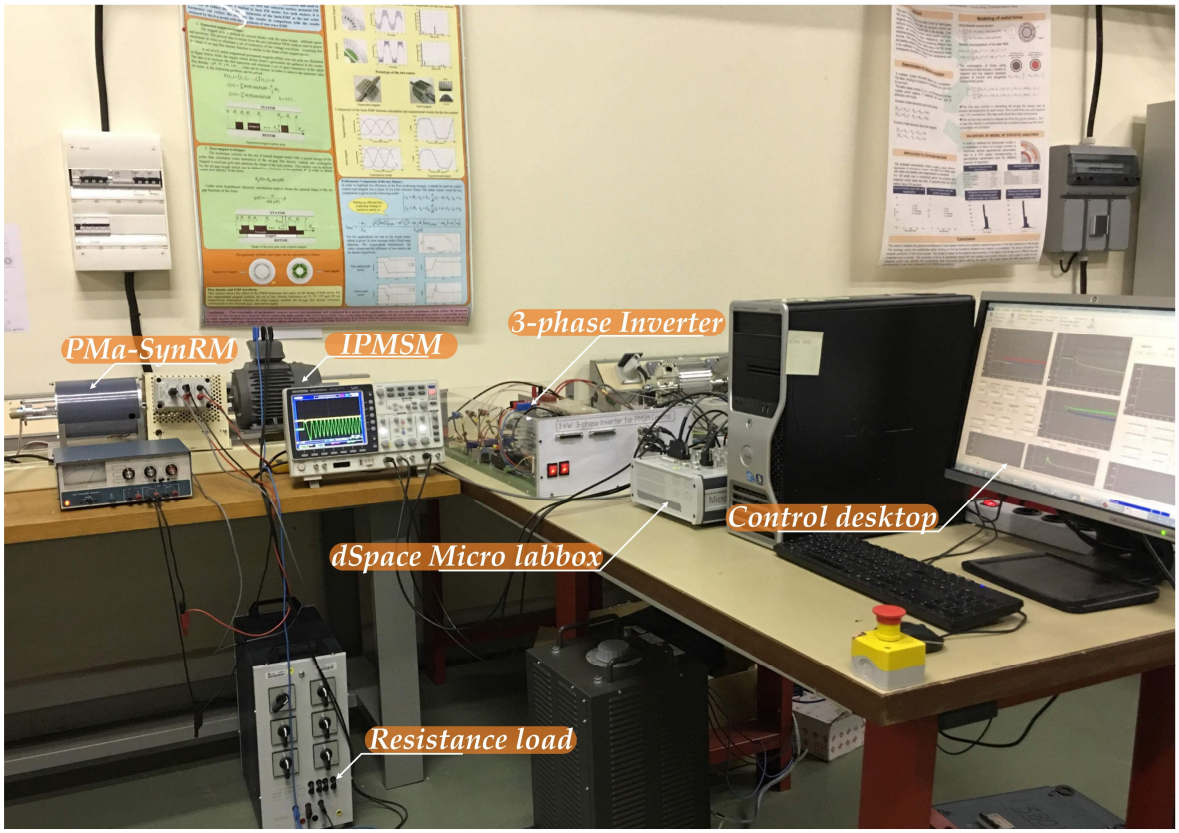

Figure 3.13 Laboratory test bench setup of PMa-SynRM drive at UL.

In order to verify the proposed control system, a laboratory test of the prototype PMa-SynRM is performed, as in Figure 3.13. and then the experimental results show in the following illustration.

Figure 3.14 demonstrates the simulation results, and Figure 3.15 represents the experimental results of the dynamic performance of the proposed control when the motor is forced to reverse direction. In Figure 3.14, Ch1 is the n_{COM}, Ch2 is the n_{REF}, Ch4 is the measured speed n, Ch5 is i_{qCOM}, Ch6 is the i_{qREF}, Ch7 is the i_q, Ch8 is i_{dCOM}, Ch9 is the i_{dREF}, and Ch10 is the i_d. In Figure 3.15, Ch1 is the n_{COM}, Ch2 is the n_{REF}, Ch4 is the measured speed n, Ch5 is i_q, Ch6 is the i_{dREF}, Ch7 is the i_d, and Ch8 is the i_{qREF}. The PMa-SynRM model is performed by MATLAB/SIMULINK software to validate that the proposed control system is appropriately designed. The results demonstrated that both simulation and experimental results are corresponding. Therefore, the PMa-SynRM model is correct, and the controller parameters are suitably designed by choosing desired parameters. The experimental results depict that the motor operates well in the regenerative mode until the speed reference is positive. Besides, the measured speed can effectively track the reference value. After that, the machine switches to motoring mode until the rotor speed reaches the speed command. The d-and q-axes currents show such good behavior without exceeding its limits. All the parameters of PMa-SynRM were guaranteed, and the proposed control provides satisfying dynamic performance.

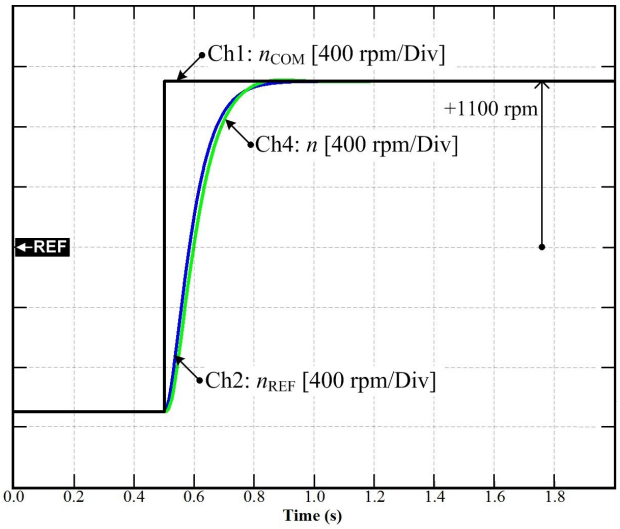

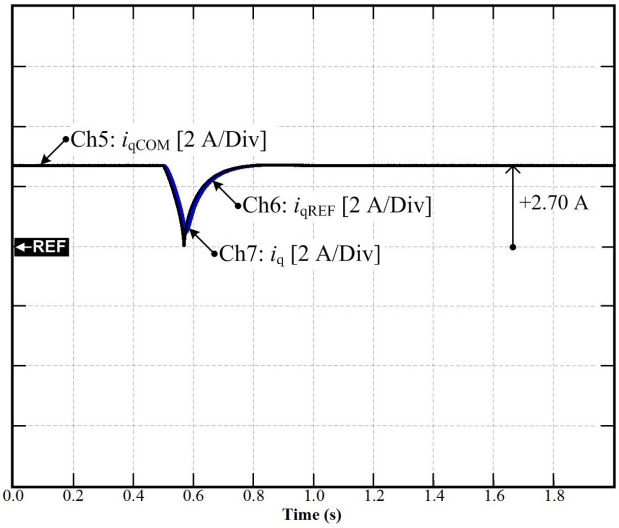

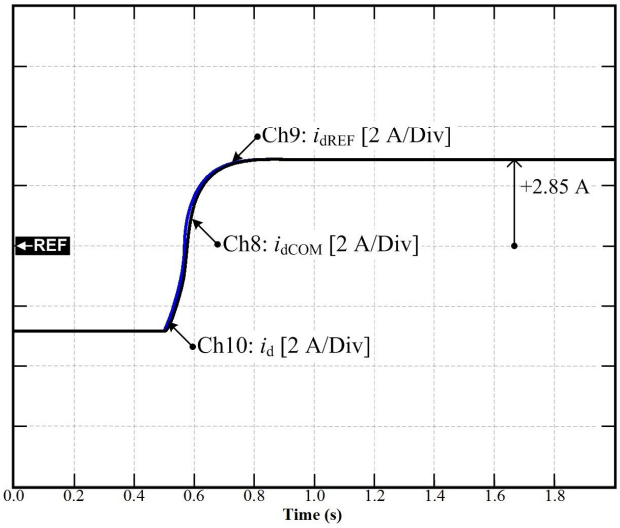

Figure 3.14 Simulation results: dynamic performance of speed reversal.

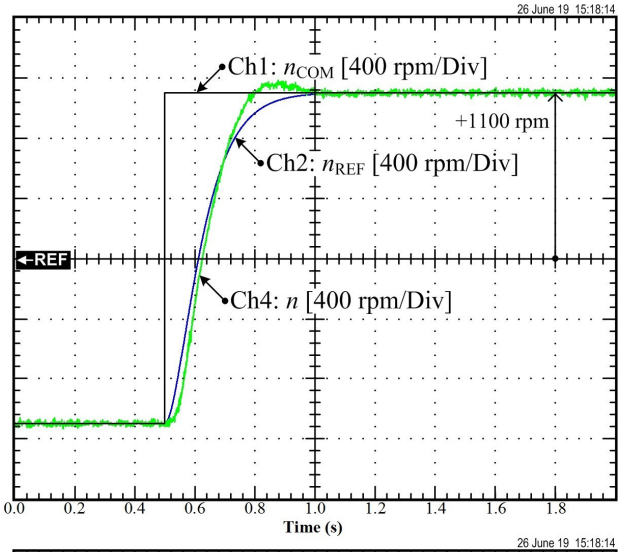

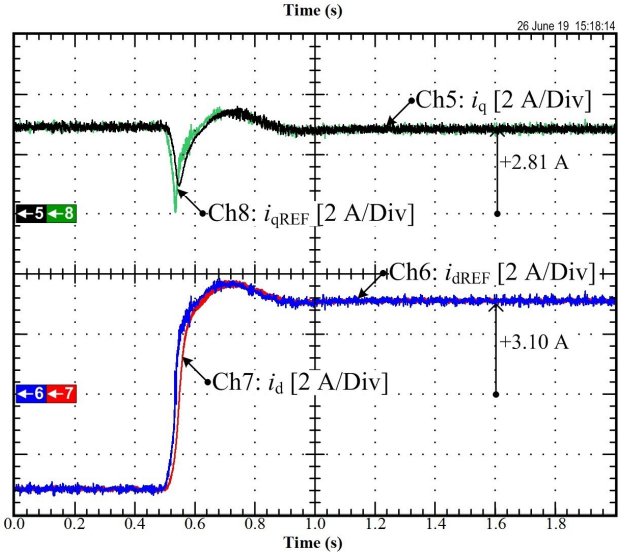

Figure 3.15 Experimental results: dynamic performance of speed reversal.

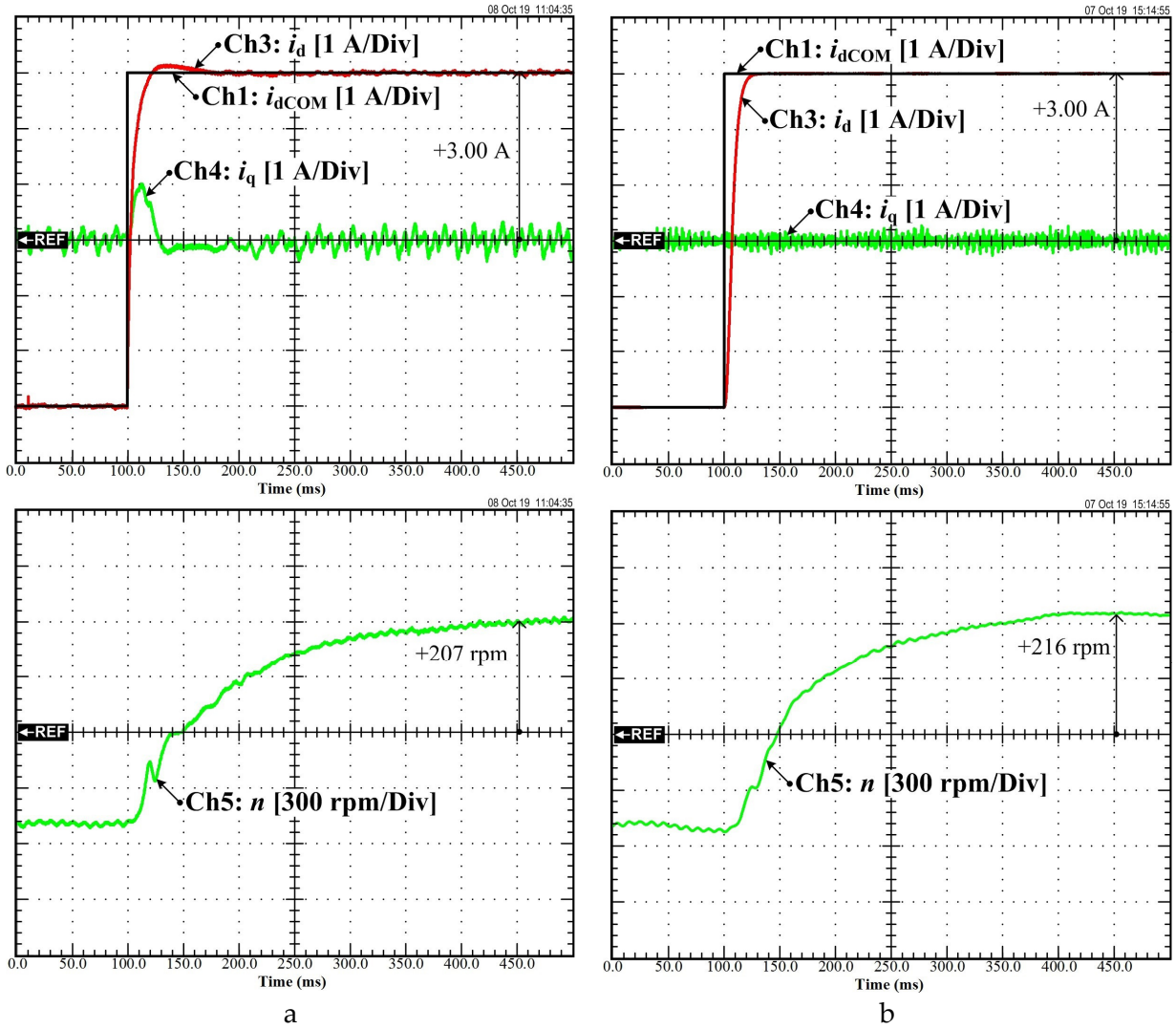

Figure 3.16 Experimental results: Dynamic performance of different control approach (a) FOC base PI controller. (b) Differential flatness-based control.

Comparing experimental validation for the FOC with PI controller and the differential flatness-based control is in the following illustration. Initially, the system performance when the torque/current loop uses traditional PI control and differential flatness is compared to depict the benefits of the proposed control scheme. Figure 3.16(a) represents the experimental results of the conventional PI control, and Figure 3.16(b) illustrates the experimental results of differential flatness control. Figure 3.16(a), Ch1 is i_{dCOM}, Ch3 is i_d, Ch4 is iq, and Ch5 is the measured speed n.

In Figure 3.16(b), Ch1 is i_{dCOM}, Ch3 is i_d, Ch4 is i_q, and Ch5 is the measured speed n. As shown in Figures 3.16(a) and 3.16(b), in the transient response, i_d using the traditional control shows slight overshoot, unlike that obtained by the differential flatness-based control, and i_q using the traditional control shows fluctuations. Thus, although PI control used decoupling and back-emf compensation, these tests show that the differential flatness-based control has a better dynamic current performance than the traditional control.

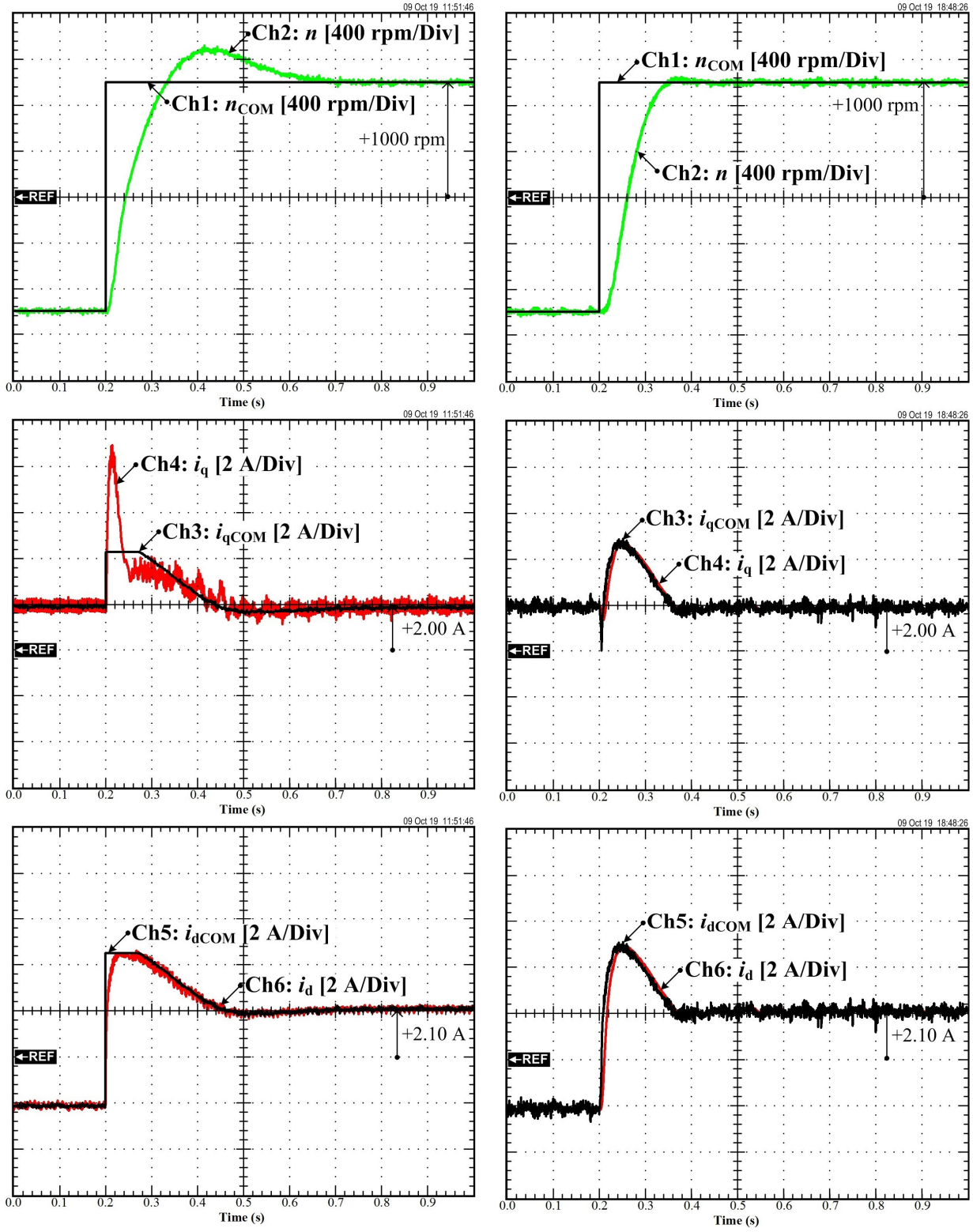

Figure 3.17 Experimental results: dynamic performance of speed reversal (a) FOC based PI controller (b) Differential flatness-based control.

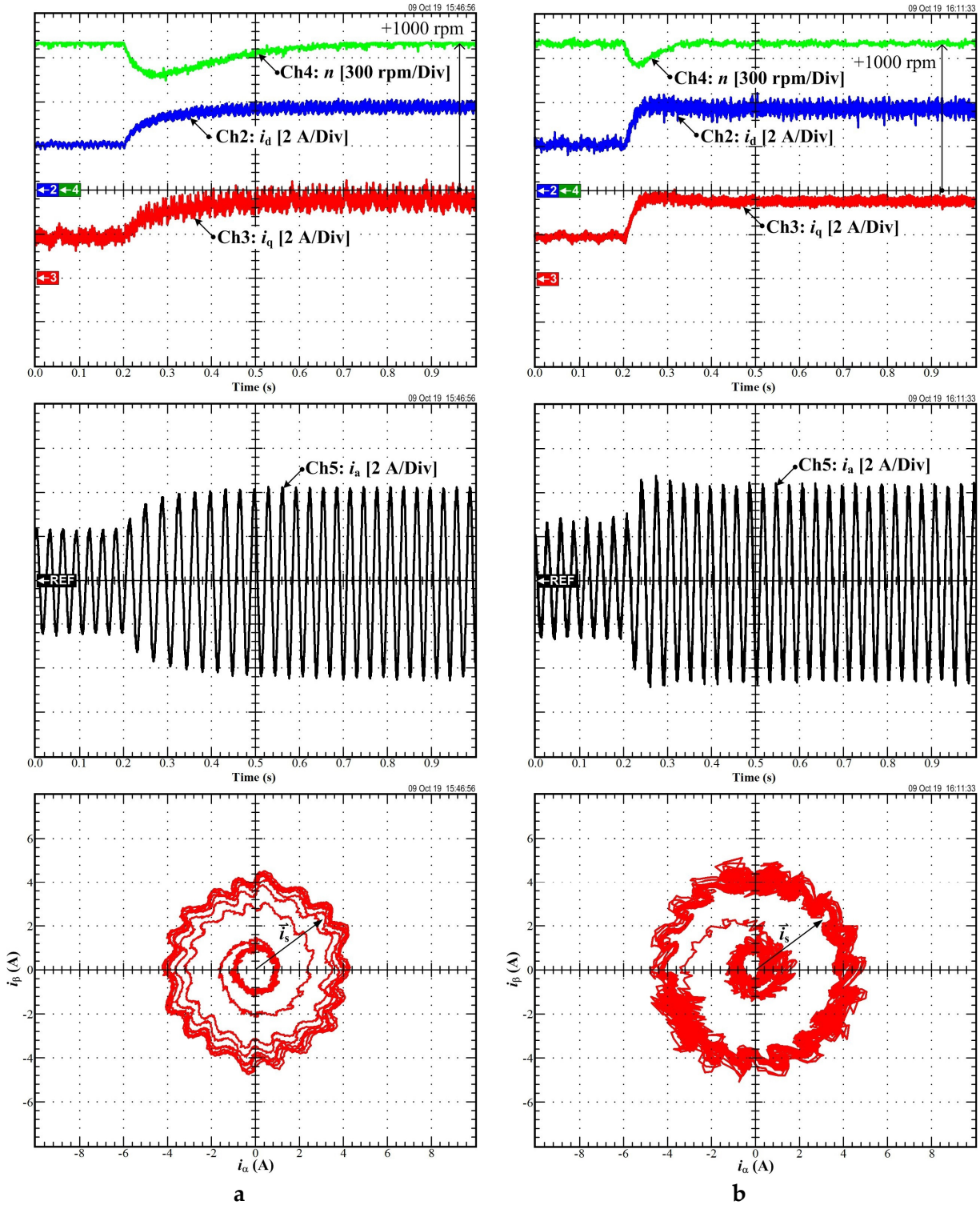

Figure 3.18 Experimental results: Disturbance rejection (a) FOC based PI controller (b) Differential flatness-based control.

Furthermore, the speed response (Ch5 of Figure 3.16(a)) using the traditional control demonstrates fluctuations, unlike the differential flatness-based control (Ch5 of Figure 3.16(b)). Then, the outer speed control loop is validated by forcing the PMa-SynRM to reverse its direction.

The system operates in a regenerative mode until the shaft speed is positive, and after that, the system switches to motoring mode until the rotor speed reaches its reference. Figure 3.17(a) shows the experimental results with the traditional control, and Figure 3.17(b) shows the experimental results using the differential flatness-based control. In Figure 3.17, Ch1 is n_{COM}, Ch2 is the measured speed n, Ch3 is i_{qCOM}, Ch4 is i_q, Ch5 is i_{dCOM}, and Ch6 is i_d.

As demonstrated in Figure 3.17(a), during the transient response, the measured speed n with the traditional control shows an overshoot, and the settling time is approximately 0.45 s. On the other hand, with the differential flatness control (Figure 3.17(b)), the response time is almost 0.15 s. Of course, the response time of the traditional controller can be improved by increasing its gains. However, this makes its stability more critical. In the meantime, the differential flatness-based control intrinsically includes the compensation of disturbing terms in the dynamic model and does not need its gains to be increased. Nevertheless, a good knowledge of the model is required. This need could be satisfied by an additional estimator considered later in this chapter.

In conclusion, the experimental results reflect that the differential flatness-based control has a better dynamic speed performance than the traditional control. However, this is at the cost of more complex implementation in terms of accurate modeling, memory usage and execution time. Moreover, the experimental validation of the comparison of the external load torque disturbance rejection is in the following expression.

Finally, Figure 3.18(a) shows the experimental results of traditional control, and Figure 3.18(b) depicts the preliminary results of the differential flatness-based control when the external torque disturbance is suddenly added. In Figure 3.18, Ch4 is the measured speed n, Ch2 is the d-axis current i_d, Ch3 is the q-axis current i_q, Ch5 is the phase-A current i_a, and the trajectories of the transient stator current are shown at the bottom. The experimental results obtained by the differential flatness-based control show a speed drop of 110 rpm, while the traditional controller cannot avoid a 220 rpm drop. The recovery time with the proposed controller is also shorter than that with the traditional controller. These results reflect that the differential flatness-based control performs better in torque/current control, speed loop control, and external disturbance rejection.

Although several control algorithms for PMa-SynRM have been published in the literature, it still remains challenging to achieve high-performance control for all conditions due to the nonlinear nature of the machine and its parameter uncertainties. Online parameter estimation is often included to consider parameter variations in the control algorithm. The next subchapter will address this topic for the differential flatness-based control of PMa-SynRM.

3.6. State Observer Parameter Estimation

This section deals with the parameter uncertainty and external disturbances that occur while electric motors operate in the real world. Notably, a PMSM is always driven by a three-phase inverter; thus, R_s is a simplified resistance representing the losses in the inverter (static and dynamics losses; deadtime; voltage drops in diodes and power transistors) and the PMSM (the stator winding resistance, hysteresis losses, and eddy current losses). Figure 3.19 shows an equivalent circuit of PMSM drive in which the resistance R_s is represented by $v_{td}(= R_s.i_d)$ for the d-axis current control loop and $v_{tq}(= R_s.i_q)$ for the q-axis current control loop. The load torque T_L is defined as an external disturbance by referring to the mechanical equation (2.39). Therefore, the torque measurement can measure it. However, the use of a torque sensor increases the cost of the system. Therefore, to deal with this, an online estimator is required to provide missing information and track parameter variations. State observers are potential candidates to play this role. For this purpose, a state observer is introduced in this section.

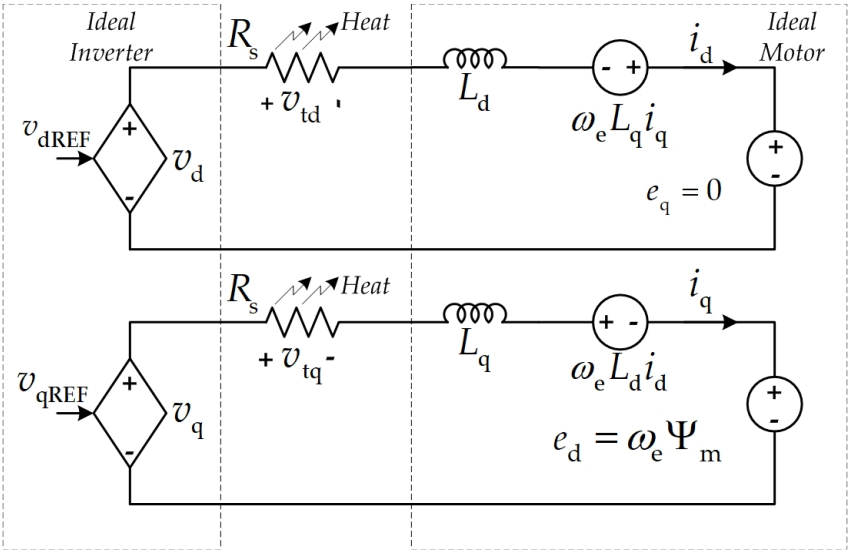

Figure 3.19 Equivalent circuit of PMSM drive.

Many different state observers can be found in the literature. Among them, two of the most classical are often used to achieve parameter estimation: the Luenberger state observer, which is valid for a linear system, and the Kalman Filter in its extended version (EKF), which made it proofs over nonlinear systems.

Before developing any state observer for parameter estimation, the observability of the interred system has to be verified since observation is not possible if this condition is not ensured. Then, in most cases, only local observability will be verified. A mathematical definition of observability can be found in [78] [85]. However, in practice, the more the system is nonlinear, the more global observability is challenging to demonstrate.

Local observability depends on the rank of the Jacobian matrix of the output vector **P**o, which is defined as follows.

$$\mathbf{P}_O = \begin{bmatrix} \mathbf{C} \\ \mathbf{CA} \\ \vdots \\ \mathbf{CA}^{n-1} \end{bmatrix} \neq 0 \tag{3.66}$$

where n is the number of state variables

For example, a simple system model represented in vector matric is

$$\mathbf{A} = \begin{bmatrix} 0 & 1 & 0 \\ 0 & 0 & 1 \\ -a_0 & -a_1 & -a_2 \end{bmatrix}, \text{and } \mathbf{C} = \begin{bmatrix} 1 & 0 & 0 \end{bmatrix}$$

Thus,

$$\mathbf{CA} = \begin{bmatrix} 0 & 1 & 0 \end{bmatrix}, \text{, and } \mathbf{CA}^2 = \begin{bmatrix} 0 & 0 & 1 \end{bmatrix}$$

Therefore, the Po is obtained as

$$\mathbf{P}_O = \begin{bmatrix} 1 & 0 & 0 \\ 0 & 1 & 0 \\ 0 & 0 & 1 \end{bmatrix} \tag{3.67}$$

The determinant of **P**o is 1, and the system is completely observable.

3.6.1. Luenberger Observer

The first state observer considered through this work is the Luenberger state observer. This method is dedicated to linear systems and will require linearization around one operating point to be used on a nonlinear system. Then, the system to be observed through the Luenberger state-observer will be written under the classical from equation (3.68).

$$\begin{aligned} \dot{x} &= \mathbf{A} \cdot x + \mathbf{B} \cdot u \\ y &= \mathbf{C} \cdot x \end{aligned} \tag{3.68}$$

where x is the state vector, u is the input vector, and y is the measurable variables or output vector. The x, u, and y are functions of time. To simplify the equations, notation x(t), represented by (2.48) and (2.49), is replaced by x in this study. **A** is an nxn square matrix, and **B** is an nxm matrix, where n is the number of states, and m is the number of inputs. **A** and **B** are constant-coefficient matrices. **C** is a hxn matrix where h is the number of outputs.

The estimated state vector $\widehat{x}$ is obtained by solving the following equation:

$$\dot{\hat{x}} = \mathbf{A}\cdot\hat{x} + \mathbf{B}\cdot u + \mathbf{L}(\mathbf{C}\cdot x - \mathbf{C}\cdot\hat{x}) \tag{3.69}$$

where **L** is a matrix with constant gains. By defining the estimation error as

$$\varepsilon = x - \hat{x} \tag{3.70}$$

One main results of the systems theory are that if the system is entirely observable, the matrix **L** can always be defined so that the tracking error is asymptotically stable, as desired.

Taking time-derivation of the estimation error (3.70) yields

$$\dot{\varepsilon} = \dot{x} - \dot{\hat{x}} \tag{3.71}$$

By substituting (3.68) and (3.69) into (3.71) and rearrangement, it yields

$$\dot{\varepsilon} = \mathbf{A}\cdot x + \mathbf{B}\cdot u - \left(\mathbf{A}\cdot\hat{x} + \mathbf{B}\cdot u + \mathbf{L}(\mathbf{C}\cdot x - \mathbf{C}\cdot\hat{x})\right) \tag{3.72}$$

or

$$\dot{\varepsilon} = (\mathbf{A} - \mathbf{LC})\cdot\varepsilon \tag{3.73}$$

It is evident that $\varepsilon(t) \to 0$ as $t \to \infty$ for initial tracking error, $\varepsilon(t_0)$

$$\det\{\lambda\cdot\mathbf{I} - (\mathbf{A} - \mathbf{LC})\} = 0 \tag{3.74}$$

Suppose the characteristic equation (3.74) has all its roots in the left of the complex s-plane. This can always be accomplished if the system is entirely observable; that is, **P**o has total rank.

3.6.2. Improve Performance of Differential Flatness-Based Control for SPMSM by the Luenberger State Observer

As mentioned earlier, the differential flatness-based control is a model-based control approach, and the inaccuracy of model parameters will significantly affect the control performance. Therefore, in order to achieve high performance, the control system, Luenberger state observer, tries to address this problem. Application of this concept to the SPMSM model, represented in the state-space representation in (2.47), is developed in the following.

As discussed in the previous chapter, SPMSM is a non-salient poles machine such that the *d*-axis current is set to zero as it does not contribute to torque generation. Consequently, ignoring the first row of (2.47), the model can be rewritten as

$$\begin{bmatrix} \frac{di_{\mathrm{q}}}{dt} \\ \frac{d\omega_{\mathrm{m}}}{dt} \end{bmatrix} = \begin{bmatrix} \left\{-R_{\mathrm{s}} i_{\mathrm{q}} - \omega_{\mathrm{e}}(L_{\mathrm{s}} i_{\mathrm{d}} + \Psi_{\mathrm{m}})\right\} / L_{\mathrm{s}} \\ \left(n_{\mathrm{p}} \Psi_{\mathrm{m}} i_{\mathrm{q}} - B_f \omega_m\right) / L_{\mathrm{s}} \end{bmatrix} + \begin{bmatrix} \frac{1}{L_{\mathrm{s}}} & 0 \\ 0 & -\frac{1}{J} \end{bmatrix} \begin{bmatrix} v_{\mathrm{q}} \\ T_{\mathrm{L}} \end{bmatrix}$$
$$y = \begin{bmatrix} 1 & 0 & 0 \\ 0 & 1 & 0 \end{bmatrix} \begin{bmatrix} i_{\mathrm{q}} \\ \omega_{\mathrm{m}} \end{bmatrix} \tag{3.75}$$

In Figure 3.19, v_{tq} represents the losses in the motor drive. A Luenberger observer will be designed to estimate v_{tq}. Furthermore, the external load torque disturbance T_{L} in the mechanical equation in (2.39) is also considered to be estimated by this observer. It is worth mentioning that both vtq and T_{L} are locally observable. Moreover, their dynamic is considered zero as they are supposed to be slowly variable. By adding v_{tq} and T_{L} into the system model in (3.75), it yields:

$$\begin{bmatrix} \frac{di_{\mathrm{q}}}{dt} \\ \frac{d\omega_{\mathrm{m}}}{dt} \\ \frac{dv_{tq}}{dt} \\ \frac{dT_L}{dt} \end{bmatrix} = \underbrace{\begin{bmatrix} \frac{-v_{tq}}{L_{\mathrm{s}}} - \frac{n_p \omega_{\mathrm{m}} \Psi_{\mathrm{m}}}{L_{\mathrm{s}}} \\ \left(n_{\mathrm{p}} \Psi_{\mathrm{m}} i_{\mathrm{q}} - B_f \omega_m\right) / J \\ 0 \\ 0 \end{bmatrix}}_{f(x)} + \underbrace{\begin{bmatrix} \frac{1}{L_{\mathrm{s}}} & -n_p \omega_{m0} \\ 0 & 0 \\ 0 & 0 \\ 0 & 0 \end{bmatrix}}_{\mathbf{B}} \begin{bmatrix} v_{\mathrm{q}} \\ i_{\mathrm{d}} \end{bmatrix}$$
$$y = \underbrace{\begin{bmatrix} 1 & 0 & 0 & 0 \\ 0 & 1 & 0 & 0 \end{bmatrix}}_{\mathbf{C}} \begin{bmatrix} i_q \\ \omega_m \end{bmatrix} \tag{3.76}$$

where i_{d} is defined as an input of the system and ω_{m0} is the operating point speed.

As mentioned earlier, Luenberger observer is dedicated to linear systems. Thus, the SPMSM model must be linearized using the Jacobian matrix **A**j. For (3.52), the Jacobian matrix is

$$\mathbf{A}_j = \begin{bmatrix} 0 & -\frac{n_{\mathrm{p}} \Psi_{\mathrm{m}}}{L_{\mathrm{s}}} & -\frac{1}{L_{\mathrm{s}}} & 0 \\ \frac{n_{\mathrm{p}} \Psi_{\mathrm{m}}}{J} & -\frac{B_{\mathrm{f}}}{J} & 0 & -\frac{1}{J} \\ 0 & 0 & 0 & 0 \\ 0 & 0 & 0 & 0 \end{bmatrix} \tag{3.77}$$

The system (3.75) has total rank and observability properties. In addition, Luenberger observer can be applied to this system.

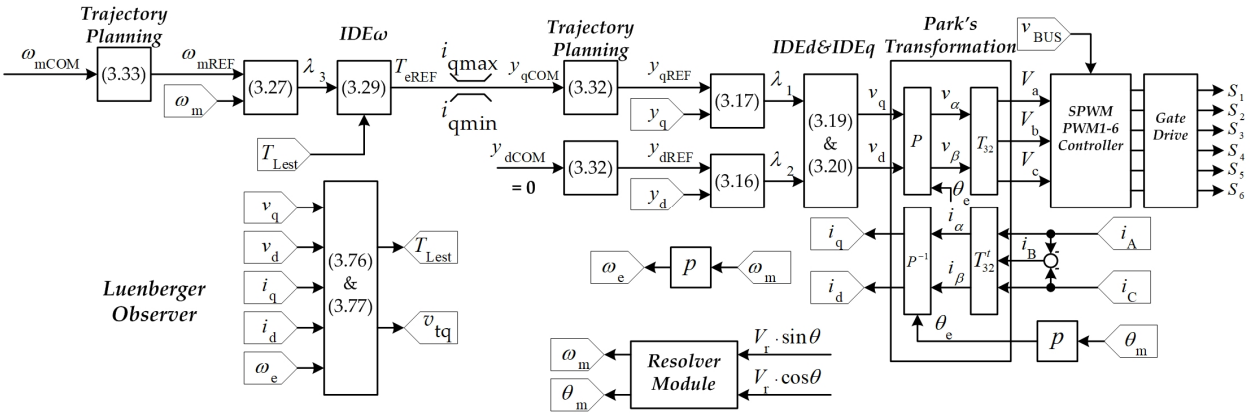

Figure 3.20 Differential flatness-based control with state observer based on Luenberger Observer (LOB).

3.6.3. Simulation results of the Luenberger state observer applied to parameter estimation for the SPMSM

Fig 3.20 presents the proposed control system schematic diagram of the SPMSM drive. In order to verify the feasibility of the design scheme, according to Figure 3.20, a differential flatness-based control simulation model based on Luenberger state observer is performed in MATLAB/Simulink environment. As a result, the speed loop adopts differential flatness-based control, the two current loops adopt differential flatness-based control, and the Luenberger observer provides compensation terms for the flatness-based control.

The parameters of the SPMSM are in Table 3.5, and the controller coefficient of the differential flatness-based control is in Table 3.2. The eigenvalues of the matrix A-LC were established at [-10,000 -10,000 -50 -500]. Those values have been tuned experimentally to achieve the best performance possible. For the operating point, at speed 1000 rpm, ω_{m0} = 104.72 rad/s, and keeping id zero. The matrix **L** is given in (3.78).

TABLE 3.5
SPMSM Parameters for the Luenberger development

Symbol	Meaning	Value
P_{rated}	Rated Power	1kW
n_{rated}	Rated Speed	3000 rpm
n_p	Number of pole pairs	3
R_s	Resistance (Motor + Inverter)	10 Ohm
$L_s = L_d = L_q$	Stator inductance	35.31 mH
Ψ_m	Permanent-magnet flux	0.2214 [Wb]
J	Equivalent inertia	0.002 kg.m2

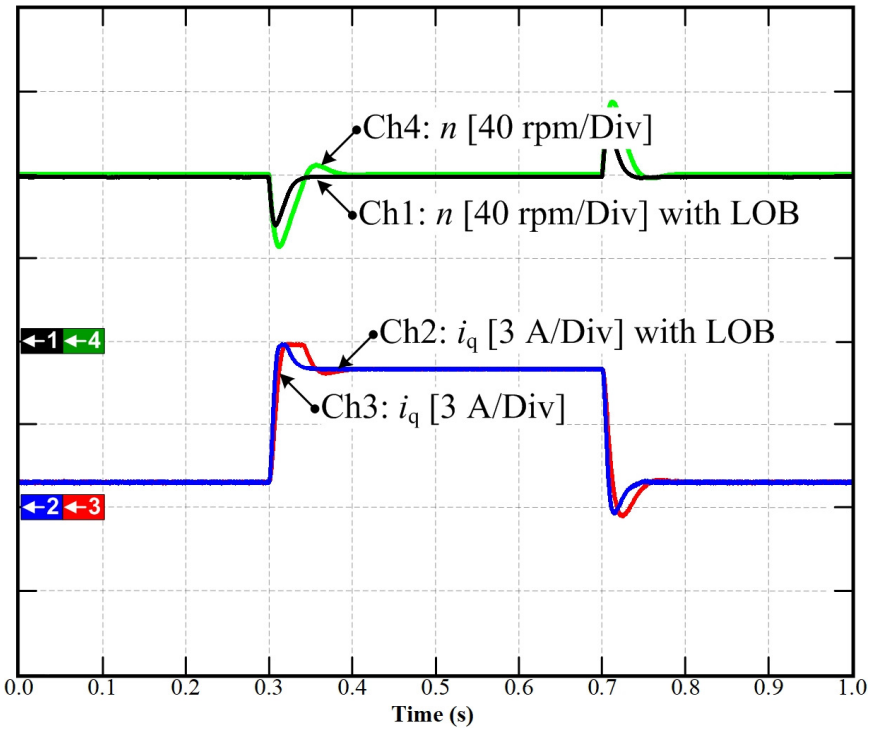

Figure 3.21 Simulation results: Comparison between the flatness-based controt with and without the Luenberger observer.

$$\mathbf{L}=\begin{bmatrix} 10,500 & -18.81 \\ 131.434 & 10,149 \\ -1.765\times10^{5} & 0 \\ 0 & 7,580 \end{bmatrix} \tag{3.78}$$

Figure 3.21 shows the simulation results of the comparison between the flatness-based control with and without Luenberger observer (LOB). The simulation conditions are set as follows: given speed: n = 1,000 rpm; a sudden increase of the load torque TL of 3 Nm at 0.3 s, running with load until 0.7 s, and then clearing the load torque. It can be seen that under the action of the Luenberger observer, when the load changes suddenly, the motor speed shows a smaller deviation, and the reference speed is recovered faster (see Ch1 and Ch4). Thus, this test has been performed under different operating conditions, and an improvement in the speed control performance has been noticed overall, which verifies the interest of the Luenberger observer in the control of SPMSM.

Ch2 and Ch3 represent the q-axis current response curve with and without LOB in this figure. It can be seen that the settling time of the q-axis current based on the differential flatness-based control with Luenberger observer is faster than that of the control system without Luenberger observer.

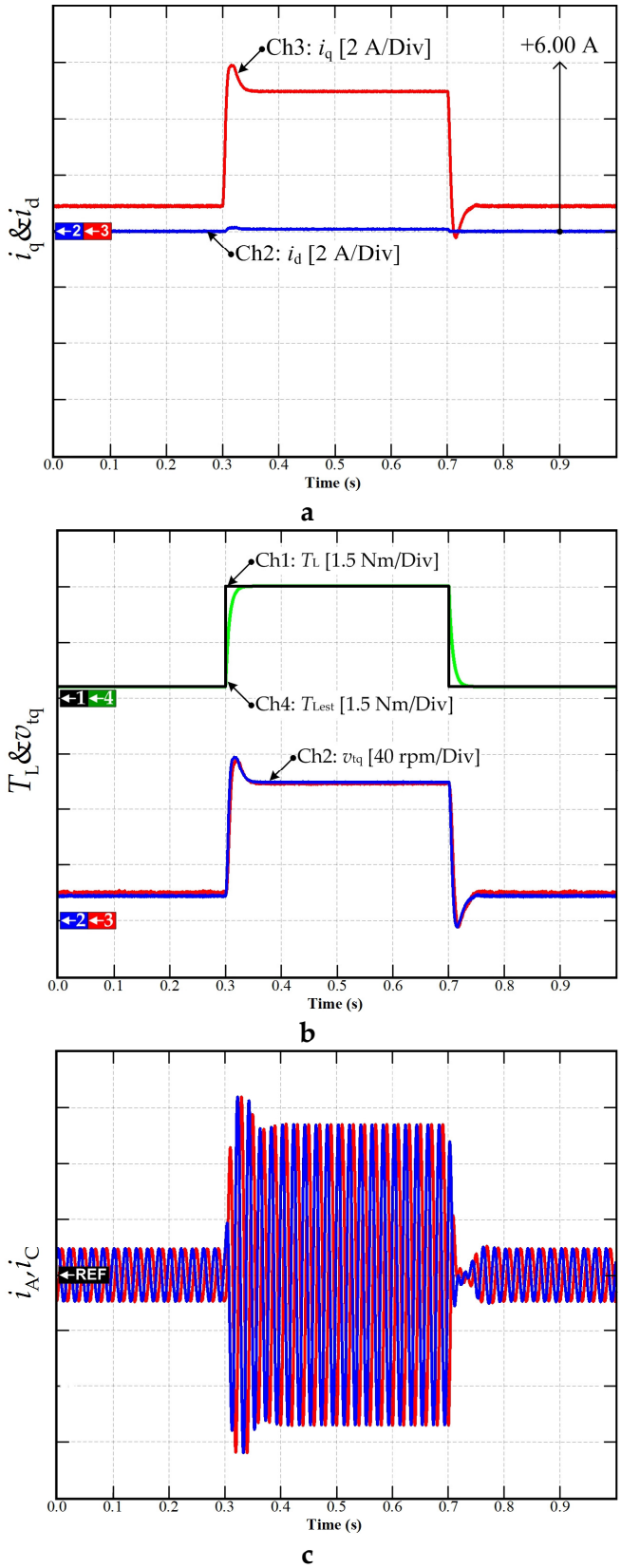

Figure 3.22 Simulation results: Dynamic performance of the proposed control scheme (a) d-axis and q-axis currents (b) T_L and estimated v_{tq} (c) the current of phase A and C.

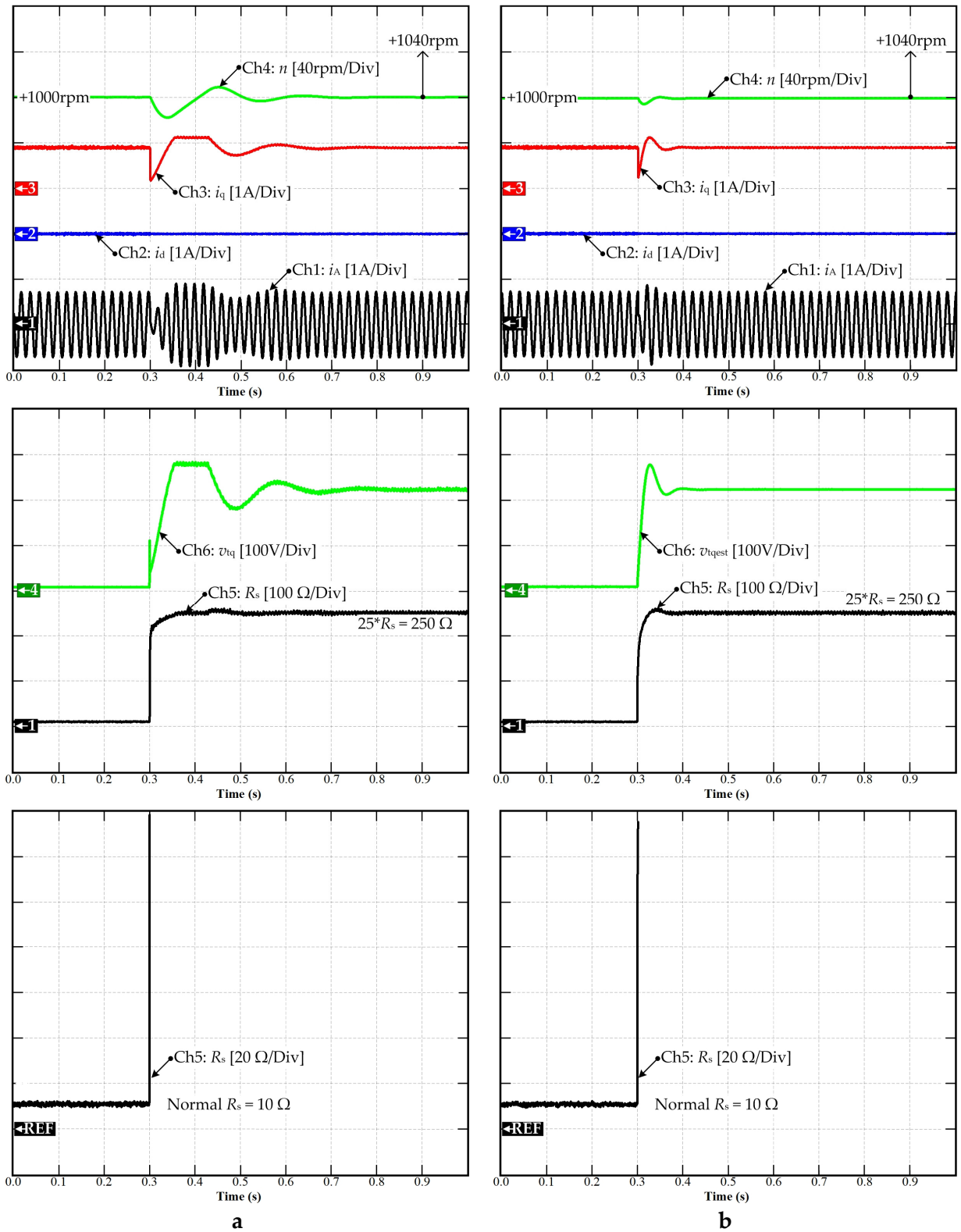

Figure 3.23 Simulation results: (a) Dynamic performance of the proposed control without an observer (b) The proposed control based on the Luenberger state observer.

Fig 3.22 shows the simulation results, in which Figure 3.22(a) is the q- and d-axis currents responses, Figure 3.22(b) is the estimated load torque T_{Lest} and the estimated voltage v_{tq}. Figure 3.22(c) shows the currents of phases A and C, respectively. As can be seen, T_{Lest} converges to the measured torque in a short time, and v_{tq} is accurately estimated by Luenberger observer. Therefore, it results in the performance of the differential flatness-based control has been improved with the estimation of unmeasured variables.

Moreover, simulation results of the resistance variation are verified in this section. The simulation conditions are set as follows: given speed: n = 1000 rpm; a sudden increase of 25 times of average resistance in Table 3.5 (R_s =10 Ohm) at 0.3 s, running at this condition to t = 1 s. Figure 3.23 shows the simulation results. Figure 3.23, Ch4 is the measured speed n, Ch2 is the d-axis current i_d, Ch3 is the q-axis current i_q, and Ch1 is the current phase. Ch5 is the voltage v_{tq} assumed as the voltage drop across power devices and winding of the machine, and Ch6 is the resistance R_s, which is defined as a variation of resistance of the motor winding. As shown in figure 3.23(b), the fluctuation of speed (Ch4) is suppressed by the observer compensation in a short time when compared to the speed response in figure 3.23(a). So, the performance of the differential flatness-based control for the inner current control loop has been improved, confirming the interest in the inclusion of the parameter estimation in the control.

3.6.4. Enhance the performance of the differential flatness-based control based on the Luenberger state observer applied for the PMa-SynRM drive

According to the PMa-SynRM model as in the equation (2.49) in Chapter 2, it is shown that the model is nonlinear, which impacts the complexity of the estimator. To start with a simple observer and evaluate its effect on the control performance, a reduced-order observer is first developed for PMa-SynRM in this section to estimate the load torque. For this purpose, and according to equation (3.69), the motor model (2.49) is rewritten as

$$\begin{bmatrix} \frac{d\omega_m}{dt} \\ \frac{dT_L}{dt} \end{bmatrix} = \underbrace{\begin{bmatrix} -\frac{T_L}{J} - \frac{B_f\omega_m}{J} \\ 0 \end{bmatrix}}_{f(x)} + \underbrace{\begin{bmatrix} \frac{1}{J} \\ 0 \end{bmatrix}}_{\mathbf{B}} \begin{bmatrix} T_e \\ 0 \end{bmatrix}$$
$$y = \begin{bmatrix} 1 & 0 \end{bmatrix} \begin{bmatrix} \omega_m \\ T_L \end{bmatrix} \tag{3.79}$$

The load torque is assumed slowly variable. The system Jacobian matrix **A**j of (3.79) is given by

$$\mathbf{A}_j = \begin{bmatrix} -\frac{B_f}{J} & -\frac{1}{J} \\ 0 & 0 \end{bmatrix} \tag{3.80}$$

The observability matrix for the above system is full rank, so it is locally observable.

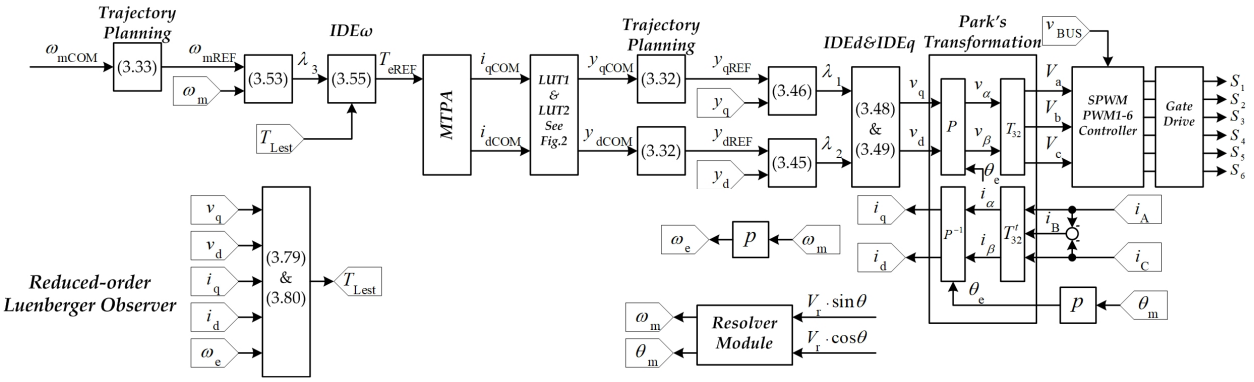

Figure 3.24 Differential flatness-based control based on the reduce-order Luenberger state observer block diagram applied to PMa-SynRM.

TABLE 3.6
PMa-SynRM Parameters for the Luenberger development

Symbol	Meaning	Value
P_{rated}	Rated Power	1kW
n_{rated}	Rated Speed	1350 rpm
n_{p}	Number of pole pairs	2
R_{s}	Resistance (Motor + Inverter)	3.2 Ohm
L_{d}	Normal *d*-axis inductance	288 mH
L_{q}	Normal *q*-axis inductance	38 mH
L_{dq}	Mutual inductance	4 mH
Ψ_{m}	Permanent-magnet flux	0.138 [Wb]
J	Equivalent inertia	0.0017 kg.m^2

Figure 3.24 presents the proposed control system schematic diagram of the PMa-SynRM drive. In order to verify the feasibility of the design scheme, according to Figure 3.24, a differential flatness-based control simulation model based on the reduced-order Luenberger state observer is performed in MATLAB/Simulink environment. As a result, the outer speed loop adopts differential flatness-based control, the two current loops adopt differential flatness-based control, and a reduced-order Luenberger observer is implemented to estimate the load torque.

The parameters of the PMa-SynRM are given in Table 3.6, and the controller coefficients of the differential flatness-based control are shown in Table 3.4. The eigenvalues of **A**-**LC** were placed at [-10000 -100]. Those values have been tuned experimentally to achieve the best performance possible. For the operating point, at speed 1000 rpm, ω_{m0} = 104.72 rad/s, and the matrix **L** is given by

$$\mathbf{L}=\begin{bmatrix}10,099\\-5053\end{bmatrix} \tag{3.81}$$

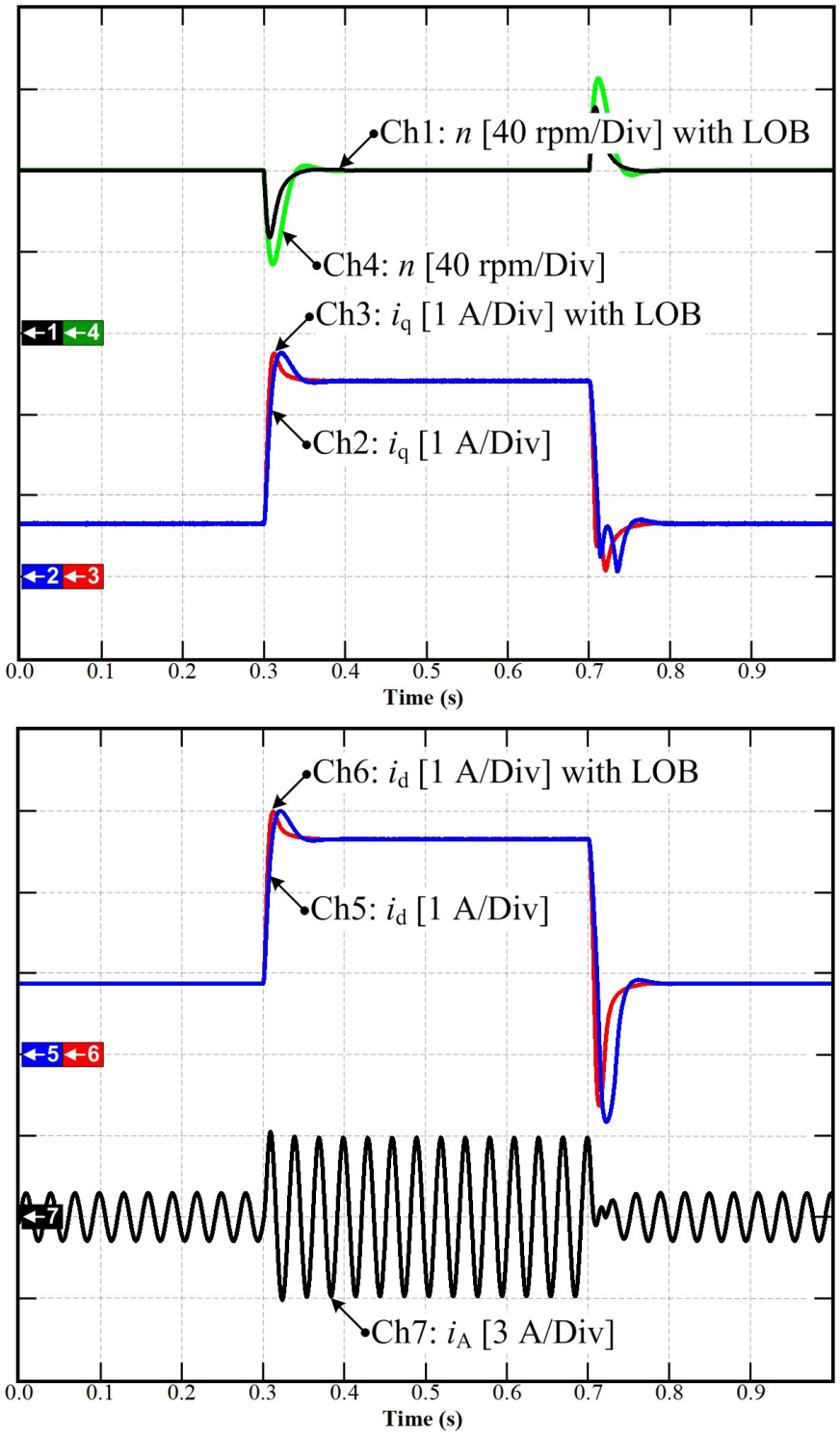

Figure 3.25 Simulation results: Dynamic performance of the proposed control based on the reduced-order Luenberger state observer applied to PMa-SynRM.

Figure 3.25 shows the simulation results of the comparison between the differential flatness-based control based on the reduced-order Luenberger observer and the control system without the observer. The simulation conditions are set as follows: given speed: n = 1000 rpm; a

sudden increase of load torque T_L of 4 Nm at 0.3 s, running with load to 0.7 s, and then removing the load torque. It can be seen that under the action of the Luenberger state observer, when the load changes suddenly, its effect on the motor speed is attenuated, and the reference speed is recovered faster (see Ch1 and Ch4). Ch2 and Ch3 in Figure 3.25 represent the *q*-axis current response. It can be seen that the settling time of the *q*-axis current with the load torque observer is improved. Ch 5 and Ch6 illustrate the *d*-axis current response. As can be seen, the *d*-axis current response is also improved with the reduced-order observer.

3.6.5. Experimental validation of the differential flatness-based control based on the Luenberger state observer

The SPMSM parameters and its flatness-based controller parameters are given in Table 3.1 and Table 3.2, respectively. The laboratory setup is shown in Figure 3.4, composed of a 6-pole, 1kW PMSM coupled with a DC motor mimicking the load. It is worth recalling that the proposed controller is implemented on a dSPACE DS1104 board, with a time step of Ts = 100 μs. The measurement of the electromagnetic torque was realized by a torque transducer mounted on the rotor shaft.

3.6.5.1. Performance of parameter estimation with Luenberger Observer

Figures 3.26(a) and 3.26(b) show the simulation and experimental results of the load torque estimation using Luenberger observer. In Figure 3.26(b), Ch2 is the measured speed *n*, Ch3 is the *q*-axis current, and Ch4 is the estimated load torque T_{Lest}. The simulation and experimental results match pretty well. The results reflect that when the load torque is suddenly stepped from 0 Nm to 2 Nm, it can be correctly estimated by the observer and the convergence time is less than 0.1 s.

Next, Figures 3.27(a) and 3.27(b) show respectively the simulation and experimental results of the estimation of v_{tq}. These results are close to each other and show the effectiveness of the proposed observer in the estimation of v_{tq}.

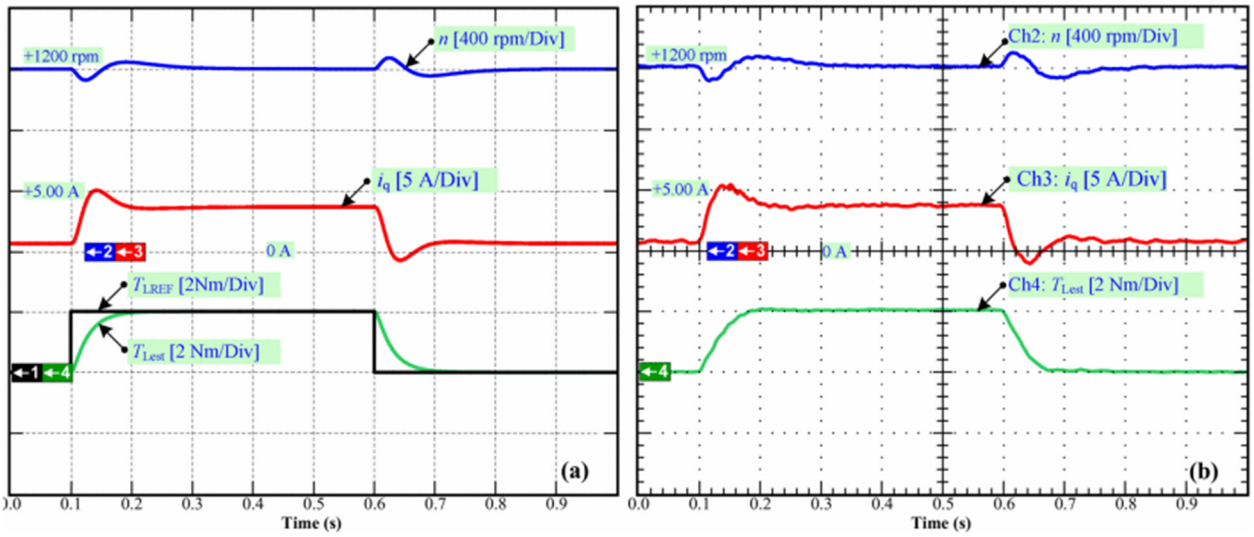

Figure 3.26 Experimental results: Simulation and experimental results of T_L estimation based on the Luenberger state observer (a) Simulation. (b) Experimental.

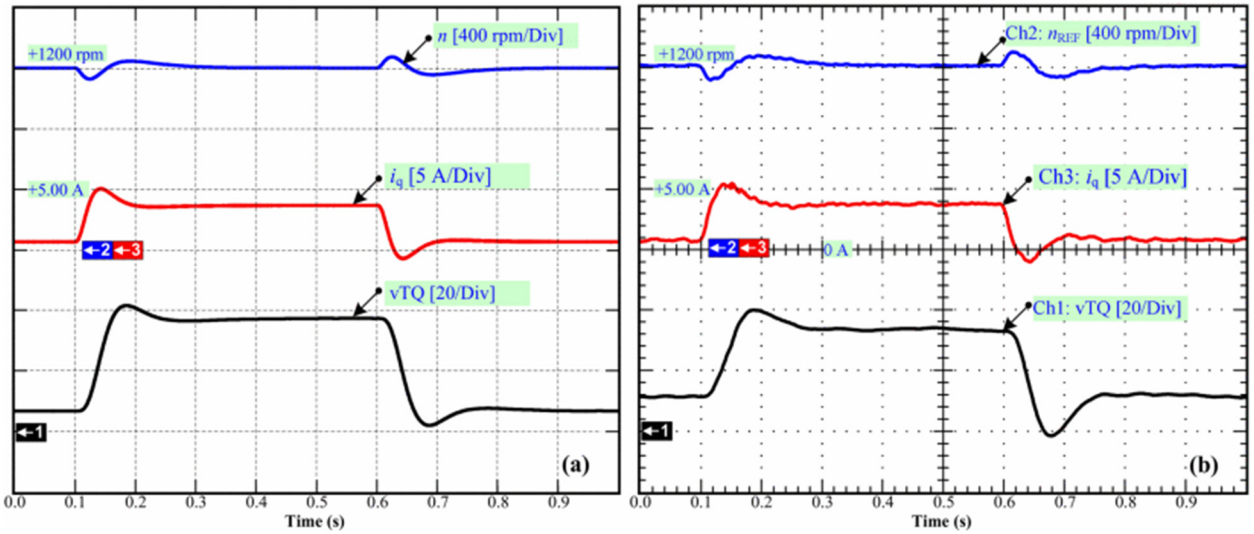

Figure 3.27 Experimental results: Simulation and experimental results of v_{tq} estimation based on the Luenberger state observer. (a) Simulation. (b) Experimental.

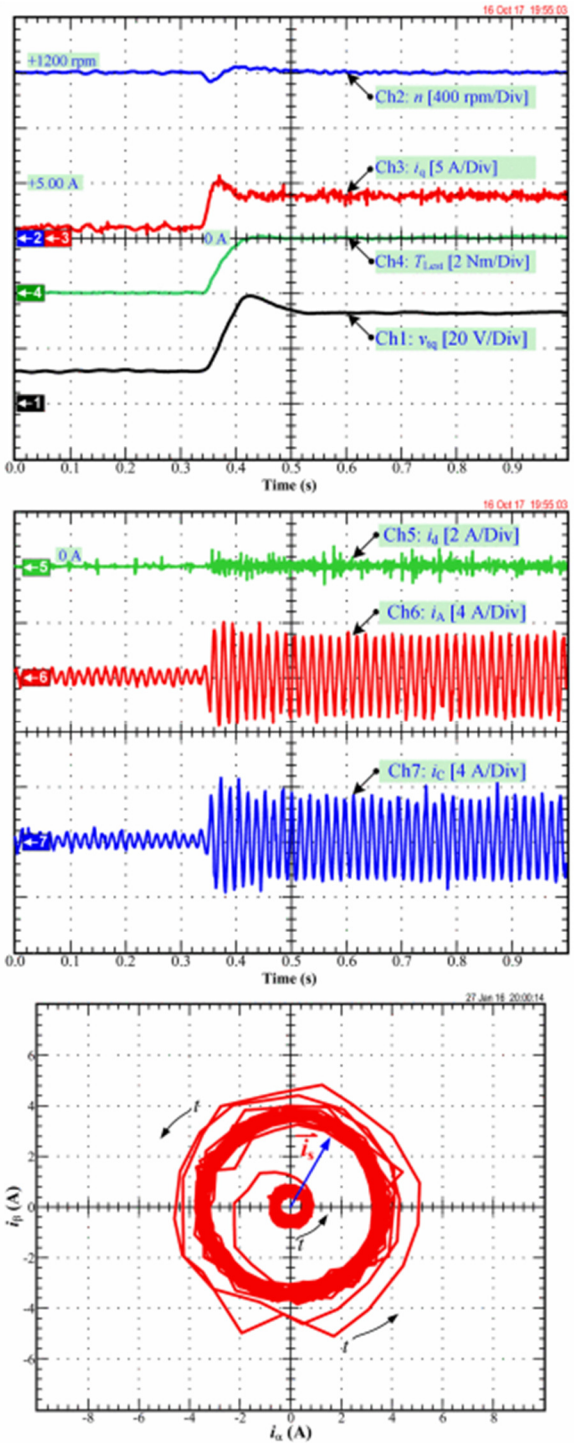

Figure 3.28 Experimental results: Disturbance rejection of the differential flatness-based control based on the Luenberger state observer.

3.6.5.2. Performance of Disturbance Rejection

The experimental results during the load torque step are shown in Figure 3.28. The oscilloscope waveforms show the speed measurement n, the q-axis current i_q, the d-axis current i_d, the estimated torque load T_{Lest}, v_{tq}, the phase currents i_A, i_C, and the trajectories of the transient stator current vector. The results reflect that the proposed control algorithm shows good stability and satisfactory performance of the speed/torque regulations.

3.6.6. Nonlinear Online Parameter Estimation

This section will introduce a Lyapunov-based observer to deal with the parameter estimation of nonlinear a class of nonlinear systems. The proposed observer is dedicated to the class of the nonlinear systems as the following expression [76] [78] [79]-[82]

$$\begin{aligned}\dot{\mathbf{X}} &= \begin{pmatrix}\dot{x}\\ \dot{d}\end{pmatrix} = \begin{pmatrix} f(x,u)+g(x,u)\cdot d \\ 0 \end{pmatrix} \\ \mathbf{Y} &= x\end{aligned} \tag{3.82}$$

where:

$\dot{x}\in\mathbb{R}^n$ is the vector of the state variables. Every state variable is supposed to be measured (i.e., $\mathbf{Y}=x$) $d\in\mathbb{R}^m$ is the vector of unknown parameters to be estimated. Vector d is supposed to be slowly variable. f and g are known nonlinear functions of x and u (command signal vector), respectively, of size $\mathbb{R}^n$ and $\mathbb{R}^m$

3.6.6.1. Lyapunov-based design of the state observer

The system represented in (3.82) is called asymptotically stable at an equilibrium point x_e if its solution x(t) starting from any initial condition, in the vicinity of the equilibrium point, satisfies $x(t)\to x_e$ as $t\to\infty$. By considering the estimation errors expressed in

$$e_x = \hat{x} - x \tag{3.83}$$

$$e_d = \hat{d} - d \tag{3.84}$$

$$\begin{pmatrix}\dot{\hat{x}}\\ \dot{\hat{d}}\end{pmatrix} = \begin{pmatrix} f(x,u)+g(x,u)\cdot\hat{d}-\mathbf{S}_1\cdot e_x \\ -g^T(x,u)\cdot e_x \end{pmatrix} \tag{3.85}$$

where

$\mathbf{S}_1$ is positive-definite square matrix bling to $\mathbb{R}^{n\times n}$

To analyze the stability of the observer, let us consider the derivative of the errors represented in (3.83) and (3.84) are

$$\begin{aligned}\dot{e}_{\mathrm{x}} &= g(x,u)\cdot e_{\mathrm{d}} - \mathbf{S}_1 e_{\mathrm{x}} \\ \dot{e}_{\mathrm{d}} &= -g^T(x,u)\cdot e_{\mathrm{x}}\end{aligned} \tag{3.86}$$

The asymptotic stability of the proposed system can be studied using the following Lyapunov function candidate

$$V = \frac{1}{2}\cdot\begin{pmatrix} e_{\mathrm{x}} & e_{\mathrm{d}}\end{pmatrix}\cdot\begin{pmatrix} e_{\mathrm{x}} \\ e_{\mathrm{d}}\end{pmatrix} \geq 0 \tag{3.87}$$

The derivative of V can be expressed as

$$\dot{V} = e_{\mathrm{x}}^T\cdot\dot{e}_{\mathrm{x}} + e_{\mathrm{d}}^T\cdot\dot{e}_{\mathrm{d}} \tag{3.88}$$

By substituting (3.83), (3.84), and (3.86) into (3.88), it yields

$$\dot{V} = e_{\mathrm{x}}^T\cdot g(x,u)\cdot e_{\mathrm{d}} - e_{\mathrm{x}}^T\cdot\mathbf{S}_1\cdot e_{\mathrm{x}} + e_{\mathrm{d}}^T(-g(x,u)\cdot e_{\mathrm{x}}) \tag{3.89}$$

It yields

$$\dot{V} = -e_{\mathrm{x}}^T\cdot\mathbf{S}_1\cdot e_{\mathrm{x}} < 0 \tag{3.90}$$

So, from (3.87) and (3.90), the asymptotic stability of the observer can be ensured by $\mathbf{S}_1$, which is a positive-definite matrix.

3.6.6.2. Exponential stability of the proposed observer

The system represented in (3.82) is called exponentially stable at an equilibrium point if its solution $x(t)$ starting from any initial condition satisfies [76], [82]

$$\|x\| \leq \mathrm{K}e^{-rt}\|x(0)\|, \forall t \geq 0 \tag{3.91}$$

for some constant **K**, r > 0.

By referring to (3.83) and (3.84), the exponential stability of the proposed observer is defined by (3.92)

$$\begin{pmatrix}\dot{\hat{x}} \\ \dot{\hat{d}}\end{pmatrix} = \begin{pmatrix} f(x,u) + g(x,u)\cdot\hat{d} - \mathbf{S}_2\cdot e_{\mathrm{x}} \\ \mathbf{K}_{\mathrm{p}}\cdot\dot{e}_{\mathrm{x}} + \mathbf{K}_{\mathrm{i}}\cdot e_{\mathrm{x}} - g^T(x,u)\cdot e_{\mathrm{x}}\end{pmatrix} \tag{3.92}$$

with:

$\mathbf{S}_2$ is the positive-definite matrix of size $\mathbb{R}^{n\times n}$.

P is the positive-definite matrix of size $\mathbb{R}^{n\times n}$.

and

$$\mathbf{K}_{\mathrm{p}} = -\mathbf{P}\cdot g^{-1}(x,u) \tag{3.93}$$

$$\mathbf{K}_{\mathrm{i}} = \mathbf{K}_{\mathrm{p}} \cdot \mathbf{S}_2 \tag{3.94}$$

It can be seen that the inverse of matrix $g(x,u)$ is required to calculate matrices $\mathbf{K}_{\mathrm{P}}$ and $\mathbf{K}_{\mathrm{i}}$. If g(x,u) is not a square matrix, its left-inverse must be used:

$$g_L^{-1} \cdot g = I_m$$

where I_m is $m \times m$ an identity matrix. It should be noted that in the case of systems where g is a constant matrix, the estimation of parameter d is made by a simple PI-type estimator. This much simplifies the implementation of the observer on a digital controller.

To demonstrate the exponential convergence of the observer, the derivative of estimation errors e_{x} and e_{d} are calculated:

$$\dot{e}_{\mathrm{x}} = \dot{\hat{x}} - \dot{x} = g(x,u) \cdot e_{\mathrm{d}} - \mathbf{S}_2 \cdot e_{\mathrm{x}} \tag{3.95}$$

$$\dot{e}_{\mathrm{d}} = \dot{\hat{d}} - \dot{d} = \mathbf{K}_{\mathrm{p}} \cdot g(x,u) \cdot e_{\mathrm{d}} - \mathbf{K}_{\mathrm{p}} \cdot \mathbf{S}_2 \cdot e_{\mathrm{x}} + \mathbf{K}_{\mathrm{i}} \cdot e_{\mathrm{x}} - g^t(x,u) \cdot e_{\mathrm{x}} \tag{3.96}$$

Then, the same Lyapunov function candidate as in (3.87) is defined. Its derivative is:

$$\dot{V} = e_{\mathrm{x}}^t \cdot g(x,u) \cdot e_{\mathrm{d}} - e_{\mathrm{x}}^t \cdot \mathbf{S}_2 \cdot e_{\mathrm{x}} + e_{\mathrm{d}}^t \cdot \mathbf{K}_{\mathrm{p}} \cdot g(x,u) \cdot e_{\mathrm{d}} - e_{\mathrm{d}}^t \cdot \mathbf{K}_{\mathrm{p}} \cdot \mathbf{S}_2 \cdot e_{\mathrm{x}} + e_{\mathrm{d}}^t \cdot \mathbf{K}_{\mathrm{i}} \cdot e_{\mathrm{x}} - e_{\mathrm{d}}^t \cdot g^t(x,u) \cdot e_{\mathrm{x}} \tag{3.97}$$

By rewriting (3.93) and (3.94) as in (3.98) and (3.99), and substituting to (3.96)

$$\mathbf{K}_{\mathrm{p}} \cdot g(x,u) = -\mathbf{P} \tag{3.98}$$

$$\mathbf{K}_{\mathrm{i}} = \mathbf{K}_{\mathrm{p}} \cdot \mathbf{S}_2 \tag{3.99}$$

It yields

$$\dot{V} = \begin{pmatrix} e_{\mathrm{x}} & e_{\mathrm{d}} \end{pmatrix} \cdot \begin{pmatrix} -\mathbf{S}_2 & 0 \\ 0 & -\mathbf{P} \end{pmatrix} \cdot \begin{pmatrix} e_{\mathrm{x}} \\ e_{\mathrm{d}} \end{pmatrix} \tag{3.100}$$

From (3.87) and (3.100), it can be written:

$$\dot{V} = \leq -a \cdot V \tag{3.101}$$

where -a < 0 is the largest eigenvalue of the matrix diag(-**S**, -**P**). in conclusion, the convergence of the estimated parameters is exponential as long as **S** and **P** are positive-define matrices. The largest eigenvalue of **S** and **P** determines the convergence rate. In practice, the eigenvalues of **S** are set to be highly greater than those of **P** the ensure that the dynamics of the state variables error e_{x} is highly faster than that of the unknown parameters error e_{d}.

3.6.7. Validation of the proposed observer for SPMSM

This section provides the validation of the proposed nonlinear estimation method. The proposed nonlinear observer will be compared to the Luenberger observer. To achieve a valuable comparison, the parameters of each estimator have been tuned practically to obtain the best performance.

3.6.7.1. Observer design for SPMSM

Referring to the SPMSM model in equation (3.75), before presenting unknown parameters $d = [v_{tq}\ T_L]^T$ estimation, their observability must be verified since it is proposed to estimate them through the above state observer. For this purpose, the extended state vector is defined as $x = [x_1\ x_2\ x_3\ x_4]^T = [i_q\ \omega_m\ v_{tq}\ T_L]^T$ and output vector y includes i_q and ω_m. Then:

$$\mathbf{P}_o = \begin{bmatrix} x_1 \\ x_2 \\ \dot{x}_1 \\ \dot{x}_2 \end{bmatrix} = \begin{bmatrix} \frac{v_q}{L_s} - \frac{x_3}{L_s} - \frac{\omega_e \Psi_m}{L_s} \\ \frac{n_p \Psi_m x_1}{J} - \frac{x_4}{J} - \frac{B_f x_2}{J} \\ x_3 \\ x_4 \end{bmatrix} \tag{3.102}$$

Local observability depends on the Jacobian matrix of the output vector **P**o. This matrix, called the observability matrix, is full rank for the studied system. Therefore, the system is locally observable: rank(Jacobian(**P**o)) = dim(x) = 4. [84]

For developing the proposed state observer, the SPMSM is written in the form of (3.82) as follows:

$$f(x,u) = \begin{bmatrix} \frac{v_q}{L_s} - \frac{x_3}{L_s} - \frac{n_p \cdot x_2 \cdot \Psi_m}{L_s} \\ \frac{n_p \cdot \Psi_m \cdot x_1}{J} - \frac{x_4}{J} - \frac{B_f \cdot x_2}{J} \end{bmatrix} \tag{3.103}$$

$$g(x,u) = \begin{bmatrix} -\frac{1}{L_s} & 0 \\ 0 & -\frac{1}{J} \end{bmatrix}$$

As the state-space model of the system can be put under the form of (3.82), the observers (3.85) and (3.92) are feasible. Furthermore, it is worth noting that the matrix g is constant.

For the observer (3.85), the matrix $\mathbf{S}_1$ must be determined. After trial and error, we use the following matrix in simulation and experimentation:

$$S_1 = \begin{bmatrix} 50 & 0 \\ 0 & 330 \end{bmatrix} \tag{3.104}$$

For the observer (3.92), the matrices $\mathbf{S}_2$ and **P** are determined by (3.105) to achieve exponential convergence. Here, we will use the following matrices:

$$\mathbf{S}_2 = \begin{bmatrix} 300 & 0 \\ 0 & 300 \end{bmatrix} \tag{3.105}$$

$$\mathbf{P} = \begin{bmatrix} 1 & 0 \\ 0 & 10 \end{bmatrix}$$

3.6.7.2. Simulation and experimental results

Simulation and experimental tests have been realized to test the effectiveness of the developed observers. The details of the test bench were mentioned in **Section 3.3.1,** and the SPMSM parameters and its controller gains are given in Table 3.1 and Table 3.2. The proposed controller is implemented on a dSPACE DS1104 board, with a time step of Ts = 100 μs. The dynamics of the three estimators have been experimentally tuned to obtain the best performance possible. This trial-and-error tuning resulted in the previously mentioned matrices $\mathbf{S}_1$, $\mathbf{S}_2$, and $\mathbf{P}$.

Figure 3.29 shows the obtained results with Luenberger observer, observer (3.85), and observer (3.92). First, for the case a Luenberger observer is implemented, Figure 3.29(a) shows the simulation and experimental results when a load torque disturbance of 2 Nm occurs between 0.1 s and 0.6 s. The speed reference is set to 1200 rpm. As can be seen in this figure, the disturbance is quickly rejected thanks to the estimation of the load torque provided by the Luenberger observer, which is used in the flatness-based speed controller. Furthermore, the simulation and experimental results are very similar and indicate both the effectiveness of the proposed approach with a disturbance rejection time of around 0.1 s.

Next, for the case of the observer (3.85), Figure 3.29(b) shows the simulation and experimental results under the same conditions as mentioned above. It can be noticed that the load torque disturbance is effectively rejected even more quickly than in the previous case. Indeed, the disturbance rejection time is less than 0.08 s with the observer (3.85).

Finally, Figure 3.29(c) shows the simulation and experimental results for the case where the observer (3.92) is implemented. The speed control performance is improved in this case as the disturbance rejection time is much shorter than the previous cases and is close to 0.04 s. This conclusion has been confirmed by experimentation, too.

It can be seen that under the action of the observer (3.92), the least deviation from the set-point is noticed when the load torque changes suddenly, and the motor speed is recovered faster compared to the other cases. As a result, the speed control loop performance is better with the observer (3.92). Indeed, the estimation of the load torque becomes much faster with this observer thanks to the PI nature of the observer (3.92), while Luenberger observer and observer (3.85) are of an integral type which introduces a lag in the estimation (compare Ch4 green waveforms). This can be clearly seen in the estimated load torques that the last observer provides the quickest convergence thanks to its additional proportional action without introducing more noises.

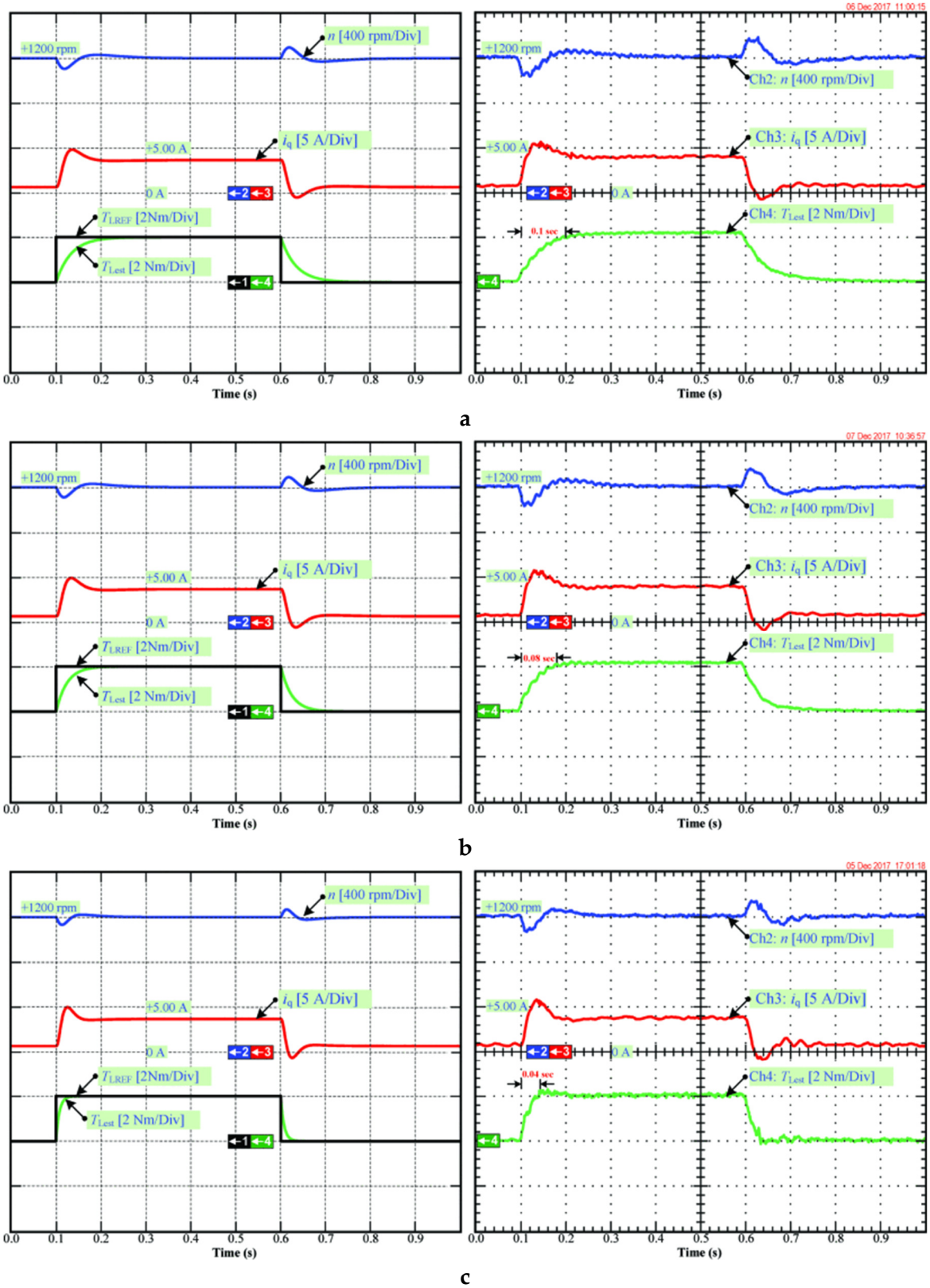

Figure 3.29 Simulation (left) and experimental (right) results: Comparison between the different state observers.

In conclusion, it can be claimed that the differential flatness-based control using online parameter estimation shows high performance in the speed control of SPMSM compared to the traditional FOC with PI controller. Among different online estimators, the PI-type observer (3.92) has an exponential convergence and provides the highest performance in load torque disturbance rejection.

3.6.7.3. Variable loss estimation

The other parameter to be estimated online is v_{tq}. It represents electrical losses in the motor drive, which are a nonlinear function of the operating point. In this section, the interest in online estimation of v_{tq} is studied through experimental tests. Figure 3.30 illustrates the system's response, including the estimation of v_{tq}. Ch1 is the voltage v_{tq}, assumed as the voltage drop across power devices and winding of the machine, Ch2 is the measured speed, Ch3 is the q-axis current i_q, and Ch4 is the estimated external load torque T_{Lest}, Ch5 is the d-axis current i_d, Ch6 and Ch7 are the currents of phase A and C i_A, i_C, and the stator current reference frame vector trajectories are shown in the last figure. The results reflect that the online estimation of v_{tq} works well, and this information is relevant to be used in the flatness-based current controller to compensate for the effect of variable losses in the system.

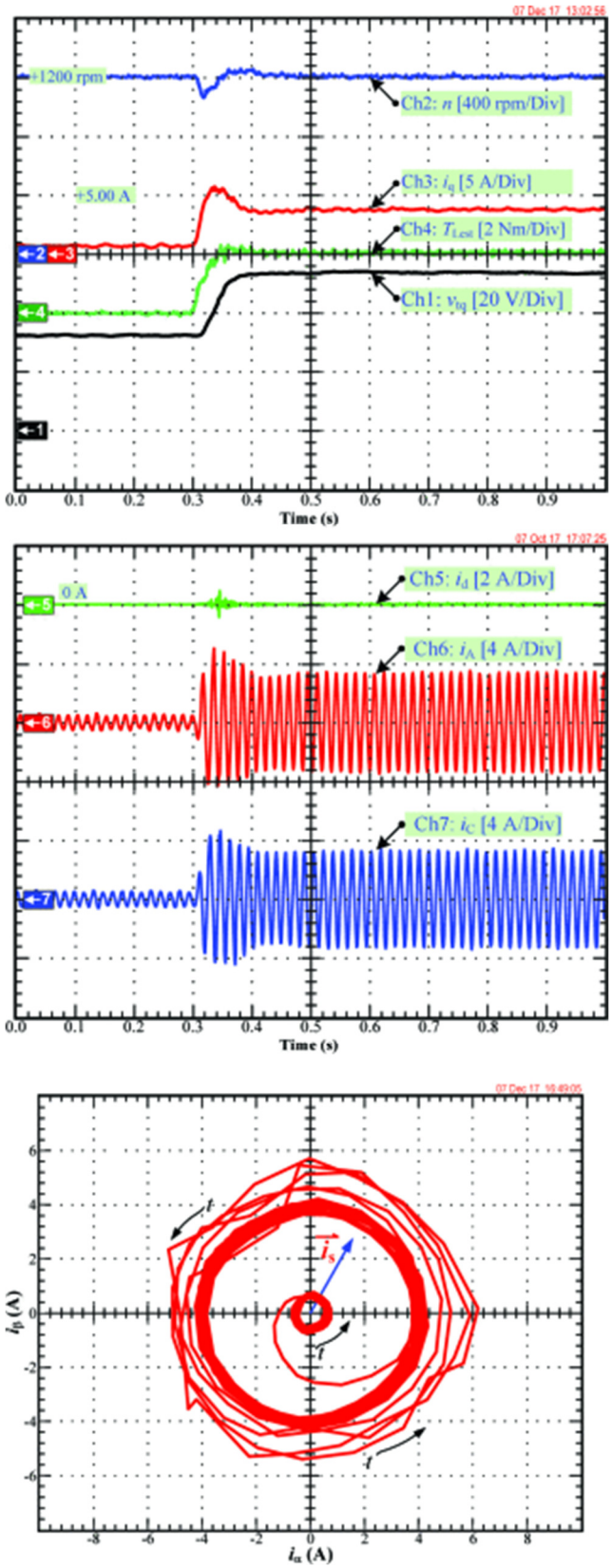

Figure 3.30 Experimental results: Dynamic performance of the external disturbance rejection.

3.6.8. Validation of the proposed observer for PMa-SynRM

As mentioned earlier in Section 3.6.4., the PMa-SynRM is nonlinear, impacting the estimation effectiveness and performance. Therefore, in this section, the proposed PI-type state observer is applied to estimate variable electrical losses through v_{td} and v_{tq} and variable load torque. The knowledge of these latter is required in the flatness-based controller to improve the closed-loop performance of the motor drive.

3.6.8.1. Observer design for PMa-SynRM

First, we analyze the local observability of the unknown parameters $d = [v_{td}\ v_{tq}\ T_L]^T$. For this purpose, we consider the state variable $x = [x_1\ x_2\ x_3\ x_4\ x_5\ x_6]^T = [i_d\ i_q\ \omega_m\ v_{td}\ v_{tq}\ T_L]^T$ and the output vector y includes id, iq and ω_m. This leads to the following vector **P**o:

$$\mathbf{P}_o = \begin{bmatrix} x_1 \\ x_2 \\ x_3 \\ \dot{x}_1 \\ \dot{x}_2 \\ \dot{x}_3 \end{bmatrix} = \underbrace{\begin{bmatrix} \frac{v_d}{L_d} - \frac{x_4}{L_d} + \frac{n_p \cdot x_3 \cdot (L_q \cdot x_2 - \Psi_m)}{L_d} \\ \frac{v_q}{L_q} - \frac{x_5}{L_q} - \frac{n_p \cdot x_3 \cdot L_d \cdot x_1}{L_q} \\ \frac{n_p \left\{ \Psi_m \cdot x_1 + (L_d - L_q) \cdot x_2 \cdot x_1 \right\}}{J} - \frac{B_f \cdot x_3}{J} \\ x_4 \\ x_5 \\ x_6 \end{bmatrix}}_{f(x,u)} \tag{3.106}$$

The rank of the Jacobian matrix of the output vector **P**o is full. Therefore, the unknown parameters are locally observable.

The PMa-SynRM model, written in (3.82), is given in (3.107) to develop the proposed state observer. The model is written under the required form for the observer. Then, matrices $\mathbf{S}_2$ and **P** must be determined before defining $\mathbf{K}_p$ and $\mathbf{K}_i$ from (3.93) and (3.94). Here, we used trial and error to determine $\mathbf{S}_2$ and **P** given in (3.108).

$$f(x,u)=\begin{bmatrix} \dfrac{v_{\mathrm{d}}}{L_{\mathrm{d}}}-\dfrac{x_4}{L_{\mathrm{d}}}+\dfrac{n_p x_3(L_{\mathrm{q}}x_2-\Psi_{\mathrm{m}})}{L_{\mathrm{d}}} \\ \dfrac{v_{\mathrm{q}}}{L_{\mathrm{q}}}-\dfrac{x_5}{L_{\mathrm{q}}}-\dfrac{n_p x_3 L_{\mathrm{d}} x_1}{L_{\mathrm{q}}} \\ \dfrac{n_{\mathrm{p}}\left\{\Psi_{\mathrm{m}}x_1-(L_{\mathrm{d}}-L_{\mathrm{q}})x_2x_1\right\}}{J}-\dfrac{B_{\mathrm{f}}x_3}{J} \end{bmatrix} \tag{3.107}$$

$$g(x,u)=\begin{bmatrix} -\dfrac{1}{L_d} & 0 & 0 \\ 0 & -\dfrac{1}{L_q} & 0 \\ 0 & 0 & -\dfrac{1}{J} \end{bmatrix}$$

$$\mathbf{S}_2=\begin{bmatrix} 1 & 0 & 0 \\ 0 & 500 & 0 \\ 0 & 0 & 3000 \end{bmatrix}, \tag{3.108}$$

$$\mathbf{P}=\begin{bmatrix} 0.5 & 0 & 0 \\ 0 & 10 & 0 \\ 0 & 0 & 100 \end{bmatrix}$$

3.6.8.2. Simulation of the proposed observer applied to PMa-SynRM

Figure 3.31 shows the simulation results of the differential flatness-based control with the state observer (3.92) applied to a PMa-SynRM. The simulation conditions are set as follows: given speed: n = 1000 rpm; a sudden increase of 4 Nm on the load torque at 0.3 s, running with load until 0.7 s, and clearing the load after. It can be seen that under the action of the proposed observer, when the load changes suddenly, the motor speed drops by 20 rpm, which is much less than 35 rpm obtained by Luenberger reduced-order observer in Section 3.6.4 (see Ch4 the green waveform). This performance is due to the fast dynamic of the load torque estimation with the proposed observer (Ch5 the green waveform) compared to the case of the Luenberger observer (Ch6 the black waveform). As a result, the speed control loop performance is meaningfully improved.

Other tests have been performed to evaluate the effect of the estimation of v_{td} and v_{tq} on the current control performance. Figure 3.32 shows the transient response of the resistance variation simulation. In Figure 3.32, Ch4 is the voltage v_{td}, assumed as the voltage drop across the power electronic devices and winding in the d-axis, Ch1 is the estimated voltage of the v_{td} (named v_{tdest}). Ch3 is the voltage v_{tq}, represented the voltage drop across the power electronic devices and winding in the q-axis, and Ch2 is the estimated voltage of the v_{tq} (named v_{tqest}). Additionally, in Figure 3.32, Ch5 is the measured q-axis current, Ch6 is the q-axis current reference i_{qREF}. Ch7 is the d-axis current reference i_{dREF}, and Ch8 is the measured d-axis current.

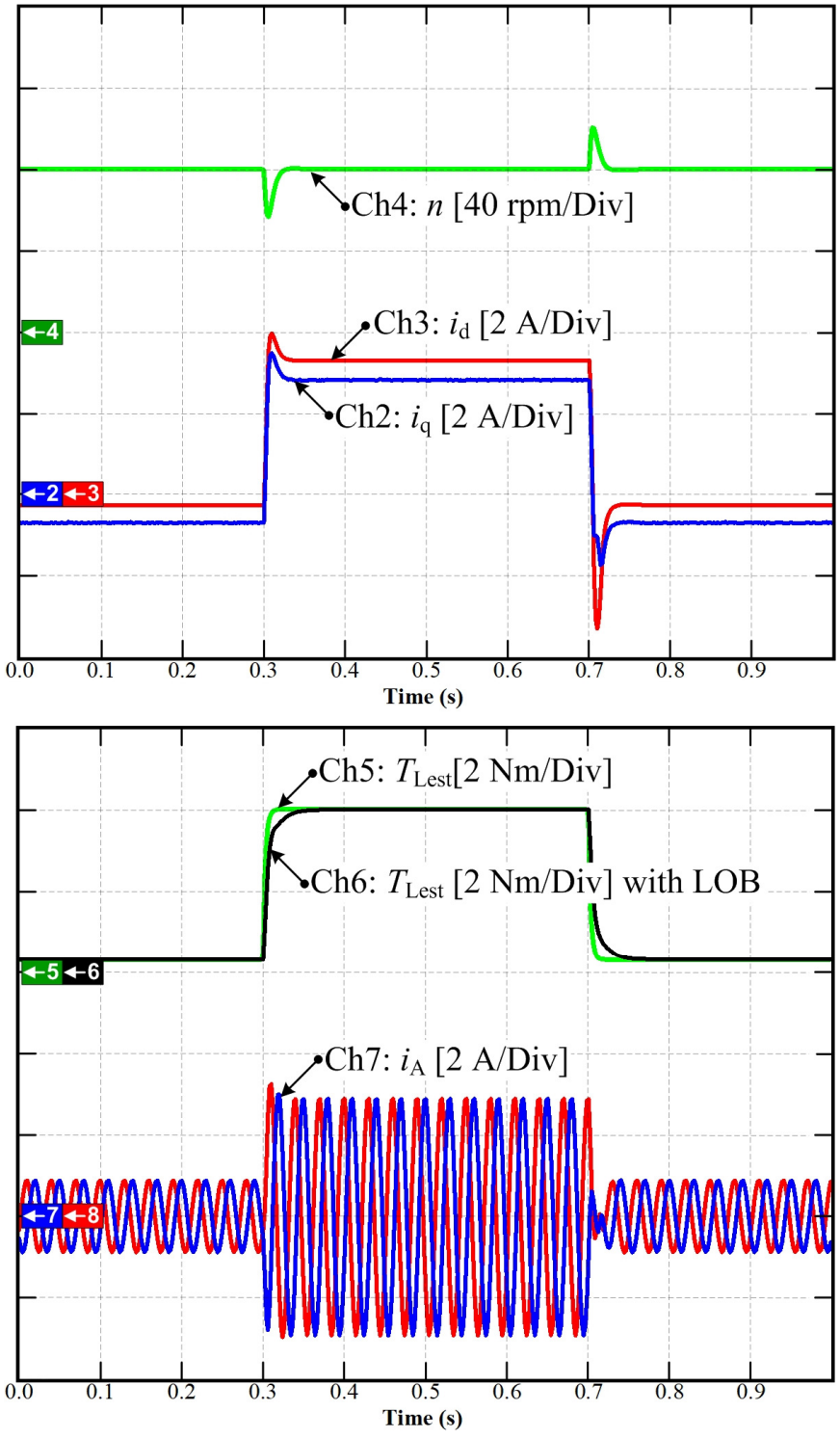

Figure 3.31 Simulation results: Dynamic performance of the external disturbance rejection.

The voltage drops v_{td} and v_{tq} cannot be accurately verified on the experimental setup as they are related to unlumped elements, and their measurement requires comprehensive test campagne. However, the estimated efficiency can be used as a means to assess the effectiveness of the estimated voltage drops. In the meantime, this assessment can be done through

simulations. Indeed, the results shown in Figure 3.32 confirm that v_{td} and v_{tq} are well estimated as the estimated values converge to the actual ones with a response time of 0.01 s.

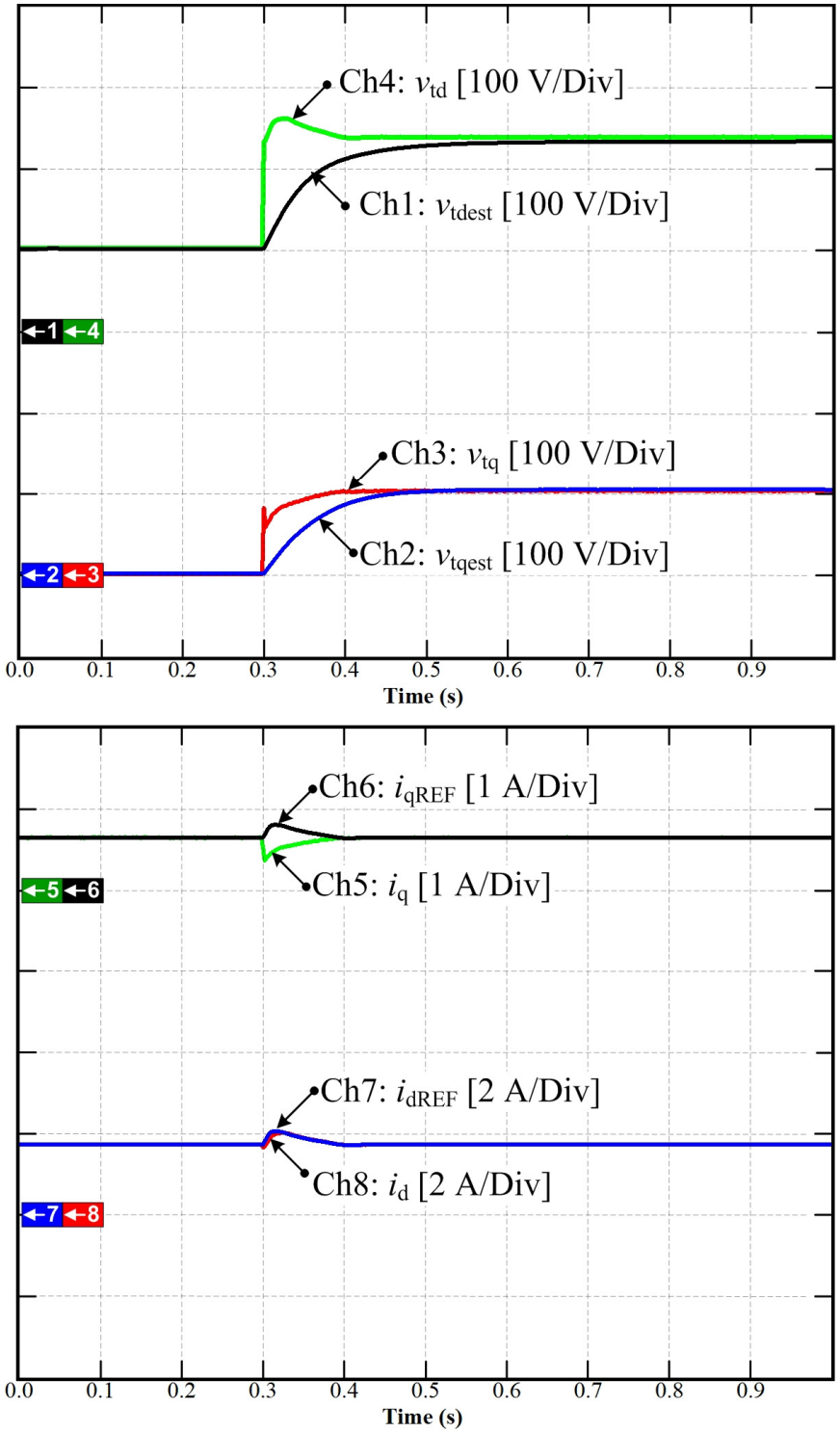

Figure 3.32 Simulation results: Dynamic performance of parameter variation.

3.6.8.3. Experimental validation of the proposed observer applied to the PMa-SynRM

The PMa-SynRM parameters and its flatness-based controller gains are given in Tables 3.3 and 3.4. The controller and the observer are implemented on a MicroLab Box dSPACE board with a time step of Ts = 62.5 μs. The laboratory test-bed with a PMa-SynRM is shown in Figure 3.13.

Figure 3.33 shows the experimental responses of the differential flatness-based control with the proposed observer (3.92) applied to a PMa-SynRM drive. The condition of the experimental test is set as follows: given speed n = 1000 rpm; sudden additional load torque of 4 Nm at 0.5 s. In Figure 3.33(a), Ch1 is the speed reference n_{REF}, Ch4 is the measured speed n, and Chs 2 and Ch3 are the q-axis current i_q and d-axis current i_d, from the MTPA lookup table as described in Section 2.9.2. Additionally, in Figure 3.33(b), Ch1 is the measured load torque provided by the mechanical load torque sensor. Ch4 is the estimated load torque T_{Lest}, and Chs 2 and 3 are the d- and q-axis currents. To complete this test, a second test has been performed where the load torque is cleared at 0.5 s. Figure 3.34 shows the corresponding experimental responses. Scope channels are assigned to the same measurements as in Figure 3.33.

As can be seen in these figures, the measured speed is disturbed only for a short time. In fact, the recovery time is approximately 0.02 s. This good performance is due to the fast estimation of the load torque by the proposed observer. The PI nature of the observer improves the convergence time without increasing the observer gains. These results are relevant to those obtained by simulation (see Figure 3.31) and consistent with the theoretical analysis in Section 3.6.8.1. These results show that the proposed observer enables to improve the disturbance rejection capability of the flatness-based controller.

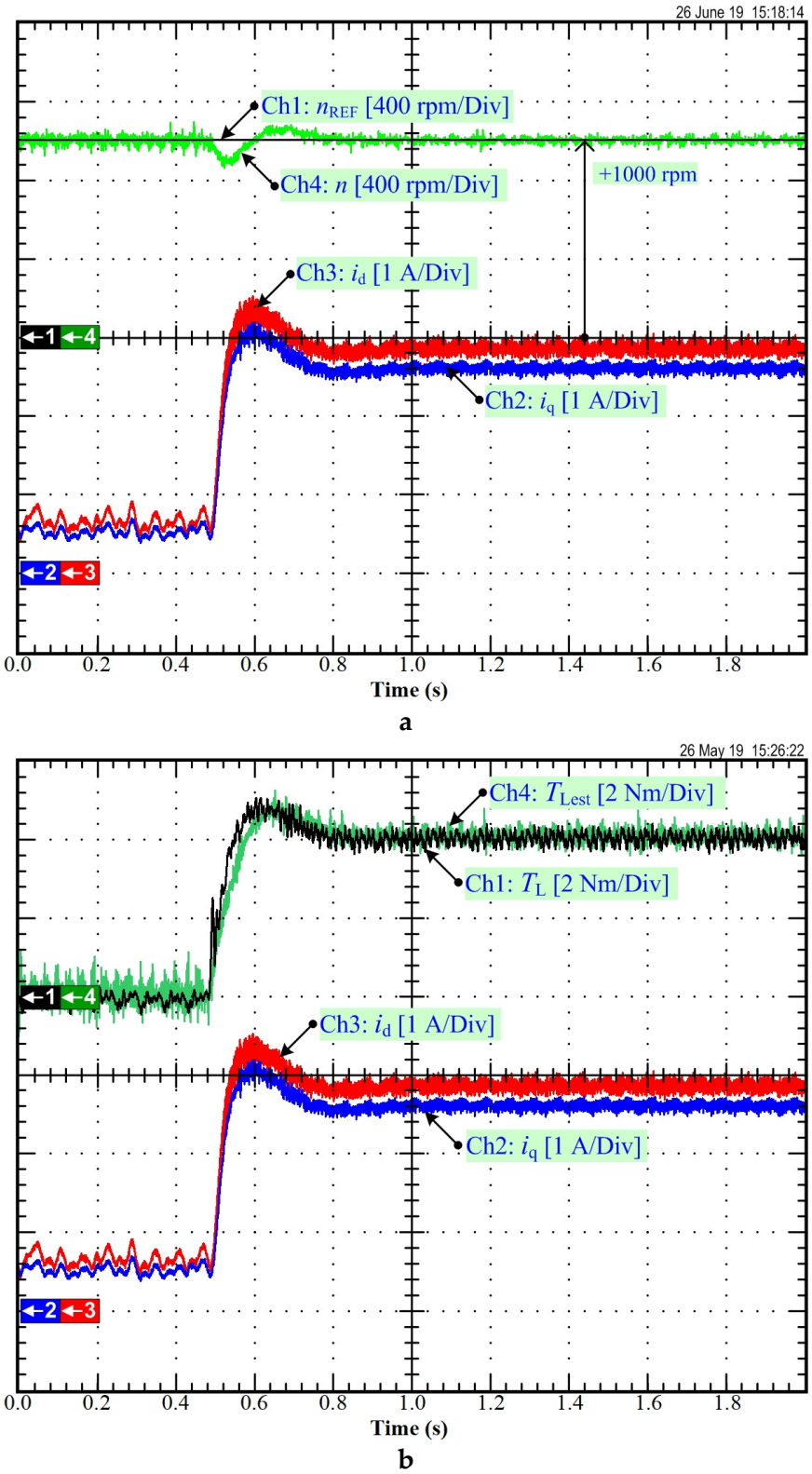

Figure 3.33 Experimental results: Dynamic performance of the external disturbance rejection during suddenly adding load torque.

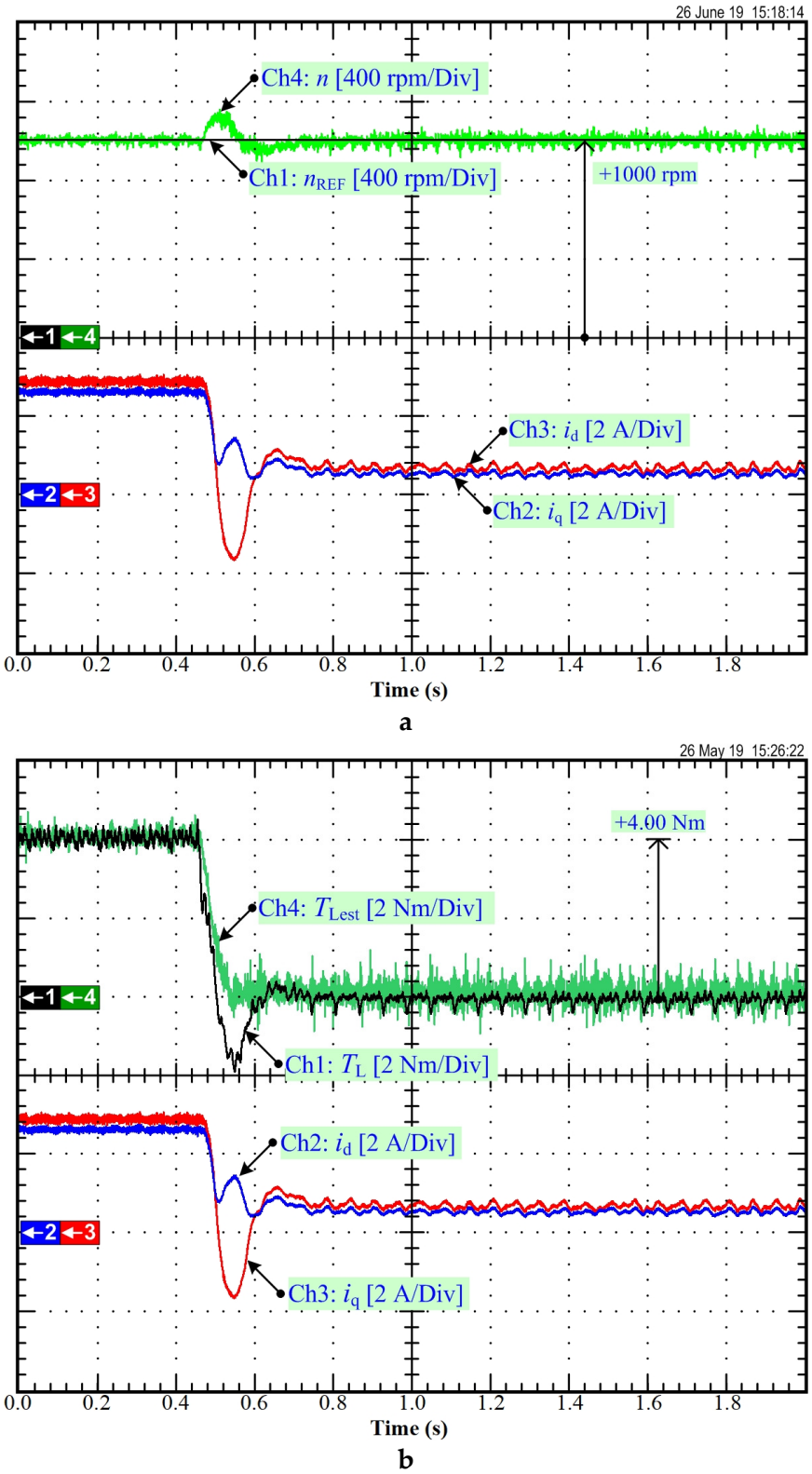

Figure 3.34 Experimental results: Dynamic performance of the external disturbance rejection during suddenly removing load torque.

3.7. Conclusion

This chapter proposed a differential flatness-based controller and an online state observer for parameter estimation for motor drive applications. It has been shown that the differential flatness-based control provides high-performance for both SPMSM and PMa-SynRM drives. In fact, compared to the FOC with the traditional PI controller, the differential flatness-based control, with an additional observer, can notably improve the control performance of the speed and current loops. The role of the observer is to provide compensation terms required in the flatness-based control. Different observers can be considered for this purpose. First, a Luenberger observer was designed and implemented experimentally. Then, another observer for a class of nonlinear systems was developed, and its convergence was proved using the Lyapunov stability theorem. Finally, the previous observer was extended to include a proportional action enabling the exponential convergence of the observer. All the above-mentioned observers have been successfully implemented and tested on SPMSM and PMa-SynRM. The performance of the differential flatness-based control depends tightly on the observer employed for estimating unknown parts of the model, which should be compensated. Among the developed observers, the last one, of PI-type, shows the best performance as it provides a fast estimation of load torque disturbance and electrical losses.

In summary, this chapter showed the effectiveness of flatness-based control in controlling electric motor drives. This model-based approach requires an accurate model. In case the model is not perfectly known, the estimation of the unknown part is necessary to achieve expected high performance. In the next chapter, another control approach will be tentatively applied to the control of SPMSM and PMa-SynRM. This approach, called model-free control, does not require an accurate model. Indeed, only very limited knowledge of the controlled system is enough to generate the control action. The advantages and drawbacks of this controller will be discussed, and its performance will be compared to the flatness-based controller in the next chapter.

Chapter-4 MODEL-FREE CONTROL

Contents

Introduction …… --
4.1. A shot briefly model-free control and control law
4.1.1. Model-Free Control briefly:
4.1.2. Control law and Intelligent PI Controller
4.1.3. Controller design
4.2. Applying Model-Free Control to SPMSM Drive
4.2.1. Model-Free Control of SPMSM: development
4.2.2. Trajectory Planning
4.3. Simulation and Experimental Validation of Model-Free Control Applied to SPMSM
4.3.1. Test Bench Setup
4.3.2. Simulation
4.3.3. Experimental validation of SPMSM drive based on the Model-Free Control
4.4. Applying Model-Free Control to PMa-SynRM Drive
4.4.1. Model-Free Control of PMa-SynRM driving development
4.4.2. Trajectory Planning
4.5. Simulation and experimental validation of the model-free control applied to PMa-SynRM
4.5.1. Test Bench Setup
4.5.2. Simulation
4.5.3. Experimental validation of PMa-SynRM drive based on the Model-Free Control
4.6. Conclusion

Introduction

With the emergence of the modern controls to develop for industrial application [85] [86], all these control theories were proposed by relying on the fact that the mathematical model or the precise model of the controlled plant is accurately available, also called Model-Based Control (MBC) approaches. Many effective MBC methods have been developed for many industrial applications in the last decades. For example, the optimal control and linear-quadratic regular (LQR) design are standard control systems designed for linear systems. In addition, the Lyapunov-based schemes include sliding mode, passivity-based control method, backstepping control, feedback linearization, adaptive control theory, estimation theory, optimal control theory. Besides, the predictive control algorithm such as finite control set model predictive control (FCS-MPC) [88]-[89] [90] [91] is dedicated to the nonlinear system. Furthermore, the differential flatness-based control proposed in the previous chapter is devoted to nonlinear systems.

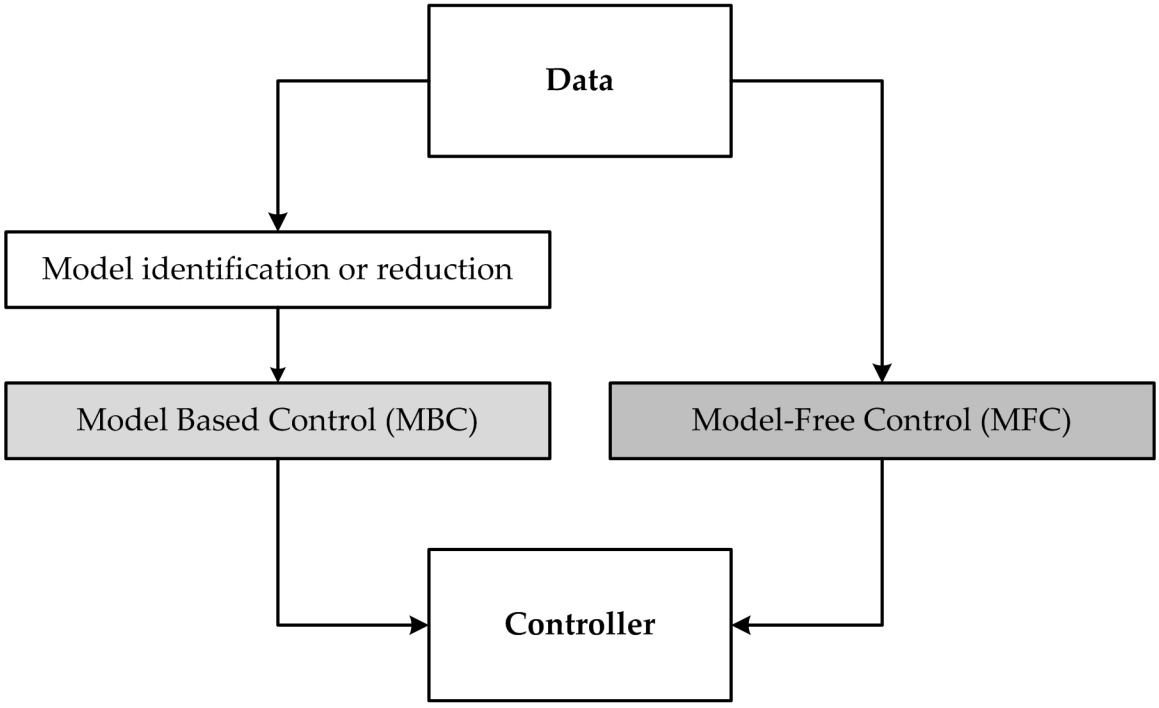

Figure 4.1 Architecture of MBC and Model-Free Control (MFC) block diagram.

Looking to the typical structure of MBC, presented in Figure 4.1 (on the left side), the mathematical model of the studied system plays a crucial role in this control design method. Relying on this fact, the control performance, safety, and reliability of MBC methods are highly dependent on the correctness of the system model used in the control design procedure. However, on the other hand, the uncertainties, parameter variation, and unmodelled dynamics are unavoidable phenomena in industrial applications and always exist. Since these factors are not considered in a mathematical model, they may affect the control system and lead to inevitable performance degradation [91]. The standard methods for the improvement of robustness include adaptive control, robust control, disturbance/ uncertainty estimation, and attenuation-based control [92] [93] (e.g., disturbance observer [94], nonlinear disturbance observer [95], sliding

mode disturbance observer [96], and active disturbance rejection control [97]). However, adding the observer makes the inevitable whole bandwidth degradation of the system. Therefore, although a reasonable control based on MBC of PMSMs has been introduced in previous publications, it remains challenging to obtain a control system with high performance due to its nonlinear property and parameter uncertainty conditions.

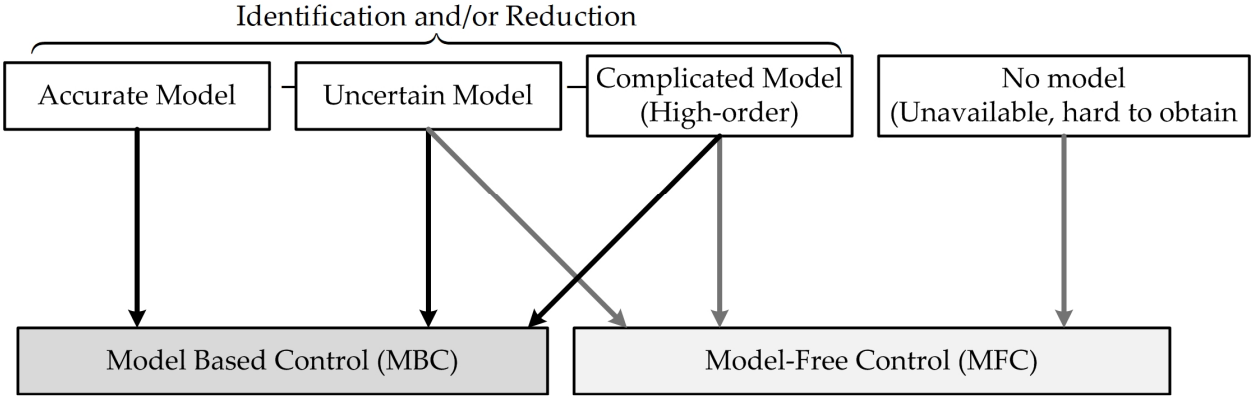

Figure 4.2 Categorization of the modern control system into MBC and MFC [97].

Many industrial applications have significantly changed with technology development and become more complex systems. Accordingly, modeling the dynamic and process of these applications using the mathematical models becomes very difficult or at least time-consuming. In this case, using the MBC methods for these kinds of applications will be impossible. Conversely, almost all industrial applications generate and save a large number of process data that contains all the necessary information related to the system's operation. In this case, it is of high importance to use these generated data, obtained online/offline, directly for designing the controller or other purposes. In this way, the Model-Free Control (MFC) foundation, as represented in Figure 4.1 (on the right side) theory, is essential in the control of industrial applications. So far, the types of the modern control system can be roughly categorized by MBC and MFC, as in Figure 4.2.

The MFC is a control method that uses only the online data obtained from the controlled system to design the controller without the additional need for information about the mathematical model or parameters of the studied system [98]. Thus, this method can be applicable for all nonlinear systems with complex or unknown structures.

This chapter introduces model-free control to deal with those mentioned above. Fliess et al. proposed its concept performed with control system application [99] [100]. This benefit is that it does not need all the system's parameters. Also, it does not use the decoupling term for PMSM control compared to conventional control like field-oriented control based on the traditional PI controller. Moreover, its control of law and stability is not complicated to design and prove. Finally, to validate the model-free control, the SPMSM and PMa-SynRM model drive will be performed to achieve high performance and improve robustness.

4.1. A shot briefly model-free control and control law

4.1.1. Model-free control briefly:

The concept of model-free based control performed for the control system application was first presented by Fliess et al. [99] [100]-[102]. A brief theory of model-free control is provided as follows. A nonlinear system given by a state-variable expression is

$$\begin{aligned} \dot{x} &= f(x,u) \\ y &= h(x,u) \end{aligned} \tag{4.1}$$

where

$$\begin{aligned} x &= \left[x_1, x_2, ..., x_n \right]^T ; x \in \mathbb{R}^n \\ u &= \left[u_1, u_2, ..., u_m \right]^T ; u \in \mathbb{R}^m \\ y &= \left[y_1, y_2, ..., y_m \right]^T ; y \in \mathbb{R}^m \end{aligned} \tag{4.2}$$

x is the state variable, u is the control variable, y is the measurable variable (or output variable), and n, $m \in$ N.

A system is flat if we can find a set of flat outputs (equal in number to the number of inputs). More precisely, if the system has state variables $x \in \mathbb{R}^n$ and input variables $u \in \mathbb{R}^m$, thus, if there exists a set of flat outputs $y \in \mathbb{R}^m$, the system is flat, as mentioned in Section 3.1.1 of Chapter 3.

A control can be defined as:

$$u = u_{ref} + u_{feedback}(\varepsilon) \tag{4.3}$$

with

$$u_{ref} = \psi(y_{ref}, \dot{y}_{ref}, \ddot{y}_{ref}, ..., y_{ref}^{(\beta+1)}) \tag{4.4}$$

and

$$u_{feedback} = K_p \cdot \varepsilon + K_i \int \varepsilon dt \tag{4.5}$$

where

$$\varepsilon = y_{ref} - y \tag{4.6}$$

ε is the error between the desired value and the measured value.

According to (4.3), this control law is suitable for wholly known all parameters system. However, if only some system parameters can be identified, the controller needs to be modified as the partial-known model, replaced by the model-free control as given in (4.7).

$$u = \frac{\hat{\alpha}(y, \dot{y}, \ddot{y}, ..., y^{(n)})}{b} + \frac{F}{b} \tag{4.7}$$

Alternatively, it can be rewritten and rearranged as a straightforward linear model as follows:

$$\dot{y} = -F + b \cdot u \tag{4.8}$$

where $\hat{\alpha}(y, \dot{y}, \ddot{y}, ..., y^{(\beta+1)})$ is known part of the $\alpha(y, \dot{y}, \ddot{y}, ...y^{(\beta+1)})$ and F stands for all the other dynamics of the system [72].

4.1.2. Control law and Intelligent PI Controller

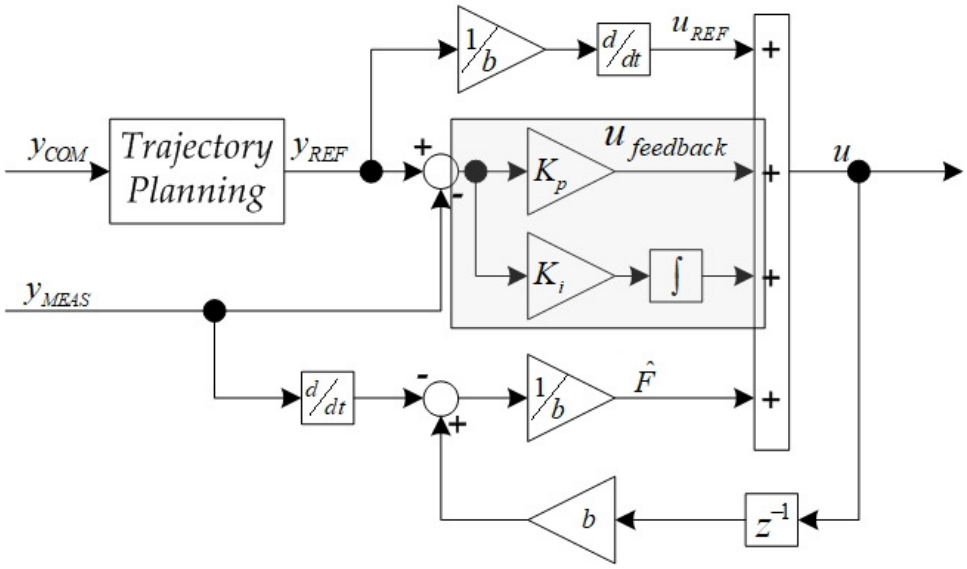

Figure 4.3 Control law of MFC.

Figure 4.3 represents the block diagram of the control law for model-free control. The control law defines as follows:

$$u = u_{\text{ref}} + u_{\text{feedback}}(\varepsilon) + \frac{\hat{F}}{b} \tag{4.9}$$

with

$$u_{\text{ref}} = \frac{\hat{\alpha}\left(y_{\text{ref}}, \dot{y}_{\text{ref}}, \ddot{y}_{\text{ref}}, ...y_{\text{ref}}^{(\beta+1)}\right)}{b} \tag{4.10}$$

and

$\hat{F}$ is the estimated value of F, which is given as:

$$\hat{F} = b \cdot u - \dot{y} \tag{4.11}$$

The feedback part u_{feedback} is given by applying PI controller as follows:

$$u_{\text{feedback}} = K_{\text{p}} \cdot \varepsilon + K_{\text{i}} \int \varepsilon dt \tag{4.12}$$

Substituting (4.9) into (4.8) and rearrangement, (4.8) can be rewritten as:

$$\dot{y} = -F + b \cdot u_{\text{ref}} + b \cdot u_{\text{feedback}}(\varepsilon) + \hat{F} \tag{4.13}$$

4.1.3. Controller design

The estimation term aims to provide an estimated value $\hat{F}$ so that $\hat{F} \to F$ as $t \to \infty$ (under global convergence assumption for the estimation) Therefore, (4.13) can be rewritten as follows:

$$\dot{y} = b \cdot u_{\text{ref}} + b \cdot u_{\text{feedback}}(\varepsilon) \tag{4.14}$$

Consequently, (4.14) stands for the dynamic of the closed-loop control system. Substituting (4.12) into (4.14) and rearrangement, (4.14) can be given as:

$$\frac{d(y_{ref} - y)}{dt} + b \cdot K_{\text{p}} \cdot \varepsilon + b \cdot K_{\text{i}} \int \varepsilon dt = 0 \tag{4.15}$$

According to the control law block diagram in figure 4.3, the controller coefficients can be determined using the following expression obtained by taking time derivation of (4.15).

$$\ddot{\varepsilon} + b \cdot K_{\text{p}} \cdot \dot{\varepsilon} + b \cdot K_{\text{i}} \cdot \varepsilon = 0 \tag{4.16}$$

Comparing (4.17) to the second-order standard equation expressed as

$$\ddot{q} + 2 \cdot \zeta \cdot \omega_n \cdot \dot{q} + \omega_n^2 \cdot q = 0 \tag{4.17}$$

The controller coefficients are given as:

$$K_{\text{p}} = \frac{2 \cdot \zeta \cdot \omega_{\text{n}}}{b} \tag{4.18}$$

and

$$K_{\text{i}} = \frac{\omega_{\text{n}}^2}{b} \tag{4.19}$$

where ζ and ωn are the desired dominant damping ratio and natural frequency.

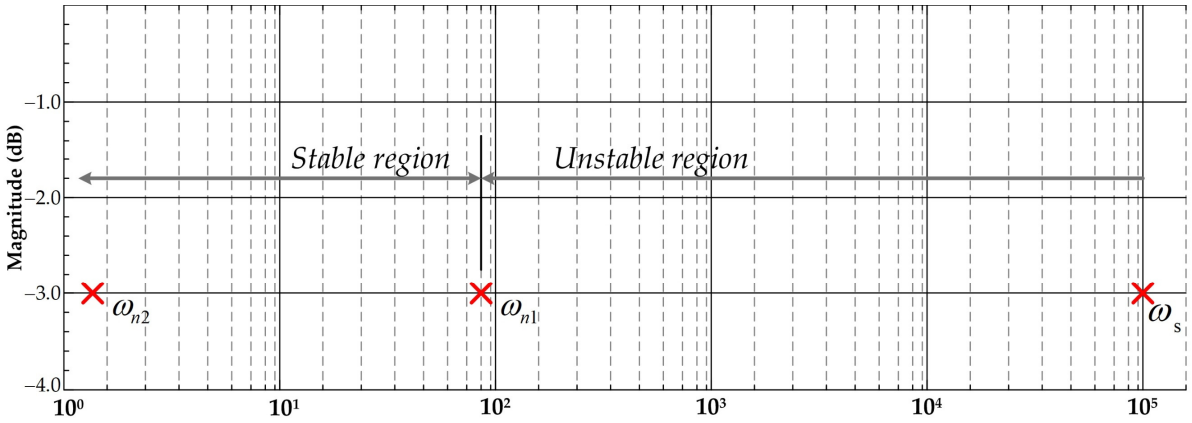

Figure 4.4 The natural frequency setting of the proposed MFC.

Note that to preserve the stability of the closed-loop system, roots of (4.17) must be placed in the stable region shown in Figure 4.4. This is done either using an expert's knowledge or by trial and error.

4.2. Applying model-free control to SPMSM drive

The SPMSM drive system is presented in Figure 4.5, and its state-space representation model is represented in (2.47). The control system of the model-free control for the SPMSM is illustrated in Figure 4.5.

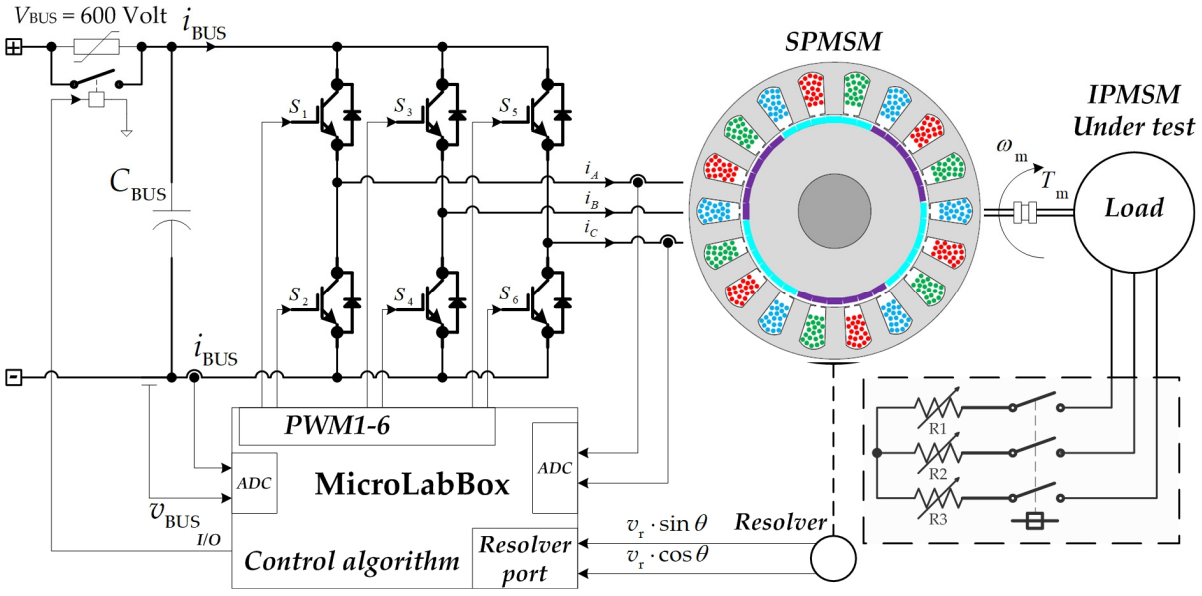

Figure 4.5 SPMSM drive system based on model-free control diagram.

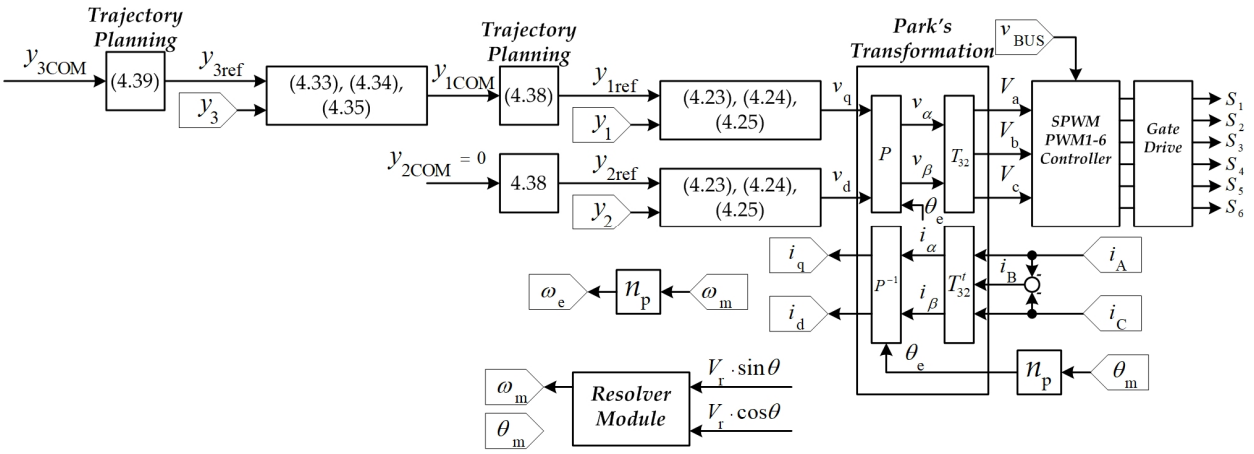

Figure 4.6 Control system of SPMSM based on model-free control diagram.

4.2.1. Model-free control of SPMSM: development

As mentioned in Section 2.9.1, SPMSM is a non-salient poles machine such that torque producing is along the q-axis proportional to i_q and keeps the d-axis current to zero in order to reach maximum efficiency. Besides the $L_s = L_d = L_q$ is defined as in Section 2.4.1.

As shown in Figure 4.6, the control system has a case cascade construction consisting of two loops (i.e., inner current control loop and outer speed control loop). The inner current loop is much faster than the outer speed control loop such that the model-free control for the current control is developed first.

By defining $u = [u_1\ u_2]^T = [v_d\ v_q]^T$, $y = [y_1\ y_2]^T = [i_d\ i_q]^T$, and rearranging of (2.47) in the form of (4.8), the SPMSM model is given as in (4.20).

$$\begin{aligned}\frac{di_d}{dt} &= -\frac{R_s i_d}{L_s} + \frac{\omega_e L_s i_q}{L_s} + v_d \cdot \frac{1}{L_s} \\ \frac{di_q}{dt} &= -\frac{R_s i_q}{L_s} - \frac{\omega_e (L_s i_d + \Psi_m)}{L_s} + v_q \cdot \frac{1}{L_s}\end{aligned} \tag{4.20}$$

Equation (4.20) can be separated to identify the known and unknown parts as in the following expression. The known parts are

$$\begin{aligned}\hat{\varphi}_1 &= \frac{\dot{y}_1}{b_1} = L_s \frac{di_d}{dt} \\ \hat{\varphi}_2 &= \frac{\dot{y}_2}{b_1} = L_s \frac{di_q}{dt}\end{aligned} \tag{4.21}$$

and unknown parts are

$$F_1 = \left(-R_s i_d + \omega_e L_s i_q\right) \cdot \frac{1}{L_s}$$
$$F_2 = \left(-R_s i_q - \omega_e (L_s i_d + \Psi_m)\right) \cdot \frac{1}{L_s} \tag{4.22}$$

According to the control law (Figure 4.3), each part of the model-free control for inner current loop control is determined as:

$$u_{1ref} = \frac{\dot{y}_{1ref}}{b_1} = L_s \frac{di_d}{dt}$$
$$u_{2ref} = \frac{\dot{y}_{2ref}}{b_2} = L_s \frac{di_q}{dt} \tag{4.23}$$

The estimation of unknown parts is given as:

$$\widehat{F}_1 = \frac{1}{L_s} u_1 - \dot{y}_1 = \frac{1}{L_s} v_d - \frac{di_d}{dt}$$
$$\widehat{F}_2 = \frac{1}{L_s} u_2 - \dot{y}_2 = \frac{1}{L_s} v_q - \frac{di_q}{dt} \tag{4.24}$$

The feedback parts of *d*- and *q*-axis current control are obtained in the following expression.

$$b_1 \cdot u_{1feedback} = b_1 \left(K_{pd} \cdot \varepsilon_d + K_{id} \int \varepsilon_d dt\right)$$
$$b_2 \cdot u_{2feedback} = b_2 \left(K_{pq} \cdot \varepsilon_q + K_{iq} \int \varepsilon_q dt\right) \tag{4.25}$$

Referring to the design procedure in Section 4.1.3, (4.25) can be rewritten and rearranged as follows:

$$\ddot{\varepsilon}_d + b_1 \cdot K_{pd} \cdot \dot{\varepsilon}_d + b_1 \cdot K_{id} \cdot \varepsilon_d = 0$$
$$\ddot{\varepsilon}_q + b_2 \cdot K_{pq} \cdot \dot{\varepsilon}_q + b_2 \cdot K_{iq} \cdot \varepsilon_d = 0 \tag{4.26}$$

The controller coefficients K_{pd}, K_{id}, K_{pq}, and K_{iq}, are determined as:

$$K_{pd} = \frac{2 \cdot \zeta_1 \cdot \omega_{n1}}{b_1}, K_{id} = \frac{\omega_{n1}^2}{b_1}$$
$$K_{pq} = \frac{2 \cdot \zeta_1 \cdot \omega_{n1}}{b_2}, K_{iq} = \frac{\omega_{n1}^2}{b_2} \tag{4.27}$$

Here, the second model-free control for the outer speed control loop is developed. The output of the speed control loop provides the reference of the q-axis current i_q according to the mechanical equation in (2.40). From (2.40) in Chapter 2, the developed torque of the SPMSM is proportional to q-axis current as of the following definition.

$$T_e = K_t \cdot i_q \tag{4.28}$$

where K_t is defined as the torque constant, that is $K_t = n_p \Psi_m$.

Therefore, T_e is chosen as the control variable of the outer speed control loop that $u_3 = T_e$. And then rewriting the mechanical equation of SPMSM in the form of (4.8) is given as:

$$\frac{d\omega_m}{dt} = \left(-B_f \cdot \omega_m - T_L\right) \cdot \frac{1}{J} + T_e \cdot \frac{1}{J} \tag{4.29}$$

Separating (4.29) into the known part and unknown parts is given as follows:
The known part is

$$\hat{\phi}_3 = \frac{\dot{y}_3}{b_3} = J\frac{d\omega_m}{dt} \tag{4.30}$$

where

$$b_3 = \frac{K_t}{J} \tag{4.31}$$

and unknown part is

$$F_3 = \left(-B_f \cdot \omega_m - T_L\right) \cdot \frac{K_t}{J} \tag{4.32}$$

Each part of the Model-Free Control for the outer speed control loop is defined as the following expression.

$$u_{3ref} = \frac{\dot{y}_{3ref}}{b_3} = J\frac{d\omega_m}{dt} \tag{4.33}$$

The estimation of the unknown part is

$$\hat{F}_3 = \frac{K_t}{J} u_3 - \dot{y}_3 = \frac{K_t}{J} \cdot i_q - \frac{d\omega_m}{dt} \tag{4.34}$$

$$b_3 u_{3feedback} = b_3 \left(K_{p\omega} \cdot \varepsilon_\omega + K_{i\omega} \int \varepsilon_\omega dt\right) \tag{4.35}$$

Referring to the design procedure in Section 4.1.3, (4.35) can be rewritten and rearranged as follows:

$$\ddot{\varepsilon}_{\omega}+b_1\cdot K_{p\omega}\cdot\dot{\varepsilon}_{\omega}+b_1\cdot K_{i\omega}\cdot\varepsilon_{\omega}=0 \tag{4.36}$$

The controller coefficients Kpω and Kiω are determined as:

$$K_{p\omega}=\frac{2\cdot\zeta_2\cdot\omega_{n2}}{b_3},K_{i\omega}=\frac{\omega_{n2}^2}{b_3} \tag{4.37}$$

where ζ_2 and ω_{n2} are the desired dominant damping ratio and natural frequency of the outer speed control loop, respectively.

4.2.2. Trajectory planning

As shown in Figure 4.3, trajectory planning is a crucial part of the model-free control because it makes the input reference y_{REF} continuous. A second-order low-pass filter is often utilized to plan the desired trajectory for the output component. The proposed trajectory planning for the two inner current control loops is:

$$\frac{y_{1REF}}{y_{1COM}}=\frac{y_{2REF}}{y_{2COM}}=1\Big/\left\{\left(\frac{s^2}{\omega_{n3}}\right)+\frac{2\zeta_3}{\omega_{n3}}s+1\right\} \tag{4.38}$$

where ζ3 and ωn3 are the desired dominant damping ratio and natural frequency.

and the trajectory planning of the outer speed loop is

$$\frac{y_{3REF}}{y_{3COM}}=1\Big/\left\{\left(\frac{s^2}{\omega_{n4}}\right)+\frac{2\zeta_4}{\omega_{n4}}s+1\right\} \tag{4.39}$$

where ζ4 and ωn4 are the desired dominant damping ratio and natural frequency of the speed loop trajectory planning.

4.3. Simulation and experimental validation of model-free control applied to SPMSM

4.3.1. Test bench setup

The main SPMSM parameters are presented in Table 2.1 (in Section 2.8), and the model-free controller parameters are defined in Table 4.1. The laboratory setup is shown in Figure 4.7; It is composed of a 6-pole, 1-kW PMSM coupled with a Separate Excited DC motor that serves as a dyno supplying a purely resistive load. The stator windings of the PMSM were fed by a 3Φ dc-ac voltage-source inverter (VSI) that operated at a switching frequency of 10 kHz. The input voltage

is obtained through a diode rectifier or DC sources, as shown in Figure 2.23. The drive system was also equipped with an incremental encoder mounted on the rotor shaft and 4096 lines/revolution resolution. The measurement of the electromagnetic torque was realized by a torque transducer mounted on the rotor shaft. The proposed controller has been implemented on a dSPACE ds1104 board, with a time step of Ts = 1e−4 s.

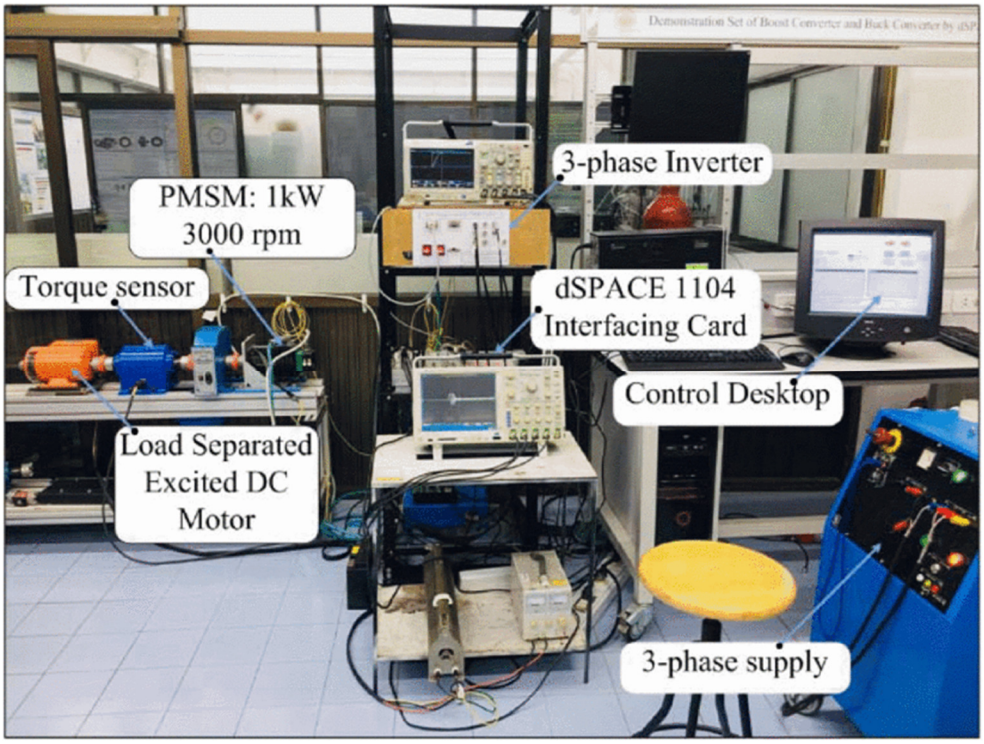

Figure 4.7 Test bench provived at KMUTNB, Bangkok.

TABLE 4.1
Speed and Current regulation parameters of SPMSM drive based on model-free control

Symbol	Meaning	Value
ζ_1	Damping ratio 1	0.7
ω_{n1}	Natural frequency 1	10000 Rad.s^{-1}
ζ_2	Damping ratio 2	0.7
ω_{n2}	Natural frequency 2	150 Rad.s^{-1}
ζ_3	Damping ratio 3	1
ω_{n3}	Natural frequency 3	1000 Rad.s^{-1}
ζ_4	Damping ratio 4	1
ω_{n4}	Natural frequency 4	150 Rad.s^{-1}
I_{dmax}	Maximum *d*-axis current	+6 A
I_{dmin}	Minimum *d*-axis current	-6 A
Vdc	DC bus voltage	600 V
f_s	Switching frequency	10 KHZ

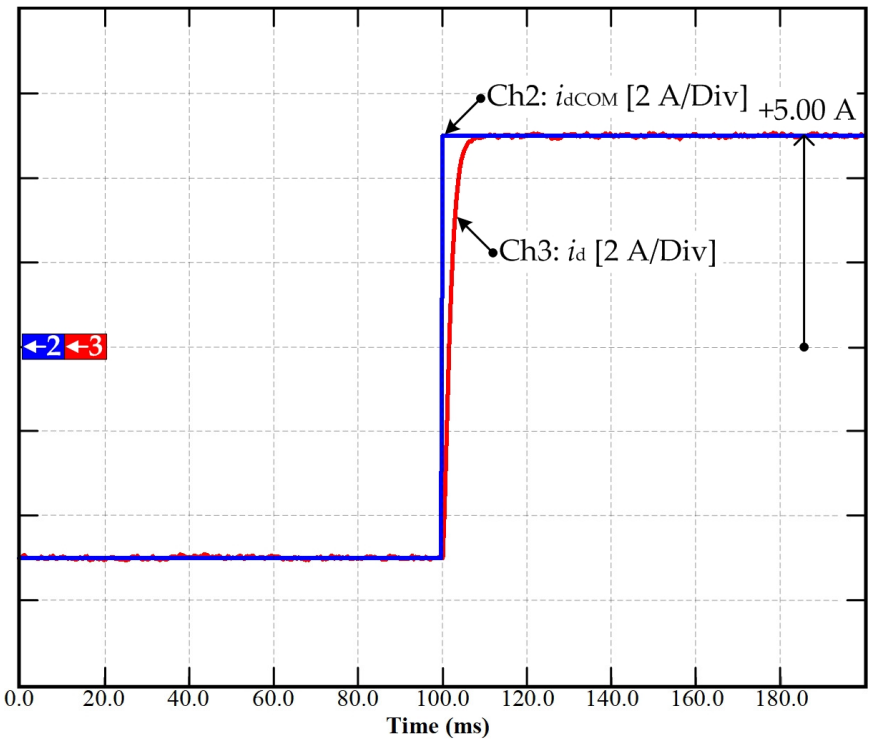

Figure 4.8 Simulation results: Dynamic response of *d*-axis currents with the controller based on the model-free control.

4.3.2. Simulation

Figure 4.8 shows the simulation results of the d-axis inner loop current control response curves based on the model-free control. As it can be distinctively seen, during a transient, the *d*-axis current can track the desired set-point with a short response time and without steady-state error. Note that the simulation condition is set as follows: for *d*-axis testing, the *q*-axis current command i_{qCOM} is set to zero.

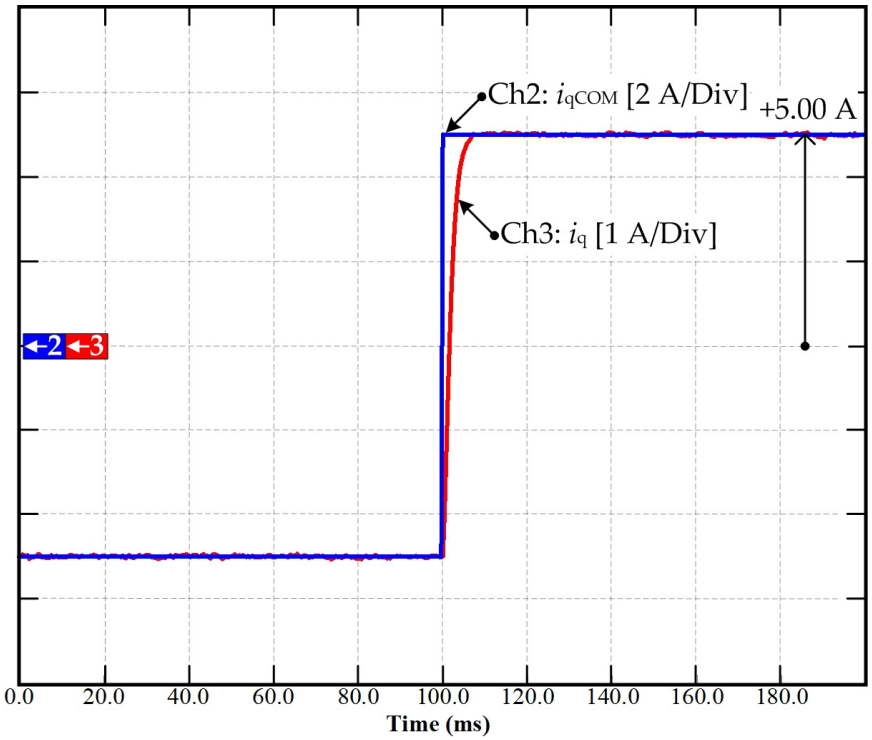

Figure 4.9 Simulation results: Dynamic response of q-axis currents with the controller based on the model-free control.

Figure 4.9 shows the simulation results of the q-axis inner loop current control response curves based on the model-free control. As it can be distinctively seen, during the transient response, the q-axis current reaches its reference in a short time. Furthermore, the tracking performance is satisfactory, where the simulation condition is set as follows: during q-axis testing, the d-axis command i_{dCOM} is set to zero with the rated load.

The developed MFC algorithm has been widely simulated in different operation conditions before its actual implementation. One of the simulation results is shown in Figure 4.10, which shows the drive's response to a pulse speed reference from 500 to 1000 rpm. In Figure 4.10, Chs 1 and 4 are the speed command and measured speed n. Chs 2 and 3 are the d- and q-axis current, and Chs 5 and 6 are the d-axis voltage and q-axis voltage, respectively. The parameters of the simulated drive are those of the test bench that has been used for experimental validation, and they are reported in Section 4.2.1. The MFC has been designed to enforce a current limit of 6A. One can note that the excellent speed response with limited overshoot and without steady-state error. Acceleration and deceleration are limited by the current limitation that affects i_q, while i_d is kept close to zero.

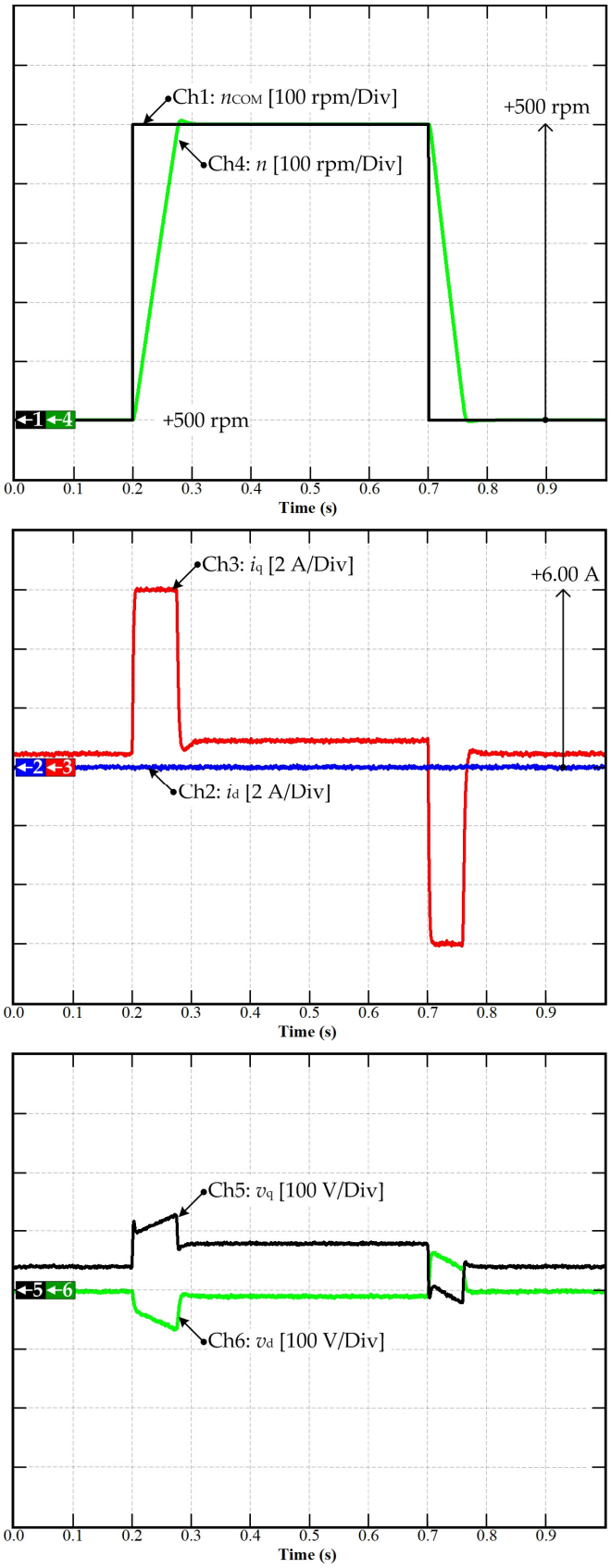

Figure 4.10 Simulation results: Speed acceleration and deceleration.

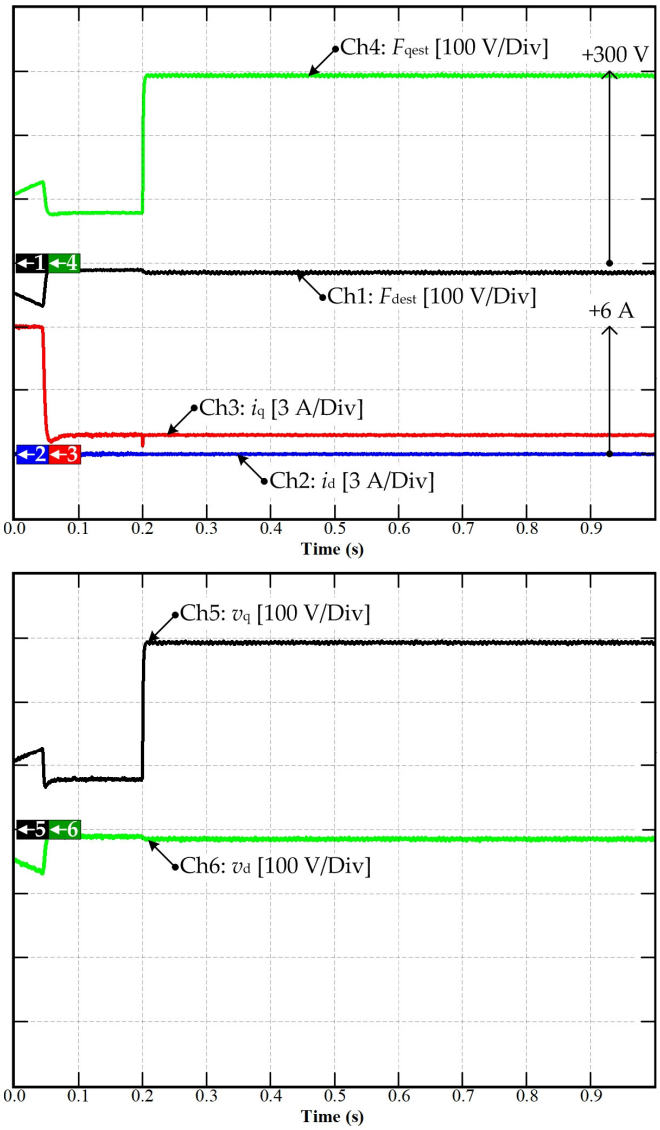

Figure 4.11 Simulation results: *R*s variation.

Simulation has been realized to confirm the validity of the developed state observers and validate the interest of the proposed state observer. Figure 4.11 shows the unknown part estimation of the *d*-axis and *q*-axis, which F_{dest} and F_{qest} represent. In this simulation, estimation is enabled at time t = 0.2 s.

In Figure 4.11, the estimation of the unknown part is verified to converge to an expected value. Indeed, it is essential to test it by simulation since it will not be possible to prove it on the experimental setup as the parameters and voltage drops in the inverter, connectors and cables are not accurately known.

The condition of the simulation is set as follows: given speed n = 1000 rpm; sudden step R_s, which represented the total losses of the voltage drop across power electronic switches and winding $25*R_s$ in 0.2 s, running with this situation to 1 s. During transients, at the time 0.2s, while the *q*-axis voltage is changing, it did not affect the *q*-axis current. That is because the output of v_q

is compensated by estimating unknown part F_{qest}. As a result, it can be seen that the MFC can superiorly manage the external disturbance and uncertainty of the model parameters.

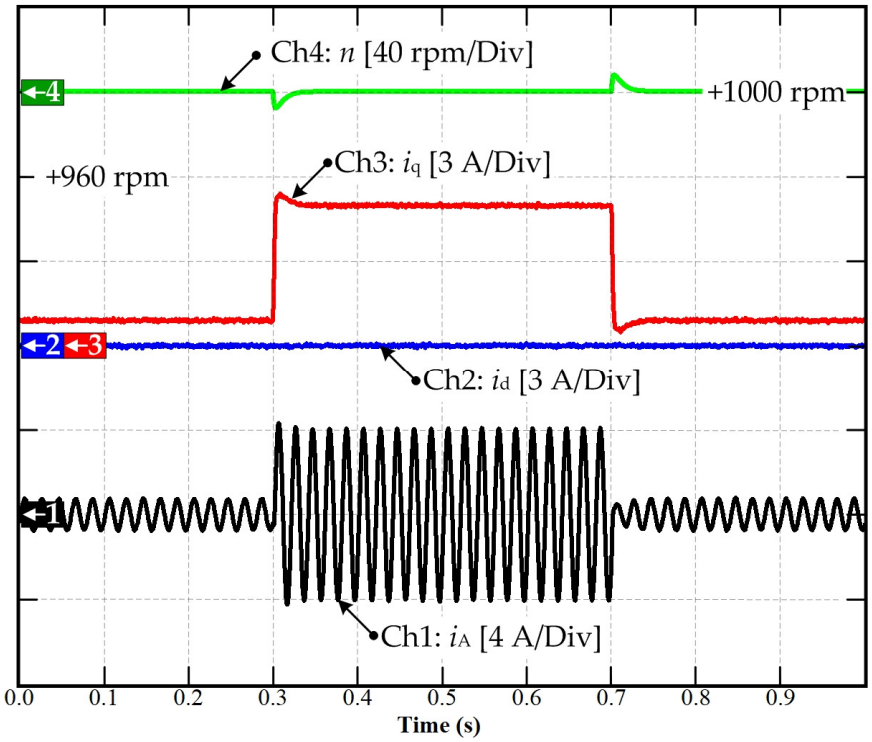

Figure 4.12 Simulation results: Disturbance rejection.

Figure 4.12 shows the simulation of the disturbance rejection ability of the MFC applied to the SPMSM drive. The simulation conditions are set as follows: given speed: n = 1000 rpm; a sudden increase of load torque T_L of 3 Nm in 0.3 s, running with load to 0.7 s, and immediately removing the load torque. It can be seen that under the action of the proposed model-free control, when the load changes suddenly, the motor speed shows a lower overshoot, and the reference speed is recovered in a short interval (see Ch4 the green one). The figure shows the MFC's good capability to limit the torque disturbance effects and achieve zero steady-state speed error. As a result, the speed loop control performance is significantly improved, verifying the feasibility of the proposed MFC.

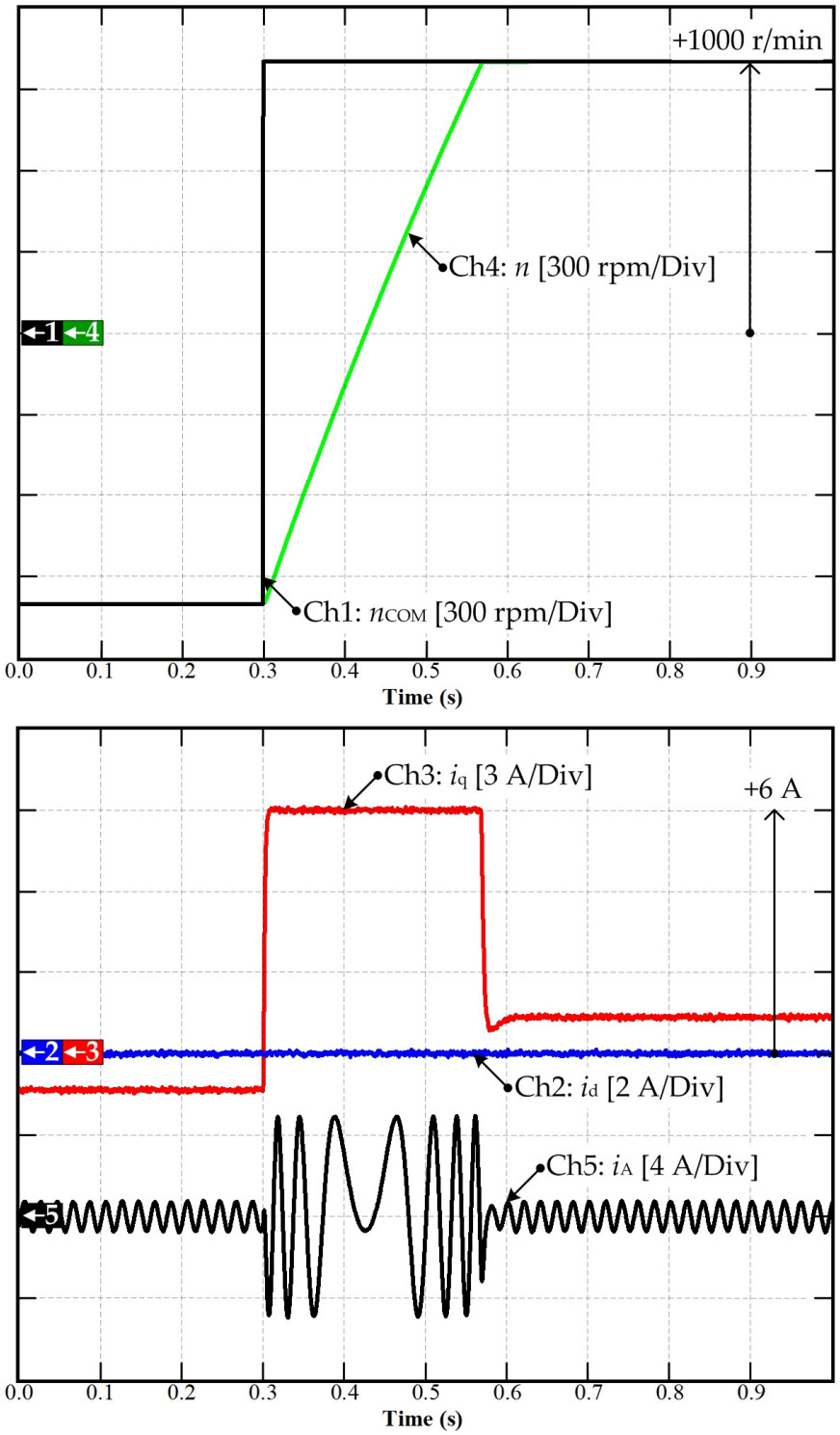

Figure 4.13 Simulation results: Speed reversal.

Figure 4.13 demonstrates the simulation results of the dynamic performance of the proposed MFC when the motor is forced to reverse direction. In Figure 4.13, Chs 1 and 4 are the

speed command n_{COM} and the measured speed n. Chs 2 and 3 are the d- and q-axis currents i_d and i_q and Ch4 is the n_{REF}, Ch4 is the currents of phases A, respectively.

The SPMSM model is performed by MATLAB/SIMULINK software to validate that the proposed control system is appropriately designed. The results depict that the motor operates well in the regenerative mode until the speed reference is positive. Besides, the measured speed can effectively track the reference value. After that, the machine switches to motoring mode until the rotor speed reaches the speed command. The d-and q-axes currents show such good behavior without exceeding its limits. It can be concluded that the proposed control provides satisfying dynamic performance.

4.3.3. Experimental validation of SPMSM drive based on the model-free control

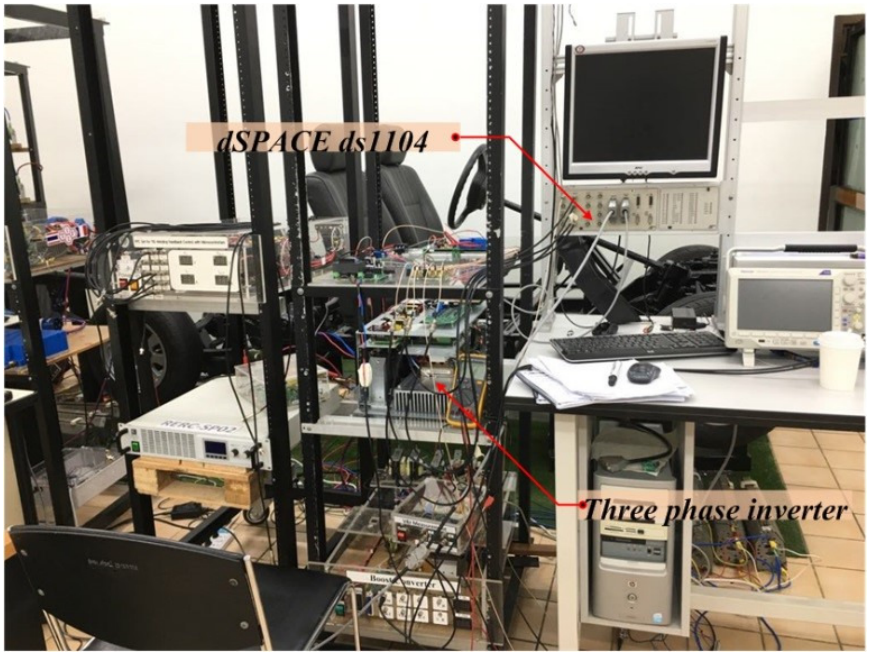

Figure 4.14 Test beach setup for SPMSM drive based on MFC.

TABLE 4.2
SPMSM Parameters for the Model-Free Control development

Symbol	Meaning	Value
P_{rated}	Rated Power	10 kW
n_{rated}	Rated Speed	1500 rpm
n_p	Number of pole pairs	2
R_s	Resistance (Motor + Inverter)	0.8 Ohm
$L_s = L_d = L_q$	Stator inductance	5 mH
Ψ_m	Permanent-magnet flux	0.12 Wb
J	Equivalent inertia	0.002 kg.m2

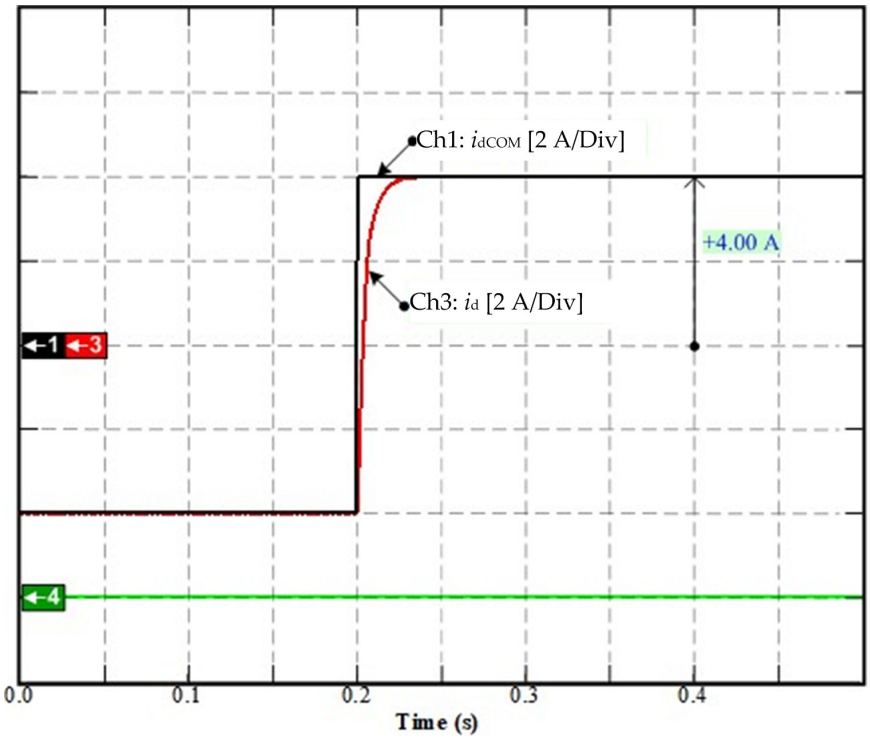

Figure 4.15 Simulation results: *d*-axis current response by FOC based on traditional PI controller.

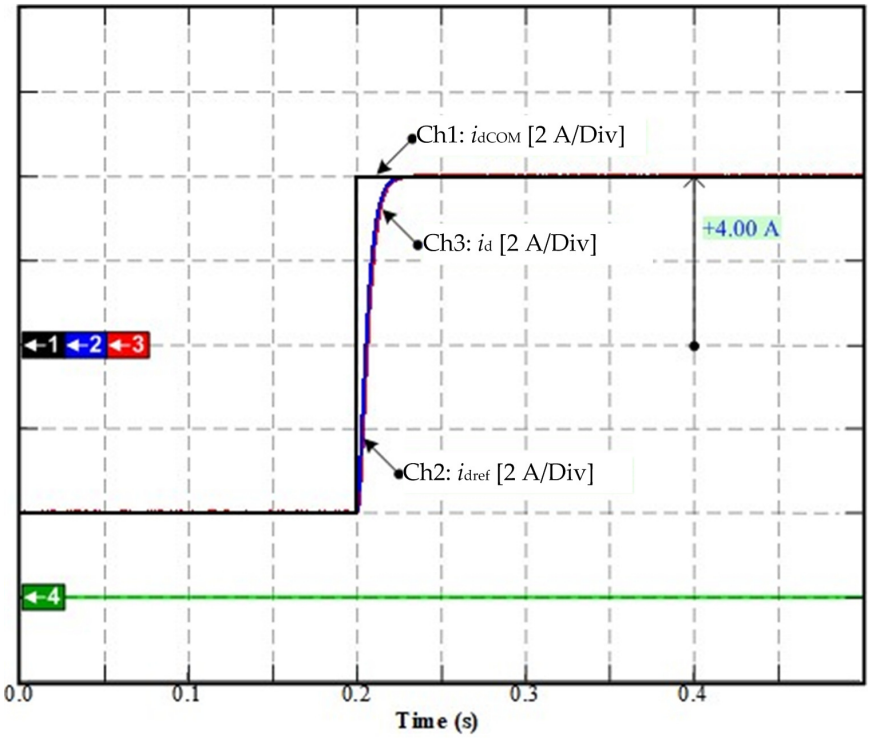

Figure 4.16 Simulation results: *d*-axis current response based on MFC.

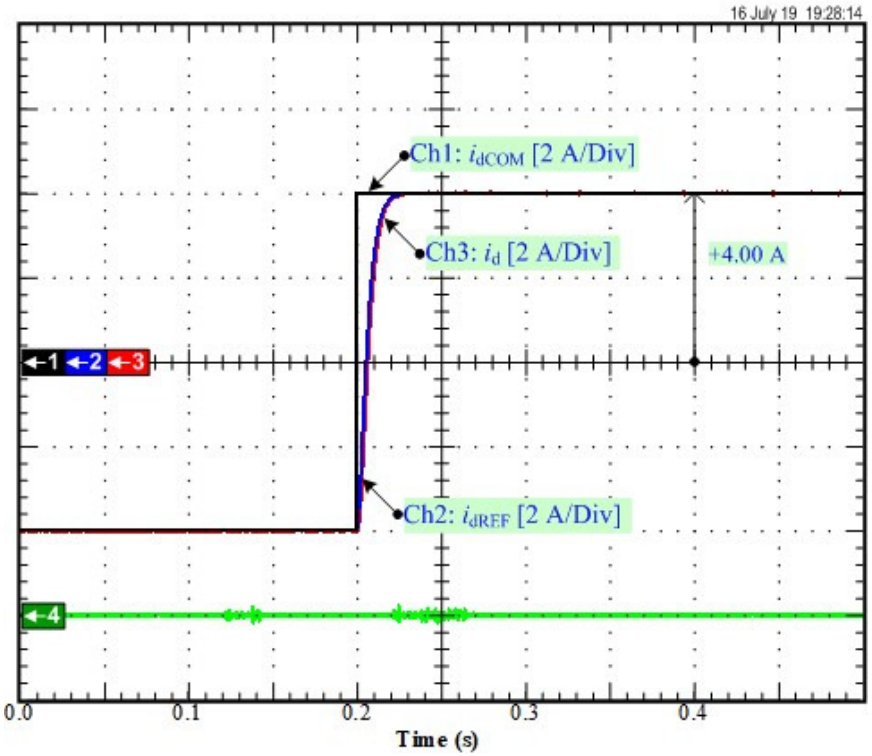

Figure 4.17 Experimental results: *d*-axis current response based on MFC.

Initially, the response of the *d*-axis current loop of the model-free control is benchmarked against the field-oriented control (FOC) with the traditional PI controller. For the system with parameters given in Table 4.2, Figure 4.15 illustrates the simulation results of the FOC with the PI controller Figure 4.16 shows the simulation results of the MFC, and Figure 4.17 depicts the experimental measurements when the MFC is applied. In Figure 4.15, Ch1 is *d*-axis current referent i_{dCOM}, Ch3 is the measured *d*-axis current i_d, and Ch4 is the *q*-axis current i_q. In Figure 4.16, Ch1 is *d*-axis current referent i_{dCOM}, Ch3 is the measurable *d*-axis current i_d, and Ch4 is the *q*-axis current i_q. In Figure 4.17, Ch1 is *d*-axis current referent i_{dCOM}, Ch3 is the measured *d*-axis current i_d, and Ch4 is the *q*-axis current i_q. As depicted in these figures, the set-point tracking performances of MFC and FOC are very close. Meanwhile, the design of the PI controller needs to linearize the system model at one single operating point while the MFC takes into account the model variations and uncertainties thanks to the estimation of the unknown part of the model.

Figure 4.18 illustrates the simulation results (on the left side) and experimental results (on the right side) of the proposed model-free control applied to the speed control of the SPMSM drive. Figure 4.18(a), Chs 1, 2, and 4 are the speed reference n_{REF}, speed command n_{COM}, and measured speed n, respectively. Figure 4.18(b), Chs 1, 2, 3, and 4 are the *q*-axis current command i_{qCOM}, *q*-axis current reference i_{qREF}, *q*-axis current. In the bottom of Figures 4.18, Chs 2 and 3 are the estimations of *d*- and *q*-axis unknown parts (F_d and F_q) in the inner loop for *dq*-currents control. The estimation of these unknown parts enables the inner loop to track the current reference in a very effective manner. Compared to Figure 4.3, the results in Figure 4.18 are the equivalent signal of each part of the MFC, where n_{COM} is y_{COM}, n_{REF} is y_{REF}, and n is y_{MEAS}, respectively.

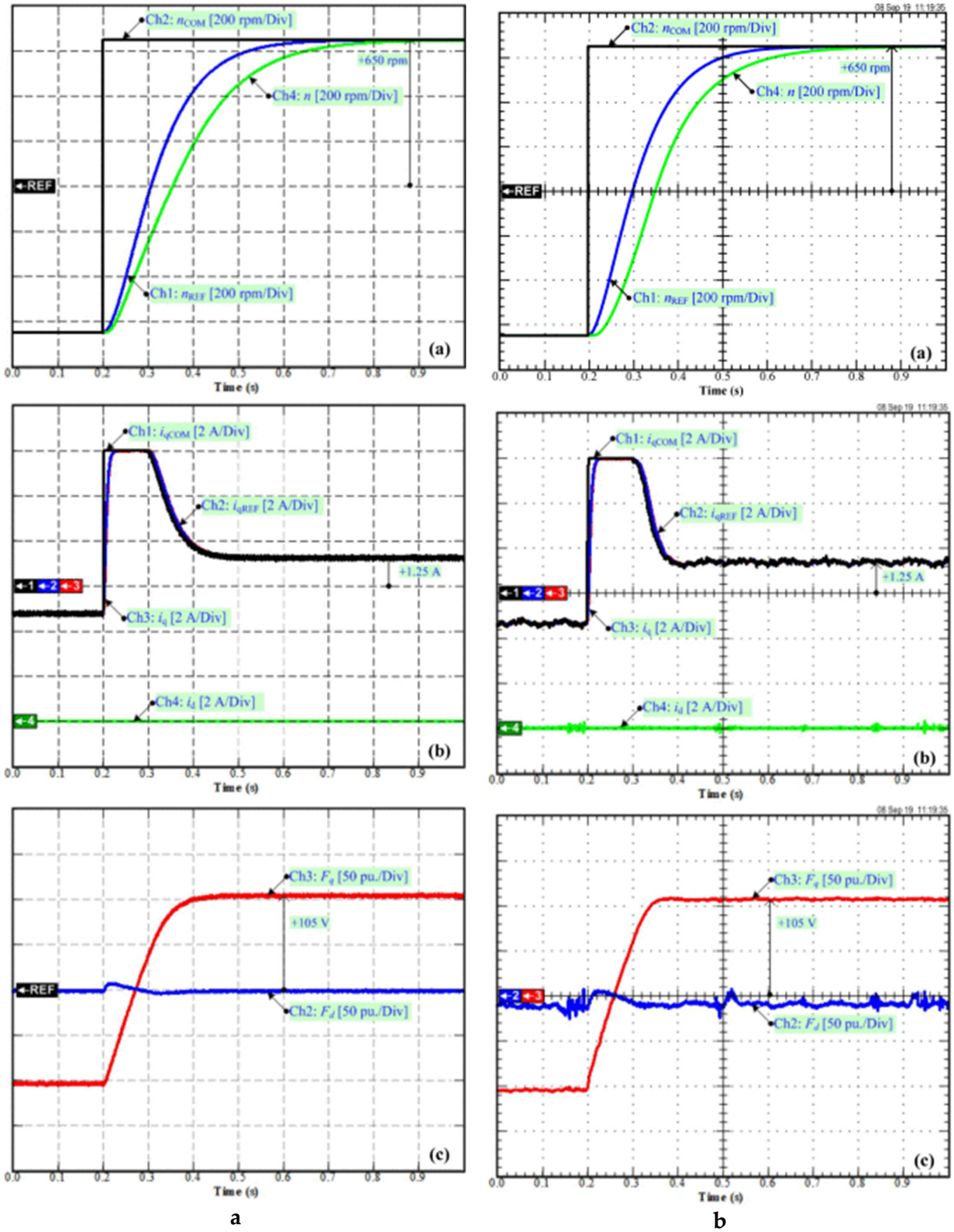

Figure 4.18 Simulation and Experimental results of MFC applied to SPMSM drive (a) Simulation (b) Experimental.

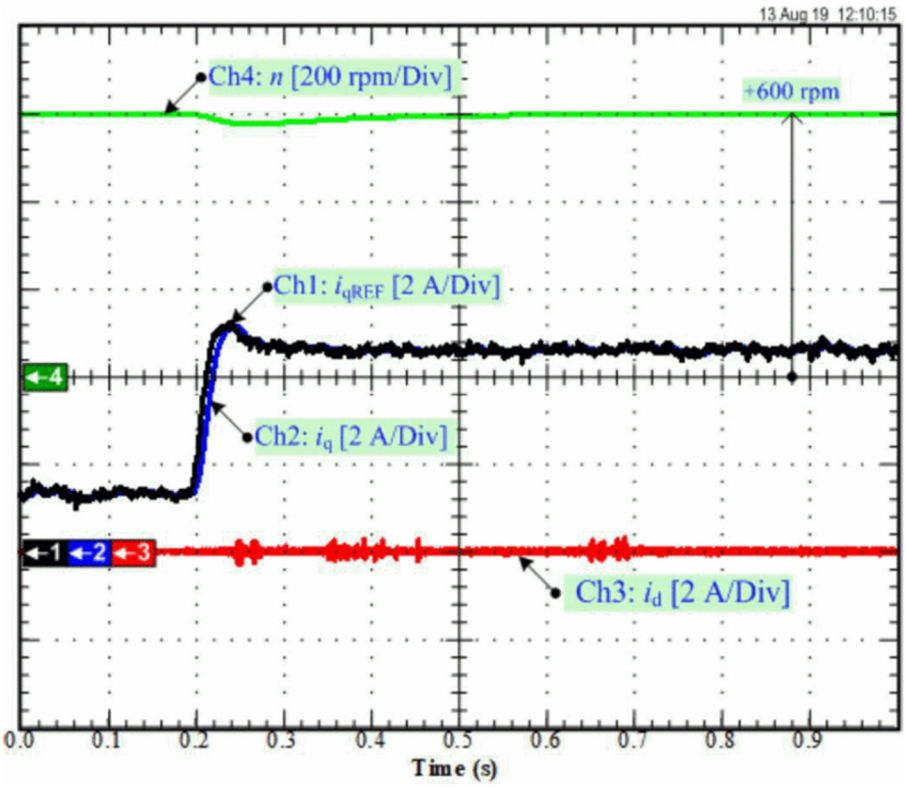

a

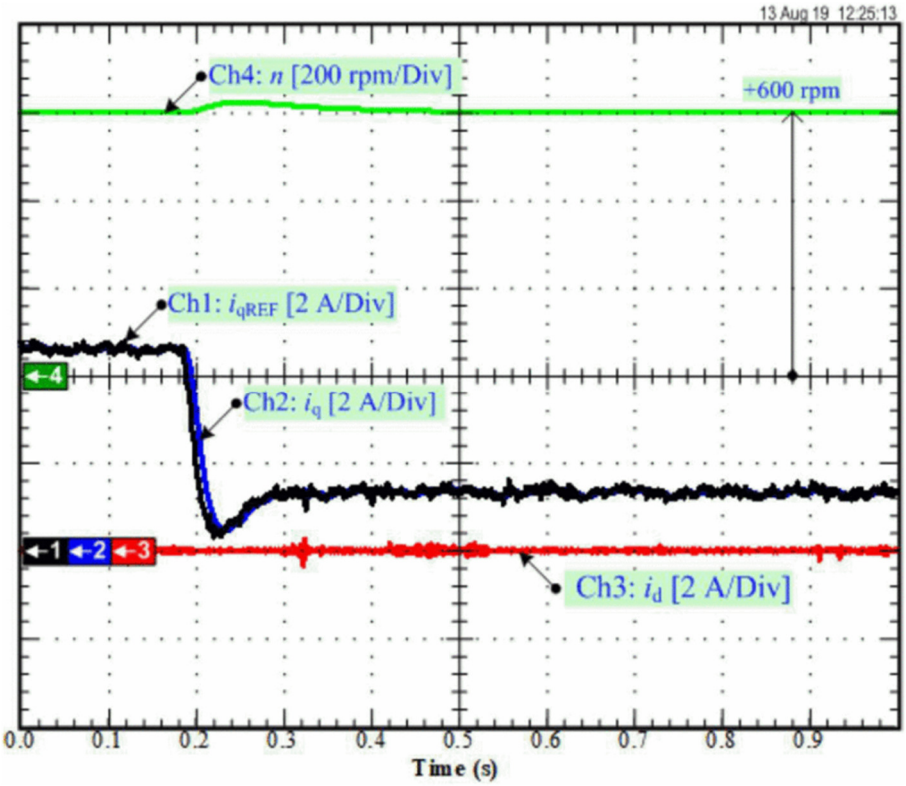

Figure 4.19 Experimental results: Disturbance rejection of MFC applied to SPMSM drive.

The n_{COM} changes from −650 to 650 rpm, including the regenerative and motoring modes, and the n_{REF} is provided by the trajectory planning of the outer speed control loop. As can be seen, the motor speed n tracks properly its reference n_{REF}. The motor torque reaches its maximum during the transient as the current limit is set to 6A. It can be noted that the speed response does not have any steady-state error, and its overshoot remains negligible. Acceleration and deceleration are limited by the current limitation that affects i_q, while i_d is kept close to zero. As can be seen, the PMSM runs up in the shortest time possible.

Finally, Figure 4.19 shows the experimental results of the disturbance rejection ability of the proposed MFC applied to the SPMSM drive. The experimental conditions are set as follows: given speed: n = 600 rpm; a sudden increase of load torque TL at 0.2 s as shown in Figure 4.19(a), and later in Figure 4.19(b), the load torque is removed at 0.2 s. It can be seen that under the action of the proposed model-free control, when the load changes suddenly, the motor speed shows a small deviation from its set-point, and it is recovered in a short time (see Ch4 green waveform). Thus, the figure shows the MFC's good capability to limit the torque disturbance effects and achieve zero steady-state speed error. As a result, the speed loop control performance is significantly improved, verifying the feasibility of the proposed MFC.

4.4. Applying model-free control to PMa-SynRM Drive

4.4.1. Model-free control of PMa-SynRM driving development

The VSD, which powers the PMa-SynRM understudy, is shown in Figure 4.20, and the block diagram of the model-free control is shown in Figure 4.21. According to the rotor geometries of the PMa-SynRM discussed in 2.3, the current control strategies differ from those applied to SPMSM. The rotor geometries of PMa-SynRM are the salient-pole where $L_d > L_q$. Therefore, the torque equation is given by (2.42). In this case, the i_d component should not be equal to zero to take advantage of the reluctance torque produced by the high saliency ratio. Therefore, the Maximum Torque per Ampere (MTPA) control strategy is recommended for PMa-SynRM and even IPMSM. The main idea of this control is to develop the requested torque using the minimum value of the stator current magnitude. Based on the torque equation (2.66), the torque of the PMa-SynRM can be divided into two parts: one is produced by the permanent-magnet flux (interaction torque), and the other is produced by the difference in the inductances of the d and q axes (reluctance torque). Therefore, to minimize the copper losses and increase the overall drive efficiency, the MTPA is used as developed in Section 2.9.2.

As shown in Figure 4.21, the control system has a case cascade construction consisting of two loops (i.e., inner current control loop and outer speed control loop). The inner current loop is much faster than the outer speed control loop such that the model-free control for the current control is developed first.

Although the development of the controller is very similar to that for the SPMSM, we show all the design steps in the following for the sake of the self-sufficientness of this sub-chapter. By defining $u = [u_1\ u_2]^T = [v_d\ v_q]^T$, $y = [y_1\ y_2]^T = [i_d\ i_q]^T$, and rearranging of (2.49) in the form of (4.8), the PMa-SynRM model is given as

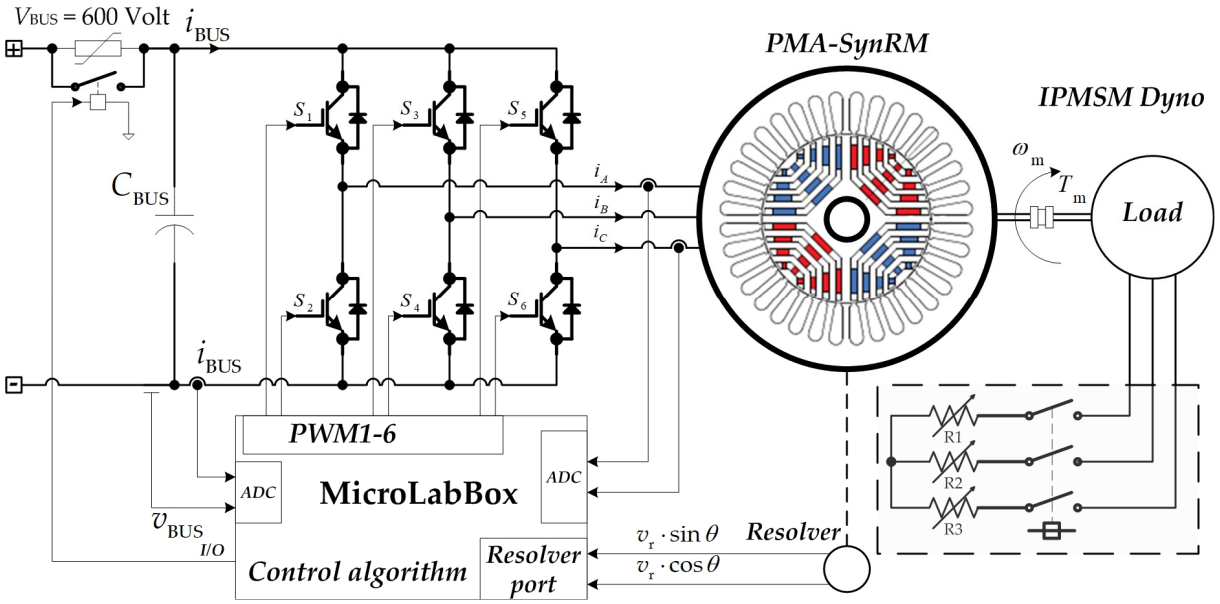

Figure 4.20 VSD inverter system powered PMSM block diagram.

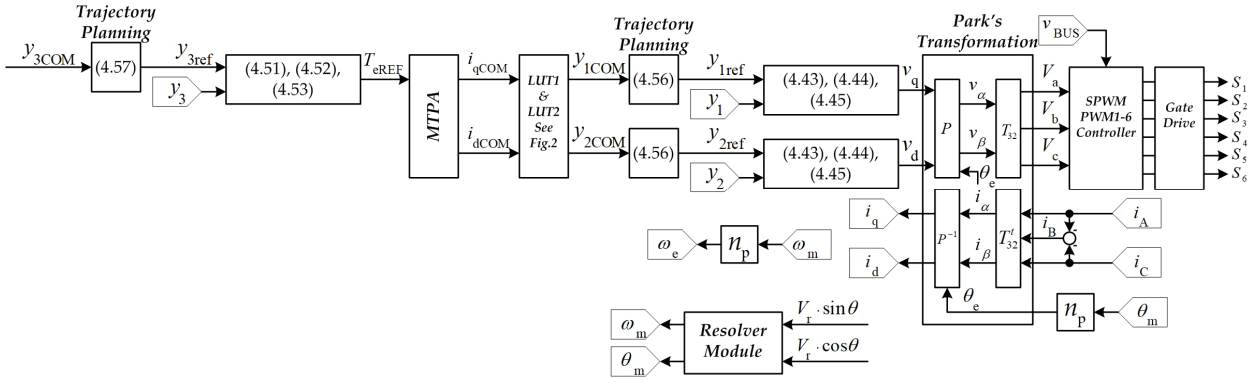

Figure 4.21 Control system of PMa-SynRM based on model-free control diagram.

$$\begin{aligned}\frac{di_d}{dt} &= -\frac{R_s i_d}{L_d} + \frac{\omega_e(L_q i_q - \Psi_m)}{L_d} + v_d \cdot \frac{1}{L_d} \\ \frac{di_q}{dt} &= -\frac{R_s i_q}{L_q} - \frac{\omega_e L_d i_d}{L_q} + v_q \cdot \frac{1}{L_q}\end{aligned} \tag{4.40}$$

This equation can be separated to identify the known and unknown parts in the following expression. The known parts are

$$\begin{aligned}\hat{\varphi}_1 &= \frac{\dot{y}_1}{b_2} = L_\mathrm{d}\frac{di_\mathrm{d}}{dt} \\ \hat{\varphi}_2 &= \frac{\dot{y}_2}{b_1} = L_\mathrm{q}\frac{di_\mathrm{q}}{dt}\end{aligned} \tag{4.41}$$

and the unknown parts are

$$\begin{aligned}F_1 &= \left\{-R_\mathrm{s}i_\mathrm{d} + \omega_\mathrm{e}(L_\mathrm{q}i_\mathrm{q} - \Psi_\mathrm{m})\right\}\cdot\frac{1}{L_\mathrm{d}} \\ F_2 &= \left(-R_\mathrm{s}i_\mathrm{q} - \omega_\mathrm{e}L_\mathrm{d}i_\mathrm{d}\right)\cdot\frac{1}{L_\mathrm{q}}\end{aligned} \tag{4.42}$$

According to the control law (Figure 4.3), the first term of the model-free control for inner current loop control is determined as:

$$\begin{aligned}u_{1\mathrm{ref}} &= \frac{\dot{y}_{1\mathrm{ref}}}{b_1} = L_\mathrm{d}\frac{di_\mathrm{d}}{dt} \\ u_{2\mathrm{ref}} &= \frac{\dot{y}_{2\mathrm{ref}}}{b_2} = L_\mathrm{q}\frac{di_\mathrm{q}}{dt}\end{aligned} \tag{4.43}$$

The estimation of unknown parts is given as:

$$\begin{aligned}\hat{F}_1 &= \frac{1}{L_\mathrm{d}}u_1 - \dot{y}_1 = \frac{1}{L_\mathrm{d}}v_\mathrm{d} - \frac{di_\mathrm{d}}{dt} \\ \hat{F}_2 &= \frac{1}{L_\mathrm{q}}u_1 - \dot{y}_2 = \frac{1}{L_\mathrm{q}}v_\mathrm{q} - \frac{di_\mathrm{q}}{dt}\end{aligned} \tag{4.44}$$

The feedback parts of *d*- and *q*-axis current control are obtained in the following expression.

$$\begin{aligned}b_1\cdot u_{1\mathrm{feedback}} &= b_1\left(K_\mathrm{pd}\cdot\varepsilon_\mathrm{d} + K_\mathrm{id}\int\varepsilon_\mathrm{d}dt\right) \\ b_2\cdot u_{2\mathrm{feedback}} &= b_2\left(K_\mathrm{pq}\cdot\varepsilon_\mathrm{q} + K_\mathrm{iq}\int\varepsilon_\mathrm{q}dt\right)\end{aligned} \tag{4.45}$$

Referring to the design procedure in Section 4.1.3, (4.45) can be rewritten as follows:

$$\begin{aligned}\ddot{\varepsilon}_\mathrm{d} + b_1\cdot K_\mathrm{pd}\cdot\dot{\varepsilon}_\mathrm{d} + b_1\cdot K_\mathrm{id}\cdot\varepsilon_\mathrm{d} &= 0 \\ \ddot{\varepsilon}_\mathrm{q} + b_2\cdot K_\mathrm{pq}\cdot\dot{\varepsilon}_\mathrm{q} + b_2\cdot K_\mathrm{iq}\cdot\varepsilon_\mathrm{d} &= 0\end{aligned} \tag{4.46}$$

The controller coefficients K_pd, K_id, K_pq, and K_iq, are determined as:

$$K_{pd}=\frac{2\zeta_1\omega_{n1}}{b_1},K_{id}=\frac{\omega_{n1}^2}{b_1}$$
$$K_{pq}=\frac{2\zeta_1\omega_{n1}}{b_2},K_{iq}=\frac{\omega_{n1}^2}{b_2} \tag{4.47}$$

The second model-free control for the outer speed control loop is developed here. According to Figure 4.21, the output of the speed control loop provides the torque reference of the MTPA algorithm generated optimized *d*- and *q*-axis current references. Therefore, T_e is chosen as a control variable of the outer speed control loop that $u_3 = T_{eREF}$. And then, rewriting the mechanical equation of PMa-SynRM represented by (2.42) in the form of Eq. (4.8) gives:

$$\frac{d\omega_m}{dt}=\left(-B_f\cdot\omega_m-T_L\right)\cdot\frac{1}{J}+T_e\cdot\frac{1}{J} \tag{4.48}$$

Separating (4.48) into the known part and unknown parts is given as follows:
The known part is

$$\hat{\phi}_3=\frac{\dot{y}_3}{b_3}=J\frac{d\omega_m}{dt} \tag{4.49}$$

Moreover, the unknown part is:

$$F_3=\left(-B_f\omega_m-T_L\right)\cdot\frac{K_t}{J} \tag{4.50}$$

Each part of the model-free control for the outer speed control loop is defined as the following expression.

$$u_{3ref}=\frac{\dot{y}_{3ref}}{b_3}=J\frac{d\omega_m}{dt} \tag{4.51}$$

The estimation of the unknown part is

$$\hat{F}_3=\frac{K_t}{J}u_3-\dot{y}_3=\frac{1}{J}\cdot T_e-\frac{d\omega_m}{dt} \tag{4.52}$$

$$b_3u_{3feedback}=b_3\left(K_{p\omega}\cdot\varepsilon_\omega+K_{i\omega}\int\varepsilon_\omega dt\right) \tag{4.53}$$

Referring to the design procedure in Section 4.1.3, (4.53) can be rewritten as follows:

$$\ddot{\varepsilon}_\omega+b_1\cdot K_{p\omega}\cdot\dot{\varepsilon}_\omega+b_1\cdot K_{i\omega}\cdot\varepsilon_\omega=0 \tag{4.54}$$

The controller coefficients $K_{p\omega}$ and $K_{i\omega}$ are determined as:

$$K_{p\omega}=\frac{2\zeta_2\omega_{n2}}{b_3},K_{i\omega}=\frac{\omega_{n2}^2}{b_3} \tag{4.55}$$

where ζ_2 and ω_{n2} are the desired dominant damping ratio and natural frequency of the outer speed control loop, respectively.

4.4.2. Trajectory planning

Finally, as shown in Figure 4.3, trajectory planning has to be implemented to generate the input reference y_{REF}. A second-order low-pass filter is often utilized to plan the desired trajectory for the output. It allows limiting the derivative terms. The proposed trajectory planning for the two inner current control loops is:

$$\frac{y_{1REF}}{y_{1COM}}=\frac{y_{2REF}}{y_{2COM}}=1\Big/\left\{\left(\frac{s^2}{\omega_{n3}}\right)+\frac{2\zeta_3}{\omega_{n3}}s+1\right\} \tag{4.56}$$

where ζ_3 and ω_{n3} are the desired dominant damping ratio and natural frequency.

and the trajectory planning of the outer speed loop is

$$\frac{y_{3REF}}{y_{3COM}}=1\Big/\left\{\left(\frac{s^2}{\omega_{n4}}\right)+\frac{2\zeta_4}{\omega_{n4}}s+1\right\} \tag{4.57}$$

where ζ_4 and ω_{n4} are the desired dominant damping ratio and natural frequency of the speed loop trajectory planning.

4.5. Simulation and experimental validation of the model-free control applied to PMa-SynRM

4.5.1. Test bench setup

The main PMa-SynRM parameters are in Table 4.3, and the model-free controller parameters are defined in Table 4.4. The model-free control applied to the PMa-SynRM was practically implemented using the dSPACE Micro LABBOX board, with a time step of Ts = 6.25e−5 s. In order to verify the proposed control system, a laboratory test of the prototype PMa-SynRM is performed, as in Figure 4.22. and then the experimental results show in the following illustration.

TABLE 4.3
PMa-SynRM Parameters (linear case) for the Model-Free Control development

Symbol	Meaning	Value
P_{rated}	Rated Power	1kWatt
n_{rated}	Rated Speed	1350 rpm
n_p	Number of pole pairs	2
R_s	Resistance (Motor + Inverter)	3.2 Ohm
L_d	Normal *d*-axis inductance	288 mH
L_q	Normal *q*-axis inductance	38 mH
L_{dq}	Mutual inductance	4 mH
Ψ_m	Permanent-magnet flux	0.138 [Wb]
J	Equivalent inertia	0.0017 kg.m^2

TABLE 4.4
Speed and Current regulation parameters of PMa-SynRM drive based on Model-free Control

Symbol	Meaning	Value
ζ_{1d}	Damping ratio 1	0.7
ω_{n1d}	Natural frequency 1	3000 Rad.s^{-1}
ζ_{1q}	Damping ratio 1	0.7 pu.
ω_{n1q}	Natural frequency 1	2000 Rad.s^{-1}
ζ_2	Damping ratio 2	0.7
ω_{n2}	Natural frequency 2	107.1419 Rad.s^{-1}
ζ_{3d}	Damping ratio 3	1
ω_{n3d}	Natural frequency 3	300 Rad.s^{-1}
ζ_{3q}	Damping ratio 3	1
ω_{n3q}	Natural frequency 3	200 Rad.s^{-1}
ζ_4	Damping ratio 4	1
ω_{n4}	Natural frequency 4	150 Rad.s^{-1}
T_{emax}	Maximum torque reference	+6 Nm
T_{emin}	Minimum torque reference	-6 Nm
Vdc	DC bus voltage	400 V
f_s	Switching frequency	16 KHZ

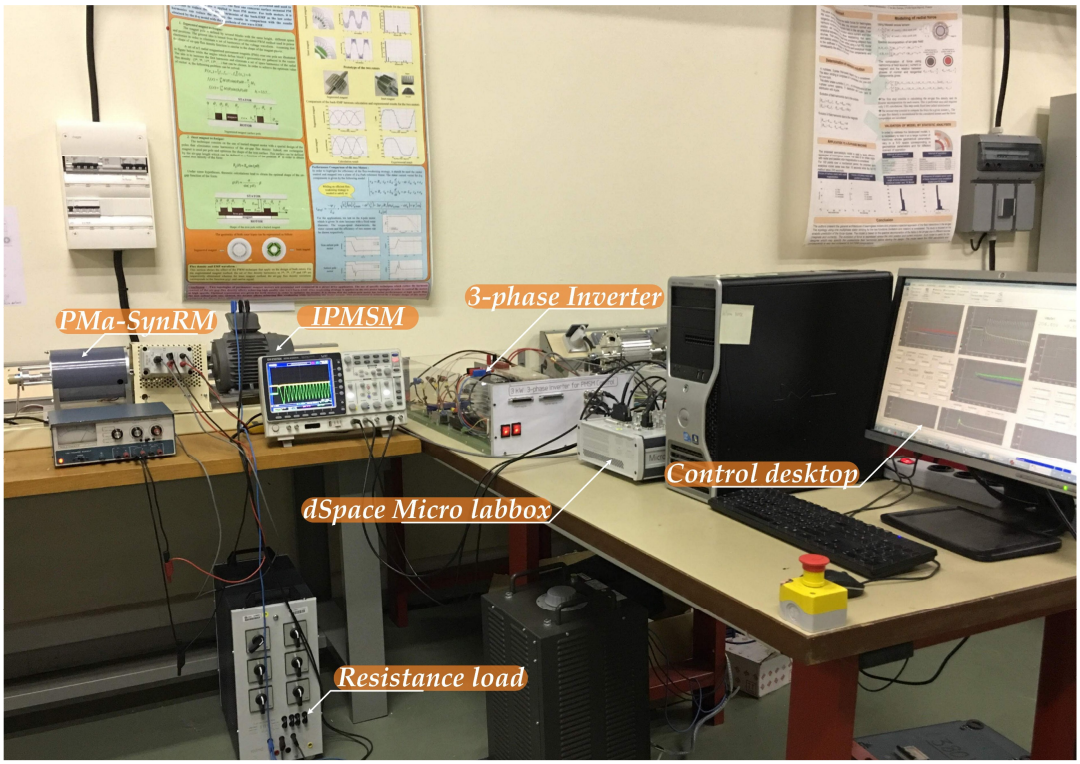

Figure 4.22 Laboratory test bench setup of PMa-SynRM drive at UL.

4.5.2. Simulation

The developed MFC algorithm for PMa-SynRM drive has been simulated under different operation conditions before its implementation. Figure 4.23 shows the simulation results of the d-axis inner loop current control response using the model-free control. As it can be distinctively seen, during the transient, the d-axis current tracks very well its reference, and there is no steady-state error. Note that the simulation condition is set as follows: for d-axis testing, the q-axis current command i_{qCOM} is set to zero.

Figure 4.24 shows the q-axis current control simulation results using the model-free control. As can be seen, the control performance is quite satisfactory with good set-point tracking and zero steady-state error. The simulation condition is set as follows: during q-axis testing, the d-axis command i_{dCOM} is set to zero, and the load is the rated one.

Another simulation result is shown in Figure 4.25. It shows the drive response to a step change on the speed reference from 0 to 1000 rpm. In this figure, Chs 1, 2, and 4 are the speed command n_{COM}, speed reference n_{REF}, and measured speed n, respectively. Chs 3, 5, and 6 are the torque reference T_{eREF}, and the d- and q-axis current i_d and i_q, and Chs 7 and 8 are the d-axis voltage and q-axis voltage, respectively. The parameters of the simulated drive are those of the test bench that will be later used for experimental validation. They are reported in Section 4.5.1. The MFC has been designed to keep the torque within the range of ±6 Nm. As can be seen, the speed response is satisfactory with small overshoot and without steady-state error.

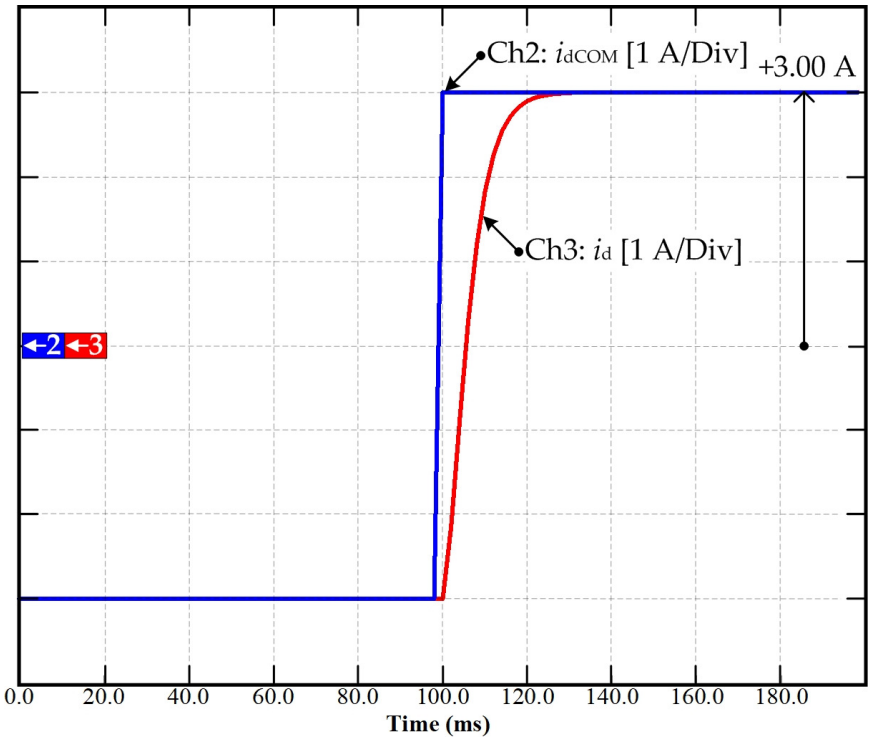

Figure 4.23 Simulation results: Dynamic response of d-axis currents with the controller based on the model-free control.

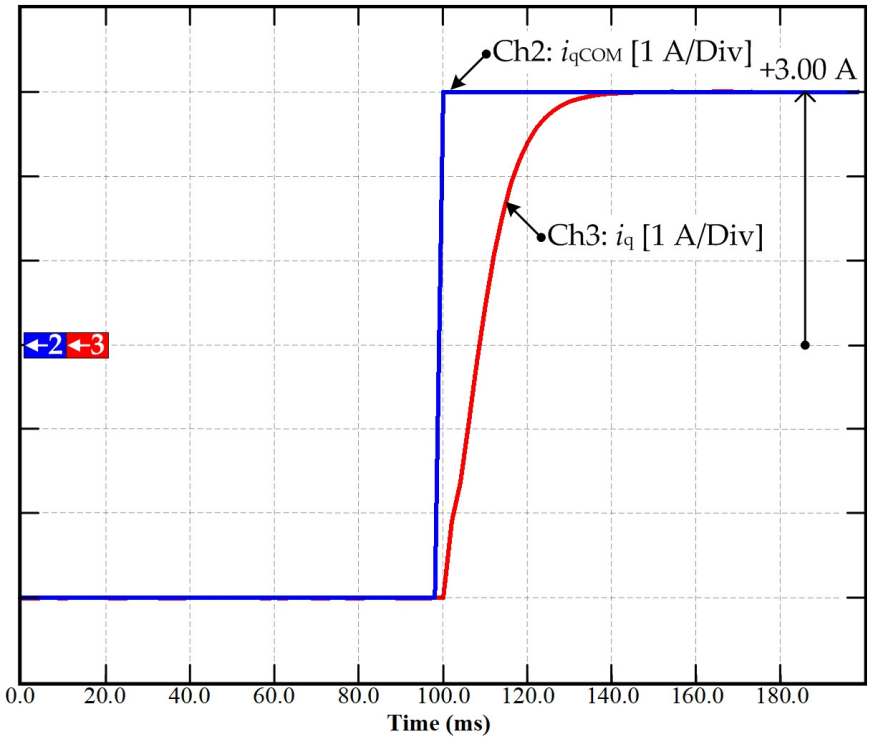

Figure 4.24 Simulation results: Dynamic response of q-axis currents with the controller based on the model-free control applied to PMa-SynRM drive.

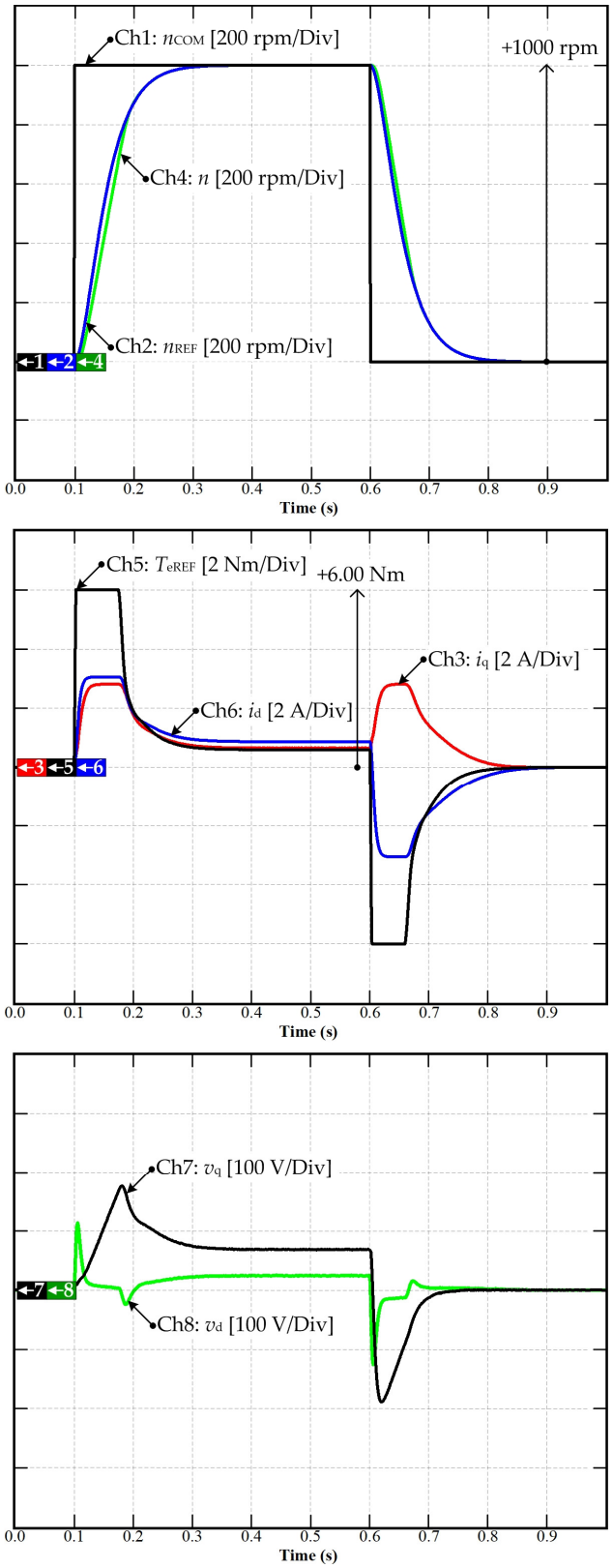

Figure 4.25 Simulation results: Simulated drive response to a 0–1000 rpm reference speed pulse. From top to bottom: speed reference and response, d- and q-currents, d- and q-voltages, and active region number of the MFC controller.

Though there is no torque sensor on the experimental setup, the torque seems to be limited to the allowed range. i_q and i_d are generated based on the MTPA algorithm, discussed in Section 2.9.2.

Figure 4.26 shows the simulation of the disturbance rejection ability of the MFC applied to the PMa-SynRM drive. In the figure, Ch 4 is the measured speed n, Ch2 is the d-axis current i_d, Ch3 is the q-axis current i_q, and Ch1 is the torque reference T_{eREF}. The simulation conditions are the following: n = 1000 rpm; a sudden increase of 3.7 Nm happens to the load torque T_L at 0.3 s, then the load torque is cleared at 0.7 s. It can be seen that under the action of the proposed model-free control, when the load changes suddenly, the motor speed deviates slightly from its set-point, but it is recovered very quickly. This figure shows the disturbance rejection capability of the MFC. As a result, the speed control performance is significantly improved, verifying the feasibility of the proposed MFC for this application.

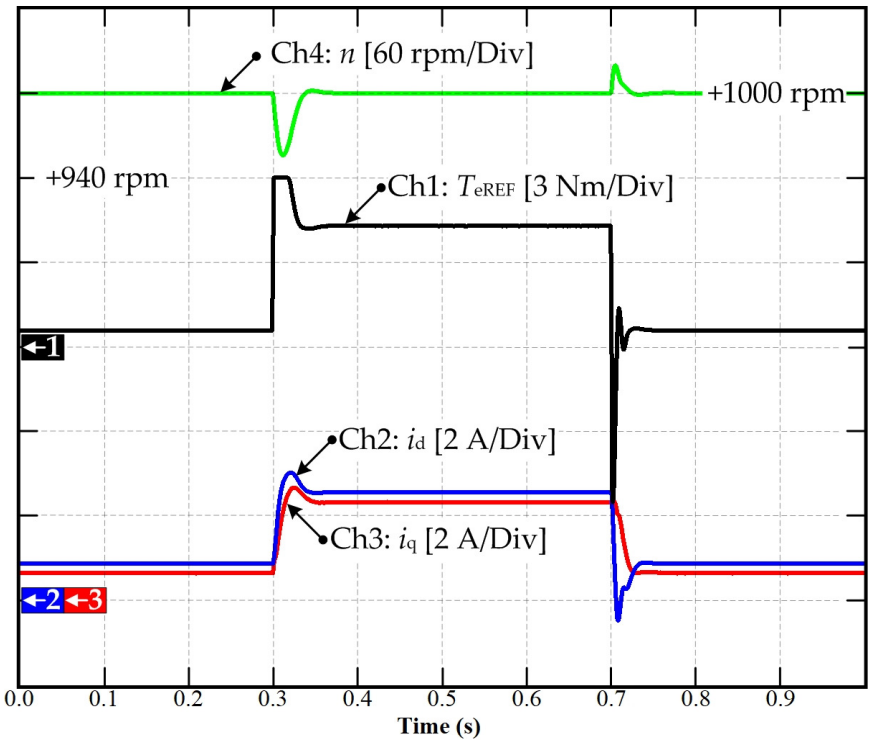

Figure 4.26 Simulation results: Disturbance rejection of MFC applied to PMa-SynRM drive.

4.5.3. Experimental validation of PMa-SynRM drive based on the model-free control

The designed MFC for PMa-SynRM drive has been experimentally validated on a laboratory test bench. The experimental setup is in Figure 4.22.

Figure 4.27 shows d-axis current reversal test. In this figure, d-axis command i_{dCOM}, d-axis reference i_{dREF}, which is provided by the d-axis trajectory planning, and the actual d-axis current

are shown. These results are similar to those obtained by simulation and confirm that the current control performance is satisfactory.

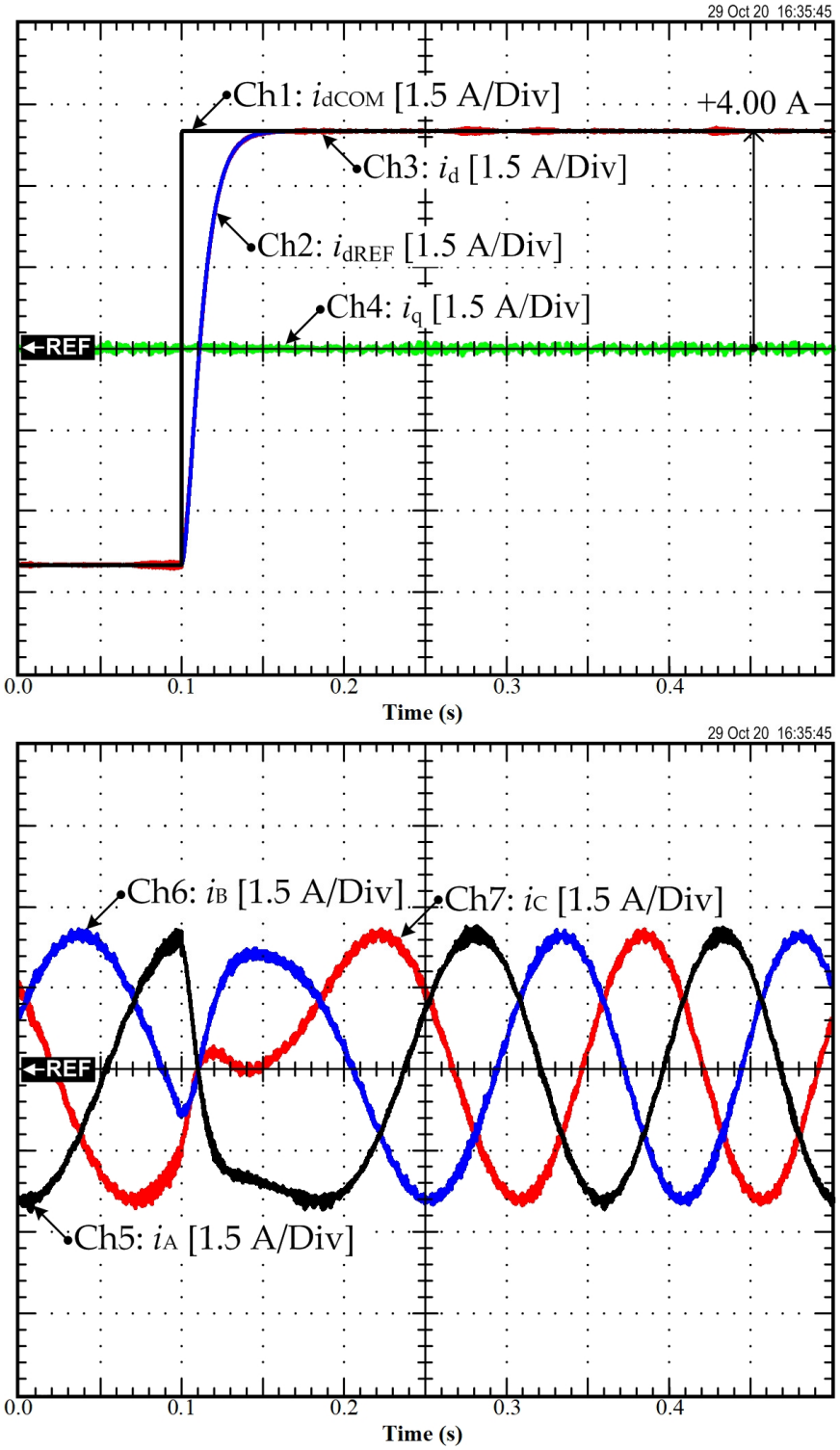

Figure 4.27 Experimental result: *d*-axis response curve based on MFC.

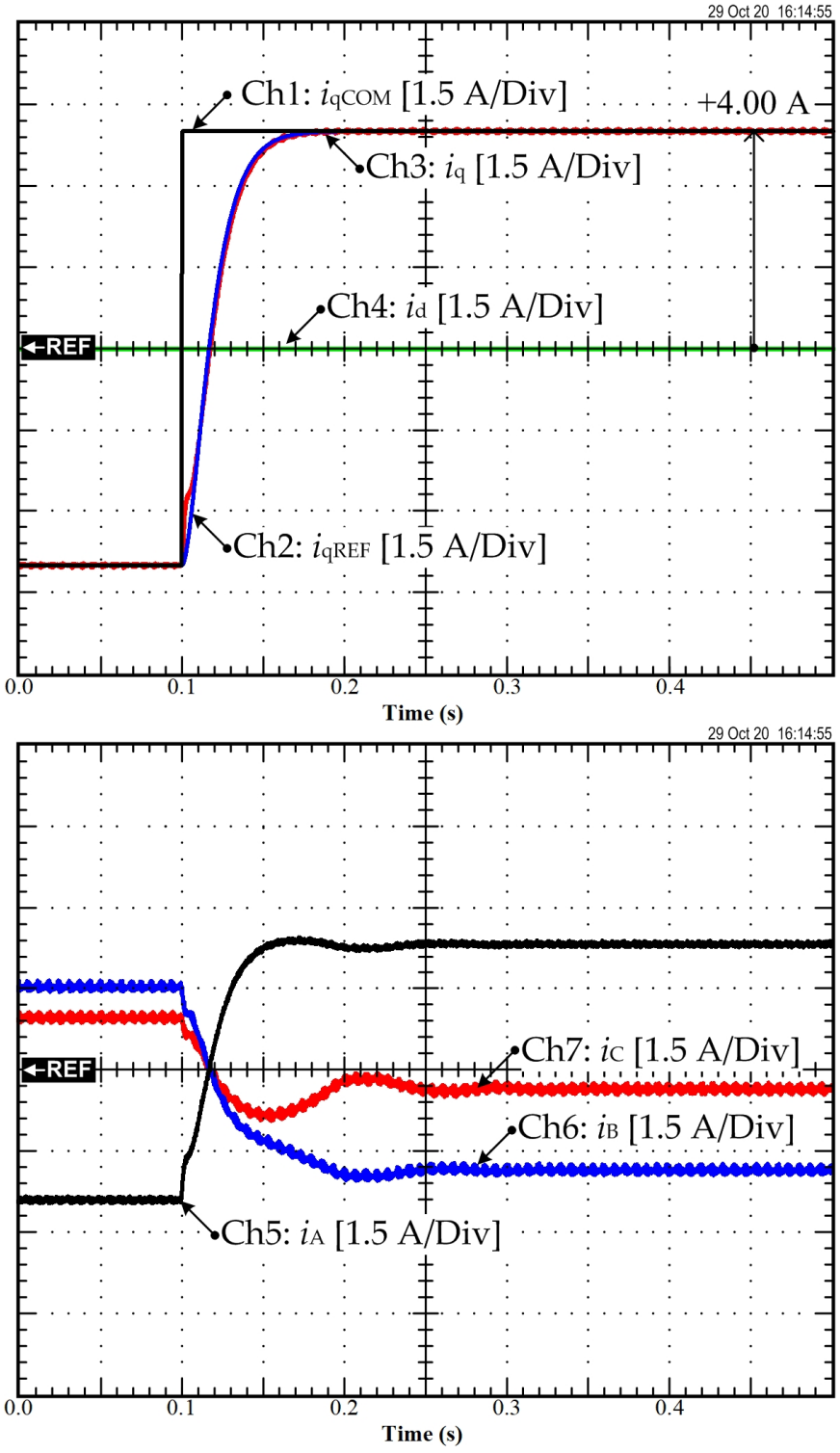

Figure 4.28 Experimental result: q-axis response curve based on MFC.

The same test is done with q-axis current while d-axis current is regulated to zero. In this case, the motor is at a stand-still. Figure 4.28 depicts the experimental data where Ch1 is q-axis

current command i_{qCOM}, Ch2 is the q-axis current reference i_{qREF}, Ch3 is the q-axis current measurement i_q. Overall, the current control performance looks satisfactory.

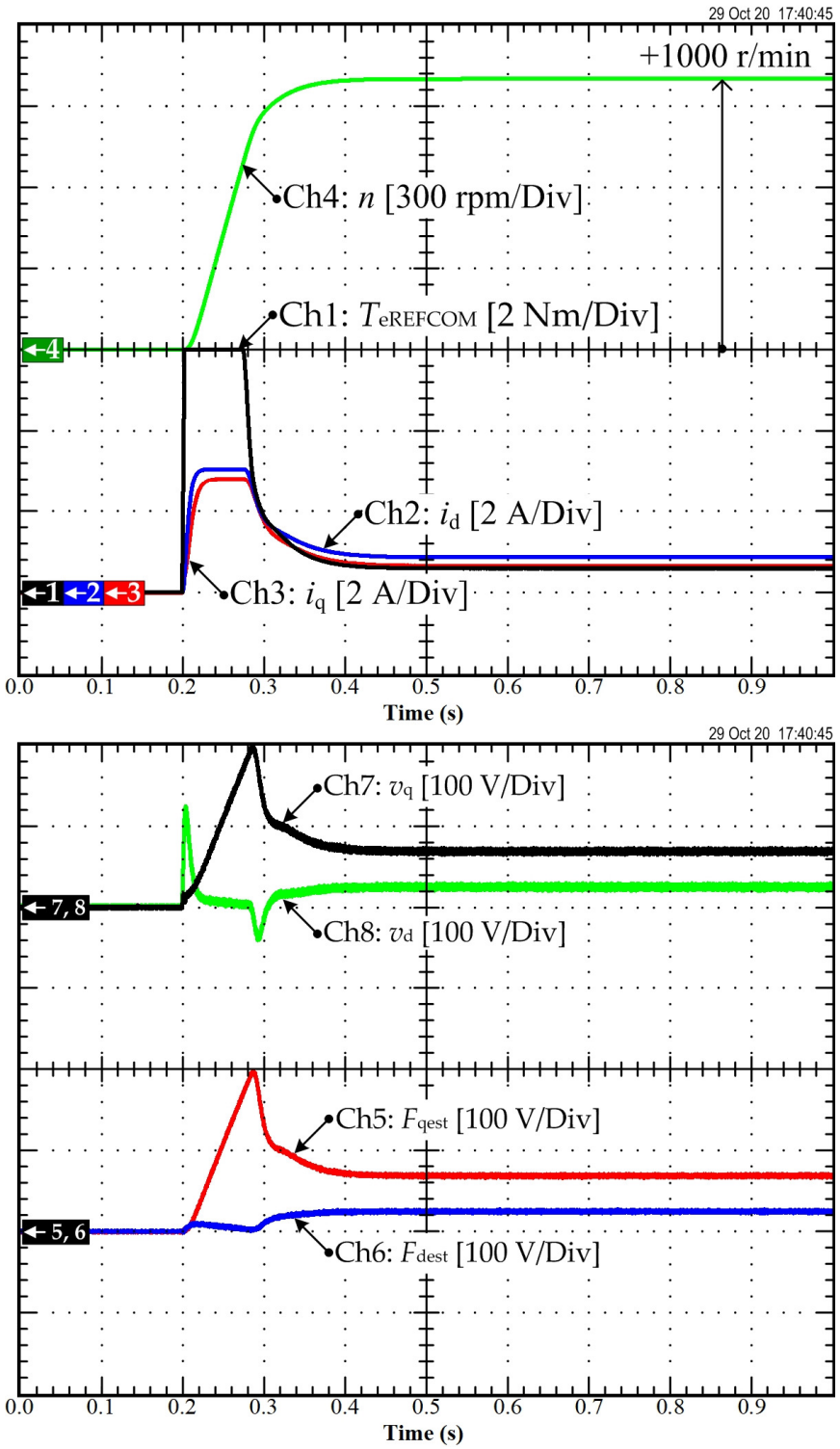

Figure 4.29 Experimental result: speed acceleration curve based on MFC.

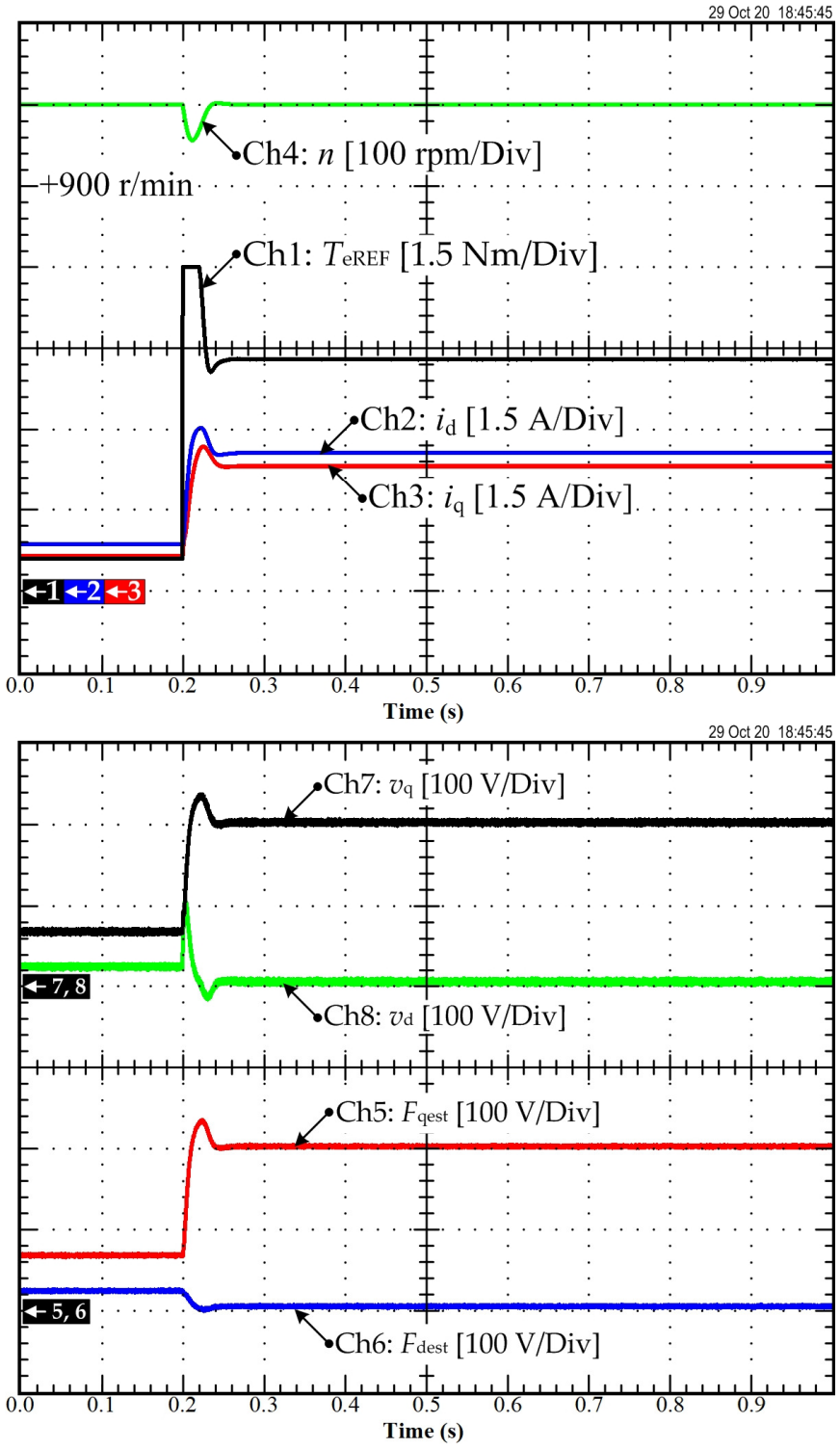

Figure 4.30 Experimental result: disturbance rejection based on MFC.

Figure 4.29 illustrates the speed startup of the PMa-SynRM drive using the MFC. In this figure, Chs 1, 2, 3, and 4 are the torque reference T_{eREF}, d-axis current i_d, q-axis current i_q, and measured speed n. Chs 5 and 6 are the output v_q and v_d, chosen as the output of the MFC.

Moreover, Chs 7 and 8 show the estimated unknown parts of the *d*- and *q*-axis models. As expected, the torque has been limited, and the speed response does not show any overshoot and steady-state error. It is worth recalling that the torque reference generates i_q and i_d command references according to the maximum torque per ampere (MTPA) algorithm.

Figure 4.30 shows the experimental validation of the disturbance rejection ability of the proposed MFC applied to the PMa-SynRM drive. In this figure, Chs 1, 2, 3, and 4 are the torque reference T_{eREF}, *d*-axis current i_d, *q*-axis current i_q, and measured speed n, respectively. Chs 5 and 6 are the output v_q and v_d, chosen as the output of the MFC. Moreover, Chs 7 and 8 show the estimated unknown parts of the *d*- and *q*-axis currents models. The experimental conditions are set as follows: with n_{REF} = 1000 rpm, a sudden increase of the load torque (T_L) by 3.7 Nm occurs at 0.2 s. It can be seen that the proposed model-free control compensates for the load torque variation and rejects its effect on the motor speed in a short time. This figure shows the effectiveness of the MFC in load torque disturbance rejection and maintaining zero steady-state speed error. As a result, the speed loop control performance is good. This confirms the feasibility of the proposed MFC for the speed control of PMa-SynRM.

4.6. Conclusion

This chapter proposed the application of a model-free controller (MFC) to the current and speed control of motor drives. This novel control approach has been applied to both SPMSM and PMa-SynRM, applicable to the combined control of the outer speed control loop and the inner current control loop. After a brief introduction of the MFC fundamentals, the design procedure is illustrated in detail, giving a step-by-step approach. Suggestions for extending the design to different drive controllers are also included. Simulations and numerous experimental results highlight the promising features and characteristics of the MFC applied to electrical motor drives. As the last contribution, the MFC potentials pointed out in this chapter should stimulate further exploration and study on this type of controller to achieve the expertise required to transfer the results to practical applications.

So far, as it can be distinctively seen, the proposed model-free control provides high-performance for both SPMSM and PMa-SynRM drives compared to the FOC with the traditional PI controller. Besides, it has higher dynamic performance than the SPMSM and PMa-SynRM drive using the differential flatness-based control.

In this chapter, both the simulation and the experimental validation has been performed by the prototype PMa-SynRM at GREEN Lab, Université de Lorraine. The machine can operate in constant torque and constant power regions if a proper field weakening control is applied. In summary, by applying the model-free control, the performance of PMa-SynRM has been improved not only on the inner current control loop but also the outer speed control loop. Moreover, the controller coefficients of the proposed MFC are not complicated to define, and a unique design approach can be applied for both SPMSM and PMa-SynRM drives.

CONCLUSION

The main objective of this work was to develop a reliable and robust high-performance nonlinear controller for permanent magnet synchronous motor (PMSM), which includes surface-mount PMSM (SPMSM) and permanent magnet assisted synchronous reluctance motor (PMa-SynRM). PMa-SynRM can improve torque density power factor, operating above the rated speed of 70% using the flux weakening control technique compared to interior PMSM and power factor improvement concerning SynRM. Especially, PMa-SynRM is being reviewed as a next-generation high-efficiency industrial motor to replace an induction motor suitable for next-generation electric vehicles (EVs). In order to achieve a high-performance drive and maximize for the EV industry, having an optimized PMa-SynRM structure is necessary. The classification choosing of PMa-SynRM present in Chapter 2. The transversely laminated (TLA) or multiple-flux barrier rotor is chosen because it is made by traditional punching or wire cutting. As a result, construction is easy and cheap.

In Chapter 2, the systemically mathematic models of the three wide varieties of permanent-magnet synchronous machines, namely surface mounted permanent magnet synchronous motor (SPMSM), interior permanent magnet synchronous motor (IPMSM), and permanent magnet assisted synchronous reluctance motor (PMa-SynRM), are analyzed in both linear and nonlinear cases. Then, based on the mathematical model, dynamic simulation models of the different machine types are performed by MATLAB/-SIMULINK software. A simulation and experimentation of field-oriented control (FOC) based on traditional PI compensation is first carried on to investigate the parameters and behavior of the machines. The results reflect that PMa-SynRM can achieve over rated speed operation of 70% and the proposed MTPA algorithm provided minimized copper losses control system of PMa-SynRM drive. Furthermore, with the advantage of PMa-SynRM, thanks to low magnetic flux compared to IPMSM, it can operate beyond a rated speed using a field weakening control technique. This control scheme was validated by both simulation and experiment. Finally, the design and control of a permanent magnet-assisted synchronous reluctance motor with copper loss minimization using MTPA are presented by using a prototype PMa-SynRM. However, the FOC based on the traditional PI controller cannot deal with a nonlinear property of PMa-SynRM.

Chapter 3 introduced a model-based control based on differential flatness-based control with state observer of online parameter estimation. Flatness-based control is a powerful design tool because it is a simplification. Many equations can be clarified and reduced to one core equation using flatness-based control. The term' flatness' does not describe a specific control algorithm; it is indeed a general approach in analyzing and designing dynamical systems. This concept has rapidly become an essential branch in designing

nonlinear continuous-time control systems. Apart from academic success, it has found its way into industrial applications. This thesis applies the differential flatness-based approach to PMSM drive systems. Two high-performance control schemes are studied, differential flatness-based control and differential flatness-based with state observer.

In Chapter 3, the SPMSM and PMa-SynRM were realized in the form of state-space representation to define a state variable, input variable, and output variable, and then determined candidate flat output. A system is said to be differentially flat if an output function exists. Therefore, the SPMSM and PMa-SynRM equations set are denoted as the system variables' differential parameterization and are used in the controller design as realized in Sections 3.2 and 3.4. A controller law is defined to deal with parameters uncertainty and make sure the measurable state converges to the desired one. Additionally, trajectory planning is defined as well in order to limit differential action of the command variable. Finally, the controller law coefficient is determined by a second-order standard equation definition and set cross-section frequency by considering switching frequency. They can be experimentally tuned to achieve optimized system response.

The PMa-SynRM prototype and SPMSM laboratory testbench perform the simulation and experimental validation. As it can be seen, both the simulation and experimental results reflect that the differential flatness-based control provides significantly high performance for both the SPMSM and PMa-SynRM drives than the FOC based on the traditional PI controller. However, the differential flatness-based control is a model-based control system. Therefore, its performance depends on system parameters. Consequently, a new state observer is introduced to obtain significantly high performance for SPMSM and PMa-SynRM drives for dealing with the problem.

The simulation and experimental validations show notable results that the proposed new state observer based on the exponential stability can accurately estimate and the converging time reaching its desired value is shorter than the state observer based on Luenberger observer. So, adding the proposed observer of the differential flatness-based control made performance improvement is possible. Thus, in the conclusion of Chapter 3, the proposed differential flatness-based control scheme has provided high-performance nonlinear control of SPMSM drive, particularly PMa-SynRM drive, because it is a strongly nonlinear system. However, adding a state observer of the differential flatness-based control increases time-consuming and degrades inevitable system performance.

Chapter 4 proposed model-free control (MFC) to deal with the problem of an obstacle to model-based control (MBC). Generally, in most control systems of PMa-SynRM,

controllers are parameter-dependent, and their performance relies on the knowledge of motor parameters. For example, electrical parameters, such as the *dq*-axis inductances and winding resistance, are usually needed to design inner current loop controllers. In contrast, mechanical parameters, such as the combined moment of inertia (J) and viscous friction coefficient (B_f), are crucial for designing speed-loop controllers. The majority of techniques for optimizing torque production are sensitive to machines parameters. Unfortunately, stator resistance and permanent magnet flux vary with motor temperature. In addition, the mechanical parameters usually vary significantly with the dimensions and the shape of mechanical loads. So, generally practical applications, online parameter estimation for necessary parameters are required to achieve maximum torque production and high performance. Performance of the advanced parameter-dependent control strategies can be improved by using the off-line model of the motor parameters. However, this is computationally intensive because of the non-linearity due to iron saturation. Moreover, such calculations are usually unreasonable in real-time.

Section 4.2 of Chapter 4 explains the MFC development for SPMSM drive in both the inner current loop control and outer speed loop control with comprehensive detail. The control system based on MFC is reasonable in real-time compared to MBC with online state observer as presented in Chapter 3 because it does not rely on system parameters variation. A controller law based on an intelligent PI controller was presented to deal with parameters uncertainty and guaranteed state measurable converging to its reference. Moreover, trajectory planning was also developed to plan state reference trajectory and limit differential action of controller law during steady state.

Section 4.4 of Chapter 4, the MFC of PMa-SynRM development, is introduced thoroughly. Each part of the design has the same composition as the MFC of the SPMSM drive has done. The proposed MFC of SPMSM and PMa-SynRM has been put on a simulation validation and practical test to show that a fundamental theory, such as MFC, gives any merits to achieve a significantly high-performance control system. Several simulation and experimental tests have been carried out to validate the effectiveness of the MFC in both current and speed control loops. The proposed control algorithm is firstly tested in simulation under several operating conditions. Startup, tracking, parameter variation, and load step are considered. The obtained simulation results represent an adequate performance of the MFC control algorithm. Comparing the experimental performance of the FOC based on PI controller and the differential flatness-based control with state observer and MFC, effective performance is concluded for MFC.

Numerous experimental tests are performed to analyze the effectiveness of the developed controller in which the obtained results highly validated the simulation performance of MFC. Furthermore, compared to the observation-based control method, since the MFC

does not depend on the system's parameters, its tracking performance is more acceptable during load or operating point variation.

In conclusion, this thesis has achieved the main objective of finding out the high-performance nonlinear control of PMa-SynRM. Using a prototype PMa-SynRM drive as a test bench provided by GREEN Lab. at Université de Loraine, this paper gives an exhaustive description of an MFC's design procedure applied to the combined motor speed control and current. After a brief introduction of the MPC fundamentals, the design is illustrated in detail, giving a step-by-step discussion of the main critical points and the hints for their successful handling. Suggestions for extending the technique to different drive controllers are also included. Simulations and numerous experimental results highlight MFC's promising features and characteristics applied to PMSM drives. As the last contribution, the MFC potentials pointed out in this dissertation should stimulate further exploration and study on this type of controller to achieve the familiarity required to transfer the results to practical applications. To summarize more precisely, the comparison of the traditional FOC + PI, Flatness-based control and Model-free control benefits are shown in the following.

Traditional FOC+PI	**Flatness-Based Control**	**Model-Free Control**
- More suitable for a linear motor drive system - Design controller coefficient using Laplace transform - Control performance depending on system parameters	- More effective with a nonlinear motor drive system - Model-based control system - Control performance depending on system parameters - Performance enhancement using observer - Require more computation resources	- Dedicated to the control of unknown or partially known systems - Partially known parameters (inductance for current control)

FUTURE WORK

Thanks to the permanent magnet volume reduction and rare-earth-free machine, the PMa-SynRM are viewed as potentially viable candidates for EV applications. However, for further investigations into the control of the electric vehicles drive system, several aspects can be discussed. First, the exiting of the sensor, which includes the current and speed sensor, can be considered in the control of the EV powertrain unit. In this context, the sensorless control based on model-free control is going to be the next issue to implement of PMa-SynRM drive system.

It could be interesting to test the solution proposed in this thesis to other electric machines, i.e., induction motor, SynRM, and switch reluctance motor (SRM), which are all potentially suitable for EV application for the sake of generality.

Regarding the intrinsic independence of MFC from any information about the model of the studied system, the presented MFC method could be used for different applications to improve the reliability of the electric powertrain. Indeed, the possibility to switch from a classic model-based controller to a model-free controller in the case of a complex nonlinear system could benefit the reliability of the whole electric system.

PUBLICATION

International journal

S. Sriprang, N. Poonnoy, D. Guilbert, B. Nahid-Mobarakeh, N. Takorabet, N. Bizon and P. Thounthong, "Design, Modeling, and Differential Flatness Based Control of Permanent Magnet-Assisted Synchronous Reluctance Motor for e-Vehicle Applications", *Sustainability*, vol. 13, no. 17, p. 9502, 2021., https://doi.org/10.3390/su13179502

S. Sriprang, B. Nahid-Mobarakeh, N. Takorabet, S. Pierfederici, P. Kumam, N. Bizon, N. Taghavi, A. Vahedi, P. Mungporn and P. Thounthong, "Design and control of permanent magnet assisted synchronous reluctance motor with copper loss minimization using MTPA", *Journal of Electrical Engineering*, vol. 71, no. 1, pp. 11-19, 2020. DOI:10.2478/jee-2020-0002

S. Sriprang, B. Nahid-Mobarakeh, N. Takorabet, S. Pierfederici, N. Bizon, P. Kuman and P. Thounthong, "Permanent Magnet Synchronous Motor Dynamic Modeling with State Observer-based Parameter Estimation for AC Servomotor Drive Application", *Applied Science and Engineering Progress*, vol. 12, no. 4, 2019. DOI: 10.14416/j.asep.2019.11.001

International conferences

S. Sriprang, B. Nahid-Mobarakeh, S. Pierfederici, N. Takorabet, N. Bizon, P. Kumam, P. Mungporn and P. Thounthong, "Robust Flatness Control with Extended Luenberger Observer for PMSM Drive", *2018 IEEE Transportation Electrification Conference and Expo, Asia-Pacific (ITEC Asia-Pacific)*, 2018. DOI: 10.1109/ITEC-AP.2018.8432600

S. Sriprang, B. Nahid-Mobarakeh, S. Pierfederici, N. Takorabet, N. Bizon, P. Kumam, P. Mungporn and P. Thounthong, "Robust Flatness-based Control with State Observer-Based Parameter Estimation for PMSM Drive", *2018 IEEE International Conference on Electrical Systems for Aircraft, Railway, Ship Propulsion and Road Vehicles & International Transportation Electrification Conference (ESARS-ITEC)*, 2018. DOI: 10.1109/ESARS-ITEC.2018.8607648

S. Sriprang, B. Nahid-Mobarakeh, N. Takorabet, S. Pierfederici, P. Mungporn, P. Thounthong, N. Bizon, P. Kuman and Z. Shah, "Model Free-Based Torque Control of Permanent Magnet Synchronous Motor Drives", *2019 Research, Invention, and Innovation Congress (RI2C)*, 2019. DOI: 10.1109/RI2C48728.2019.8999889

S. Sriprang, B. Nahid-Mobarakeh, N. Takorabet, S. Pierfederici, P. Mungpom, P. Thounthong, N. Bizon, P. Kuman and Z. Shah, "Model-Based Control of Permanent-Magnet Assisted Synchronous Reluctance Motors", *2019 Research, Invention, and Innovation Congress (RI2C)*, 2019. DOI: 10.1109/RI2C48728.2019.8999926

S. Sriprang, B. Nahid-Mobarakeh, P. Mungporn, N. Takorabet, S. Pierfederici, N. Bizon, P. Kumam and P. Thounthong, "Modeling of One-Loop Flatness-Based Control with State Observer-Based Parameter Estimation for PMSM Drive", *2018 2nd European Conference on Electrical Engineering and Computer Science (EECS)*, 2018. DOI: 10.1109/EECS.2018.00028

S. Sriprang, B. Nahid-Mobarakeh, N. Takorabet, S. Pierfederici, P. Mungporn, P. Thounthong, N. Bizon, P. Kuman and Z. Shah, "Maximum Torque per Ampere and Field-weakening Controls for the High-Speed Operation of Permanent-Magnet Assisted Synchronous Reluctance Motors", *2019 Research, Invention, and Innovation Congress (RI2C)*, 2019. DOI: 10.1109/RI2C48728.2019.8999910

Appendix:

French Version of the Introduction

Avec l'émergence du contrôle orienté champ (FOC), que K. Hasse a proposé à la fin des années 1960 pour les systèmes de moteurs à induction à courant alternatif et le développement des dispositifs de puissance à semi-conducteurs, il a été souligné qu'en théorie, le moteur à induction peut être contrôlé de la même manière que le moteur à courant continu. De plus, les dispositifs de puissance à semi-conducteurs et les micro-ordinateurs se sont développés, et le traitement numérique du signal a permis de construire des convertisseurs de fréquence pour moteurs à courant alternatif, permettant une alimentation en courant triphasé sinusoïdal avec contrôle continu de la fréquence. Ainsi, dans les années 1980, les variateurs de fréquence alimentés par convertisseur de fréquence utilisant le FOC étaient prêts à concurrencer commercialement les variateurs de courant continu. À l'heure actuelle, les machines à induction alimentées par convertisseur de fréquence sont le choix le plus courant dans l'industrie lorsqu'un fonctionnement à vitesse réglable est requis dans la plage de puissance allant de quelques centaines de watts à quelques Mwatts. De plus, récemment, des moteurs à induction à courant alternatif ont été utilisés dans des véhicules électriques (VE); par exemple, comme le montre la figure A1, le moteur électrique se trouve entre les roues arrière de la Tesla Model S, contribuant de manière significative à la répartition du poids avant/arrière de 47/53 %.

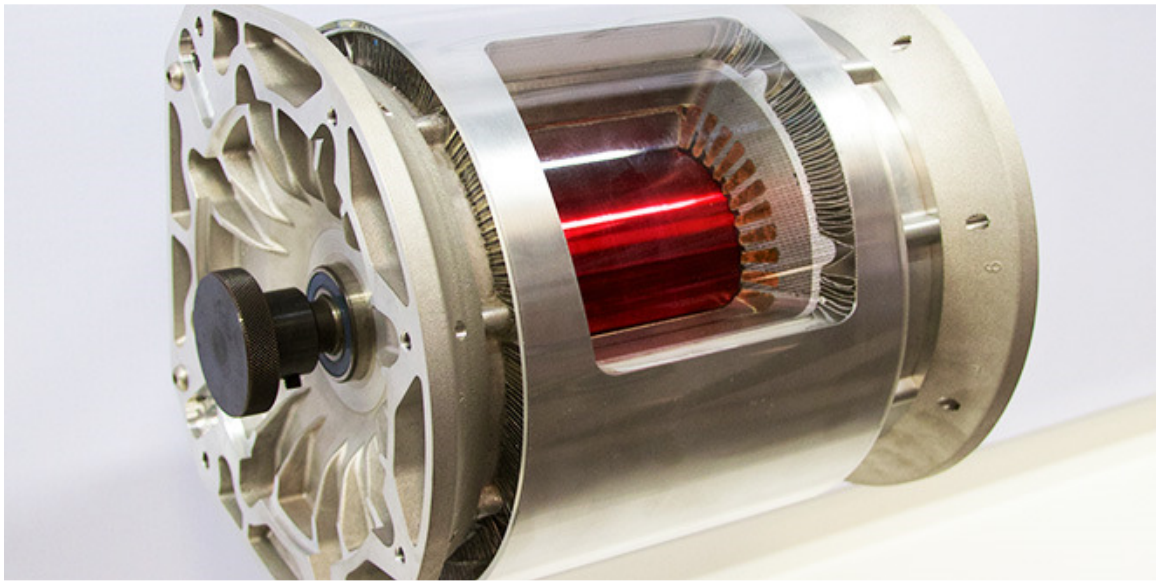

Figure A1. Moteur de traction de la Tesla Model S basé sur un moteur à induction AC [photo publiée avec l'aimable autorisation de CHARGED Electric Vehicles Magazine] [4].

Le moteur est un type à induction AC, dont les principes de base ont été démontrés dans les années 1880 par Nikola Tesla lui-même, et il n'a pas besoin de métaux de terres rares coûteux [1] [2] [3]. Le moteur de pointe de la Model S atteint un rapport puissance/poids élevé. Il génère 362 chevaux (selon les spécifications officielles) et ne pèse que 70 livres avec le refroidissement du rotor coaxial. Cependant, les moteurs à induction se caractérisent par des rendements et des facteurs de puissance relativement faibles par rapport aux moteurs à aimants permanents. Il est possible d'améliorer le rendement des moteurs à induction de forte ou moyenne puissance avec un surcoût acceptable. Néanmoins, pour les machines de faible puissance, les dimensions mécaniques des entrefers restent un obstacle important à l'obtention de performances élevées.

Les machines synchrones à aimants permanents (PMSM) ont un couple et une densité de sortie plus élevés que les machines à induction, mais comme il y a tellement d'aimants permanents, il est devenu un problème de produire des moteurs électriques bon marché avec une efficacité acceptable, et nous voulons éviter l'utilisation de terres rares. aimants permanents. Alternativement, au moins PMSM, minimisez autant que possible ce nombre d'aimants permanents dans la conception, montrant un couple de sortie et une densité plus élevés que les inducteurs, mais le nombre d'aimants permanents utilisés dans la conception est essentiel. De plus, certains inconvénients tels qu'un courant d'axe d important à haute vitesse et le mode générateur incontrôlé suite à des arrêts intempestifs de l'onduleur restreignent les applications véhicules électriques à grande vitesse de ce moteur. Le moteur synchrone à aimant permanent intérieur (IPMSM) a un facteur de sortie et une densité de couple élevés, mais le couple généré par cette machine est principalement un couple magnétique, un couple à faible réluctance et un rapport de saillance (L_d/L_q) pour fonctionner à une large plage de vitesse. . De plus, il peut offrir un fonctionnement à puissance constante par une technique d'affaiblissement de flux. Par conséquent, le moteur moderne à la pointe de la technologie est révolutionné par l'illustration suivante.

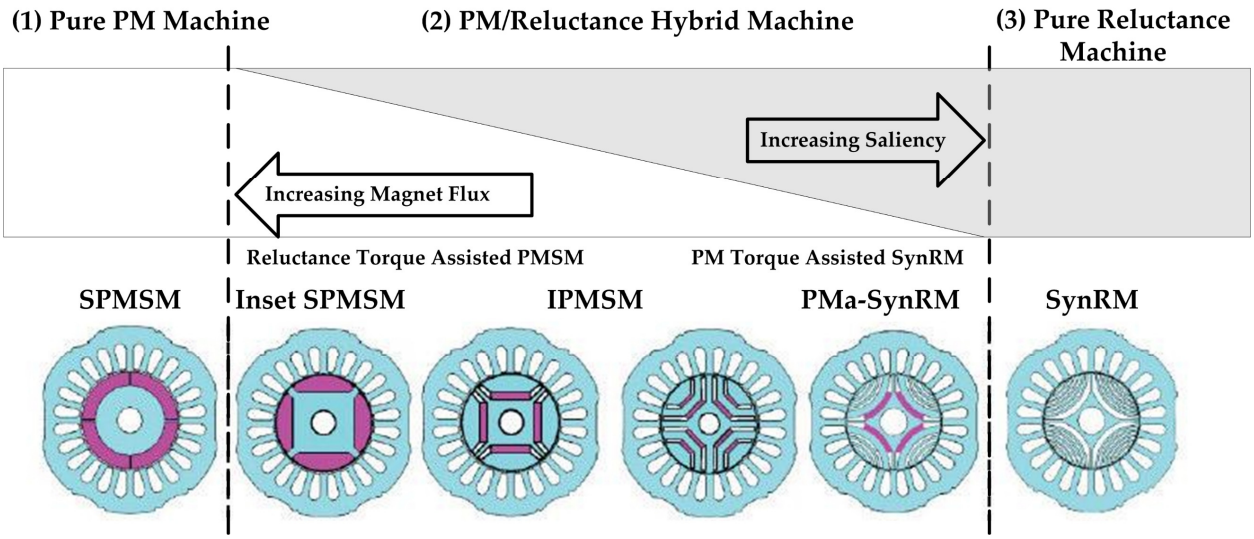

Figure A2. Classification des machines synchrones par mécanisme de génération de couple.

L'investigation ultérieure permet de pallier les inconvénients cités ci-dessus :

- Efforts pour améliorer la technologie de fabrication des ferromagnétiques en abaissant les coûts des produits et en recherchant de nouveaux alliages en vue d'améliorer la qualité des aimants permanents.
- Recherche pour trouver des solutions appropriées pour la structure de la machine afin que le système d'optimisation magnétique utilise des aimants magnétiques peu coûteux mais performants.
- Grâce à l'utilisation de semi-conducteurs de puissance modernes (c'est-à-dire SiC MOSET, GaN FET et semi-conducteurs à large bande interdite) et au traitement du signal numérique en temps réel, l'optimisation de la conception du convertisseur de fréquence et la stabilisation de la sortie sont une machine possible.
- Recherche pour obtenir un contrôle haute performance pour le moteur synchrone à aimants permanents de pointe

Selon la liste décrite ci-dessus, dans le modèle 3, la société Tesla a utilisé un moteur IPM-SynRM (Internal Permanent Magnet - Synchronous Reluctance Motor) [5] [6], également connu sous le nom de PMa-SynRM Permanent Magnet Assisted Synchronous Reluctance Motor [7].

En général, il s'agit d'un type qui combine le type de moteur à aimant permanent interne avec le type de rotor de moteur à réluctance synchrone pour obtenir une caractéristique plus souhaitée dans l'application EV - un rendement élevé à basse et haute vitesse [8]. Tesla n'est pas le premier à utiliser ce type de moteur, mais sa version est considérée

comme l'une des meilleures (tout simplement en raison du rendement élevé et de l'autonomie des voitures Tesla).



Figure A3. Unité d'entraînement Tesla Model 3 [photo publiée avec l'aimable autorisation du magazine CHARGED Electric Vehicles https://insideevs.com] [5] [6].

La figure A3 montre l'unité d'entraînement Tesla modèle 3 utilisant un moteur à réluctance commuté à aimant permanent, et la figure A4 montre l'unité de groupe motopropulseur Tesla modèle 3. L'instruction du stator et du rotor du moteur de traction Tesla modèle 3 est illustrée à la figure A5.

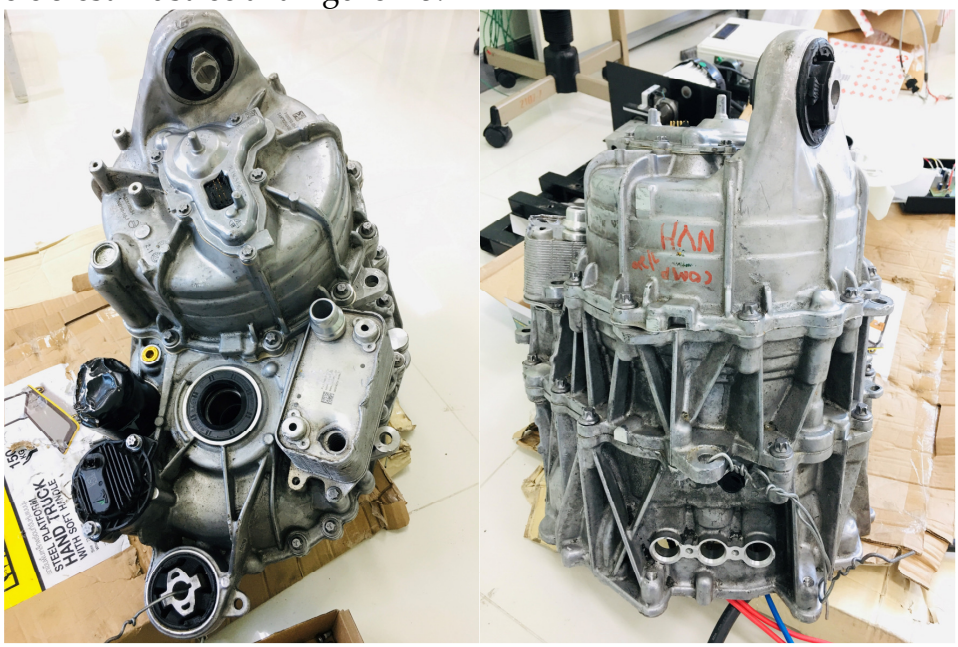

Figure A4. Groupe motopropulseur Tesla Model 3.

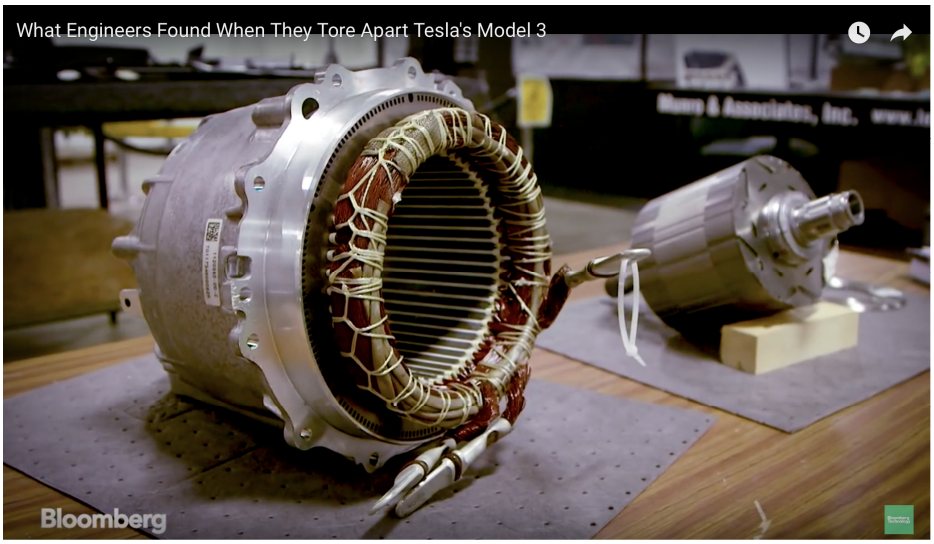

Figure A5. Le stator et le rotor font partie du moteur de traction Tesla Model 3 [photo publiée avec l'aimable autorisation de CHARGED Electric Vehicles Magazine Bloomberg] [9].

Comme on peut le constater, le moteur de traction à la pointe de la technologie du groupe motopropulseur EV souhaite réduire l'utilisation d'aimants permanents afin d'augmenter la vitesse de fonctionnement beaucoup plus large.

De plus, More Electric Aircraft (MEA) [10] [11] est devenu le consensus dans l'industrie et le milieu universitaire en tant que technologie aéronautique de nouvelle génération depuis que ce concept est apparu pour la première fois dans les années 1990. Le concept MEA consiste à utiliser des systèmes électriques dans des applications traditionnellement alimentées par une puissance hydraulique, mécanique ou pneumatique [11]. Des machines électriques vont donc remplacer ces systèmes.

Comme expliqué ci-dessus, la machine moderne a une structure beaucoup plus compliquée, affectant le système de contrôle, et son modèle est devenu beaucoup plus fortement non linéaire. Par conséquent, le contrôle traditionnel tel que le FOC basé sur le contrôleur PI ne suffit pas pour fournir des performances élevées pour toutes les conditions de fonctionnement de ces machines modernes. Tous mentionnés seront abordés dans cette thèse.

Tous les travaux de cette thèse considèrent la conception d'un système de contrôle dans le châssis orienté champ pour les machines à courant alternatif triphasées rotatives, qui comprennent un moteur synchrone à aimant permanent monté en surface. Il s'agit d'un entraînement répandu pour les systèmes d'asservissement hautement dynamiques. Outre le moteur à réluctance synchrone assisté par aimant permanent (PMa-SynRM), une

variante plutôt exotique d'une machine synchrone, la machine sans terres rares la plus prometteuse pour les prochaines générations de véhicules électriques et hybrides.

Le contrôle de la planéité différentielle basé sur un modèle et les schémas MFC sont exécutés pour ces systèmes d'entraînement. Les objectifs spécifiques sont un contrôle hautement performant, c'est-à-dire une réponse de référence rapide et précise, et un contrôle optimisé, c'est-à-dire l'exploitation de l'efficacité énergétique la plus élevée possible. Ici, cependant, certaines limitations s'appliquent. Un problème clé est la sensibilité aux incertitudes provenant des non-linéarités, des perturbations, du bruit, des interactions non modélisées des variables, ou simplement de modèles approximatifs et imprécis. Dans cette thèse, des solutions efficaces à ces problèmes sont proposées en utilisant des observateurs d'état, à la fois l'observateur d'état linéaire et l'observateur non linéaire, comme aide à la conception afin de rendre ces techniques adaptées à la pratique industrielle.

Le modèle mathématique de SPMSM et de PMa-SynRM est analysé et validé par simulation basée sur l'environnement logiciel MATLAB/SIMULINK au chapitre 2. Le chapitre 2 a également proposé le FOC basé sur le contrôleur PI traditionnel appliqué à SPMSM et PMa-SynRM. De plus, le couple maximal par ampère (MTPA) est appliqué au variateur PMa-SynRM pour optimiser le contrôle de la boucle de courant interne du courant de l'axe d et de l'axe q. Le prototype PMa-SynRM réalise pratiquement toutes les solutions présentées à l'Université de Lorraine.

La robustesse du contrôle basé sur la planéité différentielle aux incertitudes des paramètres du modèle et aux perturbations variant dans le temps est discutée au chapitre 3. Le contrôle basé sur la planéité différentielle est appliqué aux variateurs SPMSM et PMa-SynRM. La simulation du contrôle proposé est réalisée par le logiciel MATLAB/SIMULINK, et la validation expérimentale par rapport à la simulation est démontrée. par le prototype PMa-SynRM en laboratoire. De plus, un observateur d'état basé sur l'observation de l'état de Luenberger par rapport à un observateur d'état non linéaire basé sur la stabilité asymptotique et la stabilité exponentielle est proposé pour améliorer les performances de contrôle basées sur la platitude différentielle conduisant à un compromis entre les deux méthodes. Il peut améliorer la robustesse paramétrique dans une mesure suffisante tout en maintenant de bonnes performances de contrôle. De plus, il découple de manière robuste le contrôleur de l'estimateur de perturbation, de sorte que le mécanisme d'atténuation des perturbations peut être réglé extrêmement rapidement. Ensuite, les effets de perturbation variant dans le temps tels que ceux résultant de la chute de tension aux bornes des dispositifs électroniques de puissance de l'onduleur triphasé et de l'enroulement du moteur peuvent être atténués sans les identifier explicitement.

Le schéma de contrôle résultant est très performant ; il a une forte capacité de suivi et, en même temps, offre un bon rejet des perturbations. De plus, il est très robuste aux incertitudes paramétriques et moins sensible au bruit mesurable. Ces avantages sont mis en évidence par la comparaison avec le FOC basé sur un contrôleur PI traditionnel au chapitre 2 et par la validation expérimentale sur les deux types de PMSM nommés au chapitre 3.

Le chapitre 4 développe une nouvelle approche de contrôle non linéaire basée sur un contrôle non modélisé appelé Model-Free Control (MFC). Le MFC pour les incertitudes des paramètres du modèle et les perturbations variant dans le temps est discuté au chapitre 4. Après une brève introduction des principes fondamentaux du MFC, la conception est illustrée en détail, donnant une discussion étape par étape des principaux points critiques et des conseils. pour leur maniement réussi. Des suggestions pour étendre la conception à différents contrôleurs de lecteur sont également incluses. Le schéma de contrôle résultant est très performant ; il a une forte capacité de suivi et, en même temps, offre un bon rejet des perturbations.

De plus, il est très robuste aux incertitudes paramétriques et moins sensible au bruit mesurable. Ces avantages sont mis en évidence en comparant le FOC basé sur un contrôleur PI traditionnel au chapitre 2 et le contrôle différentiel basé sur la planéité avec un observateur d'état non linéaire au chapitre 3 et la validation expérimentale sur le SPMSM et le PMa-SynRM. De manière significative, le PMa-SynRM convient à la traction des véhicules électriques au lieu des machines permanentes coûteuses telles que SPMSM et IPMSM. Par conséquent, cette machine a la capacité requise pour les systèmes de traction des véhicules électriques et hybrides. En conclusion, en utilisant MFC, les performances de PMa-SynRM ont considérablement amélioré non seulement la boucle de contrôle de courant interne, mais également la boucle de contrôle de vitesse externe. De plus, le coefficient de contrôleur du MFC proposé n'est pas compliqué à définir et à obtenir le système de contrôle approprié pour le variateur SPMSM et PMa-SynRM.

Les aspects les plus importants du travail sont conclus à la fin de cette thèse, où un aperçu des travaux futurs possibles est donné.

Battery Electric Vehicles (BEV) - Inverter

	2018 Tesla Model 3 Inverter	2019 Nissan Leaf Inverter	2019 Jaguar I-Pace Inverter
			
Cost (USD)	$810.54	$468.41	$555.29
Max. Input Voltage (V_{DC})	430	450	500
Dimensions (mm)	370 x 278 x 122	386 x 386 x 223	407 x 272 x 83
Parts / Fasteners	1275 / 44	1287 / 56	2185 / 106
Weight (kg)	4.81	11.15	8.23
Coolant Medium	Water/Glycol	Water/Glycol	Water/Glycol

Cost and weights include: Housing, PCBA, IGBT Module & Cooling Structure, DC-link Capacitor, Motor Phase Lead, Connectors, Self-contained structural and connected components.

Figure A6. Onduleur pour véhicules électriques à batterie [photo publiée avec l'aimable autorisation de chargedevs.com] [12].

La figure A6 compare l'onduleur du groupe motopropulseur utilisé dans l'onduleur de traction commercial, y compris Tesla Model 3, Nissan Leaf et Jaguar I-Pace. L'onduleur de traction d'un véhicule électrique joue un rôle essentiel en tant qu'unité de conversion de puissance (PCU), qui convertit la batterie CC en courant alternatif triphasé pour le bon fonctionnement du moteur de traction électrique.

Actuellement, la recherche et le développement de nouveaux composants électroniques évoluent constamment, et avec eux aussi les résultats obtenus [13] [14] [15]. En conséquence, les entreprises développent continuellement des appareils de plus en plus performants caractérisés par une plus grande efficacité et de meilleures caractéristiques électriques. La technologie du carbure de silicium (SiC) [16] [17] offre des avantages certains parmi les technologies potentielles, principalement liés à sa résistance électrique. Grâce à cette technologie, il est possible d'obtenir la même résistance qu'avec la technologie à base de silicium mais en utilisant une masse plus faible. Des composants plus petits et plus efficaces peuvent ainsi être développés. De plus, comme les pertes de commutation sont réduites, il est possible de fonctionner à des fréquences plus élevées en utilisant des composants passifs plus petits.

De plus, les dispositifs en carbure de silicium peuvent fonctionner à des températures plus élevées et peuvent être conçus avec une conception thermique réduite. Ils offrent donc une solution idéale pour le domaine automobile. D'autres avantages découlant de l'utilisation du SiC sont les suivants [13] : des pertes de puissance, jusqu'à dix fois inférieures, peuvent être atteintes ; les appareils peuvent fonctionner à des

tensions plus élevées, avec un champ électrique de coupure (V/cm) décuplé ; le coefficient de refroidissement a triplé (conductivité thermique W/cm x °C) ; un facteur de 10 améliore la réponse en fréquence. Ces caractéristiques électriques et physiques exceptionnelles expliquent pourquoi la plupart des entreprises utilisent le carbure de silicium comme technologie principale.

Si aujourd'hui, les transistors bipolaires à grille isolée silicium (Si IGBT) dominent la gamme moyenne puissance, y compris les onduleurs pour véhicules électriques, ces technologies passent désormais à une sixième génération, avec des matériaux semi-conducteurs à large bande interdite prenant le relais : carbure de silicium pour la haute tension/ applications électriques et nitrure de gallium (GaN) pour une tension et une puissance inférieures. Ce changement permet à des modules d'alimentation plus petits et à plus haute densité de fonctionner à des températures plus élevées et crée de nouvelles opportunités de matériaux dans l'emballage du module d'alimentation.

Comme le montre la figure A6, l'onduleur de Tesla a utilisé le MOSFET SiC du modèle 3 en 2018, et Tesla est devenue la première entreprise à ajouter des MOSFET SiC, provenant de ST Microelectronics dans une conception d'onduleur interne. La conception globale comporte plusieurs innovations au-delà de l'utilisation de boîtiers SiC, mais c'est la principale. Ainsi, le poids total de l'onduleur (4,8 kg) est inférieur de moitié à celui de la Nissan Leaf 2019 (11,15 kg) et plus d'un tiers inférieur à celui de la Jaguar I-PACE (8,23 kg), qui utilise Si IGBT. onduleurs et pièces du commerce.

L'utilisation de MOSFET SiC crée en outre de nouvelles opportunités de matériaux à mesure que les limites des matériaux traditionnels sont repoussées. Cependant, comme pour toute technologie émergente, le coût a été le principal obstacle à l'adoption des MOSFET SiC et d'autres matériaux habilitants dans les boîtiers de modules de puissance. Néanmoins, Tesla semble avoir résolu ce problème également : son onduleur a subi une baisse remarquable des coûts en seulement trois ans. L'onduleur SiC de Tesla semble déjà être à égalité avec les modules Si IGBT utilisés dans les versions 2019 de la Nissan Leaf et de la Jaguar I-PACE, comme le montre la figure A7. Le résultat est que la combinaison globale de l'onduleur et du PMa-SynRM de Tesla est l'une des meilleures du marché, atteignant une efficacité de 97 %, offrant une plus grande autonomie sans augmenter la capacité coûteuse de la batterie. Le tout à un coût similaire à celui des anciennes technologies déplacées [18] [19] [20].

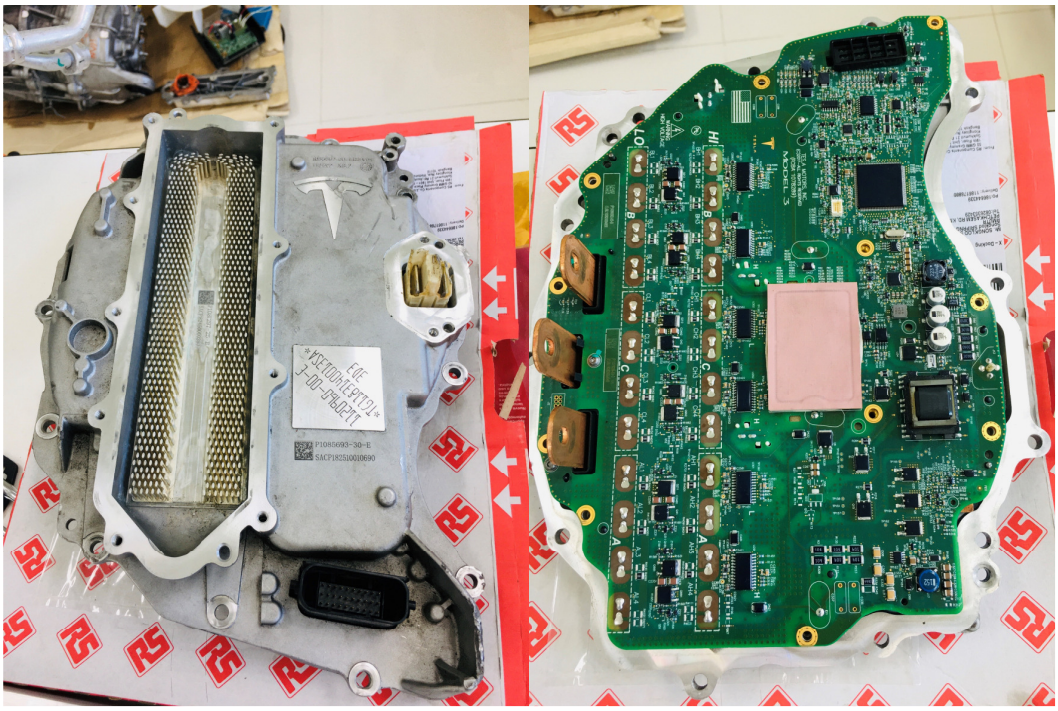

Figure A7. Onduleur SiC MOSFET de Tesla provenant de ST Microelectronics.

Jusqu'à présent, outre la meilleure conception de la combinaison moteur du groupe motopropulseur et onduleur SiC MOSFET, l'amélioration de l'entraînement global pourrait être possible en utilisant des algorithmes de contrôle plus avancés. Avec l'avènement des microprocesseurs à grande vitesse, la mise en œuvre de procédures de contrôle avancées a été possible.

Au cours des dernières années, le convertisseur de fréquence et le FOC ont contribué de manière significative au regain d'intérêt pour le PMa-SynRM. Avec le développement de nouvelles technologies, en particulier dans l'électronique numérique (c'est-à-dire le microcontrôleur, le traitement numérique rapide du signal en temps réel) et les dispositifs à semi-conducteurs de puissance, comme mentionné précédemment dans la section précédente, les performances des variateurs synchrones se sont améliorées. L'amélioration des performances du variateur et un fonctionnement synchrone stable jusqu'à des vitesses très faibles, y compris l'arrêt, ont été possibles en utilisant le FOC ou le contrôle vectoriel basé sur le contrôleur PI. Cependant, la réalisation de cette opération était compliquée par l'utilisation d'une commande V/f conventionnelle. De manière significative, le PMa-SynRM a une structure beaucoup plus compliquée, affectant le système de contrôle, et son modèle est devenu beaucoup plus fortement non linéaire. Par conséquent, le contrôle traditionnel tel que le FOC basé sur le contrôleur PI ne suffit pas pour fournir des performances élevées dans toutes les conditions de

fonctionnement. Ainsi, plusieurs méthodes de commande non linéaire ont été proposées au cours des dernières années pour faire face à ce problème.

La principale limitation de la plupart des travaux sur le contrôle optimal de PMa-SynRM est l'utilisation d'un modèle idéal pour effectuer une analyse théorique et une mise en œuvre pratique. La plupart des algorithmes de contrôle modernes sont basés sur un modèle (MBC) et dépendent des paramètres. Cependant, dans une machine réelle, les effets de la saturation et des pertes fer se traduisent par un écart de l'angle courant par rapport au point de fonctionnement optimal. De plus, les variations des paramètres PMa-SynRM dues à la température et au flux d'entrefer ont été rapportées dans la littérature et discutées dans cette thèse. Par conséquent, la connaissance des périmètres moteurs et un modèle plus réaliste sont cruciaux pour un contrôle optimal.

Dans le contrôle du courant d'un système d'entraînement PMSM, l'objectif crucial est de garantir que les courants du stator suivent leurs valeurs de référence avec un minimum d'erreurs dans les conditions transitoires et en régime permanent. Quelques approches de contrôle de courant ont été appliquées pour de meilleures performances de suivi de courant, comme proposé dans les documents suivants.

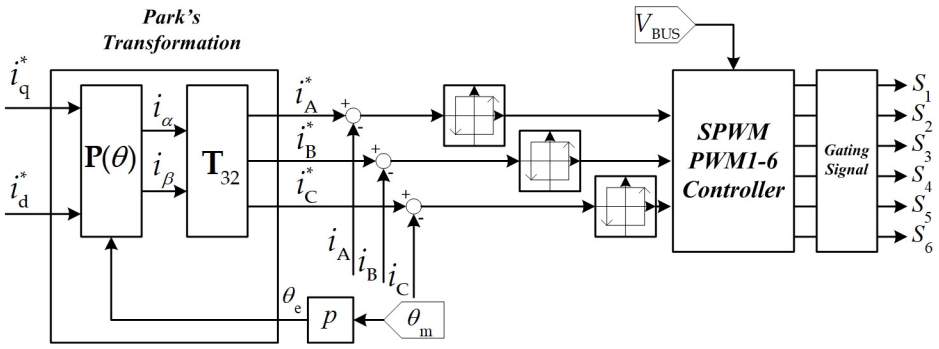

Figure A8. Le contrôle du courant du stator basé sur des comparateurs à hystérésis génère directement des signaux de grille vers l'onduleur triphasé.

Comme l'illustre la Figure 1.8 [21], les schémas de contrôle basés sur l'hystérésis sont connus depuis longtemps comme un moyen simple et efficace d'obtenir des réponses dynamiques rapides. Cependant, les implémentations les plus simples de la commande de courant d'hystérésis (HCC) sont caractérisées par une fréquence de commutation variable, des variations dépendant de la charge de la fréquence de commutation moyenne et des possibilités de fonctionnement à cycle limite avec une commutation à haute fréquence comme inconvénients bien connus.

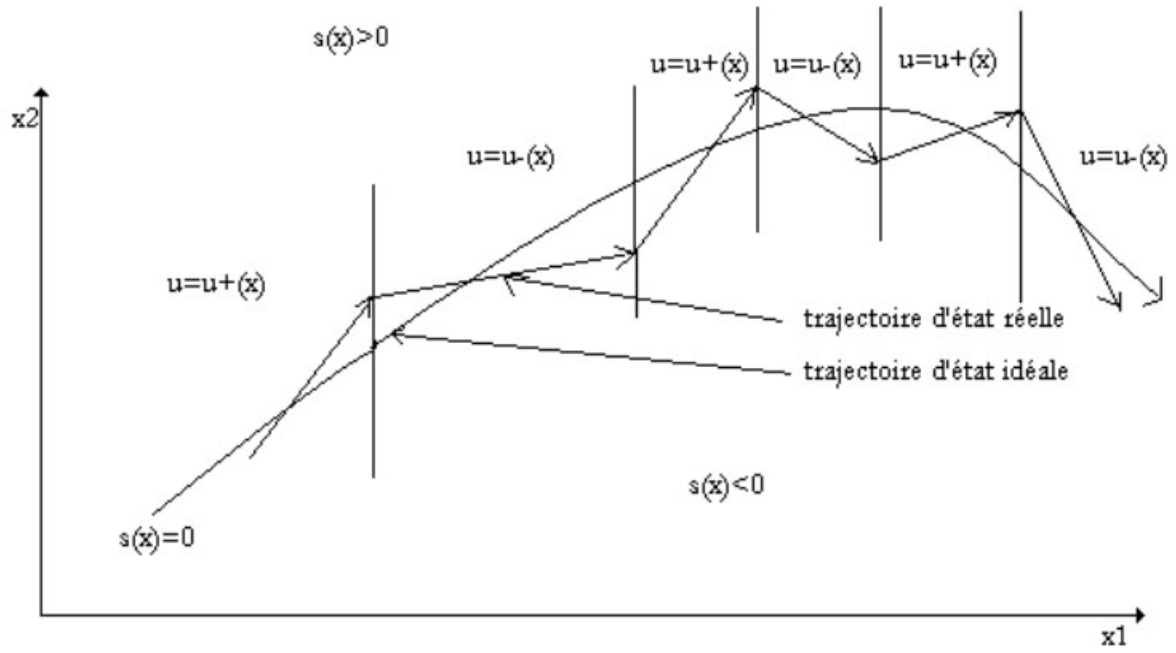

Figure A9. Définition du contrôle du mode glissant.

La commande par mode glissant (SMC) [22] [23] présente des avantages intéressants de robustesse aux perturbations et de faible sensibilité aux variations des paramètres du système. Comme définition dans la figure A9. la commande SMC offre une réponse dynamique rapide. Cependant, le phénomène de broutage existe dans la commande glissante classique [24] [25].

P. Thounthong a proposé un contrôle différentiel de vitesse/couple basé sur la planéité avec des observateurs d'état des entraînements SPMSM. Il est classé comme un contrôle basé sur un modèle proposé pour un système non linéaire, en particulier un système fortement non linéaire. La combinaison du contrôle différentiel basé sur la planéité et de l'observateur d'état permet d'améliorer l'entraînement SPMSM global. De plus, le contrôle différentiel basé sur la planéité présente une robustesse attrayante aux perturbations et une faible sensibilité aux variations des paramètres du système par rapport au FOC basé sur le contrôleur PI traditionnel.

Jusqu'à présent, afin de concevoir un contrôleur robuste avec des performances de suivi acceptables, toutes les méthodes de contrôle basées sur un modèle mentionnées nécessitent une bonne connaissance de la dynamique et du modèle du système étudié. Étant donné que la variation dynamique inattendue du système et les erreurs paramétriques sont courantes dans les applications industrielles, les performances du MBC peuvent être affectées dans de telles conditions. Cependant, dans les applications industrielles et en particulier dans les systèmes non linéaires complexes, il est assez délicat et long de trouver un modèle dynamique correct du système étudié. De plus, étant

donné que les méthodes MBC nécessitent un modèle précis du système contrôlé pour concevoir le contrôleur, ces méthodes peuvent ne pas être applicables pour les systèmes dont le modèle n'est pas disponible. Ainsi, pour surmonter la limitation de MBC, l'industrie exige des contrôleurs moins dépendants du modèle du système.

Ainsi, la technique de commande prédictive de modèle (MPC) a été proposée comme schéma de commande de courant approprié pour les machines électriques. MPC présente des avantages tels qu'une réponse dynamique élevée, une dynamique rapide, un concept simple et une structure simple, et par conséquent, il a attiré une attention favorable dans le système d'entraînement PMSM. Certaines des méthodes de contrôle prédictif couramment utilisées comprennent le contrôle prédictif deadbeat (DPC), le contrôle prédictif du modèle d'ensemble de contrôle continu (CCS-MPC) et le contrôle prédictif du modèle d'ensemble de contrôle fini (FCS-MPC) [27]. DPC est simple à mettre en œuvre. Cependant, il est très réactif aux incertitudes et aux perturbations [28]. Le processus de calcul complexe de CCS-MPC est un obstacle aux applications avec le processeur numérique. FCS-MPC prédit les états futurs du système contrôlé sur la base de l'ensemble de vecteurs de tension finis et du modèle mathématique, et le vecteur de tension optimal est choisi en fonction de la fonction de coût. Il utilise la nature discrète de l'onduleur et conçoit l'implémentation en temps réel de la commande multi-contraintes non linéaires [29]-[30] [31]. Le principe de cette méthode est basé sur la prédiction des variables contrôlées dans l'étape de calcul suivante en utilisant les variables mesurées et un modèle mathématique du système contrôlé. Ensuite, analyser les résultats prédits à l'aide d'une fonction de coût liée à la différence entre les trajectoires souhaitées du système et les sorties réelles. Par rapport aux techniques de contrôle mentionnées précédemment, la sécurité et la dynamique rapide sont deux caractéristiques remarquables de la méthode MPC.

Malgré ces avantages, puisque le MPC utilise un modèle mathématique dans la section de prédiction, ses performances dépendent de l'exactitude du modèle [31]. De plus, en utilisant la prédiction à chaque instant d'échantillonnage des algorithmes MPC, importez quelques calculs mathématiques supplémentaires dans l'algorithme de contrôle.

Afin de résoudre les problèmes mentionnés précédemment, faire face à ces limitations de MPC et MBC clarifie le rôle crucial du développement du contrôle sans modèle, qui est présenté dans cette thèse. Ce concept s'appliquera aux variateurs SPMSM et PMa-SynRM. En outre, une comparaison entre le MFC proposé et le FOC basé sur le contrôleur PI et le contrôle différentiel basé sur la planéité est également discutée en termes de réponse dynamique et de performances des différentes méthodes de contrôle.

Pour le système d'entraînement PMa-SynRM, de nombreux articles ont été proposés dans les revues de littérature suivantes. Peyman Niazi [32] a proposé pour la première fois l'estimation des paramètres en ligne de PMa-SynRM avec FOC basée sur le contrôleur PI en 2007. La solution proposée basée sur MBC est introduite dans ce travail. Une procédure différente dans [33] a été introduite pour un contrôle sans capteur robuste pour PMa-SynRM. L'autre, une nouvelle méthode de contrôle direct du couple (DTC) basée sur le couple maximal par ampère (MTPA), est proposée dans [34]. Comme mentionné ci-dessus, MBC présente un inconvénient avec une exigence de modèle exact du système contrôlé pour concevoir le contrôleur. De plus, les liaisons de flux des axes d et q dépendent de manière significative de la variation des courants des axes d et q. Par conséquent, les inductances doivent être considérées par le rapport entre les variations de liaison de flux et la légère augmentation du courant [35]. Par conséquent, les inductances doivent être considérées par le rapport entre les variations de liaison de flux et la légère augmentation du courant. Ce phénomène est présenté dans cette thèse afin d'obtenir un contrôle non linéaire performant de PMa-SynRM.

La classification au choix de PMa-SynRM présente au chapitre 2. Le rotor à lamelles transversales (TLA) ou à barrière à flux multiples est choisi car il est réalisé par poinçonnage traditionnel ou découpage au fil. En conséquence, la construction est facile et bon marché, comme le montre la figure A10.

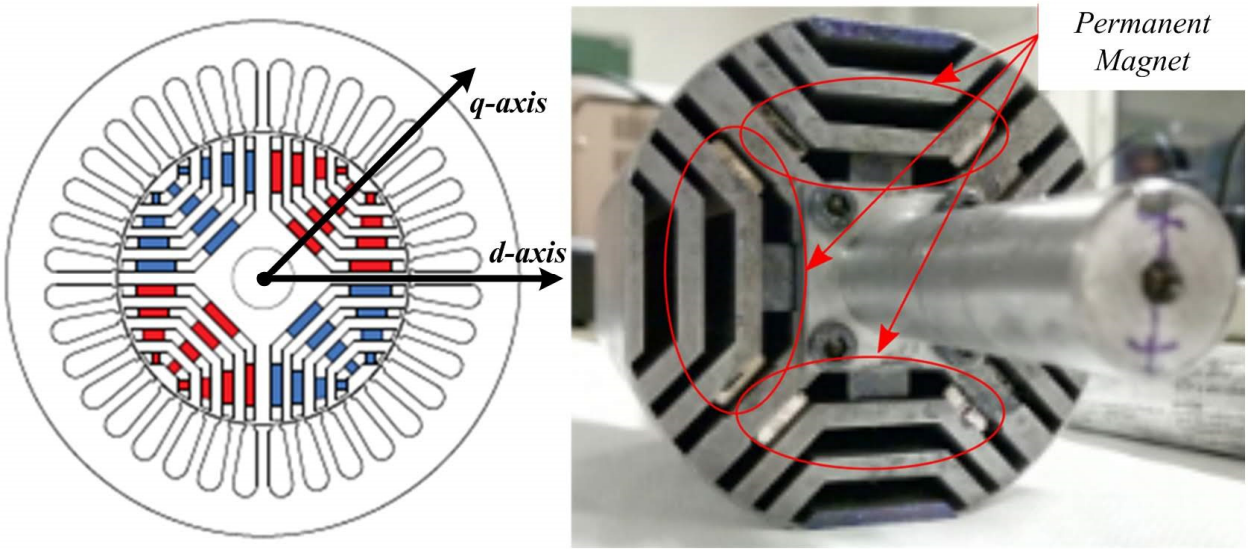

Figure A10. Structure rotorique PMa-SynRM [37].

Dans le chapitre 2, les modèles mathématiques systémiques des trois grandes variétés de machines synchrones à aimants permanents, à savoir le moteur synchrone à aimants permanents monté en surface (SPMSM), le moteur synchrone à aimants permanents intérieurs (IPMSM) et le moteur à réluctance synchrone assisté par aimants

permanents (PMa- SynRM), sont analysés dans les cas linéaires et non linéaires. Ensuite, sur la base du modèle mathématique, des modèles de simulation dynamique des différents types de machines sont réalisés par le logiciel MATLAB/-SIMULINK. Une simulation et une expérimentation de la commande orientée champ (FOC) basée sur la compensation PI traditionnelle sont d'abord menées pour étudier les paramètres et le comportement des machines. Les résultats indiquent que PMa-SynRM peut atteindre un fonctionnement à vitesse supérieure à 70 % et que l'algorithme MTPA proposé a fourni un système de contrôle des pertes de cuivre minimisé du variateur PMa-SynRM. De plus, avec l'avantage du PMa-SynRM, grâce à un faible flux magnétique par rapport à l'IPMSM, il peut fonctionner au-delà d'une vitesse nominale en utilisant une technique de contrôle par affaiblissement de champ. Ce schéma de contrôle a été validé à la fois par simulation et par expérience. Enfin, la conception et le contrôle d'un moteur à réluctance synchrone assisté par un aimant permanent avec minimisation des pertes de cuivre à l'aide de MTPA sont présentés en utilisant un prototype PMa-SynRM. Cependant, le FOC basé sur le contrôleur PI traditionnel ne peut pas traiter une propriété non linéaire de PMa-SynRM.

Le chapitre 3 a introduit un contrôle basé sur un modèle basé sur un contrôle différentiel basé sur la planéité avec un observateur d'état de l'estimation des paramètres en ligne. Le contrôle basé sur la planéité est un outil de conception puissant car il s'agit d'une simplification. De nombreuses équations peuvent être clarifiées et réduites à une seule équation centrale à l'aide d'un contrôle basé sur la planéité. Le terme "planéité" ne décrit pas un algorithme de contrôle spécifique ; il s'agit en effet d'une démarche générale d'analyse et de conception de systèmes dynamiques. Ce concept est rapidement devenu une branche essentielle dans la conception de systèmes de commande non linéaires à temps continu. Outre la réussite scolaire, il a trouvé sa place dans des applications industrielles. Cette thèse applique l'approche basée sur la planéité différentielle aux systèmes d'entraînement PMSM. Deux schémas de contrôle haute performance sont étudiés, le contrôle basé sur la planéité différentielle et le contrôle basé sur la planéité différentielle avec observateur d'état.

Dans le chapitre 3, le SPMSM et le PMa-SynRM ont été réalisés sous la forme d'une représentation d'espace d'état pour définir une variable d'état, une variable d'entrée et une variable de sortie, puis une sortie plate candidate déterminée. Un système est dit différentiellement plat s'il existe une fonction de sortie. Par conséquent, les ensembles d'équations SPMSM et PMa-SynRM sont désignés comme la paramétrisation différentielle des variables système et sont utilisés dans la conception du contrôleur comme réalisé dans les sections 3.2 et 3.4. Une loi de contrôleur est définie pour gérer l'incertitude des paramètres et assurer que l'état mesurable converge vers celui souhaité. De plus, la planification de trajectoire est également expliquée afin de limiter l'action

différentielle de la variable de commande. Enfin, le coefficient de la loi du contrôleur est déterminé par une définition d'équation standard du second ordre et une fréquence de section transversale définie en tenant compte de la fréquence de commutation. Ils peuvent être réglés expérimentalement pour obtenir une réponse système optimisée.

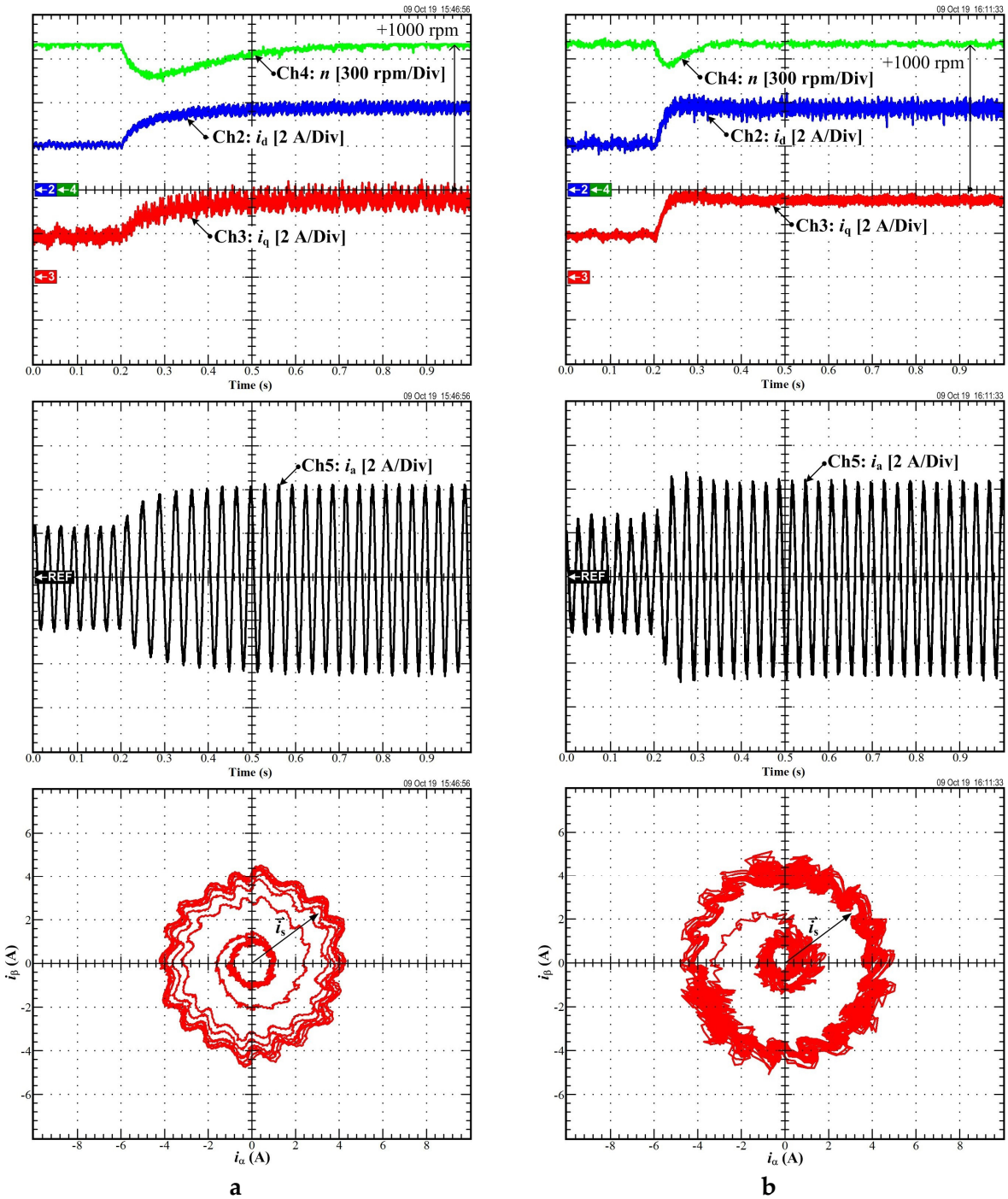

Figure A11. Résultats expérimentaux : Rejet des perturbations (a) Contrôleur PI basé sur FOC (b) Contrôle basé sur la planéité différentielle.

Le prototype PMa-SynRM et le banc d'essai du laboratoire SPMSM assurent la simulation et la validation expérimentale. Comme on peut le voir, la simulation et les résultats expérimentaux reflètent que le contrôle différentiel basé sur la planéité offre des performances significativement élevées pour les variateurs SPMSM et PMa-SynRM par rapport au FOC basé sur le contrôleur PI traditionnel comme dans la figure A11. Cependant, le contrôle basé sur la planéité différentielle est un système de contrôle basé sur un modèle. Par conséquent, ses performances dépendent des paramètres du système. Par conséquent, un nouvel observateur d'état est introduit pour obtenir des performances significativement élevées pour les lecteurs SPMSM et PMa-SynRM pour traiter le problème.

Le chapitre 4 a proposé le contrôle sans modèle (MFC) pour traiter le problème d'un obstacle au contrôle basé sur un modèle (MBC). Généralement, dans la plupart des systèmes de contrôle de PMa-SynRM, les contrôleurs dépendent des paramètres et leurs performances reposent sur la connaissance des paramètres du moteur. Par exemple, des paramètres électriques, tels que les inductances d'axe dq et la résistance d'enroulement, sont généralement nécessaires pour concevoir des contrôleurs de boucle de courant internes. En revanche, les paramètres mécaniques, tels que le moment d'inertie combiné (J) et le coefficient de frottement visqueux (Bf), sont cruciaux pour la conception des contrôleurs de boucle de vitesse. La plupart des techniques d'optimisation de la production de couple sont sensibles aux paramètres machines. Malheureusement, la résistance du stator et le flux des aimants permanents varient avec la température du moteur. De plus, les paramètres mécaniques varient généralement de manière significative avec les dimensions et la forme des charges mécaniques. Ainsi, des applications généralement pratiques, l'estimation des paramètres en ligne pour les paramètres nécessaires sont nécessaires pour obtenir une production de couple maximale et des performances élevées. Les performances des stratégies de contrôle avancées dépendant des paramètres peuvent être améliorées en utilisant le modèle hors ligne des paramètres du moteur. Cependant, cela nécessite beaucoup de calculs en raison de la non-linéarité due à la saturation en fer. De plus, de tels calculs sont généralement déraisonnables en temps réel.

De nombreux tests expérimentaux sont effectués pour analyser l'efficacité du contrôleur développé dans lequel les résultats obtenus valident fortement les performances de simulation de MFC. De plus, par rapport à la méthode de commande basée sur l'observation, puisque le MFC ne dépend pas des paramètres du système, ses performances de suivi sont plus acceptables lors de variation de charge ou de point de fonctionnement.

En conclusion, cette thèse a atteint l'objectif principal de découvrir le contrôle non linéaire haute performance de PMa-SynRM. Utilisation d'un prototype de variateur PMa-SynRM comme banc d'essai fourni par GREEN Lab. à l'Université de Lorraine, cet article donne une description exhaustive de la procédure de conception d'un MFC appliquée à la commande combinée de vitesse et de courant d'un moteur. Après une brève introduction des principes fondamentaux du MPC, la conception est illustrée en détail, donnant une discussion étape par étape des principaux points critiques et des conseils pour leur manipulation réussie. Des suggestions pour étendre la technique à différents contrôleurs de lecteur sont également incluses. Des simulations et de nombreux résultats expérimentaux mettent en évidence les fonctionnalités et caractéristiques prometteuses du MFC appliquées aux variateurs PMSM. Comme dernière contribution, les potentiels MFC soulignés dans cette thèse devraient stimuler une exploration et une étude plus approfondies sur ce type de contrôleur pour atteindre la familiarité nécessaire pour transférer les résultats vers des applications pratiques. Pour résumer plus précisément, la comparaison des avantages traditionnels du FOC + PI, du contrôle basé sur la planéité et du contrôle sans modèle est présentée ci-dessous.

Traditional FOC+PI	**Flatness-Based Control**	**Model-Free Control**
- Plus adapté à un système d'entraînement par moteur linéaire - Coefficient de contrôleur de conception à l'aide de la transformée de Laplace - Contrôler les performances en fonction des paramètres du système	- Plus efficace avec un système de motorisation non linéaire - Système de contrôle basé sur un modèle - Contrôler les performances en fonction des paramètres du système - Amélioration des performances à l'aide de l'observateur - Nécessite plus de ressources de calcul	- Dédié au contrôle de systèmes inconnus ou partiellement connus - Paramètres partiellement connus (inductance pour le contrôle du courant)

REFERENCES

[1] C. Chan, "The state of the art of electric and hybrid vehicles", *Proceedings of the IEEE*, vol. 90, no. 2, pp. 247-275, 2002.

[2] M. Zeraoulia, M. Benbouzid and D. Diallo, "Electric Motor Drive Selection Issues for HEV Propulsion Systems: A Comparative Study", *IEEE Transactions on Vehicular Technology*, vol. 55, no. 6, pp. 1756-1764, 2006.

[3] N. Hashemnia and B. Asaei, "Comparative study of using different electric motors in the electric vehicles", *2008 18th International Conference on Electrical Machines*, 2008.

[4] C. MORRIS, "Elon Musk: Cooling, not power-to-weight ratio, is the challenge with AC induction motors," November 4, 2014. [Online]. Available: https://chargedevs.com/newswire/elon-musk-cooling-not-power-to-weight-ratio-is-the-challenge-with-ac-induction-motors/.

[5] M. KANE,"First Up Close Look At Tesla Model 3 Drive Unit, Battery, Cooling & More," July 26,2018. [Online]. Available:https://insideevs.com/news/339774/first-up-close-look-at-tesla-model-3-drive-unit-battery-cooling-more/.

[6] M. KANE,"Tesla Model 3's IPM-SynRM Electric Motor Explained," Dec 22,2020. [Online]. Available:https://insideevs.com/news/461811/video-tesla-model-3-electric-motor-explained/.

[7] B. Sarlioglu, C. Morris, D. Han and S. Li, "Driving Toward Accessibility: A Review of Technological Improvements for Electric Machines, Power Electronics, and Batteries for Electric and Hybrid Vehicles", *IEEE Industry Applications Magazine*, vol. 23, no. 1, pp. 14-25, 2017.

[8] C. Chan, "The State of the Art of Electric, Hybrid, and Fuel Cell Vehicles", *Proceedings of the IEEE*, vol. 95, no. 4, pp. 704-718, 2007.

[9] Bloomberg, "What Engineers Found When They Tore Apart Tesla's Model 3," [Online]. Available:https://www.bloomberg.com/news/videos/2018-10-17/what-engineers-found-when-they-tore-apart-telsa-s-model-3-video.

[10] J. Weimer, "Electrical power technology for the more electric aircraft", *[1993 Proceedings] AIAA/IEEE Digital Avionics Systems Conference*. Available: 10.1109/dasc.1993.283509 [Accessed 4 January 2022].

[11] B. Sarlioglu and C. Morris, "More Electric Aircraft: Review, Challenges, and Opportunities for Commercial Transport Aircraft", *IEEE Transactions on Transportation Electrification*, vol. 1, no. 1, pp. 54-64, 2015.

[12] S. MUNRO, "Tesla's Inverter Technology Versus Other BEVs," April 19-22, 2021. [Online]. Available:https://chargedevs.com/teslas-inverter-technology-versus-other-bevs-ondemnad/.

[13] H. Kim, H. Chen, J. Zhu, D. Maksimovic and R. Erickson, "Impact of 1.2kV SiC-MOSFET EV traction inverter on urban driving", *2016 IEEE 4th Workshop on Wide Bandgap Power Devices and Applications (WiPDA)*, 2016.

[14] T. Burress, "Evaluation of the 2010 Toyota Prius hybrid synergy drive system", Oak Ridge National Laboratory (ORNL); *Power Electronics and Electric Machinery Research Facility Technical Report* ORNL/TM-2010/253.

[15] T. Burress, "Benchmarking state-of-the-art technologies", *Oak Ridge National Laboratory (ORNL) 2013 U.S. DOE Hydrogen and Fuel Cells Program and Vehicle Technologies Program Annual Merit Review and Peer Evaluation Meeting*.

[16] J. Reed, J. McFarland, J. Tangudu, E. Vinot, R. Trigui, G. Venkataramanan, S. Gupta and T. Jahns, "Modeling power semiconductor losses in HEV powertrains using Si and SiC devices", *2010 IEEE Vehicle Power and Propulsion Conference*, 2010.

[17] D. Aggeler, J. Biela and J. W. Kolar, "A compact high voltage 25 kW 50 kHz DC-DC converter based on SiC JFETs", Proc. *IEEE Applied Power Electronics Conference and Exposition*, pp. 801-807, 2008.

[18] Editorial Team, “Tesla’s Innovative Power Electronics: The Silicon Carbide Inverter,"Feb 23, 2021. [Online]. Available:https://www.eedesignit.com/teslas-innovative-power-electronics-the-silicon-carbide-inverter.

[19] Editorial Staff, “Benefits of SiC MOSFET in powertrain inverter for automotive applications, “May 27, 2019. [Online]. Available:https://www.powerelectronicsnews.com/benefits-of-sic-mosfet-in-powertrain-inverter-for-automotive-applications.

[20] Wolfspeed,"Designed to Support High-Voltage EV Powertrain Systems," [Online]. Available: HTTPs://www.wolfspeed.com/ev-powertrain.

[21] J. Suul, K. Ljokelsoy, T. Midtsund and T. Undeland, "Synchronous Reference Frame Hysteresis Current Control for Grid Converter Applications", *IEEE Transactions on Industry Applications*, vol. 47, no. 5, pp. 2183-2194, 2011.

[22] Yong Feng, Jianfei Zheng, Xinghuo Yu and Nguyen Vu Truong, "Hybrid Terminal Sliding-Mode Observer Design Method for a Permanent-Magnet Synchronous Motor Control System", *IEEE Transactions on Industrial Electronics*, vol. 56, no. 9, pp. 3424-3431, 2009.

[23] X. Zhang, L. Sun, K. Zhao and L. Sun, "Nonlinear Speed Control for PMSM System Using Sliding-Mode Control and Disturbance Compensation Techniques", *IEEE Transactions on Power Electronics*, vol. 28, no. 3, pp. 1358-1365, 2013.

[24] K. Paponpen and M. Konghirun, "An improved sliding mode observer for speed sensorless vector control drive of PMSM", *Proc. IEEE IPEMC*, vol. 2, pp. 1-5, 2006-Aug.-1416.

[25] K. L. Kang, J. M. Kim, K. B. Hwang and K. H. Kim, "Sensorless control of PMSM in high speed range with iterative sliding mode observer", *Proc. IEEE APEC*, vol. 2, pp. 1111-1116, 2004-Feb.-2226.

[26] P. Thounthong, S. Sikkabut, N. Poonnoy, P. Mungporn, B. Yodwong, P. Kumam, N. Bizon, B. Nahid-Mobarakeh and S. Pierfederici, "Differential flatness based speed/torque control with state-observers of permanent magnet synchronous motor drives", *2016 IEEE Industry Applications Society Annual Meeting*, 2016.

[27] R. Kennel, M. Kazmierkowski, J. Rodriguez and P. Cortes, "Predictive control in power electronics and drives", *2008 IEEE International Symposium on Industrial Electronics*, 2008.

[28] F. Morel, Xuefang Lin-Shi, J. Retif, B. Allard and C. Buttay, "A Comparative Study of Predictive Current Control Schemes for a Permanent-Magnet Synchronous Machine Drive", *IEEE Transactions on Industrial Electronics*, vol. 56, no. 7, pp. 2715-2728, 2009.

[29] S. Vazquez, J. Rodriguez, M. Rivera, L. Franquelo and M. Norambuena, "Model Predictive Control for Power Converters and Drives: Advances and Trends", *IEEE Transactions on Industrial Electronics*, vol. 64, no. 2, pp. 935-947, 2017.

[30] Y. Zhou, H. Li, R. Liu and J. Mao, "Continuous Voltage Vector Model-Free Predictive Current Control of Surface Mounted Permanent Magnet Synchronous Motor", *IEEE Transactions on Energy Conversion*, vol. 34, no. 2, pp. 899-908, 2019.

[31] S. Bolognani, S. Bolognani, L. Peretti and M. Zigliotto, "Design and Implementation of Model Predictive Control for Electrical Motor Drives", *IEEE Transactions on Industrial Electronics*, vol. 56, no. 6, pp. 1925-1936, 2009.

[32] P. Niazi and H. Toliyat, "Online Parameter Estimation of Permanent-Magnet Assisted Synchronous Reluctance Motor", *IEEE Transactions on Industry Applications*, vol. 43, no. 2, pp. 609-615, 2007.

[33] K. Joo, I. Kim, J. Lee and S. Go, "Robust Speed Sensorless Control to Estimated Error for PMa-SynRM", *IEEE Transactions on Magnetics*, vol. 53, no. 6, pp. 1-4, 2017.

[34] P. Sarkar and S. Srinivas, "MTPA based DTC for Permanent Magnet assisted Synchronous Reluctance Motor for Electric Vehicle application", *2019 IEEE Transportation Electrification Conference and Expo, Asia-Pacific (ITEC Asia-Pacific)*, 2019.

[35] Tingting Ding, N. Takorabet, F. Sargos and Xiuhe Wang, "Design and Analysis of Different Line-Start PM Synchronous Motors for Oil-Pump Applications", *IEEE Transactions on Magnetics*, vol. 45, no. 3, pp. 1816-1819, 2009.

[36] S. Morimoto, M. Sanada and Y. Takeda, "Performance of PM-assisted synchronous reluctance motor for high-efficiency and wide constant-power operation", *IEEE Transactions on Industry Applications*, vol. 37, no. 5, pp. 1234-1240, 2001.

[37] B. Kerdsup, N. Takorabet and B. Nahidmobarakeh, "Design of Permanent Magnet-Assisted Synchronous Reluctance Motors with Maximum Efficiency-Power Factor and Torque per Cost", *2018 XIII International Conference on Electrical Machines (ICEM)*, 2018.

[38] T. Jahns, "Uncontrolled generator operation of interior PM synchronous machines following high-speed inverter shutdown", *Conference Record of 1998 IEEE Industry Applications Conference. Thirty-Third IAS Annual Meeting* (Cat. No.98CH36242).

[39] P. Niazi, H. Toliyat and A. Goodarzi, "Robust Maximum Torque per Ampere (MTPA) Control of PM-Assisted SynRM for Traction Applications", *IEEE Transactions on Vehicular Technology*, vol. 56, no. 4, pp. 1538-1545, 2007.

[40] S. Bonthu, S. Choi, A. Gorgani and K. Jang, "Design of permanent magnet assisted synchronous reluctance motor with external rotor architecture", *2015 IEEE International Electric Machines & Drives Conference (IEMDC)*, 2015.

[41] Jeihoon Baek, M. Rahimian and H. Toliyat, "Optimal design of PM assisted synchronous reluctance generators using lumped parameter model and Differential Evolution Strategy", *2009 IEEE Energy Conversion Congress and Exposition*, 2009.

[42] P. Niazi, "Permanent Magnet Assisted Synchronous Reluctance Motor Design and Performance Improvement," *Ph.D. thesis, Texas A&M University*, 2005.

[43] W. Soong, S. Han and T. Jahns, "Design of interior PM machines for field-weakening applications", *2007 International Conference on Electrical Machines and Systems (ICEMS)*, 2007.

[44] S. Sriprang, B. Nahid-Mobarakeh, N. Takorabet, S. Pierfederici, P. Kumam, N. Bizon, N. Taghavi, A. Vahedi, P. Mungporn and P. Thounthong, "Design and control of permanent magnet assisted synchronous reluctance motor with copper loss minimization using MTPA", *Journal of Electrical Engineering*, vol. 71, no. 1, pp. 11-19, 2020.

[45] I. Boldea, S.A. Nasar, "Electrical drives", *CRC Press*, 1999.

[46] A. Emami-Naeini and J. Powell, Feedback Control of Dynamic Systems, *Global Edition*.

[47] W. Leonhard, Control of Electrical Drives. *Berlin: Springer Berlin*, 2013.

[48] H. Ertan, *Modern electrical drives*. Dordrecht: Springer, 2011.

[49] A. Glumineau and J. León Morales, *Sensorless AC Electric Motor Control*.

[50] J. K. Author, "Etude et optimisation de machines à aimants permanents à démarrage direct sur le réseau," *Ph.D. dissertation, UL. Département de Formation Doctorale ''Electronique et Electrotechnique''*, Docteur de l'Université Henri Poincaré, Nancy, France, 2011.

[51] Chen, Xiao et al. "A High-Fidelity And Computationally Efficient Model For Interior Permanent-Magnet Machines Considering The Magnetic Saturation, Spatial Harmonics, And Iron Loss Effect".*IEEE Transactions On Industrial Electronics*, vol 62, no. 7, pp. 4044-4055, July 2015.

[52] P. Vas, Sensorless vector and direct torque control. *Oxford: Oxford University Press*, 2003.

[53] K. Rajashekara and A. Kawamura, "Sensorless control of permanent magnet AC motors", *Proceedings of IECON'94 - 20th Annual Conference of IEEE Industrial Electronics*.

[54] K. Rajashekara, A. Kawamura and K. Matsuse, Sensorless control of AC motor drives. Piscataway, N.J.: *IEEE Press*, 1996.

[55] J. Holtz, "Sensorless control of induction motor drives", *Proceedings of the IEEE*, vol. 90, no. 8, pp. 1359-1394, 2002.
[56] M. Malinowski, "Sensorless Control Strategies for Three-Phase PWM Rectifiers", *PhD Thesis, Warsaw University of Technology*, 2001.
[57] Ch. Perera, "Sensorless Control of Permanent Magnet Synchronous Motor Drives", *PhD thesis, Institute of Energy Technology*, 2002.
[58] S. Lee, "Closed-Loop Estimation of Permanent Magnet Synchronous Motor Parameters by PI Controller Gain Tuning", *IEEE Transactions on Energy Conversion*, vol. 21, no. 4, pp. 863-870, 2006.
[59] Jang-Mok Kim and Seung-Ki Sul, "Speed control of interior permanent magnet synchronous motor drive for the flux weakening operation", *IEEE Transactions on Industry Applications*, vol. 33, no. 1, pp. 43-48, 1997.
[60] Ping-Yi Lin and Yen-Shin Lai, "Voltage Control Technique for the Extension of DC-Link Voltage Utilization of Finite-Speed SPMSM Drives", *IEEE Transactions on Industrial Electronics*, vol. 59, no. 9, pp. 3392-3402, 2012.
[61] P. Martin and P. Rouchon, "Flatness and Induction Motors", *IFAC Proceedings Volumes*, vol. 30, no. 27, pp. 451-454, 1997.
[62] M. Fliess, J. Levine, P. Martin and P. Rouchon, "A Lie-Backlund approach to equivalence and flatness of nonlinear systems", *IEEE Transactions on Automatic Control*, vol. 44, no. 5, pp. 922-937, 1999.
[63] P. Martin, R. Murray and P. Rouchon, "Flat systems, equivalence and feedback", *Advances in the control of nonlinear systems*, pp. 5-32.
[64] FLIESS, M.; LÉVINE, J.; MARTIN, P.; ROUCHON, P. Flatness and defect of non-linear systems: introductory theory and examples. *International Journal of Control 1995*, 61, 1327-1361.
[65] M. Fliess, J. Lévine, Ph. Martin, and P. Rouchon. Sur les systèmes non linéaires différentiellement plats. *C.R. Acad. Sci. Paris*, 1-315:619-624, 1992.
[66] M. Fliess, J. Lévine, Ph. Martin, and P. Rouchon. Flatness and defect of nonlinear systems: introductory theory and examples. Int. J. *Control*, 61 (6): 1327-1361, 1995.
[67] S. Sriprang et al., "Permanent Magnet Synchronous Motor Dynamic Modeling with State Observer-based Parameter Estimation for AC Servomotor Drive Application", Applied Science and Engineering Progress, vol. 12, no. 4, 2019. Available: 10.14416/j.asep.2019.11.001.
[68] P. Thounthong, S. Pierfederici, and B. Davat, "Analysis of differential flatness-based control for a fuel cell hybrid power source," *IEEE Trans. Energy Convers.*, vol. 25, no. 3, pp. 909–920, Sep. 2010.
[69] M. H. Variani and K. Tomsovic, "Two-Level control of doubly fed induction generator using flatness-based approach," *IEEE Trans. Power Syst.*, vol. 31, no. 1, pp. 518–525, Jan. 2016.
[70] M. Zandi, R. Gavagsaz Ghoachani, M. Phattanasak, J. Martin, B. Nahidmobarakeh, S. Pierfederici, B. Davat and A. Payman, "Flatness based control of a non-ideal DC/DC boost converter", *IECON 2011 - 37th Annual Conference of the IEEE Industrial Electronics Society*, 2011.
[71] A. Battiston, J. Martin, E. Miliani, B. Nahid-Mobarakeh, S. Pierfederici and F. Meibody-Tabar, "Control of a PMSM fed by a Quasi Z-source inverter based on flatness properties and saturation schemes", *2013 15th European Conference on Power Electronics and Applications (EPE)*, 2013.
[72] A. Houari, A. Battiston, J. Martin, S. Pierfederici and F. Meibody-Tabar, "Flatness-based-control for parallel operation of N voltage-source inverters", *2013 15th European Conference on Power Electronics and Applications (EPE)*, 2013.
[73] P. Thounthong, "Control of a Three-Level Boost Converter Based on a Differential Flatness Approach for Fuel Cell Vehicle Applications", *IEEE Transactions on Vehicular Technology*, vol. 61, no. 3, pp. 1467-1472, 2012.

[74] A. Battiston, E. Miliani, J. Martin, B. Nahid-Mobarakeh, S. Pierfederici and F. Meibody-Tabar, "A Control Strategy for Electric Traction Systems Using a PM-Motor Fed by a Bidirectional Z-Source Inverter", *IEEE Transactions on Vehicular Technology*, vol. 63, no. 9, pp. 4178-4191, 2014.

[75] Kerdsup, B.; Takorabet, N.; Nahidmobarakeh, B. Design of Permanent Magnet-Assisted Synchronous Reluctance Motors with Maximum Efficiency-Power Factor and Torque per Cost. 2018 XIII International Conference on Electrical Machines (ICEM) 2018.

[76] Menhour, L.; d'Andrea-Novel, B.; Fliess, M.; Gruyer, D.; Mounier, H. An Efficient Model-Free Setting for Longitudinal and Lateral Vehicle Control: Validation Through the Interconnected Pro-SiVIC/RTMaps Prototyping Platform. *IEEE Transactions on Intelligent Transportation Systems 2018*, 19, 461-475.

[77] Fliess, M.; Join, C. Model-free control. *International Journal of Control 2013*, 86, 2228-2252.

[78] Renaudineau, H.; Martin, J.; Nahid-Mobarakeh, B.; Pierfederici, S. DC-DC Converters Dynamic Modeling With State Ob-server-Based Parameter Estimation. IEEE Transactions on Power Electronics 2015, 30, 3356-3363.

[79] R. Hermann and A. Krener, "Nonlinear controllability and observability", *IEEE Transactions on Automatic Control*, vol. 22, no. 5, pp. 728-740, 1977.

[80] Thounthong, P.; Sikkabut, S.; Poonnoy, N.; Mungporn, P.; Yodwong, B.; Kumam, P.; Bizon, N.; Nahid-Mobarakeh, B.; Pierfederici, S. Nonlinear Differential Flatness-Based Speed/Torque Control With State-Observers of Permanent Magnet Synchronous Motor Drives. *IEEE Transactions on Industry Applications 2018*, 54, 2874-2884.

[81] P. Thounthong, S. Pierfederici and B. Davat, "Analysis of Differential Flatness-Based Control for a Fuel Cell Hybrid Power Source", *IEEE Transactions on Energy Conversion*, vol. 25, no. 3, pp. 909-920, 2010.

[82] Sriprang, S. Modeling of Nonlinear Control with Disturbance Observer-Based Parameter Estimation for Permanent Magnet Synchronous Motor. *INTERNATIONAL JOURNAL OF MATHEMATICS AND COMPUTERS IN SIMULATION 2019*, 13, 27-37.

[83] F. Veeser, T. Braun, L. Kiltz and J. Reuter, "Nonlinear Modelling, Flatness-Based Current Control, and Torque Ripple Compensation for Interior Permanent Magnet Synchronous Machines", *Energies*, vol. 14, no. 6, p. 1590, 2021.

[84] A. Corne, N. Yang, J. Martin, B. Nahid-Mobarakeh and S. Pierfederici, "Nonlinear Estimation of Stator Currents in a Wound Rotor Synchronous Machine", *IEEE Transactions on Industry Applications*, vol. 54, no. 4, pp. 3858-3867, 2018.

[85] R. Dorf and R. Bishop, Modern control systems. *Upper Saddle River (New Jersey): Prentice-Hall*, 2001.

[86] R. Kalman, "A New Approach to Linear Filtering and Prediction Problems", *Journal of Basic Engineering*, vol. 82, no. 1, pp. 35-45, 1960.

[87] R. E. Kalman et al., "Contributions to the theory of optimal control", *Boletín de la Sociedad Matemática Mexicana*, vol. 5, no. 2, pp. 102-119, 1960.

[88] P. Cortes, M. Kazmierkowski, R. Kennel, D. Quevedo and J. Rodriguez, "Predictive Control in Power Electronics and Drives", *IEEE Transactions on Industrial Electronics*, vol. 55, no. 12, pp. 4312-4324, 2008.

[89] Y. Zhang, J. Jin and L. Huang, "Model-Free Predictive Current Control of PMSM Drives Based on Extended State Observer Using Ultralocal Model", *IEEE Transactions on Industrial Electronics*, vol. 68, no. 2, pp. 993-1003, 2021.

[90] L. Xu, G. Chen and Q. Li, "Ultra-Local Model-Free Predictive Current Control Based on Nonlinear Disturbance Compensation for Permanent Magnet Synchronous Motor", *IEEE Access*, vol. 8, pp. 127690-127699, 2020.

[91] C. Agustin, J. Yu, C. Lin, J. Jai and Y. Lai, "Triple-Voltage-Vector Model-Free Predictive Current Control for Four-Switch Three-Phase Inverter-Fed SPMSM Based on Discrete-Space-Vector Modulation", *IEEE Access*, vol. 9, pp. 60352-60363, 2021.

[92] R. Skelton, "Model error concepts in control design", *International Journal of Control*, vol. 49, no. 5, pp. 1725-1753, 1989.

[93] W. Chen, "Disturbance Observer Based Control for Nonlinear Systems", *IEEE/ASME Transactions on Mechatronics*, vol. 9, no. 4, pp. 706-710, 2004.

[94] J. Yang, W. Chen, S. Li, L. Guo and Y. Yan, "Disturbance/Uncertainty Estimation and Attenuation Techniques in PMSM Drives—A Survey", *IEEE Transactions on Industrial Electronics*, vol. 64, no. 4, pp. 3273-3285, 2017.

[95] HongZhe Jin and JangMyung Lee, "An RMRAC Current Regulator for Permanent-Magnet Synchronous Motor Based on Statistical Model Interpretation", *IEEE Transactions on Industrial Electronics*, vol. 56, no. 1, pp. 169-177, 2009.

[96] R. Errouissi, M. Ouhrouche, W. Chen and A. Trzynadlowski, "Robust Cascaded Nonlinear Predictive Control of a Permanent Magnet Synchronous Motor With Antiwindup Compensator", *IEEE Transactions on Industrial Electronics*, vol. 59, no. 8, pp. 3078-3088, 2012.

[97] S. Chang, P. Chen, Y. Ting and S. Hung, "Robust current control-based sliding mode control with simple uncertainties estimation in permanent magnet synchronous motor drive systems", *IET Electric Power Applications*, vol. 4, no. 6, p. 441, 2010.

[98] S. Li, C. Xia and X. Zhou, "Disturbance rejection control method for permanent magnet synchronous motor speed-regulation system", *Mechatronics*, vol. 22, no. 6, pp. 706-714, 2012.

[99] S. Sriprang, B. Nahid-Mobarakeh, N. Takorabet, S. Pierfederici, P. Mungporn, P. Thounthong, N. Bizon, P. Kuman and Z. Shah, "Model Free-Based Torque Control of Permanent Magnet Synchronous Motor Drives", *2019 Research, Invention, and Innovation Congress (RI2C)*, 2019.

[100] M. Fliess and C. Join, "Model-free control," *International Journal of Control*, vol. 86, pp. 2228-2252, 2013.

[101] M. FLIESS and C. JOIN, "MODEL-FREE CONTROL AND INTELLIGENT PID CONTROLLERS: TOWARDS A POSSIBLE TRIVIALIZATION OF NONLINEAR CONTROL?", *IFAC Proceedings Volumes*, vol. 42, no. 10, pp. 1531-1550, 2009.

[102] M. Fliess and C. Join, "Stability margins and model-free control: A first look", *2014 European Control Conference (ECC)*, 2014.